

Copyright
By
Jaime Fernando Argudo
2006

The Dissertation Committee for Jaime Fernando Argudo certifies that this is the approved version of the following dissertation:

**NON-DESTRUCTIVE EVALUATION OF GRAVITY LOAD
CARRYING CAPACITY AND LATERAL LOAD DAMAGE
OF REINFORCED CONCRETE SLAB-COLUMN
CONNECTIONS**

Committee:

James O. Jirsa, Supervisor

Oguzhan Bayrak

Stanislav Emelianov

Kenneth H. Stokoe II

Sharon L. Wood

**NON-DESTRUCTIVE EVALUATION OF GRAVITY LOAD
CARRYING CAPACITY AND LATERAL LOAD DAMAGE
OF REINFORCED CONCRETE SLAB-COLUMN
CONNECTIONS**

by

Jaime Fernando Argudo, B.S.E.; M.S.E.

Dissertation

Presented to the Faculty of the Graduate School of
The University of Texas at Austin
in Partial Fulfillment
of the Requirements
for the Degree of

Doctor of Philosophy

The University of Texas at Austin

May 2006

Dedication

To Magdalena, Carolina, Fernanda and Jaime J.

Acknowledgements

This dissertation was conducted under the project “Gravity Load Capacity of Earthquake Damaged Slab-Column Connections” sponsored by The National Science Foundation (NSF). I express my gratitude to NSF and the project for providing financial to this dissertation.

I wish to express my gratitude and appreciation to Dr. James O. Jirsa for his guidance and support in my research. Working under his supervision has been a unique learning experience of research techniques and structural engineering principles governing flat-plate systems.

I am grateful for the contributions of Widiyanto and Ying Tian, Ph.D. students with whom I shared research activities under NSF projects. Learning as a group has been an important part of this research experience. I am also grateful for the support and comments of the dissertation committee who have also helped to guide this research.

The support staff at the Ferguson Structural Engineering Laboratory (FSEL) has been helpful in many ways. I thank the lab technicians, Blake Stasney, Mike Bell, Dennis Phillip, Eric Schell and Mike Wason for their knowledge and time spent assisting the project. I thank the office staff Regina Forward, Hortensia Peoples and Barbara Howard, for their help on various issues during the time I have been at FSEL.

I appreciate the support and camaraderie of the graduate students working in the laboratory, who have provided help to various project activities.

**NON-DESTRUCTIVE EVALUATION OF GRAVITY LOAD
CARRYING CAPACITY AND LATERAL LOAD DAMAGE
OF REINFORCED CONCRETE SLAB-COLUMN
CONNECTIONS**

Publication No. _____

Jaime Fernando Argudo, Ph.D.

The University of Texas at Austin, 2006

Supervisor: James O. Jirsa

The objective of this study was to develop a procedure to quantify the load carrying capacity of a slab-column connection as a function of the structural damage. To fulfill this objective, guidelines for damage assessment of reinforced concrete flat-plate buildings were developed. The intent of the guidelines was to assist engineers assess lateral load damage in the field and estimate the gravity load carrying capacity of the slab-column connection after an earthquake.

The relationship between gravity load carrying capacity and degree of lateral load damage was studied in laboratory. Gravity load tests were conducted on four slab-column connections and lateral load tests on five slab-column connections. It was found that when the degree of damage was slight to moderate, there was no reduction in the gravity-load-carrying-capacity of the connection. However, when the degree of damage was severe, a reduction in the gravity load carrying capacity should be expected.

The degree of lateral load damage was defined into four categories (slight, low, moderate and severe) and was characterized by the extent of cracking, stiffness degradation and yielding of the reinforcement in the slab-column connection. The degree of lateral load damage was also a function of the lateral drift level experienced by the structure.

Four assessment techniques were utilized to infer the lateral drift level. The techniques were based on results from visual observations and non-destructive testing conducted on four slab-column connections. Slab vertical deflection, crack density, crack depth, extent of areas of concrete delamination, and Seismic Wave Attenuation (SWA) measurements provided useful information for estimating the amount of damage due to cycles of lateral drift. The SWA method is a non-destructive method that has not been used previously for assessing damage in slab structures.

The guidelines provide an empirical approach for estimating the gravity load carrying capacity of a slab-column connection based on three steps: (1) assessment techniques for inferring the drift level experienced by the structure, (2) correlation of the inferred drift level with the degree of lateral load damage, and

(3) estimation of the gravity load carrying capacity of the connection based on the degree of lateral load damage.

Table of Contents

LIST OF TABLES.....	xvii
LIST OF FIGURES.....	xix
CHAPTER 1 INTRODUCTION.....	1
1.1 General	1
1.2 Scope of overall research project on reinforced concrete slab-column connections.....	3
1.3 Objectives of the project “Gravity Load Capacity of Earthquake Damaged Slab-Column Connections.”	4
1.4 Organization of the research project	5
1.5 Objectives.....	6
1.6 Scope.....	6
CHAPTER 2 EXPERIMENTAL PROGRAM	9
2.1 Introduction	9
2.2 Fabrication of Specimens	11
2.2.1 Prototype Structure.....	11
2.2.2 Specimen Dimensions	13
2.2.3 Materials.....	14
2.2.4 Specimen Design.....	16
2.2.5 Construction Sequence and Details.....	17
2.3 Test Setup.....	22
2.3.1 Lateral Loading Tests.....	22
2.3.2 Punching Shear Tests	23

2.3.3	Instrumentation.....	26
2.4	Lateral Displacement Protocols	28
CHAPTER 3 TEST RESULTS		30
3.1	Lateral Loading Test L0.5.....	30
3.2	Lateral Loading Tests on Specimens LG0.5, LR _{ST} G0.5, LR _{SH} 0.5 and LG1.0.....	31
3.3	Threshold Deflection Limits Defining Severe Lateral Load Damage.....	33
3.4	Punching Shear Tests on Specimens G0.5, G1.0, LG0.5 and LG1.0..	36
3.5	Punching Shear Failure Threshold Deflection Limits.....	38
CHAPTER 4 IDENTIFICATION OF DAMAGE UNDER LATERAL LOADING		41
4.1	Introduction	41
4.2	Crack width measurements	41
4.2.1	Specimen L0.5.....	41
4.2.2	Specimen LG0.5.....	45
4.2.3	Specimen LR _{ST} G0.5	47
4.2.4	Specimen LG1.0.....	49
4.2.5	Analysis of combined crack width data for all specimens	51
4.2.6	Conclusions on the use of crack widths to predict story drifts	52
4.3	Crack Patterns	54
4.3.1	Crack Plots	54
4.3.2	Crack Density	54
4.3.3	Specimen L0.5.....	55

4.3.4	Specimen LG0.5.....	61
4.3.5	Specimen LR _{ST} G0.5.....	66
4.3.6	Specimen LG1.0.....	70
4.3.7	Analysis of combined crack density data for all specimens	74
4.3.8	Relationship between crack density and story drift	76
4.3.9	Conclusions on the use of Crack Densities to predict Story Drifts.....	76

CHAPTER 5 NON-DESTRUCTIVE TECHNIQUES FOR DAMAGE ASSESSMENT 79

5.1	Introduction.....	79
5.2	Spectral Analysis of Surface Waves (SASW).....	80
5.2.1	Background	80
5.2.2	Damage assessment applications	86
5.2.3	Feasibility of using SASW method for damage assessment in flat-plate buildings.....	87
5.3	Impulse Response (IR).....	88
5.3.1	Background	88
5.3.2	Parameters involved in the IR test.....	89
5.3.3	Examples of mobility plots for sound and defective slabs.....	91
5.3.4	Damage assessment applications	93
5.3.5	Feasibility of using IR method for damage assessment in flat-plate buildings	94
5.4	Ultrasonic Pulse Echo	94
5.4.1	Background	94
5.4.2	Damage assessment applications	95
5.4.3	Feasibility of using Ultrasonic-Pulse-Echo method for damage assessment in flat-plate buildings	97

5.5	Nonlinear Elastic Wave Spectroscopy (NEWS)	98
5.5.1	Background	98
5.5.2	Damage assessment applications	100
5.5.3	Feasibility of using NEWS method for damage assessment in flat-plate buildings.....	102
5.6	Impact Echo.....	103
5.6.1	Background	103
5.6.2	Damage assessment applications	109
5.6.3	Feasibility of using the Impact Echo method for damage assessment in flat-plate buildings	110
5.7	Conclusions on the use of non-destructive techniques for damage assessment of flat-plate buildings	110

CHAPTER 6 DAMAGE ASSESSMENT USING IMPACT ECHO METHOD..... 112

6.1	Introduction	112
6.2	Impact Echo Technique to Determine Crack Depth	112
6.3	Impact Echo Technique to Determine Areas of Concrete Delamination	115
6.4	Test conducted on Specimen L0.5	117
6.4.1	Load-deformation envelope for specimen L0.5	117
6.4.2	Crack depth measurements in specimen L0.5	118
6.4.3	Areas of concrete delamination in specimen L0.5	125
6.4.4	Progression of damage and collapse mechanism for specimen L0.5	127
6.5	Crack Depth Measurements in Specimen LR _{ST} G0.5	132
6.5.1	Unconstrained P-wave Velocity	132
6.5.2	Procedure and Results from Crack Depth measurements	134

6.6	Crack Depth Measurements in Specimen LG1.0	136
6.6.1	Unconstrained P-wave Velocity	136
6.6.2	Procedure and Results from Crack Depth measurements	137
6.7	Evaluation of Crack Depth Data for All Tests	139
6.8	Use of Crack Depth and Delamination to Predict Drift Levels.....	142

CHAPTER 7 SEISMIC WAVE ATTENUATION METHOD..... 144

7.1	Introduction	144
7.2	Outline of the SWA method.....	145
7.3	Data Acquisition System.....	147
7.3.1	Computer and Data Acquisition Card	148
7.3.2	Signal Conditioning Module	148
7.3.3	Accelerometers.....	150
7.4	Seismic Wave Source.....	153
7.5	Use of SWA Technique on Slab-column Connections	157
7.5.1	SWA tests on specimen L0.5	157
7.5.2	SWA Tests on Specimen LG0.5	178
7.5.3	SWA Tests on Specimen LR _{ST} G0.5.....	194
7.5.4	SWA Tests on Specimen LG1.0	203
7.6	Relationship between Attenuation Ratios and Drift Levels	212
7.6.1	Analysis of linear correlations obtained for the 9/16-in. ball.....	212
7.6.2	Data scattering.....	216
7.6.3	Relationships between Drift Levels and SWA measurements	219
7.6.4	Use of Drift-SWA relationships	219

**CHAPTER 8 GUIDELINES FOR DAMAGE ASSESSMENT OF REINFORCED
CONCRETE FLAT-PLATE BUILDINGS 222**

8.1 Methodology 222

8.2 Inference of the Lateral Drift Level Experienced by the Structure... 223

 8.2.1 Introduction 223

 8.2.2 Use of the Crack Density Parameter to estimate Drift
 Level..... 225

 8.2.3 Use of Areas of Concrete Delamination and Crack
 Depth and to estimate Drift Level 226

 8.2.4 Use of the normalized vertical deflection of the slab to
 estimate Drift Level..... 230

 8.2.5 Use of the SWA technique to estimate Drift Level..... 232

8.3 Relationship between Drift Level and Degree of Damage
Experienced by the Connection..... 235

8.4 Relationship between Gravity Load Carrying Capacity And Degree
of Lateral Load Damage..... 236

CHAPTER 9 SUMMARY, CONCLUSIONS AND RECOMMENDATIONS..... 239

9.1 Summary 239

9.2 Conclusions 240

 9.2.1 Behavior of slab-column connections 240

 9.2.2 Identification of Lateral Load Damage through Visual
 Observations..... 241

 9.2.3 Lateral Load Damage Assessment through NDT
 methods 243

 9.2.4 Guidelines for Field Assessment..... 244

9.3 Recommendations for Future Research 245

APPENDIX A IMPULSE RESPONSE TEST ON A SLAB.....	247
A.1 Introduction	247
A.1.1 Objective of the Test	247
A.1.2 Specimen	248
A.1.3 Slab-Impulse-Response System	249
A.2 Test set-up	250
A.2.1 Loading and Support conditions	250
A.2.2 Data points.....	253
A.3 Test results.....	253
A.3.1 Average Mobility	253
A.3.2 Tests sequence and results.....	255
A.4 Interpretation of results	264
A.4.1 Observations.....	264
A.4.2 Conclusions	266
 APPENDIX B RESONANCE AND DIRECT-ARRIVAL TESTS	 267
B.1 Introduction	267
B.2 Tests procedure and Results	267
B.2.1 Direct Arrival Tests.....	267
B.2.2 Resonance Tests	269
B.2.3 Results	270

APPENDIX C UPGRADED DATA ACQUISITION SYSTEM FOR SWA AND IMPACT ECHO MEASUREMENTS.....	271
C.1 Introduction	271
C.2 Configuration of the Upgraded Data Acquisition	271
C.2.1 Accelerometers.....	271
C.2.2 Data Acquisition Card.....	272
C.2.3 Signal Conditioning Module	273
 APPENDIX D TYPICAL TIME HISTORY RECORDS AND FAST FOURIER TRANSFORM (FFT) PLOTS FROM SWA AND CRACK DEPTH MEASUREMENTS.....	 274
D.1 Typical Time History Records and FFT plots from SWA Measurements.....	274
D.2 Typical Time History Records and FFT plots from Crack-Depth Measurements.....	274
 REFERENCES.....	 298
 VITA.....	 302

List of Tables

Table 2.1	Test program of NSF projects	10
Table 2.2	Compressive Strength of Specimens	16
Table 3.1	Punching shear strength of non-rehabilitated specimens	37
Table 4.1	Length and density of cracks in Specimen L0.5	56
Table 4.2	Length and density of cracks in Specimen LG0.5	62
Table 4.3	Length and density of cracks in Specimen LR _{ST} G0.5	66
Table 4.4	Length and density of cracks in Specimen LG1.0	71
Table 6.1	Crack Depth Measurements in Specimen L0.5	123
Table 6.2	Crack Depth Measurements in Specimen LR _{ST} G0.5	135
Table 6.3	Crack Depth Measurements in Specimen LG1.0	139
Table 6.4	Summary of Crack Depth Measurements	140
Table 7.1	SWA Equations for Drift Levels as a function of Attenuation Ratios	219
Table 8.1	Inference of the Lateral Drift Level based on the Crack Density parameter	226
Table 8.2	Inference of Lateral Drift Level based on the Depth of a Critical Crack and the Identification of Areas of Concrete Delamination ...	227
Table 8.3	Inference of the Lateral Drift Level based on the Normalized Vertical Deflection of the slab	231
Table 8.4	Inference of Lateral Drift Level from SWA measurements at a crack formed at three different locations	235
Table 8.5	Relationship between Drift Level and Degree of Damage	237
Table 8.6	Relationship between Gravity Load Carrying Capacity and Degree of Lateral Load Damage	238
Table A.1	Mean Average Mobility for a simply supported slab at rest	264
Table A.2	Mean Average Mobility for a simply supported slab under a midpoint load	265
Table A.3	Mean Average Mobility for a cantilevered slab under a load applied at the end of the cantilever	265

Table B.1 Results from Direct Arrival and Resonance Tests270

List of Figures

Figure 2.1	Typical floor plan from the prototype building.....	11
Figure 2.2	Slab-column connection isolated from the prototype building	12
Figure 2.3	Slab-column connection tested in laboratory	13
Figure 2.4	Stress-stress curve for No.3 reinforcing bar	14
Figure 2.5	Stress-strain curve for No. 4 reinforcing bar.....	15
Figure 2.6	Reinforcement layout for specimens L0.5, G0.5, LG0.5, LR _{ST} G0.5 and LR _{SH} G0.5.....	18
Figure 2.7	Reinforcement layout for specimens G1.0 and LG1.0.....	19
Figure 2.8	Steel reinforcement prior to placement of concrete pour	20
Figure 2.9	Curing of concrete after placement of slab and bottom column ...	21
Figure 2.10	Specimen ready to be lifted.....	21
Figure 2.11	Set-up for lateral loading tests.....	24
Figure 2.12	Set-up for punching shear tests	25
Figure 2.13	Load cells, LVDT, linear potentiometer and pressure transducer installed in specimens.....	27
Figure 2.14	Displacement Protocol for specimen L0.5	29
Figure 2.15	Displacement Protocol for specimens LG0.5, LG1.0, LR _{ST} G0.5 and LR _{SH} G0.5.....	29
Figure 3.1	Hysteretic loop for specimen L0.5	31
Figure 3.2	Load – deformation envelopes for all laterally loaded specimens	32
Figure 3.3	Horizontal drift versus normalized vertical Deflection for all laterally loaded specimens	34
Figure 3.4	Determination of the Normalized Vertical Deflection of the slab in the model (specimens).....	35
Figure 3.5	Vertical load versus normalized vertical deflection for non- rehabilitated specimens	39
Figure 4.1	Critical crack in Specimen L0.5 (North axis)	42
Figure 4.2	Crack width measurements in Specimen L0.5	43
Figure 4.3	Critical crack in Specimen LG0.5 (North axis).....	46
Figure 4.4	Crack width measurements in Specimen LG0.5	47

Figure 4.5	Critical flexural crack in Specimen LR _{ST} G0.5 (North axis)	48
Figure 4.6	Critical crack in Specimen LR _{ST} G0.5 (South axis).....	48
Figure 4.7	Crack width measurements in Specimen LR _{ST} G0.5	49
Figure 4.8	Critical crack in Specimen LG1.0 at 1.25% drift (North axis)	50
Figure 4.9	Crack width measurements in Specimen LG1.0	51
Figure 4.10	Crack widths for all specimens	53
Figure 4.11	Gravity Load only (Specimen L0.5)	56
Figure 4.12	0.25% Lateral Drift (Specimen L0.5).....	57
Figure 4.13	0.5% Lateral Drift (Specimen L0.5).....	57
Figure 4.14	0.75% Lateral Drift (Specimen L0.5).....	58
Figure 4.15	1% Lateral Drift (Specimen L0.5).....	58
Figure 4.16	1.5% Lateral Drift (Specimen L0.5).....	59
Figure 4.17	1.75% Lateral Drift (Specimen L0.5).....	59
Figure 4.18	2% Lateral Drift (Specimen L0.5).....	60
Figure 4.19	2.5% Lateral Drift (Specimen L0.5).....	60
Figure 4.20	Bottom of the Slab at 2.5% Lateral Drift (Specimen L0.5)	61
Figure 4.21	Gravity Load only (Specimen LG0.5).....	62
Figure 4.22	0.25% Lateral Drift (Specimen LG0.5).....	63
Figure 4.23	0.5% Lateral Drift (Specimen LG0.5).....	63
Figure 4.24	0.75% Lateral Drift (Specimen LG0.5).....	64
Figure 4.25	1% Lateral Drift (Specimen LG0.5).....	64
Figure 4.26	1.25% Lateral Drift (Specimen LG0.5).....	65
Figure 4.27	Bottom of the Slab at 1.25% Lateral Drift (Specimen LG0.5)	65
Figure 4.28	Gravity Load only (Specimen LR _{ST} G0.5).....	67
Figure 4.29	0.25% Lateral Drift (Specimen LR _{ST} G0.5).....	67
Figure 4.30	0.5% Lateral Drift (Specimen LR _{ST} G0.5).....	68
Figure 4.31	0.75% Lateral Drift (Specimen LR _{ST} G0.5).....	68
Figure 4.32	1% Lateral Drift (Specimen LR _{ST} G0.5).....	69
Figure 4.33	1.25% Lateral Drift (Specimen LR _{ST} G0.5).....	69
Figure 4.34	Bottom of the Slab at 1.25% Lateral Drift (Specimen LR _{ST} G0.5)	70

Figure 4.35	0.25% Lateral Drift (Specimen LG1.0).....	71
Figure 4.36	0.5% Lateral Drift (Specimen LG1.0).....	72
Figure 4.37	0.75% Lateral Drift (Specimen LG1.0).....	72
Figure 4.38	1% Lateral Drift (Specimen LG1.0).....	73
Figure 4.39	1.25% Lateral Drift (Specimen LG1.0).....	73
Figure 4.40	Bottom of the Slab at 1.25% Lateral Drift (Specimen LG1.0)	74
Figure 4.41	Relationship between Crack Density and Story Drift	75
Figure 5.1	General configuration of SASW testing (Nazarian, et al., 1988)..	81
Figure 5.2	Expected dispersion curve for a concrete member with a vertical crack to a depth h (Roesset, J.M., et al, 1990).	85
Figure 5.3	Dispersion curve for a 6” deep beam with No Damage, 1”, 2” and 3” deep cracks (Bowen, 1992).	87
Figure 5.4	Slab Impulse Response Test (Olson, 2004)	89
Figure 5.5	Typical mobility plot for sound concrete (Davis, 2003)	90
Figure 5.6	Mobility record for a sound 6.7-in thick slab (Olson, 2004).....	92
Figure 5.7	Mobility record for a thin 2.6-in thick damaged slab (Olson, 2004).....	92
Figure 5.8	Ultrasonic phased array of piezo-composite transducers (Dumas, et al., 2002)	96
Figure 5.9	Ultrasonic phased array probe (Acoustic Control Systems, 2006)	96
Figure 5.10	View of electronic scanning (Poguet, et al, 2002)	97
Figure 5.11	Nonlinear effect of cracks on natural frequencies of a bell (Johnson, 1999)	100
Figure 5.12	Generation of harmonic and sideband frequencies in a nonlinear system (Johnson, 1999)	101
Figure 5.13	Spectroscopy of automobile engine bearing caps (Johnson, 1999)	101
Figure 5.14	Outline of the Impact-Echo Method.....	105
Figure 5.15	The principle of frequency analysis in the Impact –Echo Method (Sansalone and Streett, 1997).....	106
Figure 5.16	The P-wave thickness mode of vibration of a plate (Sansalone and Streett, 1997)	108

Figure 5.17	Example of the use of the Impact-Echo Method (Sansalone and Streett, 1997)	109
Figure 6.1	Scheme of the Time of Flight technique to determine crack depth (Sansalone M. J. and Streett W. B., 1997)	113
Figure 6.2	Impact Echo response of a concrete slab with and without delamination (Sansalone M. J. and Streett W. B., 1997).	116
Figure 6.3	Load Deformation Envelope Curve for Specimen L0.5.....	118
Figure 6.4	Detection of the Thickness Frequency in Specimen L0.5.....	120
Figure 6.5	Layout of accelerometers used to measure depth of critical crack in Specimen L0.5 (North Axis)	121
Figure 6.6	Crack depth measurements using a steel pipe to drop the ball at the precise position of impact.....	122
Figure 6.7	Typical locations where crack depths were measured using the Impact Echo method and visual observations.....	124
Figure 6.8	Example of the use of time-history records to measure crack depth in specimen L0.5	126
Figure 6.9	Specimen L0.5 at 0.25% Lateral Drift (North Axis).....	129
Figure 6.10	Specimen L0.5 at 0.75% Lateral Drift (North Axis).....	129
Figure 6.11	Specimen L0.5 at 1.35% Lateral Drift (North Axis).....	130
Figure 6.12	Specimen L0.5 at 1.5% Lateral Drift (North Axis).....	130
Figure 6.13	Specimen L0.5 at 1.75% Lateral Drift (North Axis).....	131
Figure 6.14	Specimen L0.5 at 2% Lateral Drift (North Axis).....	131
Figure 6.15	Failure of Specimen L0.5	132
Figure 6.16	Detection of Thickness Frequency in Specimen LR _{ST} G0.5	133
Figure 6.17	Layout of accelerometers used to measure depth of critical crack in Specimen LR _{ST} G0.5 (South Axis).....	135
Figure 6.18	Detection of Thickness Frequency in Specimen LG1.0.....	137
Figure 6.19	Layout of accelerometers used to measure depth of critical crack in Specimen LG1.0 (North Axis)	138
Figure 7.1	Attenuation of acceleration amplitudes in concrete	146
Figure 7.2	Data Acquisition System.....	147
Figure 7.3	Data Acquisition Card NI PCI-6052E.....	148
Figure 7.4	Signal Conditioning Module, NI SCXI-1531	149

Figure 7.5	Very High Sensitivity Accelerometer Model 355B04	150
Figure 7.6	High Sensitivity Accelerometer Model 352C65	151
Figure 7.7	High Sensitivity Accelerometer Model 352C33	151
Figure 7.8	Low Sensitivity Accelerometer Model 352C17	152
Figure 7.9	Low Sensitivity Accelerometer Model 352A60.....	152
Figure 7.10	Force-time function for the impact of a 9/16-in. ball (Sansalone and Streett, 1997)	155
Figure 7.11	Distribution of frequencies corresponding to the force-time function of a steel ball impacting a solid material (Sansalone and Streett, 1997)	156
Figure 7.12	Specimen L0.5.....	158
Figure 7.13	PVC pipe used to drop steel balls on concrete column	159
Figure 7.14	SWA tests on Specimen L0.5 along its North Axis	160
Figure 7.15	SWA tests on Specimen L0.5 along its East Axis.....	160
Figure 7.16	Cracking of Specimen L0.5 in the NW quadrant	162
Figure 7.17	Ch0/Ch1 Attenuation Ratios for 9/16 in. ball on North Axis.....	166
Figure 7.18	Ch0/Ch1 Attenuation Ratios for 1 ½ in. ball on North Axis.....	166
Figure 7.19	Ch0/Ch2 Attenuation Ratios for 9/16 in. ball on North Axis.....	167
Figure 7.20	Ch0/Ch2 Attenuation Ratios for 1 ½ in. ball on North Axis.....	167
Figure 7.21	Ch0/Ch3 Attenuation Ratios for 9/16 in. ball on North Axis.....	168
Figure 7.22	Ch0/Ch3 Attenuation Ratios for 1 ½ in. ball on North Axis.....	168
Figure 7.23	Ch1/Ch2 Attenuation Ratios for 9/16 in. ball on North Axis.....	169
Figure 7.24	Ch1/Ch2 Attenuation Ratios for 1 ½ in. ball on North Axis.....	169
Figure 7.25	Ch1/Ch3 Attenuation Ratios for 9/16 in. ball on North Axis.....	170
Figure 7.26	Ch1/Ch3 Attenuation Ratios for 1 ½ in. ball on North Axis.....	170
Figure 7.27	Ch2/Ch3 Attenuation Ratios for 9/16 in. ball on North Axis.....	171
Figure 7.28	Ch2/Ch3 Attenuation Ratios for 1 ½ in. ball on North Axis.....	171
Figure 7.29	Ch0/Ch2 Attenuation Ratios for 9/16 in. ball on East Axis	173
Figure 7.30	Ch0/Ch2 Attenuation Ratios for 1 ½ in. ball on East Axis	173
Figure 7.31	Cracking on East Axis of specimen L0.5 at 0.5% drift.....	174
Figure 7.32	Cracking on East Axis of specimen L0.5 at 2% drift.....	174

Figure 7.33	Alternative location of sensors for the East axis, in a plane eccentric to column centerline.....	178
Figure 7.34	Specimen LG0.5.....	179
Figure 7.35	SWA tests on specimen LG0.5 along its North axis	181
Figure 7.36	SWA tests on specimen LG0.5 along its East axis	181
Figure 7.37	Ch0/Ch1 Attenuation Ratios, 9/16 and 5/16 in. balls (North Axis)	185
Figure 7.38	Ch0/Ch2 Attenuation Ratios, 9/16 and 5/16 in. balls (North Axis)	185
Figure 7.39	Ch0/Ch3 Attenuation Ratios, 9/16 and 5/16 in. balls (North Axis)	186
Figure 7.40	Ch1/Ch2 Attenuation Ratios, 9/16 and 5/16 in. balls (North Axis)	186
Figure 7.41	Ch1/Ch3 Attenuation Ratios, 9/16 and 5/16 in. balls (North Axis)	187
Figure 7.42	Ch2/Ch3 Attenuation Ratios, 9/16 and 5/16 in. balls (North Axis)	187
Figure 7.43	Ch0/Ch1 Attenuation Ratios, 9/16 and 5/16 in. balls on East Axis	190
Figure 7.44	Ch0/Ch2 Attenuation Ratios, 9/16 and 5/16 in. balls on East Axis	190
Figure 7.45	Ch0/Ch3 Attenuation Ratios, 9/16 and 5/16 in. balls on East Axis	191
Figure 7.46	Ch1/Ch2 Attenuation Ratios, 9/16 and 5/16 in. balls on East Axis	191
Figure 7.47	Ch1/Ch3 Attenuation Ratios, 9/16 and 5/16 in. balls on East Axis	192
Figure 7.48	Ch2/Ch3 Attenuation Ratios, 9/16 and 5/16 in. balls on East Axis	192
Figure 7.49	Specimen LR _{ST} G0.5, after the application of gravity loads	194
Figure 7.50	SWA tests on specimen LR _{ST} G0.5 along its North axis	196
Figure 7.51	Crack at slab-column interface in specimen LR _{ST} G0.5	196
Figure 7.52	Ch0/Ch1 Attenuation Ratios, 9/16 and 5/16 in. balls (North Axis)	200
Figure 7.53	Ch0/Ch2 Attenuation Ratios, 9/16 and 5/16 in. balls	

	(North Axis)	200
Figure 7.54	Ch0/Ch3 Attenuation Ratios, 9/16 and 5/16 in. balls (North Axis)	201
Figure 7.55	Ch1/Ch2 Attenuation Ratios, 9/16 and 5/16 in. balls (North Axis)	201
Figure 7.56	Ch1/Ch3 Attenuation Ratios, 9/16 and 5/16 in. balls (North Axis)	202
Figure 7.57	Ch2/Ch3 Attenuation Ratios, 9/16 and 5/16 in. balls (North Axis)	202
Figure 7.58	Specimen LG1.0, after application of lateral loads, at 1.25% drift.....	203
Figure 7.59	SWA tests on specimen LG1.0 along its North axis	205
Figure 7.60	Critical crack formed in specimen LG1.0 at 4 in. from column .	205
Figure 7.61	Ch0/Ch1 Attenuation Ratios, 9/16 in. ball (North Axis).....	209
Figure 7.62	Ch0/Ch2 Attenuation Ratios, 9/16 in. ball (North Axis).....	209
Figure 7.63	Ch0/Ch3 Attenuation Ratios, 9/16 in. ball (North Axis).....	210
Figure 7.64	Ch1/Ch2 Attenuation Ratios, 9/16 in. ball (North Axis).....	210
Figure 7.65	Ch1/Ch3 Attenuation Ratios, 9/16 in. ball (North Axis).....	211
Figure 7.66	Ch2/Ch3 Attenuation Ratios, 9/16 in. ball (North Axis).....	211
Figure 7.67	Regression lines for Ch0/Ch1 Attenuation Ratios	213
Figure 7.68	Regression lines for Ch0/Ch2 Attenuation Ratios	214
Figure 7.69	Regression lines for Ch0/Ch3 Attenuation Ratios	214
Figure 7.70	Regression lines for Ch1/Ch2 Attenuation Ratios	215
Figure 7.71	Regression lines for Ch1/Ch3 Attenuation Ratios	215
Figure 7.72	Regression lines for Ch2/Ch3 Attenuation Ratios	216
Figure 7.73	Standard Deviation of data for Ch1/Ch2 attenuation ratios in specimen L0.5	218
Figure 8.2	Determination of the Normalized Vertical Deflection of the slab in the prototype building.....	231
Figure A.1	Reinforced concrete slab for SIR test.....	248
Figure A.2	Reinforcement details for the slab.....	249
Figure A.3	Slab-Impulse-Response Data Collection (Olson, 2004)	249
Figure A.4	Olson Instruments Freedom Data PC.....	250

Figure A.5	Simply supported beam loading condition.....	251
Figure A.6	End loading condition	252
Figure A.7	Support condition for Impulse Response tests conducted at rest	253
Figure A.8	Grid defining points for impulse response tests	254
Figure A.9	Mobility plot for point E5 measured for a simply supported beam condition and midpoint loading equal to P_y	254
Figure A.10	Average Mobility results for a sound slab at rest, Stage 1	255
Figure A.11	Average Mobility results for a slab with first crack on top (load $0.15P_y$), Stage 2.....	256
Figure A.12	Average Mobility results for a slab cracked on top (load $0.5P_y$), Stage 3.....	257
Figure A.13	Average Mobility results for a slab fully cracked on top (load P_y), Stage 4.....	258
Figure A.14	Average Mobility results for a slab at rest fully cracked on top, Stage 5.....	259
Figure A.15	Average Mobility results for a slab uncracked on bottom and fully cracked on top (load $0.1P_y$), Stage 6.....	260
Figure A.16	Average Mobility results for a slab cracked on bottom and fully cracked on top (load $0.5P_y$), Stage 7	261
Figure A.17	Average Mobility results for a slab fully cracked on bottom and top (load P_y), Stage 8.....	262
Figure A.18	Average Mobility results for a slab at rest fully cracked on bottom and top, Stage 9.....	263
Figure B.1	Direct Arrival Tests	268
Figure B.2	Resonance Tests – Location of Sensors	268
Figure B.3	Resonance Tests – Location of Impact Energy	269
Figure C.1	Upgraded Data Acquisition Card	272
Figure C.2	Upgraded Signal Conditioning Module	273
Figure D.1	Time History and FFT for SWA Record 001, Ch 0, Specimen L0.5, North Axis, Condition at Rest, 0% Drift	275
Figure D.2	Time History and FFT for SWA Record 001, Ch 2, Specimen L0.5, North Axis, Condition at Rest, 0% Drift	275

Figure D.3	Time History and FFT for SWA Record 001, Ch 3, Specimen L0.5, North Axis, Condition at Rest, 0% Drift	276
Figure D.4	Time History and FFT for SWA Record 001, Ch 0, Specimen L0.5, North Axis, Condition at Rest, 0.25% Drift	276
Figure D.5	Time History and FFT for SWA Record 001, Ch 1, Specimen L0.5, North Axis, Condition at Rest, 0.25% Drift	277
Figure D.6	Time History and FFT for SWA Record 001, Ch 2, Specimen L0.5, North Axis, Condition at Rest, 0.25% Drift	277
Figure D.7	Time History and FFT for SWA Record 001, Ch 3, Specimen L0.5, North Axis, Condition at Rest, 0.25% Drift	278
Figure D.8	Time History and FFT for SWA Record 001, Ch 0, Specimen L0.5, North Axis, Condition at Rest, 0.5% Drift	278
Figure D.9	Time History and FFT for SWA Record 001, Ch 1, Specimen L0.5, North Axis, Condition at Rest, 0.5% Drift	279
Figure D.10	Time History and FFT for SWA Record 001, Ch 2, Specimen L0.5, North Axis, Condition at Rest, 0.5% Drift	279
Figure D.11	Time History and FFT for SWA Record 001, Ch 3, Specimen L0.5, North Axis, Condition at Rest, 0.5% Drift	280
Figure D.12	Time History and FFT for SWA Record 001, Ch 0, Specimen L0.5, North Axis, Condition at Rest, 0.75% Drift	280
Figure D.13	Time History and FFT for SWA Record 001, Ch 1, Specimen L0.5, North Axis, Condition at Rest, 0.75% Drift	281
Figure D.14	Time History and FFT for SWA Record 001, Ch 2, Specimen L0.5, North Axis, Condition at Rest, 0.75% Drift	281
Figure D.15	Time History and FFT for SWA Record 001, Ch 3, Specimen L0.5, North Axis, Condition at Rest, 0.75% Drift	282
Figure D.16	Time History and FFT for SWA Record 001, Ch 0, Specimen L0.5, North Axis, Condition at Rest, 1% Drift	282
Figure D.17	Time History and FFT for SWA Record 001, Ch 1, Specimen L0.5, North Axis, Condition at Rest, 1% Drift	283
Figure D.18	Time History and FFT for SWA Record 001, Ch 2, Specimen L0.5, North Axis, Condition at Rest, 1% Drift	283
Figure D.19	Time History and FFT for SWA Record 001, Ch 3, Specimen L0.5, North Axis, Condition at Rest, 1% Drift	284
Figure D.20	Time History and FFT for SWA Record 001, Ch 0, Specimen L0.5, North Axis, Condition at Rest, 1.5% Drift	284

Figure D.21	Time History and FFT for SWA Record 001, Ch 1, Specimen L0.5, North Axis, Condition at Rest, 1.5% Drift	285
Figure D.22	Time History and FFT for SWA Record 001, Ch 2, Specimen L0.5, North Axis, Condition at Rest, 1.5% Drift	285
Figure D.23	Time History and FFT for SWA Record 001, Ch 3, Specimen L0.5, North Axis, Condition at Rest, 1.5% Drift	286
Figure D.24	Time History and FFT for SWA Record 001, Ch 0, Specimen L0.5, North Axis, Condition at Rest, 1.75% Drift	286
Figure D.25	Time History and FFT for SWA Record 001, Ch 1, Specimen L0.5, North Axis, Condition at Rest, 1.75% Drift	287
Figure D.26	Time History and FFT for SWA Record 001, Ch 2, Specimen L0.5, North Axis, Condition at Rest, 1.75% Drift	287
Figure D.27	Time History and FFT for SWA Record 001, Ch 3, Specimen L0.5, North Axis, Condition at Rest, 1.75% Drift	288
Figure D.28	Time History and FFT for SWA Record 001, Ch 0, Specimen L0.5, North Axis, Condition at Rest, 2% Drift	288
Figure D.29	Time History and FFT for SWA Record 001, Ch 1, Specimen L0.5, North Axis, Condition at Rest, 2% Drift	289
Figure D.30	Time History and FFT for SWA Record 001, Ch 2, Specimen L0.5, North Axis, Condition at Rest, 2% Drift	289
Figure D.31	Time History and FFT for SWA Record 001, Ch 3, Specimen L0.5, North Axis, Condition at Rest, 2% Drift	290
Figure D.32	Time History and FFT for SWA Record 001, Ch 0, Specimen L0.5, North Axis, Condition at Rest, 2.5% Drift	290
Figure D.33	Time History and FFT for SWA Record 001, Ch 1, Specimen L0.5, North Axis, Condition at Rest, 2.5% Drift	291
Figure D.34	Time History and FFT for SWA Record 001, Ch 2, Specimen L0.5, North Axis, Condition at Rest, 2.5% Drift	291
Figure D.35	Time History and FFT for SWA Record 001, Ch 3, Specimen L0.5, North Axis, Condition at Rest, 2.5% Drift	292
Figure D.36	Time History and FFT for Crack-Depth Record 001, Ch 1, Specimen LG1.0, North Axis, Condition at Rest, 0.25% Drift...	292
Figure D.37	Time History and FFT for Crack-Depth Record 001, Ch 2, Specimen LG1.0, North Axis, Condition at Rest, 0.25% Drift...	293
Figure D.38	Time History and FFT for Crack-Depth Record 001, Ch 1, Specimen LG1.0, North Axis, Condition at Rest, 0.5% Drift.....	293

Figure D.39	Time History and FFT for Crack-Depth Record 001, Ch 2, Specimen LG1.0, North Axis, Condition at Rest, 0.5% Drift.....	294
Figure D.40	Time History and FFT for Crack-Depth Record 001, Ch 1, Specimen LG1.0, North Axis, Condition at Rest, 0.75% Drift...	294
Figure D.41	Time History and FFT for Crack-Depth Record 001, Ch 2, Specimen LG1.0, North Axis, Condition at Rest, 0.75% Drift...	295
Figure D.42	Time History and FFT for Crack-Depth Record 001, Ch 1, Specimen LG1.0, North Axis, Condition at Rest, 1% Drift.....	295
Figure D.43	Time History and FFT for Crack-Depth Record 001, Ch 2, Specimen LG1.0, North Axis, Condition at Rest, 1% Drift.....	296
Figure D.44	Time History and FFT for Crack-Depth Record 001, Ch 1, Specimen LG1.0, North Axis, Condition at Rest, 1.25% Drift...	296
Figure D.45	Time History and FFT for Crack-Depth Record 001, Ch 2, Specimen LG1.0, North Axis, Condition at Rest, 1.25% Drift...	297

CHAPTER 1

Introduction

1.1 GENERAL

Flat plates are widely used in residential and commercial buildings. They are popular among developers, architects and builders, because of their versatility in configuring spaces, simplicity of formwork, low story heights and overall economy. However, flat plate systems pose special problems for structural engineers because of their inherent flexibility due to the lack of beams, limited elastic response, and complex inelastic behavior.

Many researchers have studied extensively the most common mode of failure for flat plates, the punching shear failure that is produced when the slab separates from the supporting column around the perimeter of the column at the connection. Failure of flat plates in punching shear has been the cause of numerous casualties during earthquakes. Earthquakes, winds or other sources of lateral loading, can cause substantial damage to the slab-column connection, which may reduce its ability to sustain gravity loads. Failure due to punching shear may trigger a progressive collapse of the entire building, leading to a “pancake” type failure mode, a brittle failure mechanism in which slabs collapse onto other slabs with little warning to the building occupants.

The behavior of slab-column connections under lateral loads has also been extensively studied by previous researchers, for conditions where the slab is

supporting different levels of gravity loads. However, the relationship between lateral load damage and gravity load carrying capacity has not been studied and the effects of damage induced by earthquakes in existing flat plates on the gravity load carrying capacity is not well understood.

Detailing of the slab-column connection is essential for providing ductility to the connection or the ability to sustain large lateral displacements without reduction in the lateral load carrying capacity of the connection. The current design code ACI 318-05 has several requirements to address this issue; however older structures lack these details and often require strengthening to achieve adequate strength and ductility.

Research on techniques to strengthen existing structures and to rehabilitate structures damaged by earthquakes is required. There is also a need for better understanding of the relationship between lateral load damage and gravity load carrying capacity at different drift levels and deformation limits.

Currently, there is insufficient technical data on which to base safe deformation limits for protecting the gravity load carrying capacity of reinforced concrete slab-column connections, for selecting appropriate rehabilitation techniques and for evaluating their effectiveness. Therefore, the outcome of this research will be valuable for evaluating the structural condition of existing buildings, for retrofit and strengthening of earthquake damaged structures, for rehabilitation of undamaged vulnerable structures, and for design of new systems.

1.2 SCOPE OF OVERALL RESEARCH PROJECT ON REINFORCED CONCRETE SLAB-COLUMN CONNECTIONS

To address the need for further studies of the behavior of slab-column connections in flat plate buildings, two research projects sponsored by the National Science Foundation (NSF) were combined to develop a study that permitted investigation of many of the issues described above. The two projects were titled:

- i. Gravity Load Capacity of Earthquake Damaged Slab-Column Connections
- ii. Punching Shear Upgrade of Reinforced Concrete Flat Plates

In the first project, the relationship between lateral load damage and gravity load carrying capacity of the slab-column connection in a flat plate building was investigated. In the second project, the behavior of identical connections after strengthening to improve punching shear capacity was investigated. Two methods were used to strengthen the connections: fiber reinforced polymers and steel collars.

This dissertation was conducted under the framework and objectives of the NSF project “Gravity Load Capacity of Earthquake Damaged Slab-Column Connections.”

1.3 OBJECTIVES OF THE PROJECT “GRAVITY LOAD CAPACITY OF EARTHQUAKE DAMAGED SLAB-COLUMN CONNECTIONS.”

The aim of the project “Gravity Load Capacity of Earthquake Damaged Slab-Column Connections” was to study the relationships between the gravity load carrying capacity of a reinforced concrete slab-column connection and the degree of damage that has occurred previously as a result of earthquake loads.

The overall objective was to develop procedures to quantify the load carrying capacity of the slab-column connection as a function of the structural damage. The main goals of the project were:

- i. To determine the conditions under which punching shear failure due to gravity loads will occur after the structure has suffered earthquake damage
- ii. To develop response characteristics for slab-column connections
- iii. To establish reasonable deformation limits for evaluation and design of rehabilitation schemes for existing slab-column structures
- iv. To evaluate the feasibility of strengthening slab-column connections

A series of tests were conducted to determine the relationship between punching shear capacity of the slab-column connection under gravity loads and

the level of previous damage to the slab by earthquake loads. The gravity loading was increased incrementally until a punching shear failure occurred.

1.4 ORGANIZATION OF THE RESEARCH PROJECT

Work was organized into two separate studies:

- i. Behavior and modeling of lightly-reinforced flat plate-column connections under different loading histories
- ii. Non-destructive evaluation of gravity load carrying capacity and lateral load damage of reinforced concrete slab-column connections

In the first study, the response characteristics of the slab-column connections were investigated using results from tests conducted under this project and tests reported in the literature and from mathematical models.

The second study, which is presented in this dissertation, was focused on establishing relationships between lateral load damage and gravity load carrying capacity of the slab-column connections, using test results and non-destructive methods of evaluation.

1.5 OBJECTIVE

The objective of this dissertation is to develop tools that can be used to assess damage in the field and to estimate the capacity of the slab-column connection after an earthquake. For such purpose, the most difficult issue to resolve is the development of empirical relationships based on assessment techniques used to evaluate the capacity of damaged slab-column connections.

1.6 SCOPE

Guidelines for field assessment of the structural condition of earthquake damaged flat-plate buildings are based on an empirical approach developed to assess the structural condition of a damaged slab-column connection. Visual observations and non destructive testing were used to develop such an empirical approach.

The structural condition is characterized by the level of damage experienced by the connection, which is defined in terms of the lateral drift ratio, the density of cracks, the extent of yielding of the reinforcement in the slab at the connection and results from non-destructive testing (NDT).

Visual observations include measurements of crack widths, the study of cracking patterns and the computation of crack densities for damage assessment.

Assessment techniques using NDT include the use of the Impact Echo (IE) method to calculate crack depths and the development of the Seismic Wave Attenuation (SWA) method to estimate the loss of energy experienced by seismic waves when they travel through critical cracks.

Results from visual observations and assessment techniques are used to infer the drift level in the connection. The inferred drift level is correlated with the damage level and strength in the connection and finally a relationship between lateral load damage and punching shear capacity is obtained.

A description of the experimental program is presented in Chapter 2 and the results from experiments conducted on slab-column connections are presented in Chapter 3. The identification of damage under lateral loading is presented in Chapter 4. Damage is identified through visual observations of crack widths and crack densities.

Several non-destructive techniques for damage assessment are described in Chapter 5. The feasibility of using such techniques for assessing damage in the slab-column connections will be evaluated and discussed. The seismic wave attenuation method, a method implemented in this study for damage assessment in slab-column connections, is presented in Chapter 6. Chapter 7 contains the assessment of damage through crack depth measurements performed using the Impact-Echo method.

Guidelines for field assessment of the structural condition of earthquake damaged flat-plate buildings are presented in Chapter 8. Conclusions and recommendations for future research are given in Chapter 9.

Four Appendixes are provided: (A) results from Impulse Response tests on a slab, (B) results from resonance and direct-arrival tests, (C) specifications for an upgraded data acquisition system for seismic wave attenuation (SWA) and impact-echo (IE) measurements, and (D) examples of response records from SWA and IE measurements.

CHAPTER 2

Experimental Program

2.1 INTRODUCTION

Under the combined projects, ten slab-column specimens were tested. The test program is summarized in Table 2.1.

In Table 2.1, the notation is as follows: “L” stands for lateral load test, “G” for gravity load test, “LG” for lateral load test followed by gravity load test, “LR_{ST}G” for lateral load test followed by rehabilitation with CFRP stirrups and gravity load test, “LR_{SH}G” for lateral load followed by rehabilitation with CFRP sheets and gravity load test, “R_CG” for rehabilitation with steel collar followed by gravity load test, and “R_CL” for rehabilitation with steel collar followed by lateral load test. The slab top reinforcement ratio, 0.5 or 1.0%, in the (c+3h) region within the column strip is included at the end of the specimen notation.

Tests of specimens strengthened with steel collars (R_CG0.5, R_CG1.0 and R_CL1.0) and specimens rehabilitated with Carbon-Fiber-Reinforced-Polymers (CFRP) stirrups and sheets (LR_{ST}G0.5 and LR_{ST}G1.0), were conducted under the project on “Punching Shear Upgrade of Reinforced Concrete Flat Plates.” Results from those tests can be found in Widiyanto (2006).

Data from lateral loading and punching shear tests on specimens without strengthening (L0.5, G0.5, G1.0, LG0.5 and LG1.0) and data from tests LR_{ST}G0.5 and LR_{ST}G1.0 (prior to rehabilitation) were utilized by the project on “Gravity Load Capacity of Earthquake Damaged Slab-Column Connections.” Results from those tests are presented in this section.

Table 2.1 *Test program of NSF projects*

Specimen	Type of Test
L0.5	Lateral loading up to failure
G0.5	Punching shear loading up to failure
G1.0	Punching shear loading up to failure
LG0.5	Lateral loading up to 1.25% drift and then punching shear loading up to failure
LG1.0	Lateral loading up to 1.25% drift and then punching shear loading up to failure
LR _{ST} G0.5	Lateral loading up to 1.25% drift, rehabilitated by external CFRP stirrups and then punching shear loading up to failure
LR _{SH} G0.5	Lateral loading up to 1.25% drift, rehabilitated by CFRP sheets and then punching shear loading up to failure
R _C G0.5	Strengthening of G0.5 with a steel collar and then punching shear loading up to failure
R _C G1.0	Strengthening of G1.0 with a steel collar and then punching shear loading up to failure
R _C L1.0	Strengthening of LG1.0 with a steel collar and then lateral loading up to failure

2.2 FABRICATION OF SPECIMENS

2.2.1 Prototype Structure

The prototype structure is an office building with 12-ft story height, 21-ft wide bays, 24-in square columns and 9-in slab thickness. The prototype building was designed according to ACI 318-63, for a live load equal to 50 psf and without consideration of seismic effects. A typical floor plan from the prototype building is shown in Figure 2.1.

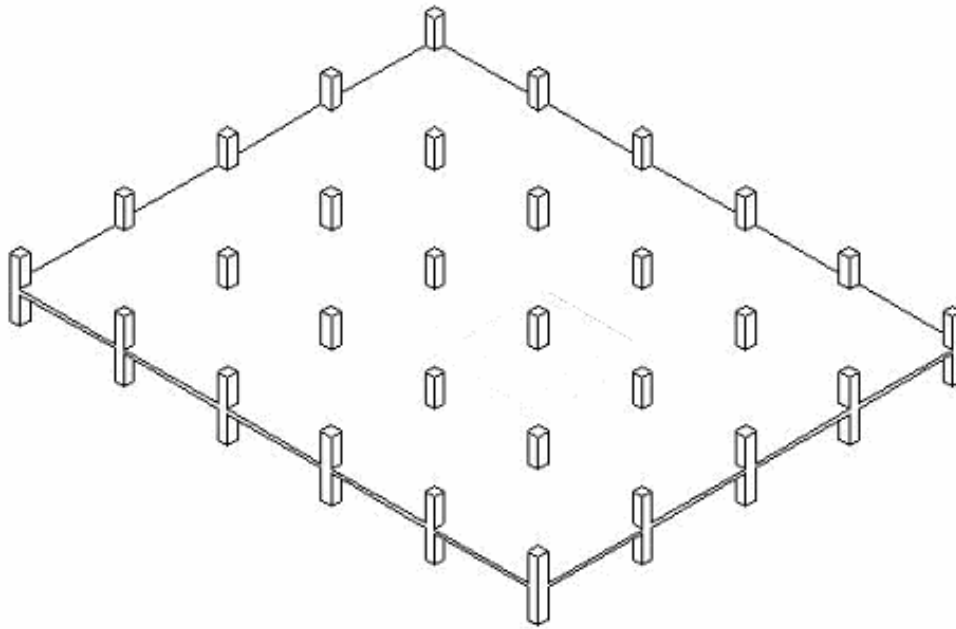


Figure 2.1 Typical floor plan from the prototype building

Figure 2.2 shows a slab-column connection isolated along lines of symmetry, lines of inflection in the slab and points of inflection in the columns, when the structure is subjected to pure lateral loading.

In the prototype building, an isolated slab-column connection consists of a 21-ft square panel, a 9-in thick slab and a 12-ft story height.

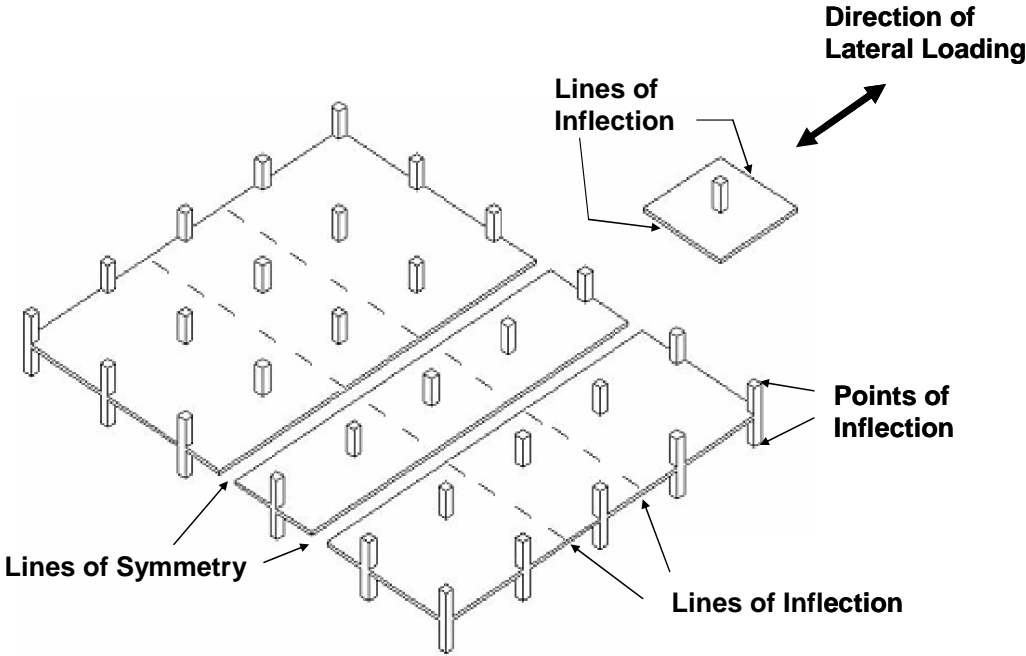


Figure 2.2 *Slab-column connection isolated from the prototype building*

2.2.2 Specimen Dimensions

The specimens described in Table 2.1 were built at 2/3 scale of the prototype building to fit the dimensions of the laboratory floor-wall reaction system. The story (column) height was 8-ft and the slab 14-ft by 14-ft square. The column was 16-in square and the slab was 6-inch thick. Figure 2.3 shows a slab-column connection tested in laboratory.



Figure 2.3 Slab-column connection tested in laboratory

2.2.3 Materials

2.2.3.1 Reinforcing bars

Reinforcing bars were Grade 60 steel that satisfy ASTM A 706-04 specifications. US #3 and #4 bars were used, with actual average yield strength measured from axial tension tests equal to 66 ksi and 63 ksi respectively. Three bars were tested from each type of bar. Stress-strain curves are shown in Figure 2.4 and Figure 2.5.

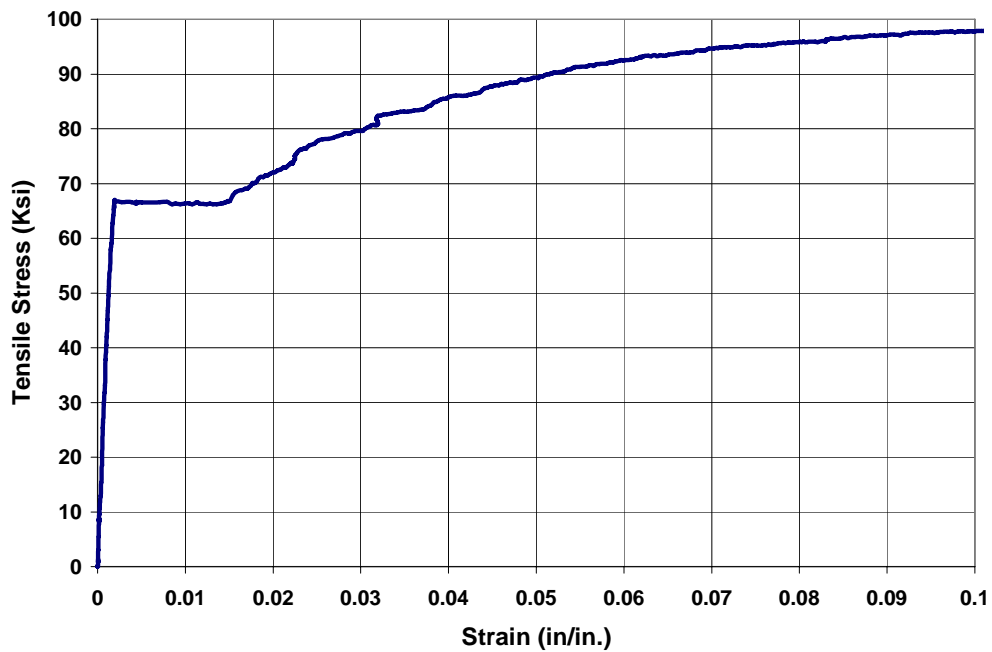


Figure 2.4 Stress-stress curve for No.3 reinforcing bar

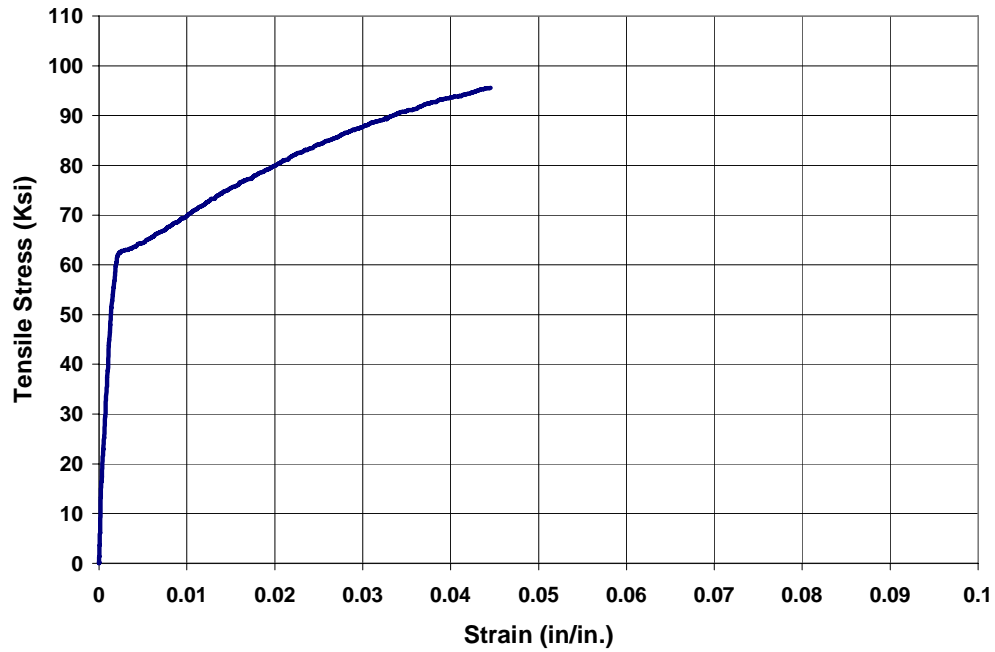


Figure 2.5 Stress-strain curve for No. 4 reinforcing bar

2.2.3.2 Concrete

Compressive strength f'_c was specified as 4,000 psi. Actual strength measured from concrete cylinders ranged from 3,710 to 4,930 psi as reported in Table 2.2.

Table 2.2 Compressive Strength of Specimens

Specimen	Compressive Strength (psi)	Age of Testing (days)
L0.5	3710	104
G0.5	4550	53
G1.0	4070	64
LG0.5	4860	84
LG1.0	4000	140
LR _{ST} G0.5	4930	138
LR _{SH} G0.5	4630	145

2.2.4 Specimen Design

Specimens L0.5, G0.5, LG0.5, LR_{ST}G0.5 and LR_{SH}G0.5 were designed for the conditions described for the prototype building in Section 2.2.1. Figure 2.6 shows the reinforcement layout for these specimens. US #4 and #3 bars were used in the top layer for the column and middle strips, respectively. US #3 bars were used in the bottom layer. The reinforcement ratio in the negative moment region in the column strip was 0.5%. The reinforcement ratio was 0.25% at all other regions (column and middle strip).

To study the effects of a higher top reinforcement ratio on the relationship between lateral loading and punching shear capacity, specimens G1.0 and LG1.0 were designed with 1% top reinforcement ratio in the $(c+3h)$ region within the column strip as referenced in Section 13.5.3.2 of ACI 318-05 ($c = 16$ in. is the column width and $h = 6$ in. is the slab depth), 0.5% top reinforcement ratio in the rest of the column strip and 0.25% reinforcement ratio elsewhere. The reinforcement layout for these specimens is shown in Figure 2.7.

For all specimens, the top and bottom reinforcement layers in the lateral loading direction had a clear cover equal to 0.5 in. and an average effective depth of slab reinforcement d equal to 5 in.

Since the specimens were designed according to ACI 318-63, the bottom reinforcement was not continuous and was terminated 2-in. from the slab centerline. This is a significant detailing difference from current code provisions, which require continuity of the bottom reinforcement layer to prevent progressive collapse of the structure.

2.2.5 Construction Sequence and Details

Wooden forms were constructed to cast specimens. Forty-eight PVC pipes were used in each specimen to create holes at locations where steel struts were connected. As explained later, steel struts were used to conduct lateral load and gravity load tests. Figure 2.8 shows the steel reinforcement installed in the forms prior to placing the concrete.

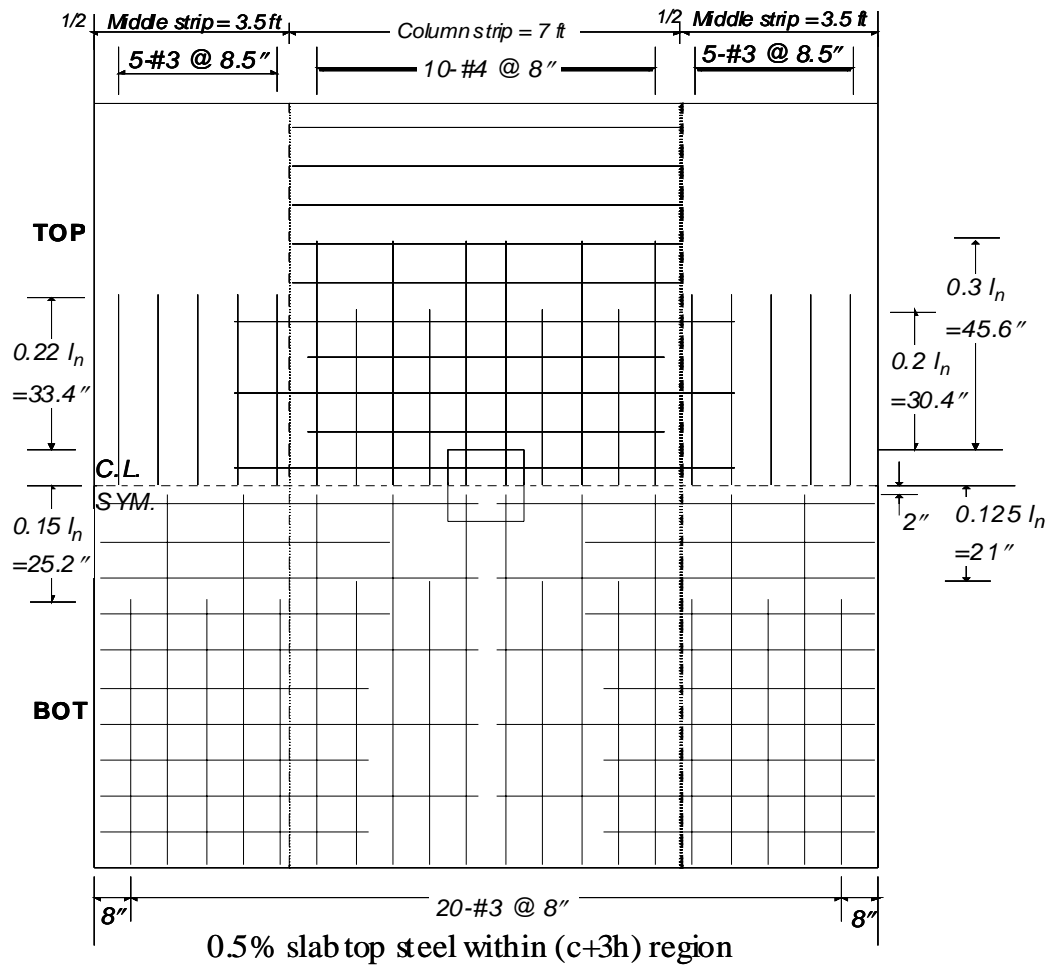


Figure 2.6 Reinforcement layout for specimens L0.5, G0.5, LG0.5,
 LR_{ST}G0.5 and LR_{SH}G0.5

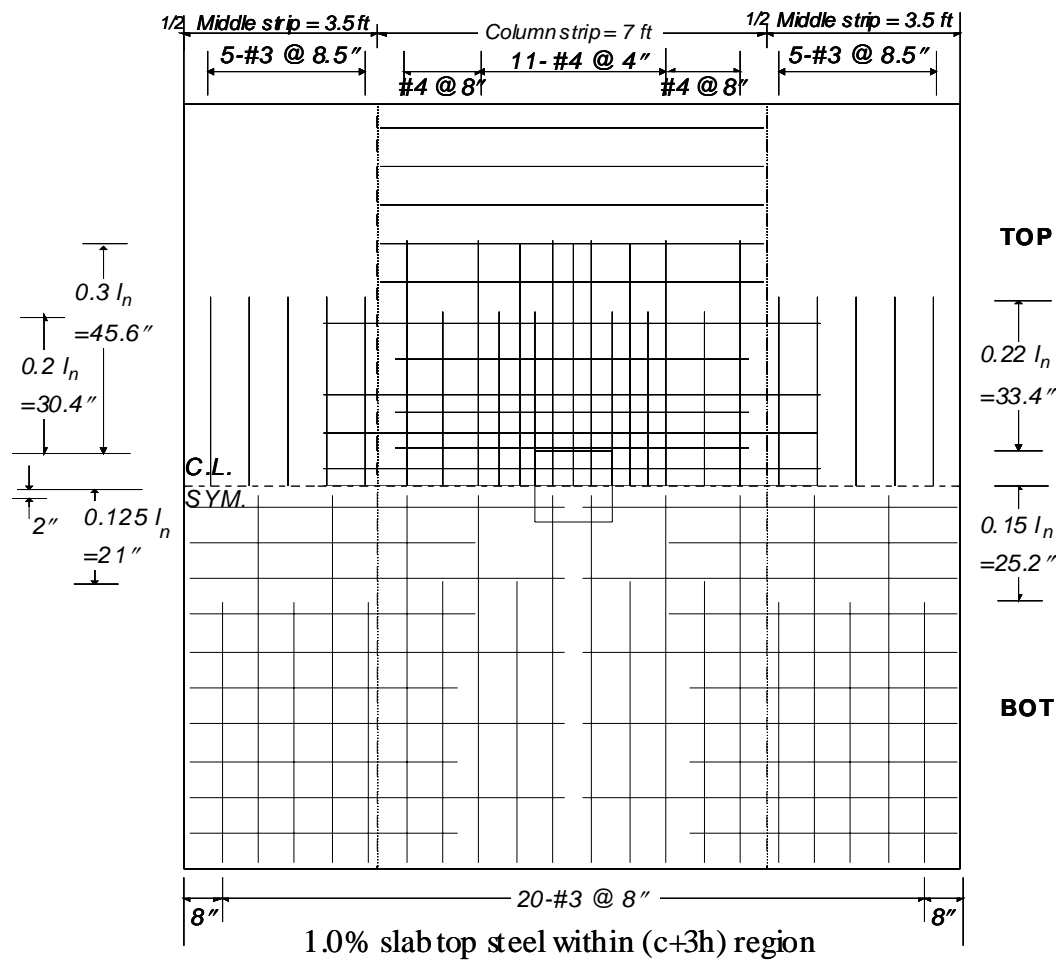


Figure 2.7 Reinforcement layout for specimens G1.0 and LG1.0

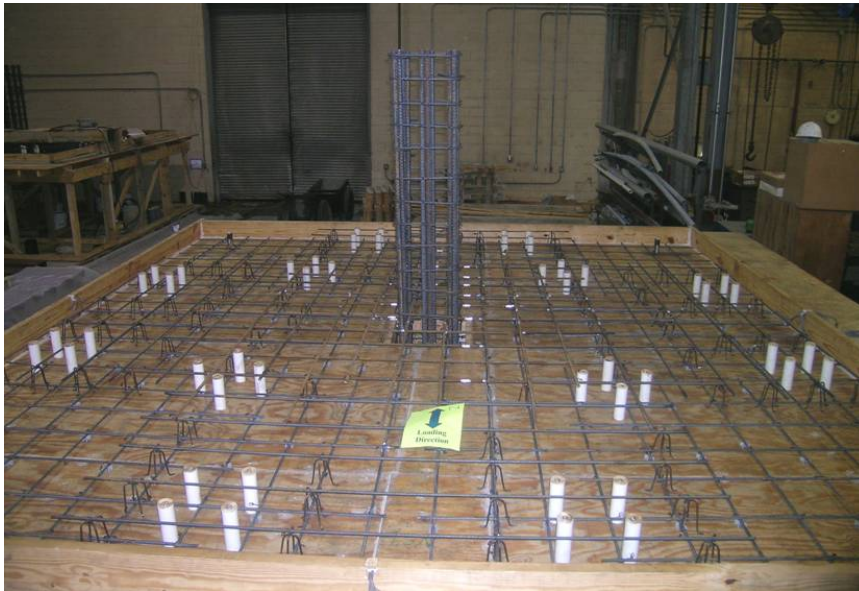


Figure 2.8 *Steel reinforcement prior to placement of concrete pour*

The slab and the bottom column were cast first and the top column was cast a few days after. A cold joint was formed between the slab and the top column. The slab surface at that interface was left intentionally rough for better force transfer across the cold joint. Figure 2.9 shows a specimen after the slab and the bottom column were cast.

Four steel coils were embedded at the slab corners to install lifting devices. Four PVC pipes were installed in the top column to create holes at locations where the horizontal actuator was connected. As explained later, a horizontal actuator was used to conduct lateral load tests. The steel coils and holes in the column were used to install the lifting devices. Figure 2.10 shows a specimen ready to be lifted from the formwork and moved to test area.



Figure 2.9 Curing of concrete after placement of slab and bottom column



Figure 2.10 Specimen ready to be lifted

2.3 TEST SETUP

2.3.1 Lateral Loading Tests

The set-up for lateral loading tests is shown in Figure 2.11. Specimens were placed on 8 vertical struts located along the slab perimeter and a vertical ram was located under the column.

Vertical struts were connected to the slab through clevises that allowed rotation in the direction of loading (north-south) but restrained vertical displacements. The location of the struts and clevises was selected based on results from finite element analyses (Tian, 2006), where a boundary condition of zero moment at the position of clevises was used to simulate inflection points at mid-spans of the slab in the prototype building.

The ram installed under the column provided a constant upward vertical load equivalent to dead plus 25% live load. Shear stresses acting on the critical shear perimeter " b_o " located " $d/2$ " away from the column were produced by loading the column against the direction of gravity loads.

A horizontal strut and a clevis were connected to the end of the bottom column, to provide rotational freedom along the direction of loading (north-south) and restraint against horizontal displacements at the end of the bottom column. In this manner, the inflection point located at the mid-height of the bottom column in the prototype building was modeled. Lateral loading along the north-south direction was provided by a horizontal actuator connected at the end of the top

column. The end of the top column was free to displace and rotate. In this manner, the inflection point located at the mid-height of the top column in the prototype building was modeled. To prevent any rotational movement in the plane of the slab, two horizontal struts were attached to the slab at its North and South sides.

2.3.2 Punching Shear Tests

The set-up for punching shear tests is shown in Figure 2.12. Specimens were placed on 4 vertical struts located at approximately 2-feet from the center of the column. A vertical ram was located under the column. The position of the vertical struts was selected based on results from finite elements analyses (Ying, 2006) that modeled the shear stresses at the critical shear perimeter “ b_o ” under a condition of pure gravity load applied to the slab.

No lateral loads were induced during punching shear tests, but the horizontal actuator at the end of the top column provided lateral stability to the specimens. Similarly to lateral loading tests, two horizontal braces were attached to the slab at its North and South sides, to prevent any rotational movement in the plane of the slab.

Vertical loading was provided through the ram located under the column. Loads in the ram were gradually increased until punching shear failure was achieved.

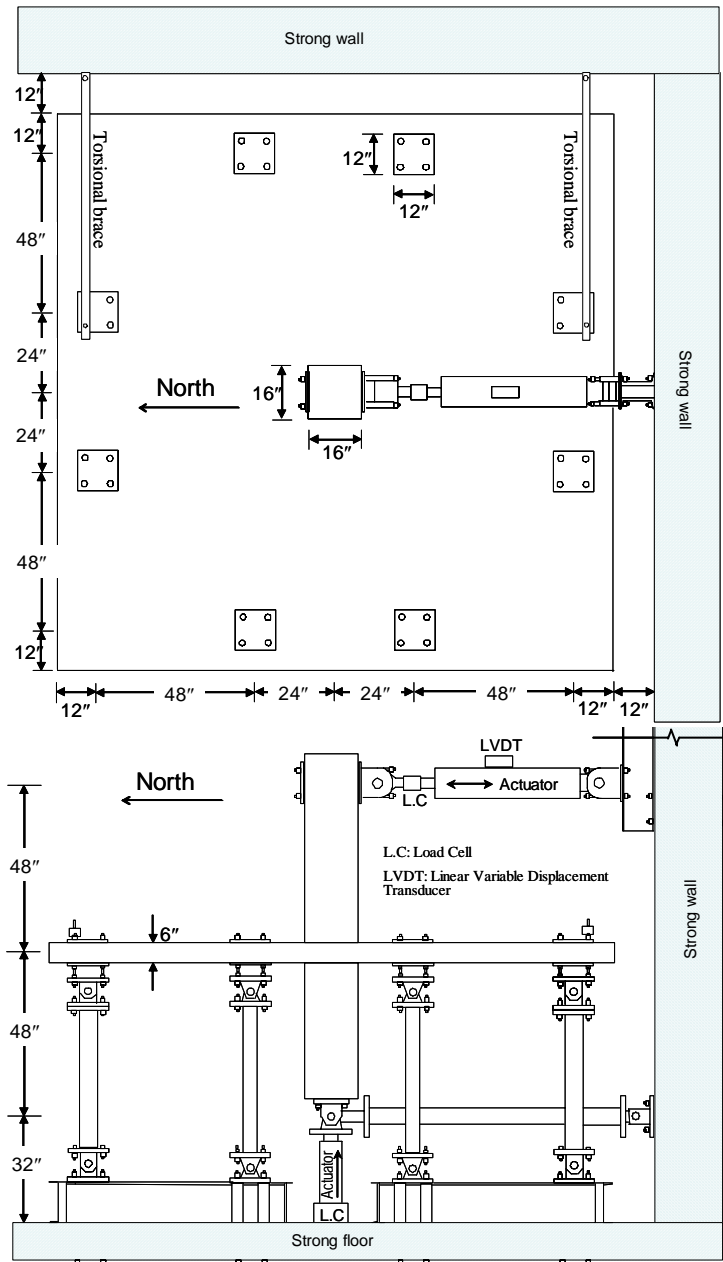


Figure 2.11 *Set-up for lateral loading tests*

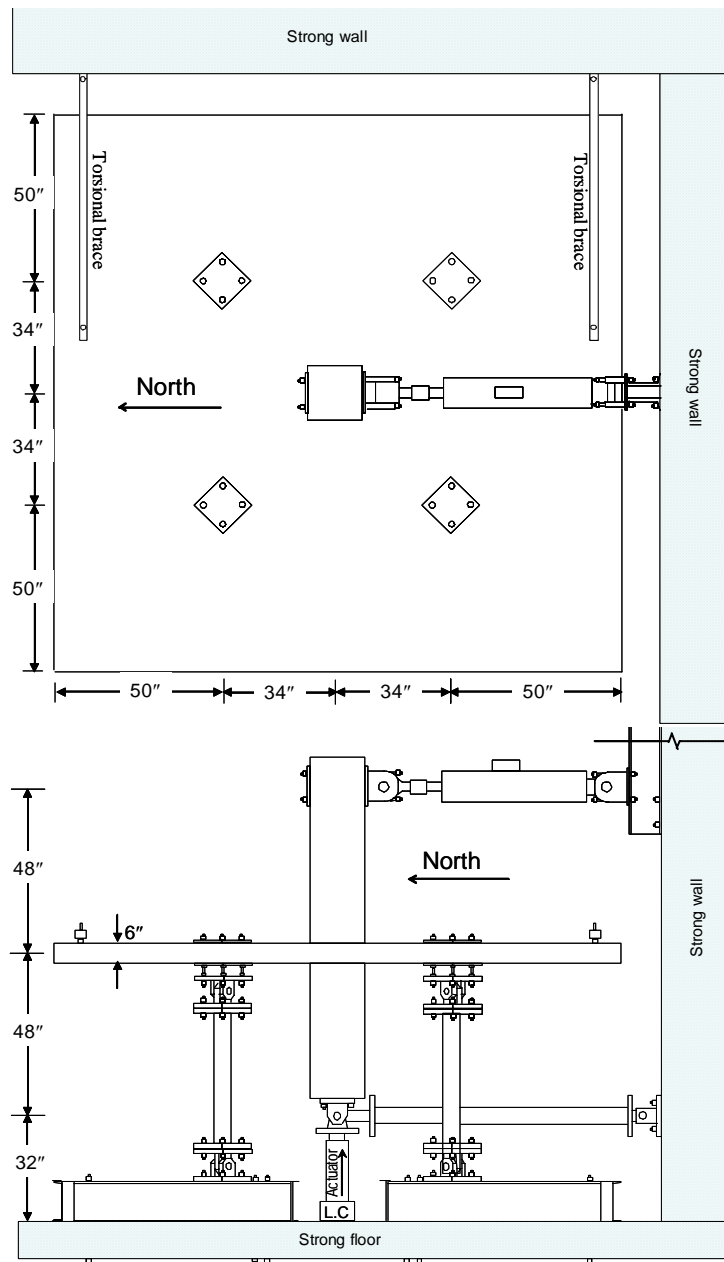


Figure 2.12 *Set-up for punching shear tests*

2.3.3 Instrumentation

The following instrumentation was used (Figure 2.13):

- i. A Linear Variable Displacement Transducer (LVDT) and a load cell were installed at the upper end of the top column, at the position where the horizontal actuator was connected to the column. Such sensors are integrated components of the horizontal actuator. The horizontal displacement measured by the LVDT was used to compute the story drift. The load cell provided measurements of the lateral load applied to the slab-column connection.
- ii. A load cell was installed under the ram located below the bottom column. This load cell was used to measure the vertical load applied to the column. A pressure transducer attached to the pump provided a redundant measurement of the applied vertical load.
- iii. A linear potentiometer was installed under the bottom column to measure the vertical displacement of the connection. Measurements from this linear potentiometer were used to compute the slab vertical deflection. Two additional linear potentiometers were installed at the SW and SE corners of the slab, between the slab and the reaction wall, to measure the horizontal displacement of the slab in the loading direction. Measurements from such linear potentiometers were used to verify that no rotation was experienced by the slab in its own plane.

- iv. A number of strain gages were installed on the slab reinforcement, to investigate the strain and stress distribution in the slab.

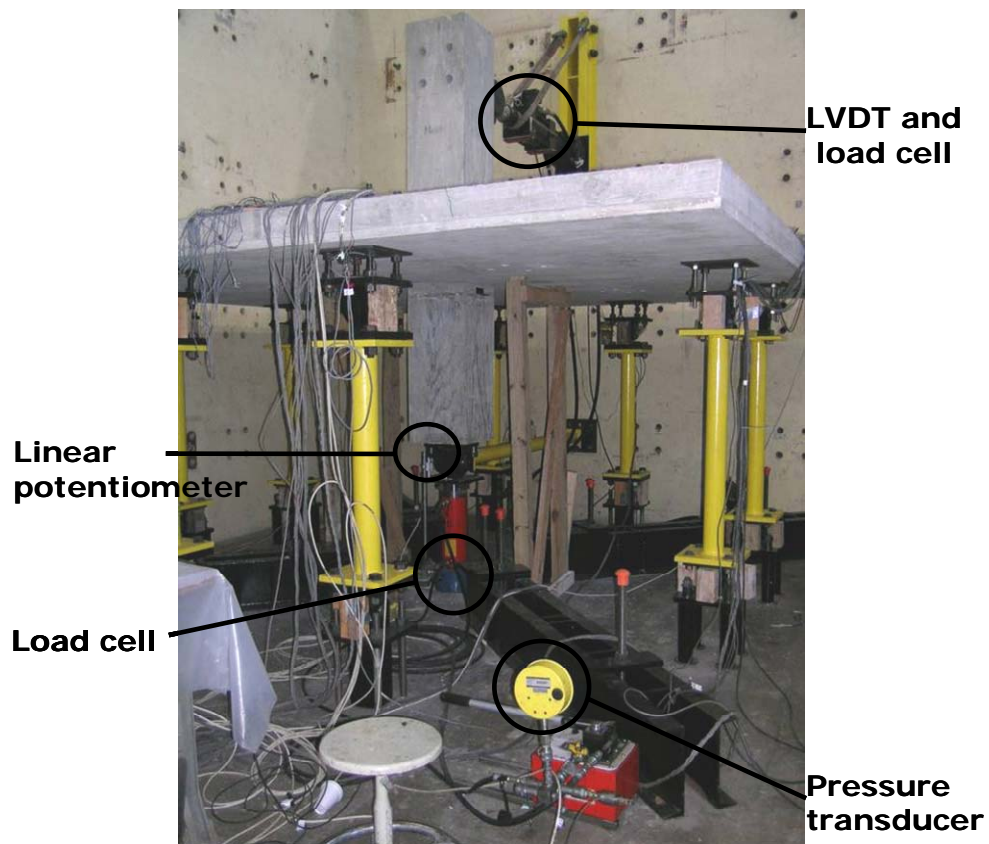


Figure 2.13 Load cells, LVDT, linear potentiometer and pressure transducer installed in specimens

2.4 LATERAL DISPLACEMENT PROTOCOLS

Lateral loads followed displacement protocols or functions presented in Figure 2.14 and Figure 2.15. Therefore, lateral loading tests were displacement controlled and the connection was subjected to incremental displacement steps or levels, each of which comprised three fully-reversed displacement cycles.

Five specimens were laterally loaded. Specimen L0.5 was loaded up to failure, using the displacement protocol shown in Figure 2.14, which ends at a story drift equal to 2.5%. Specimens LG0.5, LG1.0, LR_{ST}G0.5 and LR_{SH}G0.5 were only loaded up to 1.25% drift, using the displacement protocol shown in Figure 2.15.

In all lateral loading tests, the column axial load was kept constant to produce a shear force “ V ” on the critical shear perimeter equal to $0.92\sqrt{f'_c}b_o d$, where $b_o = 84$ in. is the critical shear perimeter, $d = 5$ in. is the average depth of the slab reinforcement and f'_c is the concrete compressive strength. V was set equal to dead load plus 25% live load on the prototype structure.

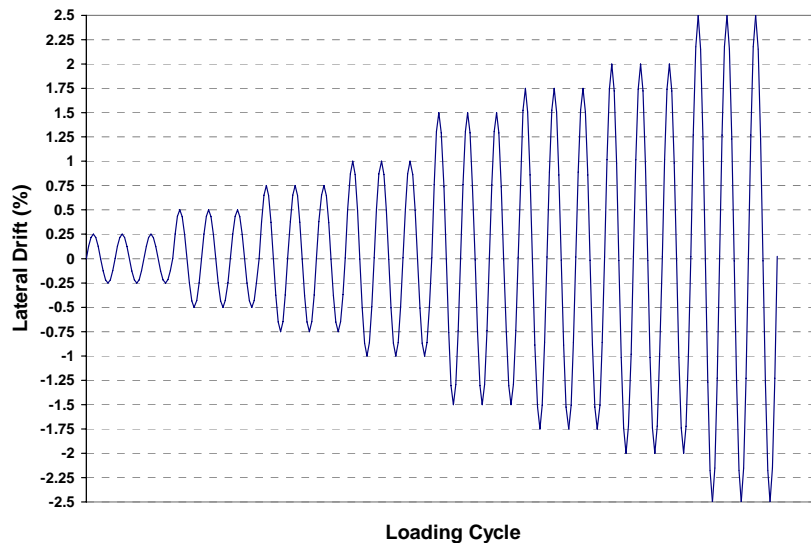


Figure 2.14 Displacement Protocol for specimen L0.5

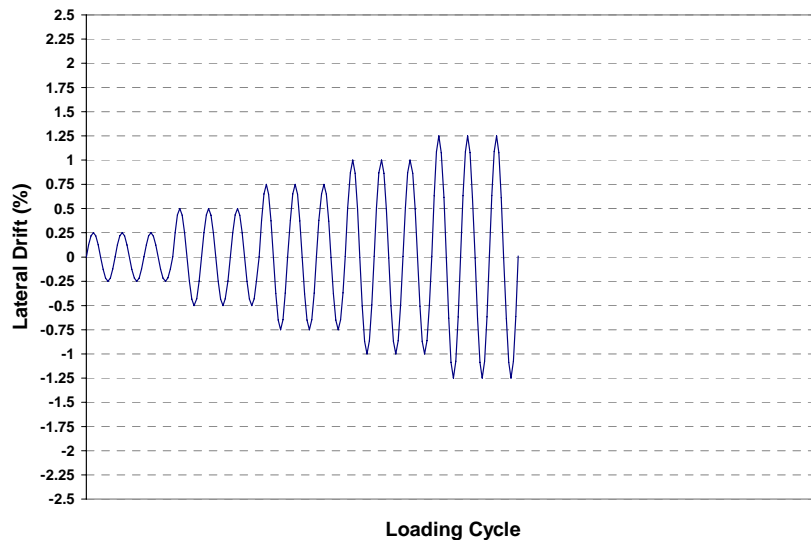


Figure 2.15 Displacement Protocol for specimens LG0.5, LG1.0, LR_{ST}G0.5 and LR_{SH}G0.5

CHAPTER 3

Test Results

3.1 LATERAL LOADING TEST L0.5

Specimen L0.5 was subjected to lateral loading up to failure. The specimen failed in punching shear at 2% drift, when the axial load in the column was 23.5 kips ($0.92\sqrt{f'_c b_o d}$). The hysteretic response for specimen L0.5 is shown in Figure 3.1. The specimen reached its maximum lateral loading capacity (11 kip North and -11.8 kip South) at 1.5% drift, after which the capacity dropped and failure followed shortly thereafter.

Based on results from visual observations and assessment techniques presented in Chapter 4, Chapter 6 and Chapter 7, it was concluded that the specimen experienced severe structural damage at 1.5% drift. Structural damage was from slight to moderate below 1.5% drift. Results from tests of specimen L0.5 were used to select 1.25% drift as the level to which all other specimens were laterally loaded prior to apply gravity loads to reach punching shear capacity.

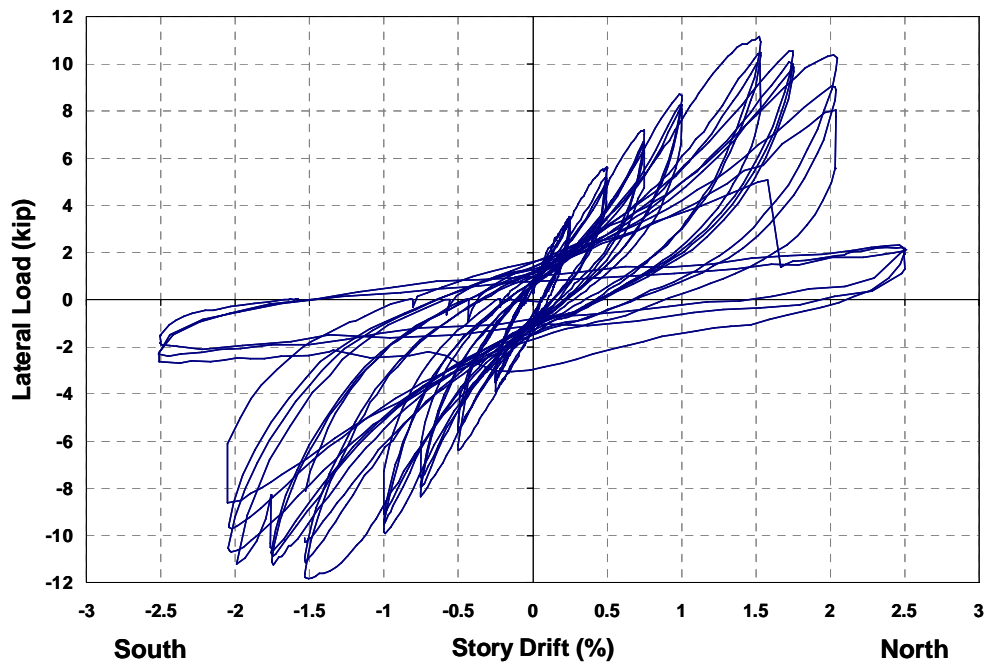


Figure 3.1 Hysteretic loop for specimen L0.5

3.2 LATERAL LOADING TESTS ON SPECIMENS LG0.5, LR_{ST}G0.5, LR_{SH}0.5 AND LG1.0

Specimens LG0.5, LR_{ST}G0.5, LR_{SH}0.5 and LG1.0 were laterally loaded up to 1.25% drift to induce moderate lateral load damage that could be used to evaluate the punching shear capacity of non-rehabilitated earthquake damaged specimens (LG0.5 and LG1.0) and earthquake damaged specimens rehabilitated with CFRP stirrups and sheets (LR_{ST}G0.5 and LR_{SH}0.5). The load-deformation envelopes for all laterally loaded specimens are presented in Figure 3.2.

It can be seen that the load-deformation envelopes for specimens LG0.5, LR_{ST}G0.5 and LR_{SH}0.5 fall in a narrow band similar to that for specimen L0.5. These specimens were fabricated with the same reinforcement layout (Figure 2.1).

The load-deformation envelope for specimen LG1.0 had a higher capacity than the others because it was fabricated with 1% top reinforcement ratio in the (c+3h) region within the column strip (Figure 2.2), while others had 0.5% reinforcement ratio in the same location.

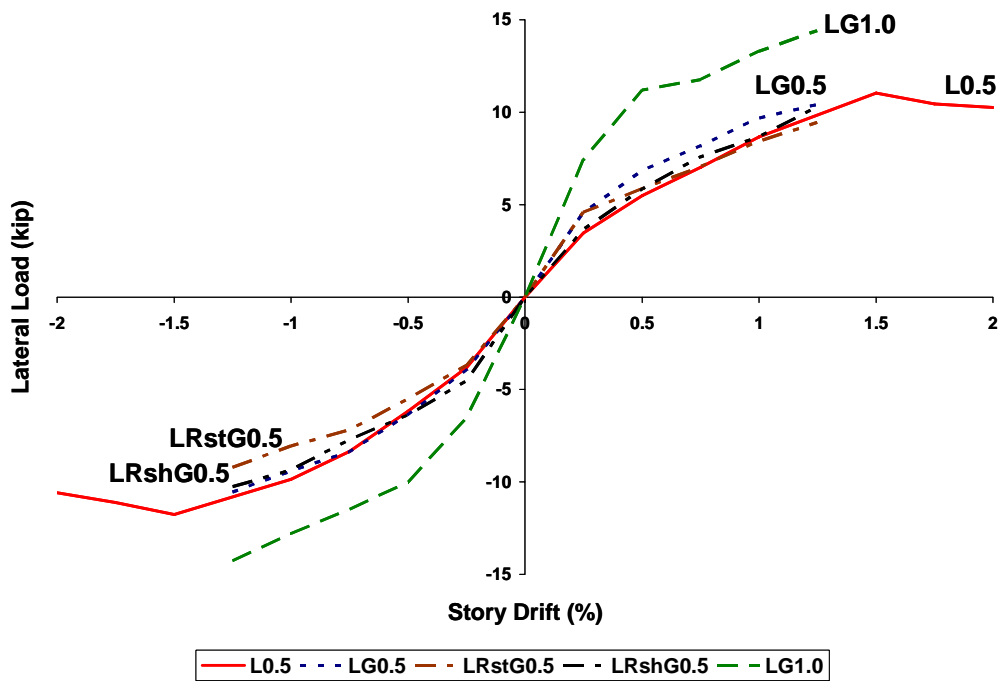


Figure 3.2 Load – deformation envelopes for all laterally loaded specimens

Figure 3.2 shows that the trend of data from specimen LG1.0 is parallel to the trend of data from other specimens after 0.5% drift. Results from punching shear tests (Section 3.4) showed that the specimen with 1.0% reinforcement ratio in the $(c+3h)$ region had less deformation capacity than specimens with 0.5% reinforcement ratio in the same region. Based on those observations, it is expected that specimens with 1% reinforcement ratio will reach their maximum lateral loading capacity and start to experience severe structural damage around 1.5% drift and will fail at 2% drift or slightly below that drift level.

3.3 THRESHOLD DEFLECTION LIMITS DEFINING SEVERE LATERAL LOAD DAMAGE

A plot of horizontal drift versus vertical deflection for all laterally loaded specimens is presented in Figure 3.3. Threshold deflection limits were defined from these data to indicate where severe lateral load damage is anticipated.

The horizontal drift of the specimen was computed by dividing the horizontal displacement measured by the LVDT at the horizontal actuator axis by the story height (8-ft). The story height is equivalent to the distance between the horizontal actuator axis and the pin-end support (clevis) located under the bottom column.

The normalized vertical deflection “ Δ_m ” of the slab (Figure 3.4) was computed dividing the vertical displacement measured by the linear potentiometer installed under the bottom “ δ_m ” column by the distance between vertical struts (12

ft.). The distance between struts was chosen because the deflection of the slab was known to be zero at the position of the struts and the vertical displacement under the column was measured relative to this datum.

For specimens with 0.5% top reinforcement ratio in the (c +3h) region, a normalized vertical deflection 1/200 can be considered a threshold deflection limit for severe structural damage. At a normalized vertical deflection of 1/200, lateral drifts were below 1.5% and the observed lateral load damage was moderate.

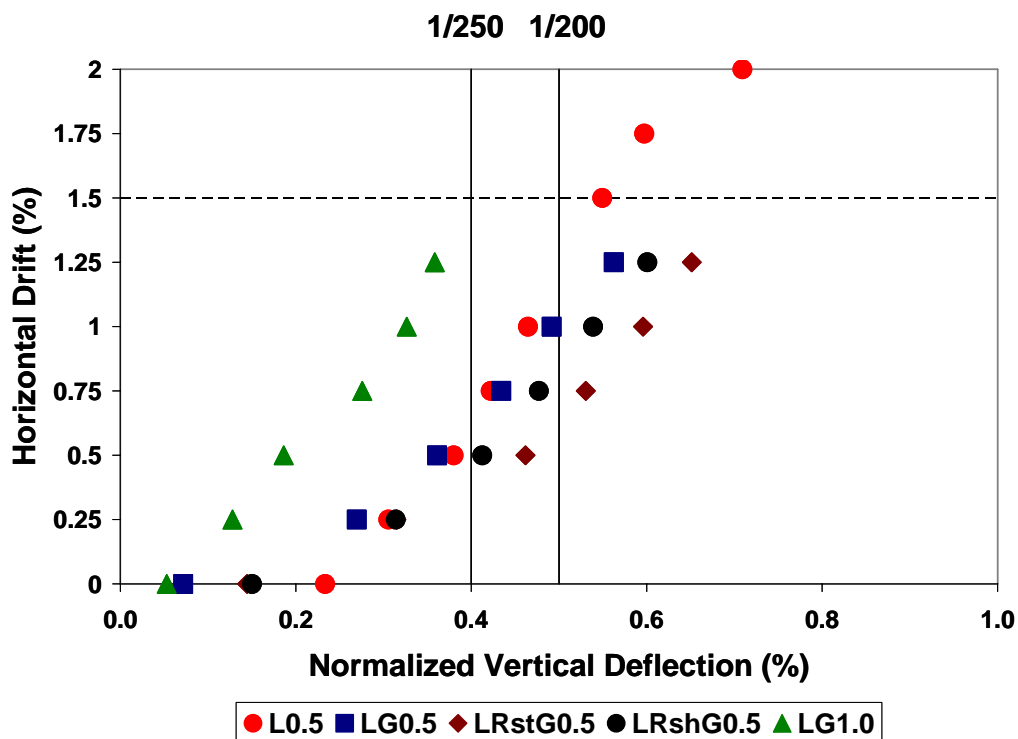


Figure 3.3 Horizontal drift versus normalized vertical Deflection for all laterally loaded specimens

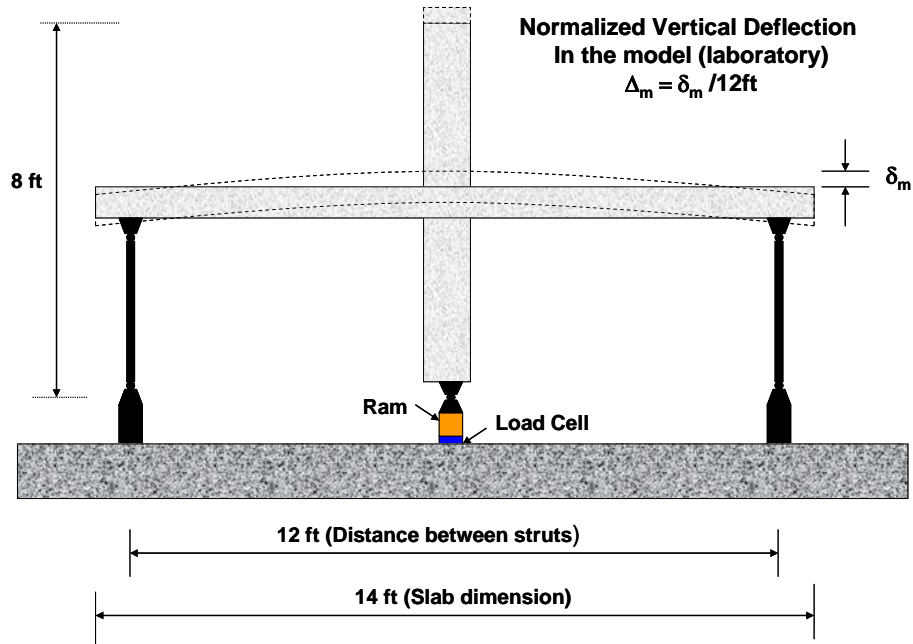


Figure 3.4 *Determination of the Normalized Vertical Deflection of the slab in the model (specimens)*

Based on the trend of data presented in Figure 3.3, at a normalized vertical deflection 1/200, specimen LG1.0 would have experienced lateral drifts above 1.5% and severe structural damage. At any drift level, specimen LG1.0 shows lower vertical deflections than other specimens and the trend of data from specimen LG1.0 is parallel to the trend of data from other specimens. That is because specimen LG1.0 is stiffer than others. The greater stiffness of specimen LG1.0 is provided by a larger top reinforcement ratio in the (c+3h) region within the column strip (1%), as compared to other specimens (0.5%).

For the specimen LG1.0 with 1% top reinforcement ratio in the (c +3h) region, a normalized vertical deflection of 1/250 is estimated to represent a threshold deflection limit beyond which severe structural damage would be expected.

It should be noted that limited data was available to develop the above mentioned conclusions. Normalized deflections measured in the field are not expected to be equal to those measured in the laboratory, due to simplifications introduced in modeling boundary conditions and gravity loads.

3.4 PUNCHING SHEAR TESTS ON SPECIMENS G0.5, G1.0, LG0.5 AND LG1.0

Punching shear tests were conducted on non-rehabilitated specimens G0.5, G1.0, LG0.5 and LG1.0 to obtain the punching shear capacity of specimens with different loading history and top reinforcement ratio in the (c+3h) region within the column strip. Results are shown in Table 3.1.

Specimens G0.5 and G1.0 were tested in punching shear without any prior damage due to lateral loading. Specimens LG0.5 and LG1.0 were laterally loaded up to 1.25% drift experiencing moderate earthquake damage prior to be tested in punching shear.

By comparing results from specimens G0.5 and LG0.5, specimens with 0.5% of top reinforcement ratio in the (c+3h) region, there was no reduction in the punching shear capacity of a specimen that has previously experienced moderate earthquake damage. The shear stress at the critical punching shear perimeter was equal for specimens G0.5 and LG0.5. A similar observation was found comparing results from specimens G1.0 and LG1.0, specimens with 1% of top reinforcement ratio in the (c+3h) region.

Table 3.1 *Punching shear strength of non-rehabilitated specimens*

Specimen	Top reinforcement ratio in (c+3h) region	Punching load, V (kip)	Shear stress at critical perimeter, * $v = V/(b_o d)$
G0.5	0.5%	70.0	$2.47 \sqrt{f'_c}$
G1.0	1.0%	90.9	$3.39 \sqrt{f'_c}$
LG0.5	0.5%	72.7	$2.48 \sqrt{f'_c}$
LG1.0	1.0%	89.8	$3.38 \sqrt{f'_c}$

* $d = 5$ in. is the average effective depth of the slab reinforcement and b_o is the critical perimeter at a distance $d/2$ from column

A reduction in the punching shear capacity is expected to occur in specimens that had been previously subjected to severe structural damage (1.5% drift or above). The gravity load carrying capacity of the connection is expected to decrease from the original design capacity found at 1.25% drift to a smaller capacity, equivalent to a loading condition of dead plus 25% of live load, found at 2% drift.

Shear stress at the critical perimeter for all tested specimens was lower than the design value of $4\sqrt{f'_c}$ provided by ACI 318-05. The provision is unconservative for slab-column connections tested in this study. Considering that the design of slab-column connections following current code provisions ACI 318-05 will result in slabs with top reinforcement ratio in the (c+3h) region within the column strip on the order of 1%, lowering the design value of $4\sqrt{f'_c}$ should be studied. A detailed investigation of the punching shear strength of lightly reinforced specimens can be found in Ying, 2006.

3.5 PUNCHING SHEAR FAILURE THRESHOLD DEFLECTION LIMITS

The vertical load versus vertical deflection is presented in Figure 3.5 for all non-rehabilitated specimens. It was found that specimens with 1% top reinforcement ratio in the (c+3h) region within the column strip were stiffer and showed less deformation capacity than specimens with 0.5% reinforcement ratio.

For specimens with 1% top reinforcement ratio in the (c+3h) region within the column strip, a normalized vertical deflection 1/200 is considered a threshold deflection limit against punching shear failure.

For specimens with 0.5% top reinforcement ratio in the (c+3h) region within the column strip, a normalized vertical deflection 1/150 is considered a threshold deflection limit against punching shear failure.

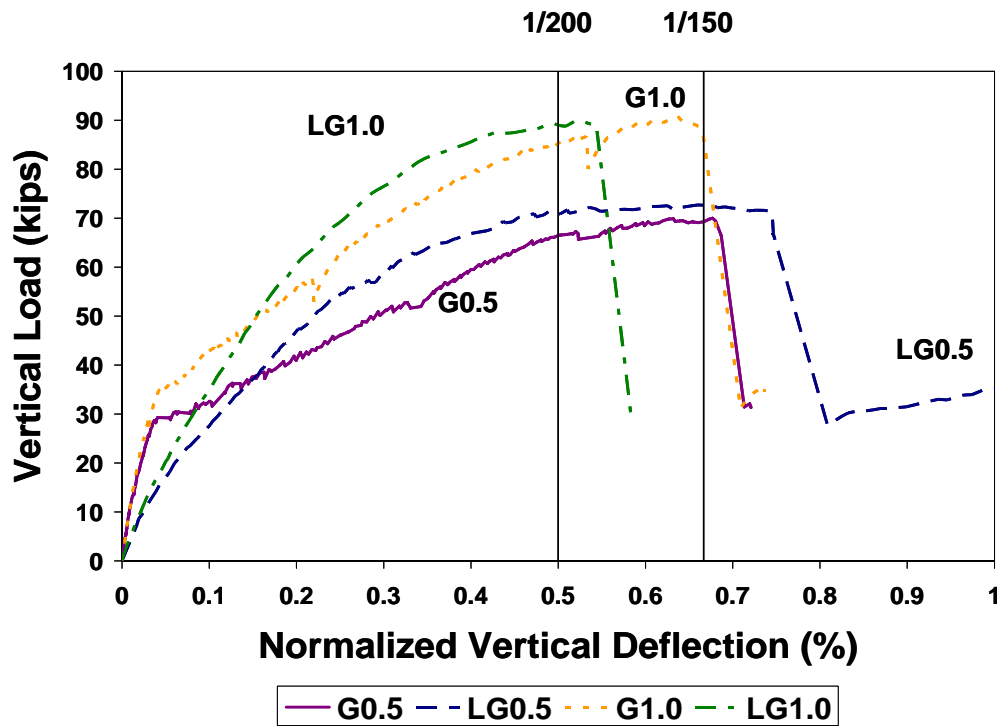


Figure 3.5 Vertical load versus normalized vertical deflection for non-rehabilitated specimens

Lateral load damage reduced deformation capacity of 1% type specimens (LG1.0 versus G1.0), but no reduction was found for 0.5% type specimens (LG0.5 versus G0.5). Based on the trend of data, it can not be concluded that lateral load damage reduces deformation capacity in punching shear.

There is a difference between deformation capacities of LG type specimens with 0.5% (LG0.5) and 1% (LG1.0) reinforcement ratio in the (c+3h) region within the column strip. Increasing the amount of reinforcement seems to reduce the deformation capacity in punching shear, of specimens that have been previously subjected to earthquake loads.

CHAPTER 4

Identification of damage under lateral loading

4.1 INTRODUCTION

Damage identification under lateral loading was performed through visual observations of the test specimens. Crack widths were monitored at critical cracks that opened on the North or South axes. Crack patterns were marked, analyzed and used to compute crack densities for each specimen subjected to lateral loading.

A critical crack was defined as a crack that opened parallel to a column face, at a distance equal or less than 6 in., a distance equivalent to the slab depth. These cracks were considered critical because they were wide, deep and located in a region where the punching shear failure surface formed.

4.2 CRACK WIDTH MEASUREMENTS

4.2.1 Specimen L0.5

When the gravity load was applied following the procedure described in Section 2.3.1, a critical crack reopened on the North axis of specimen L0.5, 2.5 in.

from the face of the column (Figure 4.1). This crack was originally formed when an instantaneous vertical load was accidentally applied to the specimen. Because the specimen was accidentally cracked, when the gravity loads were applied, cracks became wider than what they would have been if the instantaneous load had not been applied.

After the application of the gravity load, lateral loads were applied to sustain story drifts that incrementally varied from 0 to 0.25, 0.5, 0.75, 1, 1.5, 1.75, 2 and 2.5% until failure of the specimen was achieved.

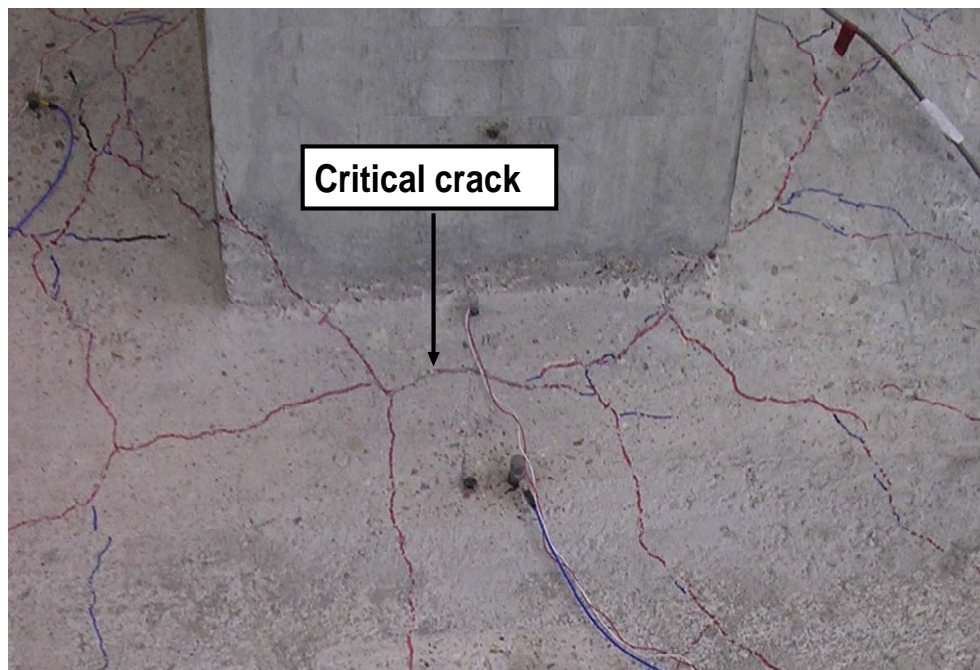


Figure 4.1 *Critical crack in Specimen L0.5 (North axis)*

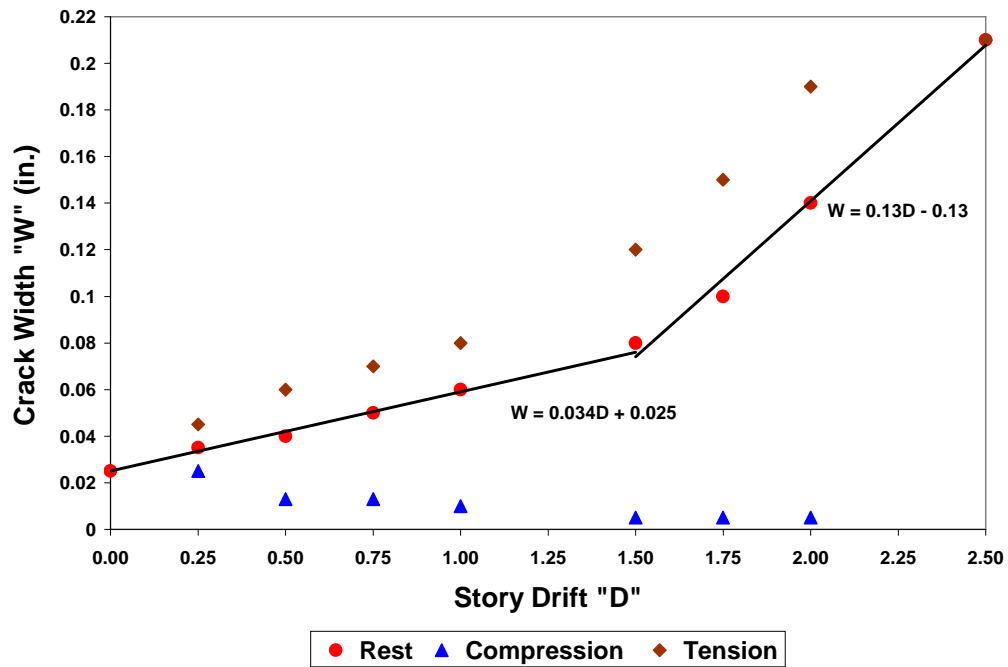


Figure 4.2 Crack width measurements in Specimen L0.5

Crack width measurements were conducted in the north side of the slab. Figure 4.2 shows results for three different conditions: top of the slab in tension (lateral loads applied), top of the slab in compression (lateral loads applied), and specimen at rest (lateral loads not applied). In all conditions, gravity load was applied. From the results presented in Figure 4.2 the following observations were obtained:

- i. The critical crack was fully open when the top of the slab was in tension in the north axis and it was almost closed when the top of the slab was in compression.

The “rest” condition shows two linear correlations between lateral drift and crack width. The trend of data can be described with two lines, the first for data below 1.5% drift and the second for data above 1.5% drift, where yielding of the bottom reinforcement was observed. The bottom reinforcement in the column region yielded in tension when the tensile stress induced by lateral load minus the compressive stress caused by gravity load resulted in a net tensile stress large enough to cause yielding.

Anchorage failure was not observed for the bottom reinforcement, despite the fact that this reinforcement was not continuous and it was embedded 6 in. in the column, a length that is less than the required development length computed using ACI 318-05 Equation 12-1 (11 in.). The absence of anchorage failure of the bottom reinforcement along the NS direction could be explained by the fact that bars were also affected by local bending due to dowel action caused by a vertical displacement across the crack.

- ii. At 1.5% drift water was poured in the critical crack and immediately appeared from the bottom of the slab. The critical crack was found to be opened to the full depth of the slab. With the critical crack fully opened and the crack width increasing at a much larger rate after 1.5% drift, the aggregate interlock was considered lost and the concrete shear strength equal to zero at the critical crack within the column region. When the shear strength was lost at the critical cracks on the north and south sides of the specimen, shear stresses were redistributed

to the east and west sides of the specimen. After 1.5% drift, the specimen is considered to be severely damaged and its punching shear capacity reduced (loss of aggregate interlock) at critical cracks.

4.2.2 Specimen LG0.5

On the north axis, after applying the gravity load, a critical crack formed at 2.5 in. from the column. When the lateral drift was 0.25%, a hairline crack (< 0.001 in.) developed at the slab-column interface (Figure 4.3).

The crack at the slab-column interface remained unchanged until 1 % drift was achieved. From 1% to 1.25% drift, the critical crack did not change in width and the crack at the slab-column interface started to increase in width. Based on results from specimen L0.5, it was decided to measure crack widths for the “at rest” condition only, for the following reasons:

- i. Crack width measurements when the top of the slab is in compression do not provide any significant information, other than the observation that when the top of the slab is in compression, the crack closes and the crack width tends to be zero.
- ii. The data trends for crack width measurements when the top of the slab is in tension and at rest are very similar. Either of them could be a good indicator of the progression of damage. However, measurements for the “at rest” condition are more valuable, since they can be

compared with field data obtained from damaged structures, where only “at rest” measurements are feasible.

Critical crack measurements are presented in Figure 4.4. From the results presented in Figure 4.4, the following observations were obtained:

- i. The control crack width remained constant after 1% drift because the crack at the slab-column interface became active.
- ii. There is a linear correlation between drift level and crack width for lateral drifts from 0 to 1%.

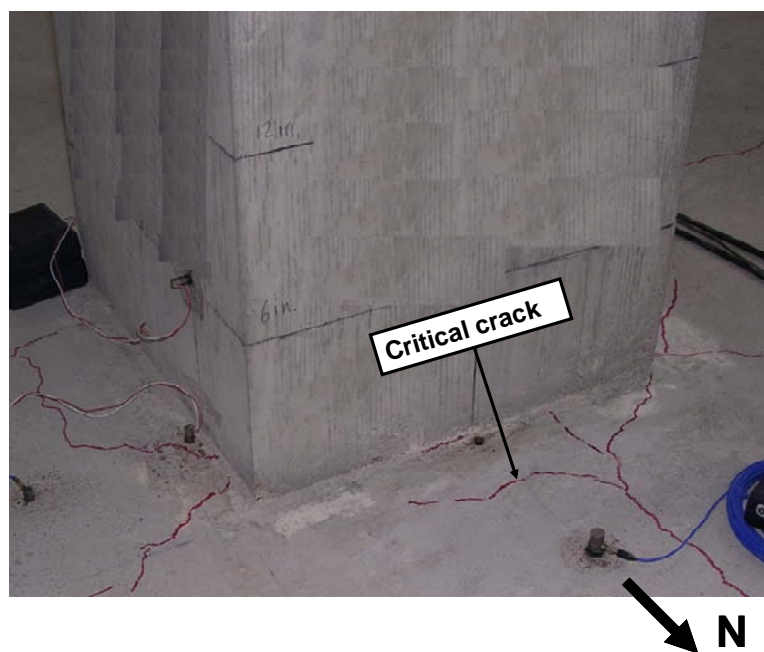


Figure 4.3 Critical crack in Specimen LG0.5 (North axis)

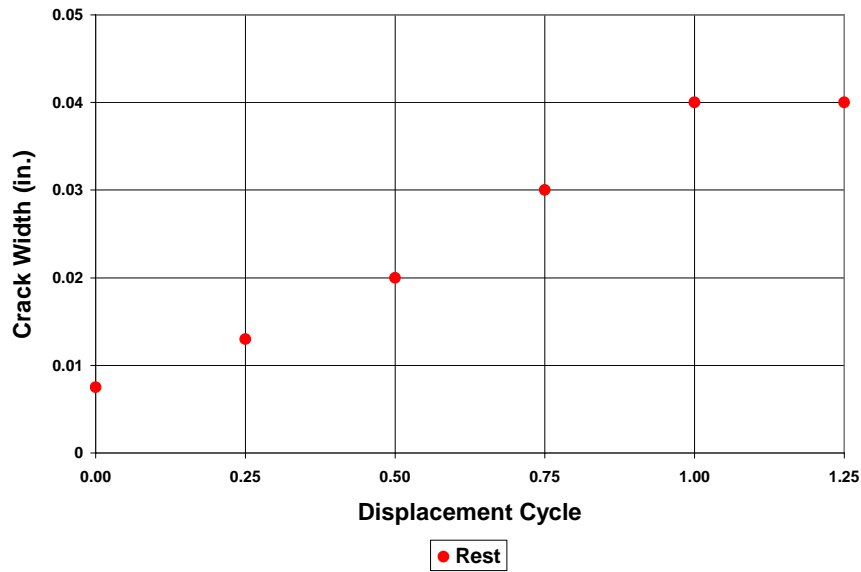


Figure 4.4 Crack width measurements in Specimen LG0.5

4.2.3 Specimen LR_{ST}G0.5

After applying the gravity load, a critical crack was formed at the slab-column interface on the north axis (Figure 4.5) and on the south axis, at 1.5 in. from the column (Figure 4.6). The critical crack on the north axis was not accessible with the crack gauge; therefore crack widths were measured for the critical crack on the south axis. Results are presented in Figure 4.7. Visual observations during testing showed that widths of both, the north and south critical cracks were similar at every lateral drift level. From the results presented in Figure 4.7, it was observed that there is a nearly linear correlation between drift level and crack width.

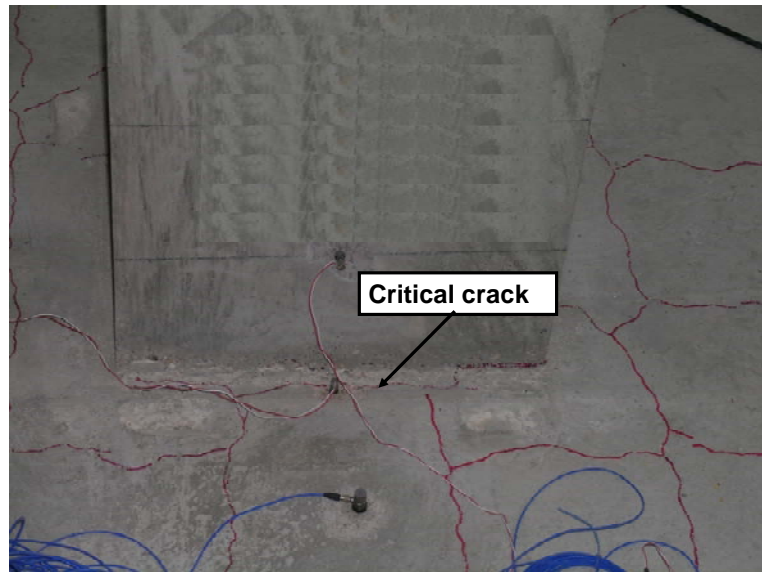


Figure 4.5 Critical flexural crack in Specimen LR_{ST}G0.5 (North axis)



Figure 4.6 Critical crack in Specimen LR_{ST}G0.5 (South axis)

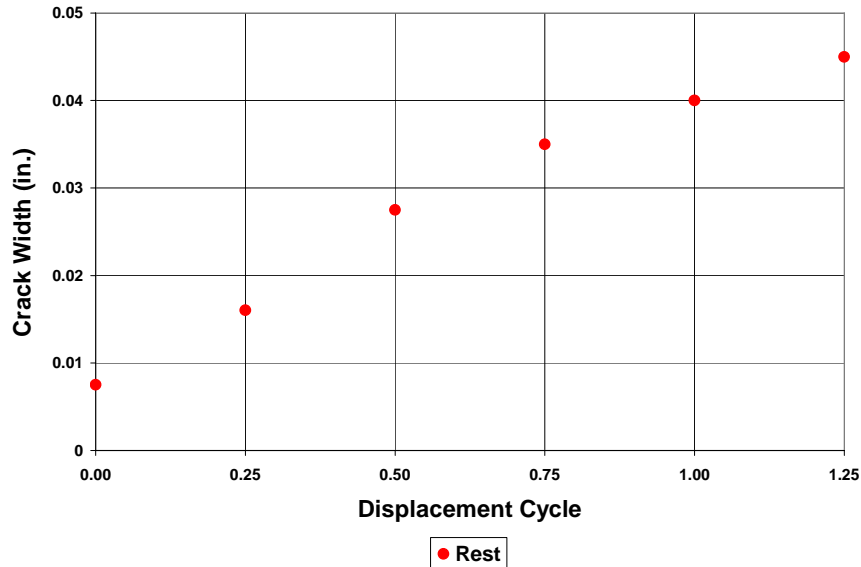


Figure 4.7 Crack width measurements in Specimen LR_{ST}G0.5

4.2.4 Specimen LG1.0

Specimen LG1.0 remained uncracked when the gravity load was applied. A critical crack opened at 0.25%, 4 in. from the column face and its width was monitored until 1.25% drift (Figure 4.8). Control crack measurements are presented in Figure 4.9, from which the following observations were obtained:

- i. There is a linear correlation between drift level and crack width for lateral drifts from 0.25 to 1.25%.

- ii. There is not good agreement between crack widths measured for specimen LG1.0 and specimens L0.5, LG0.5 and LR_{ST}G0.5. Crack widths for specimen LG1.0 are much smaller than those measured for other specimens. That is attributed to the higher top reinforcement ratio (1%) in specimen LG1.0 than the ratio used for other specimens (0.5%). A high reinforcement ratio produces a well distributed pattern of cracks of fairly uniform width. Likewise, a low reinforcement ratio produces a pattern of cracks of variable width.

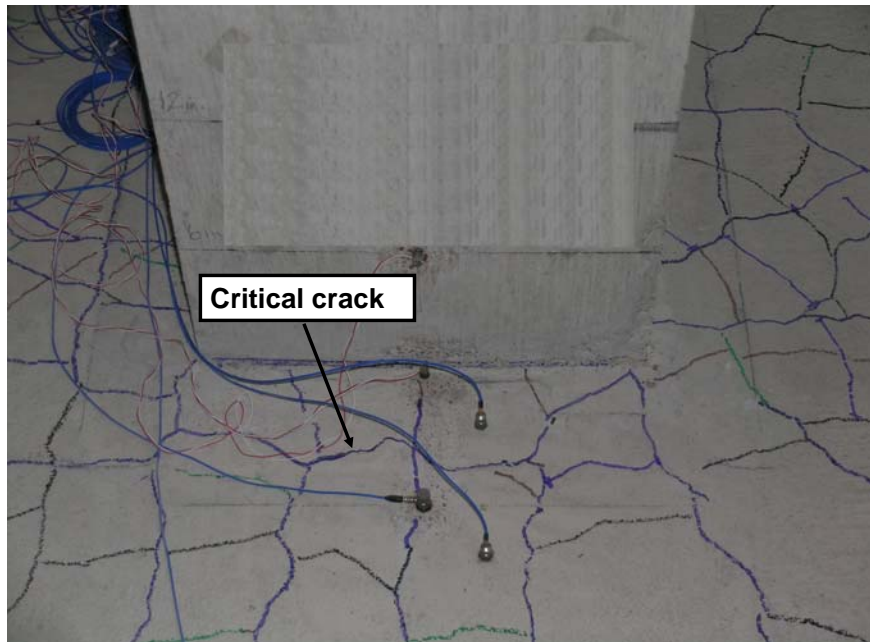


Figure 4.8 Critical crack in Specimen LG1.0 at 1.25% drift (North axis)

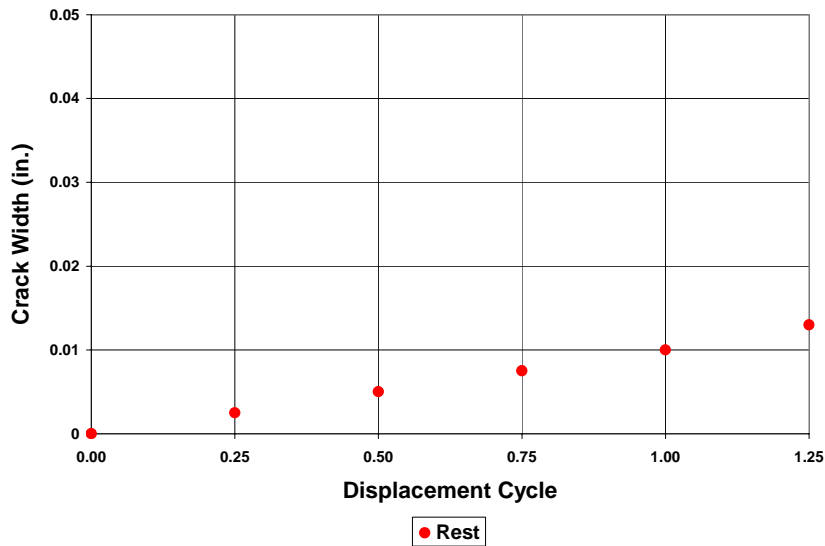


Figure 4.9 Crack width measurements in Specimen LG1.0

4.2.5 Analysis of combined crack width data for all specimens

Crack widths for all specimens are presented in Figure 4.10. The analysis of combined data leads to the following observations:

- i. Data from specimens LG0.5 and LR_{ST}G0.5 are very similar and follow the same linear trend. However, it should be noted that width of the critical crack of specimen LR_{ST}G0.5 did not grow after 1% drift because a redistribution of stresses caused this crack to become inactive at 1.25% drift, while the crack at the slab-column interface started to grow.

- ii. For story drifts from 0 to 1.25%, the linear trend for specimen L0.5 has almost same slope as for specimens LG0.5 and LR_{ST}G0.5. The three specimens have the same reinforcement pattern, with a reinforcement ratio in the top layer within the column strip equal to 0.5%. Data from specimen L0.5 is offset approximately 0.017 in. from data from specimens LG0.5 and LR_{ST}G0.5, which is attributed to the instantaneous accidental loading of specimen L0.5 prior to the application of gravity loads.

- iii. The slope of the linear trend for specimen LG1.0 is smaller than that for specimens L0.5, LG0.5 and LR_{ST}G0.5, and crack widths are also smaller for specimen LG1.0 than for other specimens. This is attributed to the larger top reinforcement ratio in specimen LG1.0 (1%), which allows the formation of a well distributed pattern of cracks of similar and small width.

4.2.6 Conclusions on the use of crack widths to predict story drifts

Results from experiments showed that for general applications crack widths should not be used to predict story drifts. They are a function of the reinforcement ratio, loading history and stress redistribution within the specimen, factors that greatly influence their magnitude and rate of change. Crack widths could be successfully used to predict story drifts through a linear correlation for

particular applications where the reinforcement ratio, loading history and stress redistribution are known.

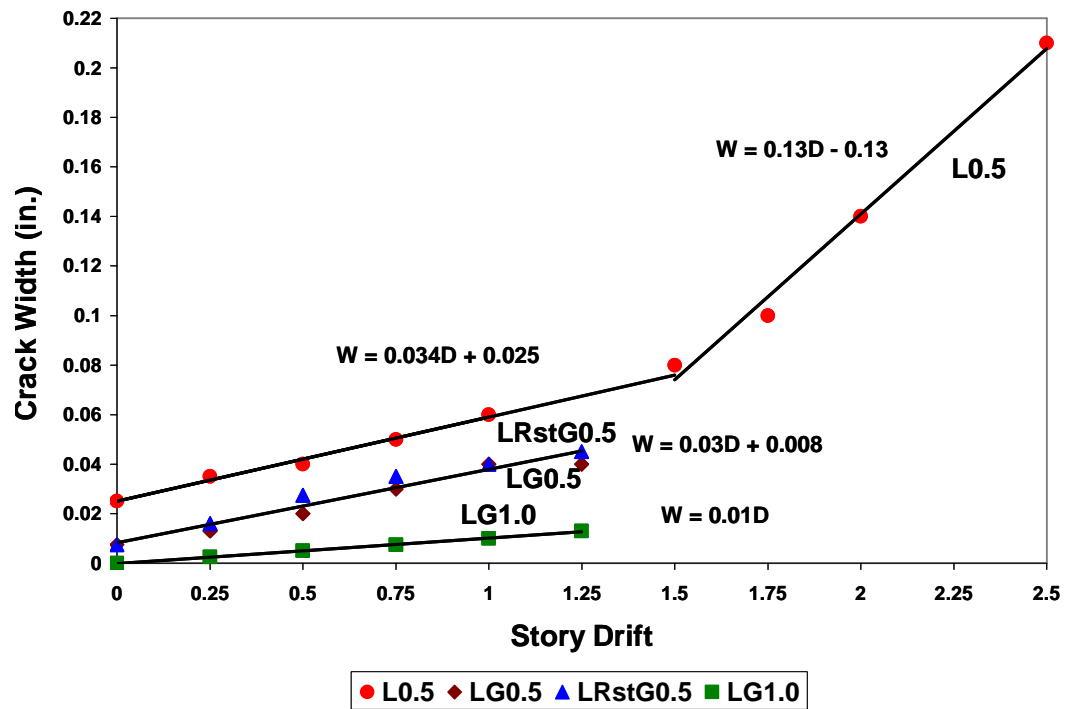


Figure 4.10 Crack widths for all specimens

4.3 CRACK PATTERNS

4.3.1 Crack Plots

For every specimen, cracks were plotted at each drift level. The progression of cracks when the story drift is increased shows the nature and intensity of damage experienced by the specimens.

4.3.2 Crack Density

For every specimen, crack lengths were measured at each drift level. The total length of cracks was divided by the area of the slab (14' by 14') to obtain the crack density. All cracks visible to a naked eye were measured.

For simplicity, only lengths from cracks on top of the slab were measured. Compared with the amount of cracking on the top of the slab, cracking on the bottom of the slab was limited and inclusion of those cracks did not change the trend of data. It was also considered that crack density can be used for the structural condition assessment of buildings damaged by earthquakes and typically accessing and measuring cracks on the bottom of the slab is complicated in the field. However, measuring crack lengths on top of the slab could be difficult in cases where floor finishes interfere with visual observations.

Crack length measurements were conducted for the total area of the slab in the specimen, which corresponds with the area of a slab defined by mid spans, for simplicity of use in the field.

4.3.3 Specimen L0.5

Crack plots for specimen L0.5 are presented in Figure 4.11 through Figure 4.20. The following color code was used to plot cracks: gravity load (red), 0.25% drift (blue), 0.5% drift (black), 0.75% drift (green), 1% drift (brown), 1.5% drift (purple), 1.75% drift (yellow), 2% drift (cyan) and 2.5% (gray). It can be seen that there is significant cracking due to the application of gravity load alone. It should be noted that the specimen was accidentally cracked prior to the application of gravity load and induced cracking that exceeded cracking under the specified gravity loads.

At low drift levels (0.25% and 0.5%) cracks are predominantly concentrated on the North and South sides, where flexural action is developed. At 0.75% drift cracks are formed predominantly on the East and West sides of the specimen where torsional action is developed. The increase in torsional cracking at 0.75% drift coincides with yielding of the top reinforcement of the slab. Another increase in torsional cracking occurs on the East and West sides of the specimen at 1.75% drift, after the bottom reinforcement has yielded.

Prior to 1.5% drift, cracks on the bottom of the slab are limited to the slab-column interface, where hairline cracks (< 0.01 in. width) were measured. After the bottom reinforcement of the slab yielded, torsional cracks on the bottom of the slab grew from the corners of the column (Figure 4.20). The specimen failed at 2% drift; however it was loaded up to 2.5% drift to find the residual strength of the connection after failure had occurred.

Results for crack lengths and densities are presented in Table 4.1.

Table 4.1 Length and density of cracks in Specimen L0.5

Story Drift (%)	Crack Length (ft)	Crack Density (in/sqf)
0	89	5
0.25	118	7
0.5	136	8
0.75	161	10
1	183	11
1.5	201	12
1.75	220	13
2	241	15
2.5	259	16

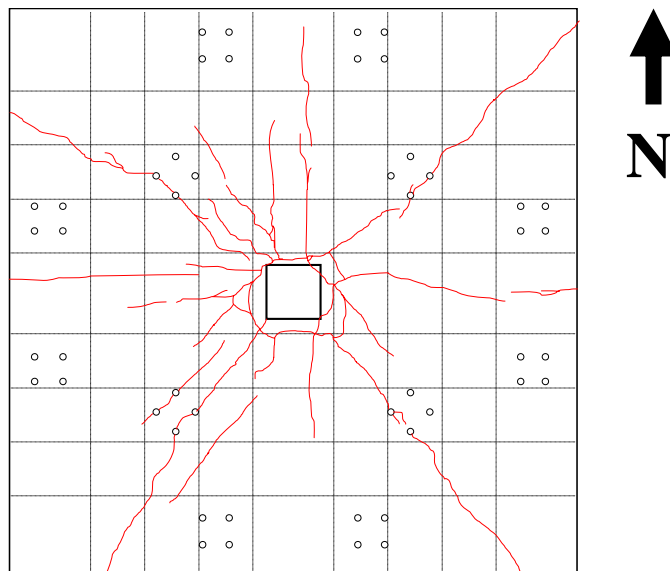


Figure 4.11 Gravity Load only (Specimen L0.5)

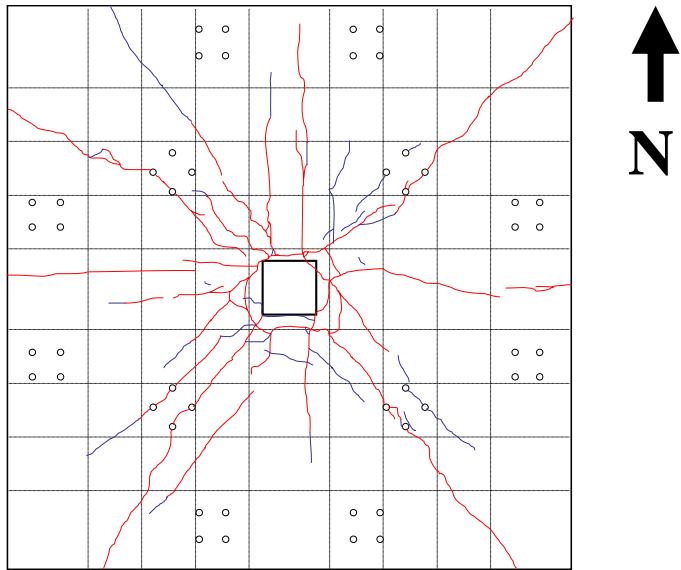


Figure 4.12 0.25% Lateral Drift (Specimen L0.5)

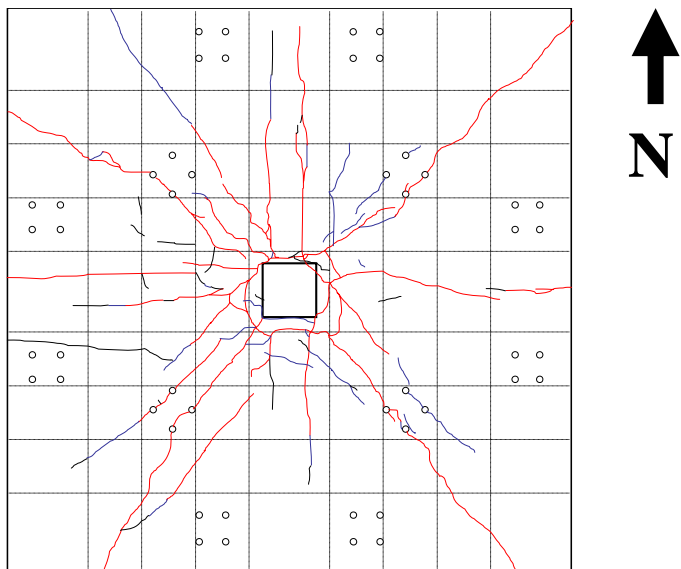


Figure 4.13 0.5% Lateral Drift (Specimen L0.5)

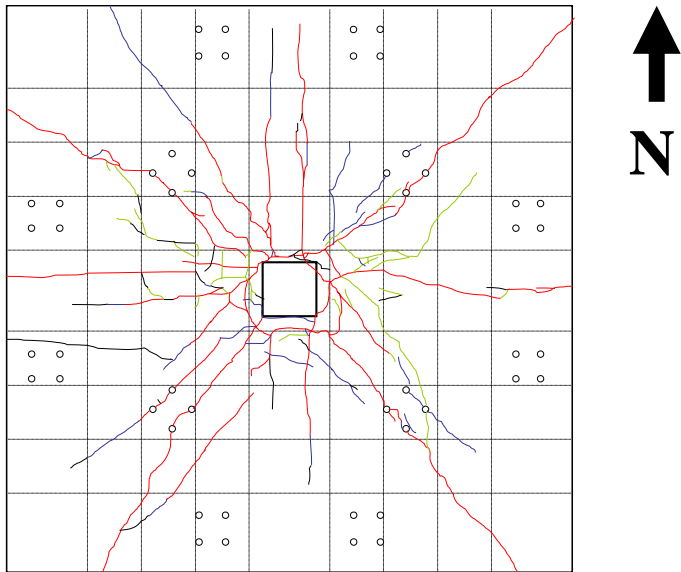


Figure 4.14 0.75% Lateral Drift (Specimen L0.5)

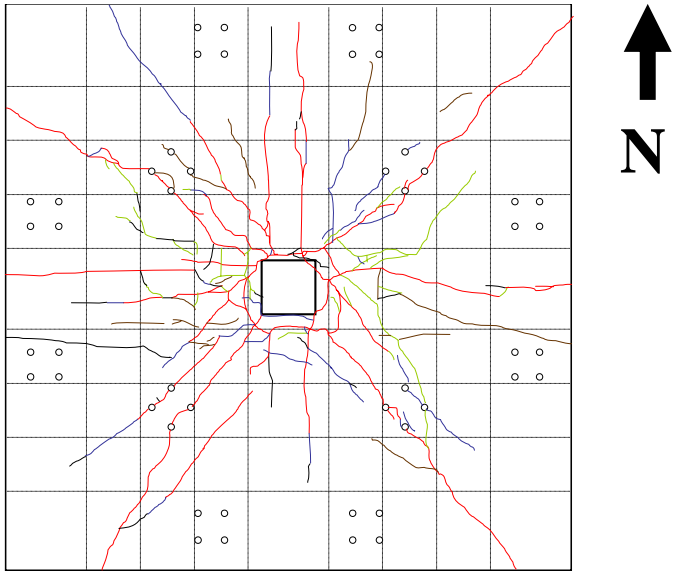


Figure 4.15 1% Lateral Drift (Specimen L0.5)

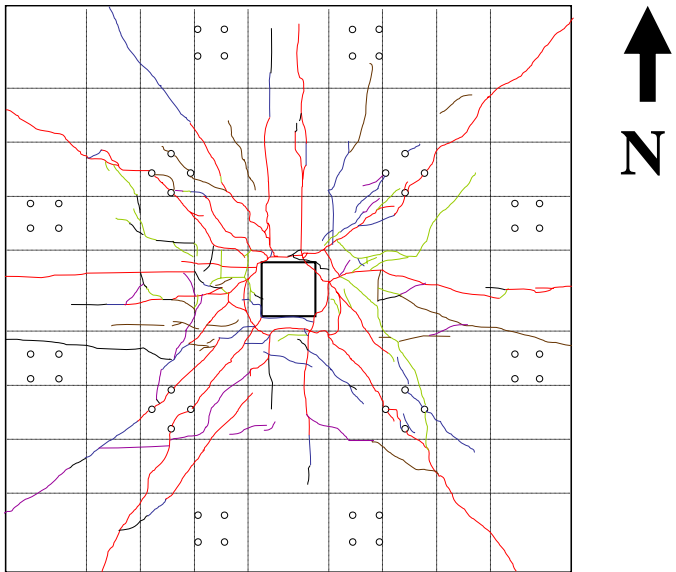


Figure 4.16 1.5% Lateral Drift (Specimen L0.5)

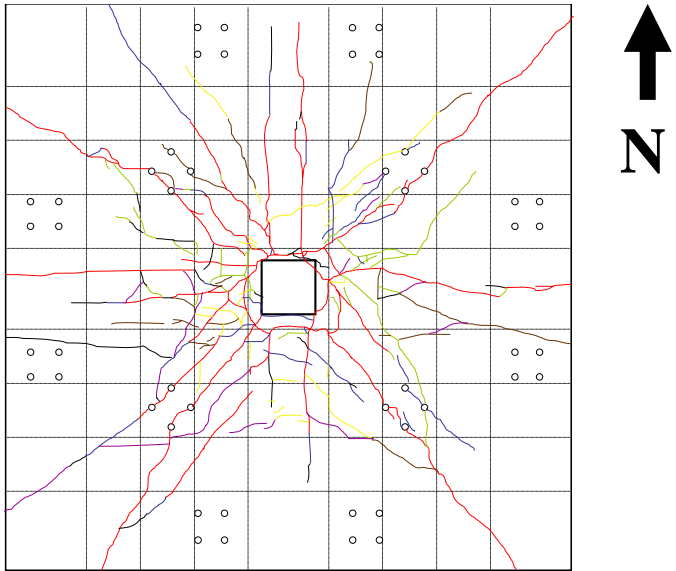


Figure 4.17 1.75% Lateral Drift (Specimen L0.5)

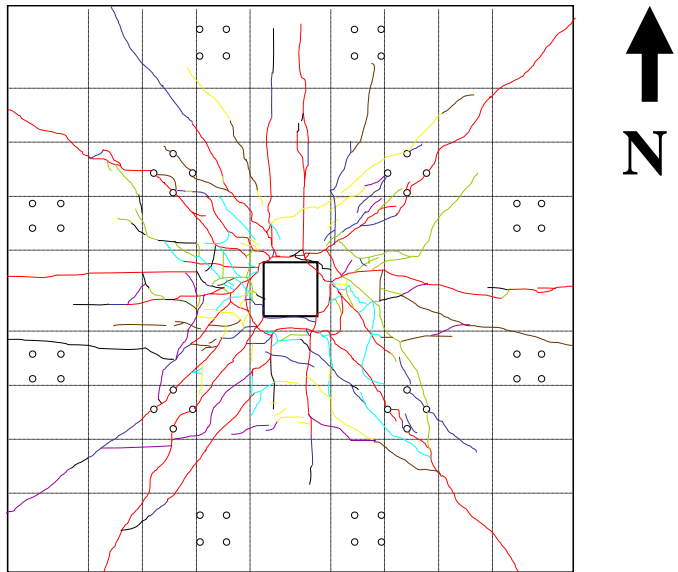


Figure 4.18 2% Lateral Drift (Specimen L0.5)

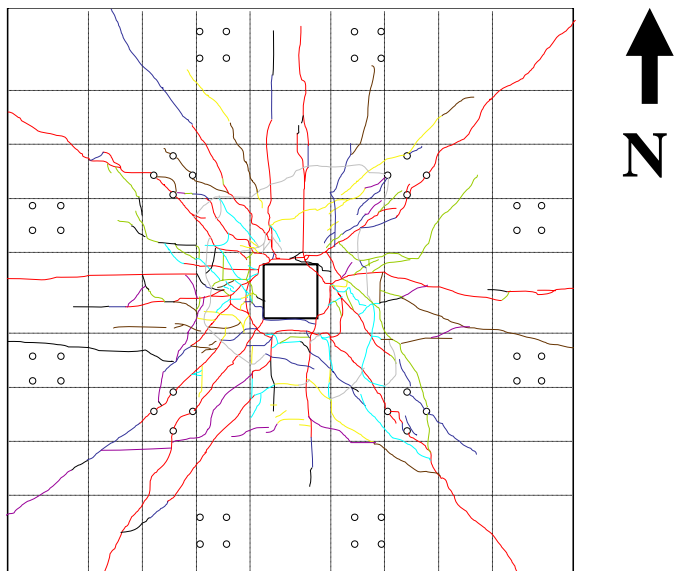


Figure 4.19 2.5% Lateral Drift (Specimen L0.5)

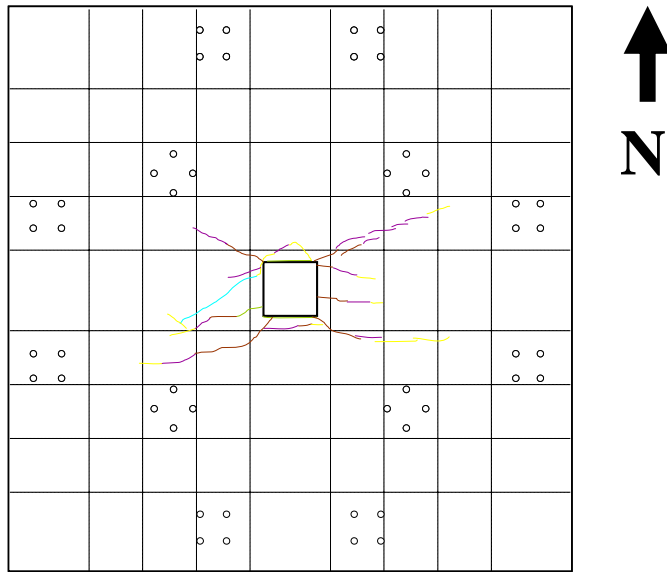


Figure 4.20 *Bottom of the Slab at 2.5% Lateral Drift (Specimen L0.5)*

4.3.4 Specimen LG0.5

Crack plots for specimen LG0.5 are presented in Figure 4.21 through Figure 4.27. The following color code was used to plot cracks: gravity load (red), 0.25% drift (blue), 0.5% drift (black), 0.75% drift (green), 1% drift (brown), 1.25% drift (purple). The cracking under gravity load in specimen LG0.5 is much less than in specimen L0.5. Similarly to what was observed for specimen L0.5, torsional cracking on the East and West sides of specimen LG0.5 increases at 0.75% drift, when the top reinforcement of the slab had yielded. Hairline cracks (< 0.01 in. width) started to develop at 0.75% drift on the bottom of the slab. Results for crack lengths and densities are presented in Table 4.2.

Table 4.2 *Length and density of cracks in Specimen LG0.5*

Story Drift (%)	Crack Length (ft)	Crack Density (in/sqf)
0	36	2
0.25	93	6
0.5	126	8
0.75	157	10
1	172	11
1.25	191	12

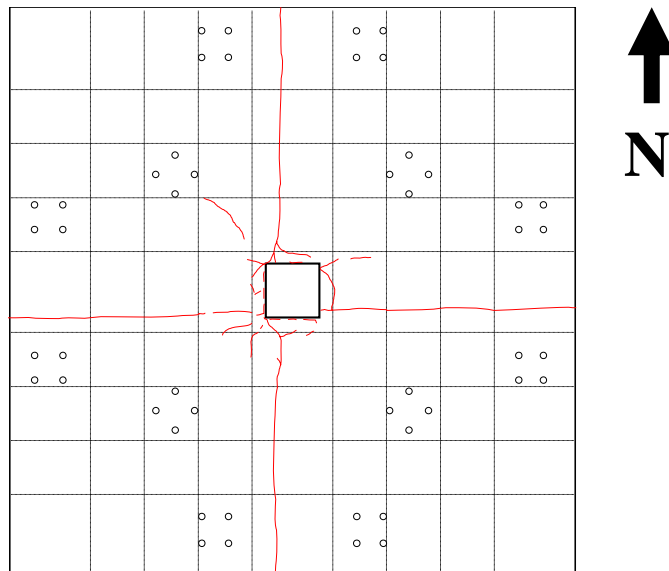


Figure 4.21 *Gravity Load only (Specimen LG0.5)*

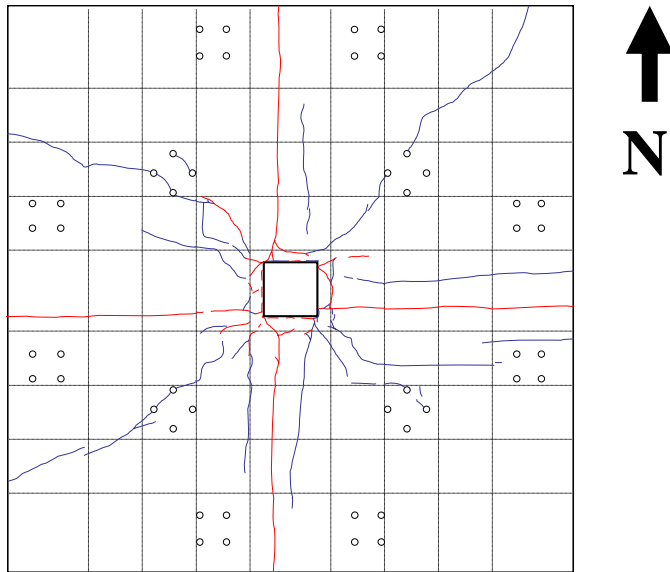


Figure 4.22 0.25% Lateral Drift (Specimen LG0.5)

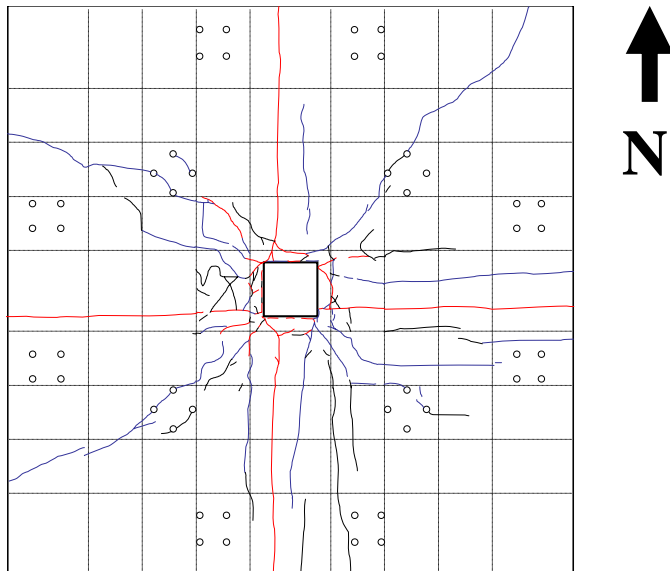


Figure 4.23 0.5% Lateral Drift (Specimen LG0.5)

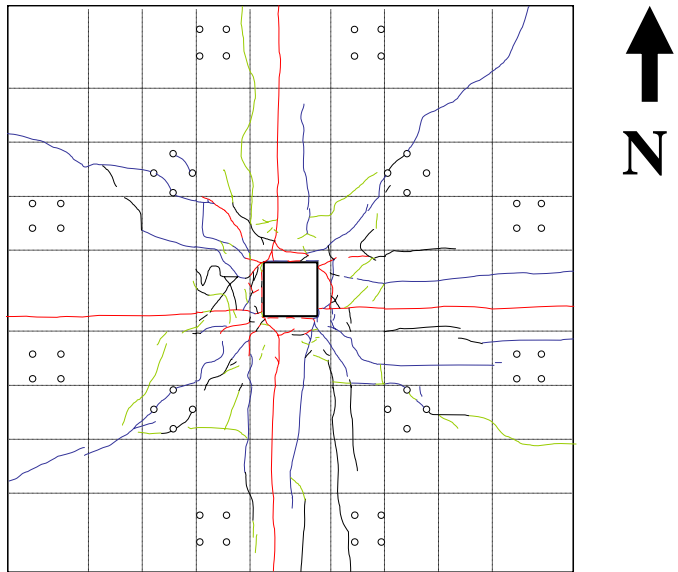


Figure 4.24 0.75% Lateral Drift (Specimen LG0.5)

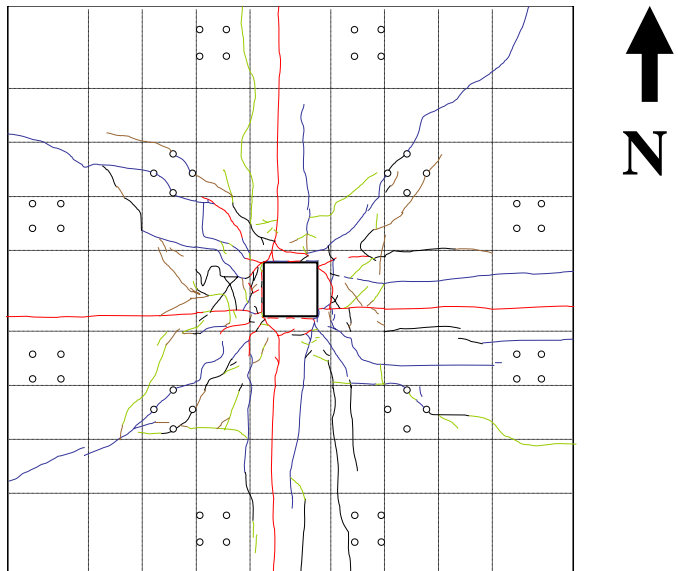


Figure 4.25 1% Lateral Drift (Specimen LG0.5)

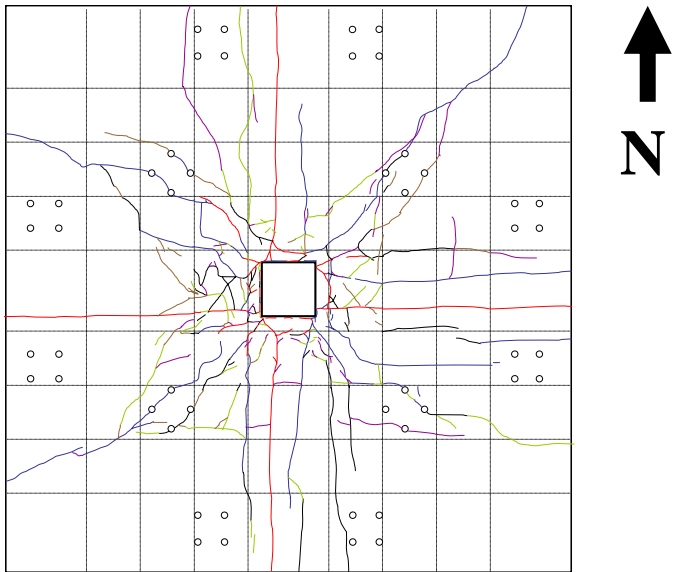


Figure 4.26 1.25% Lateral Drift (Specimen LG0.5)

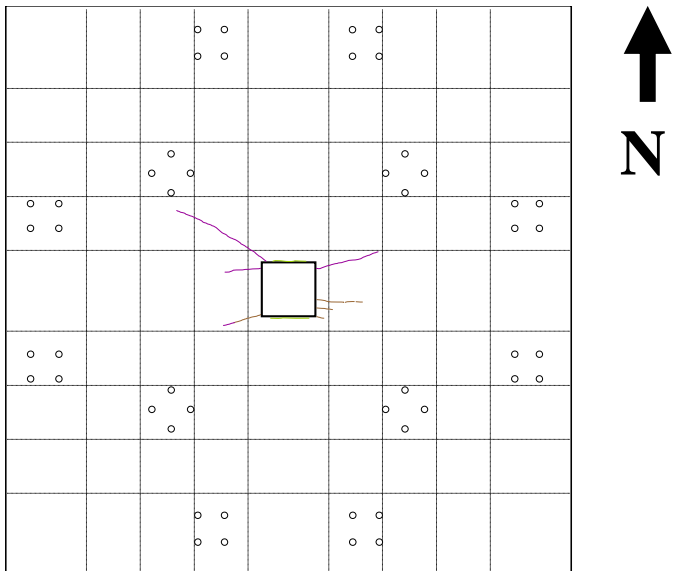


Figure 4.27 Bottom of the Slab at 1.25% Lateral Drift (Specimen LG0.5)

4.3.5 Specimen LR_{ST}G0.5

Crack plots for specimen LR_{ST}G0.5 are presented in Figure 4.28 through Figure 4.34. The following color code was used to plot cracks: gravity load (red), 0.25% drift (blue), 0.5% drift (black), 0.75% drift (green), 1% drift (brown), 1.5% drift (purple). Cracking when the gravity load was applied was more extensive than in specimen LG0.5 and less than in specimen L0.5.

Similarly to what was observed for specimens L0.5 and LG0.5, torsional cracking on the East and West sides of specimen LR_{ST}G0.5 increased when the top reinforcement of the slab yielded at 0.75% drift. Hairline cracks (< 0.01 in. width) started to develop at 0.75% drift on the bottom of the slab. Results for crack lengths and densities are presented in Table 4.3.

Table 4.3 *Length and density of cracks in Specimen LR_{ST}G0.5*

Story Drift (%)	Crack Length (ft)	Crack Density (in/sqf)
0	68	4
0.25	114	7
0.5	164	10
0.75	188	12
1	209	13
1.25	225	14

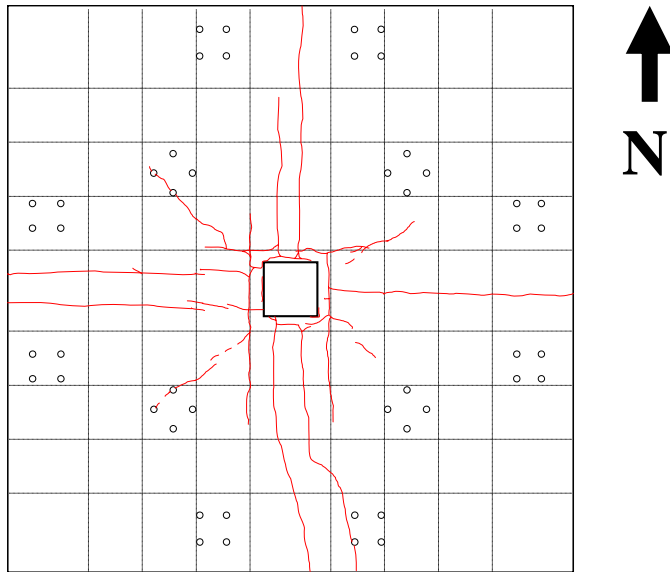


Figure 4.28 Gravity Load only (Specimen LR_{ST}G0.5)

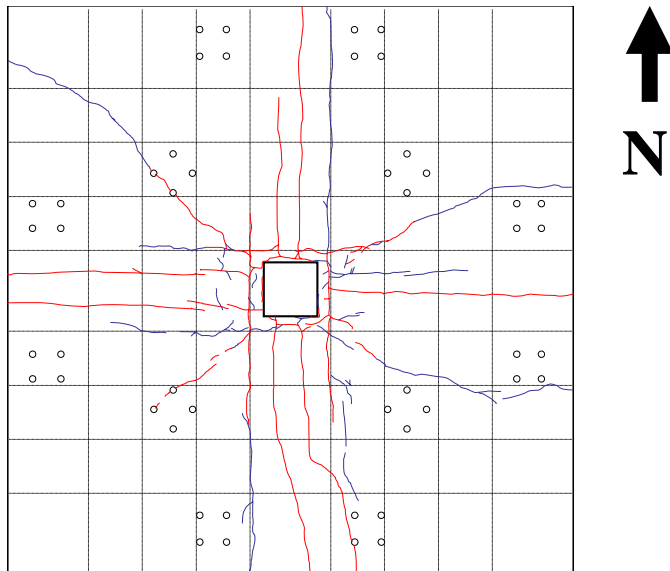


Figure 4.29 0.25% Lateral Drift (Specimen LR_{ST}G0.5)

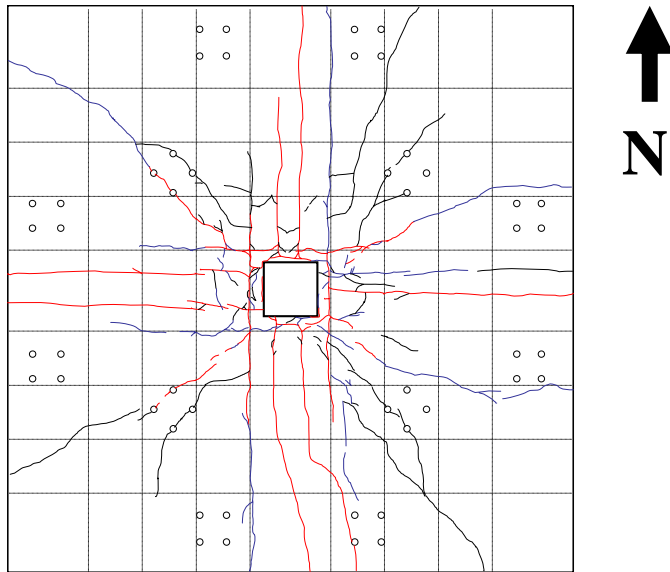


Figure 4.30 0.5% Lateral Drift (Specimen LR_{ST}G0.5)

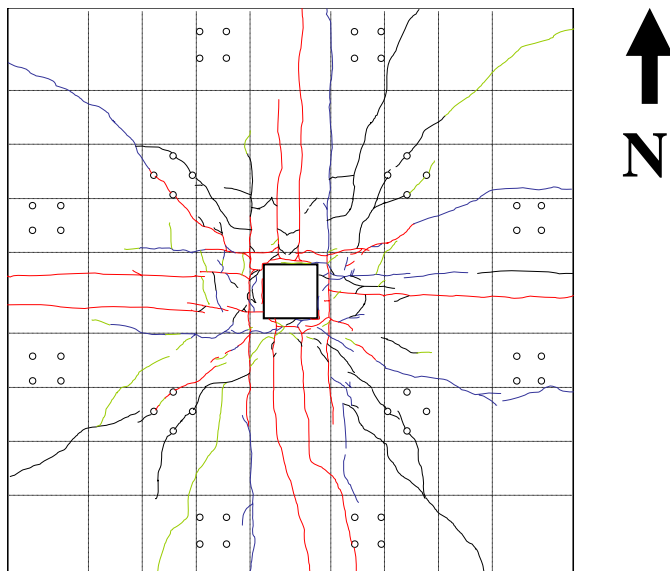


Figure 4.31 0.75% Lateral Drift (Specimen LR_{ST}G0.5)

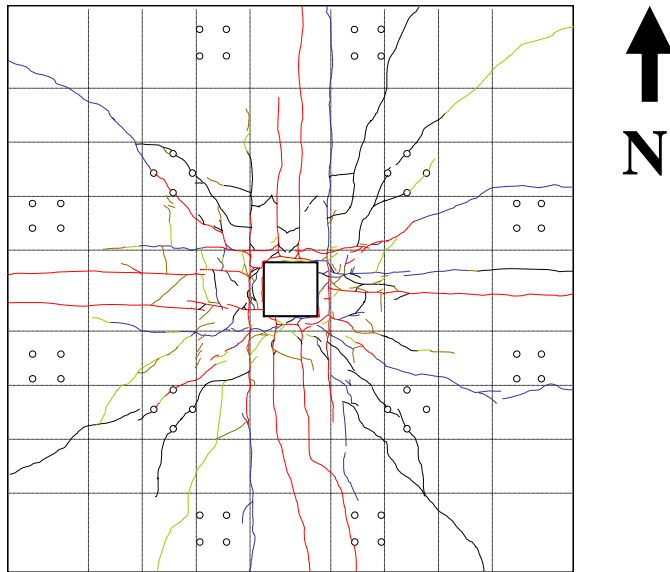


Figure 4.32 1% Lateral Drift (Specimen LR_{ST}G0.5)

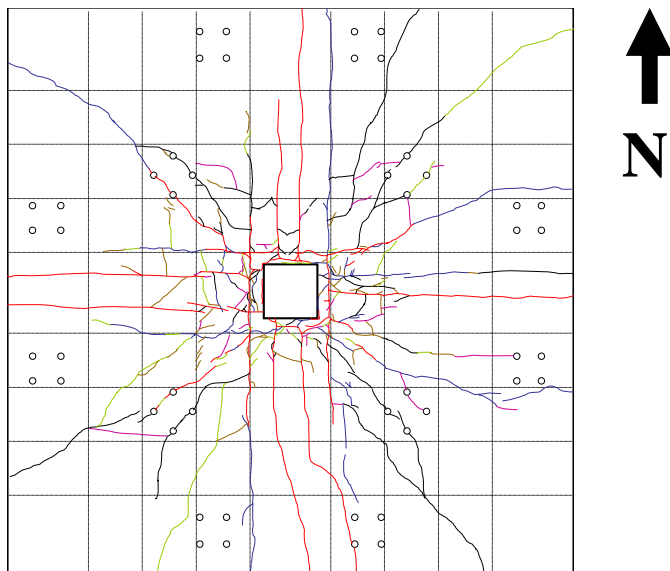


Figure 4.33 1.25% Lateral Drift (Specimen LR_{ST}G0.5)

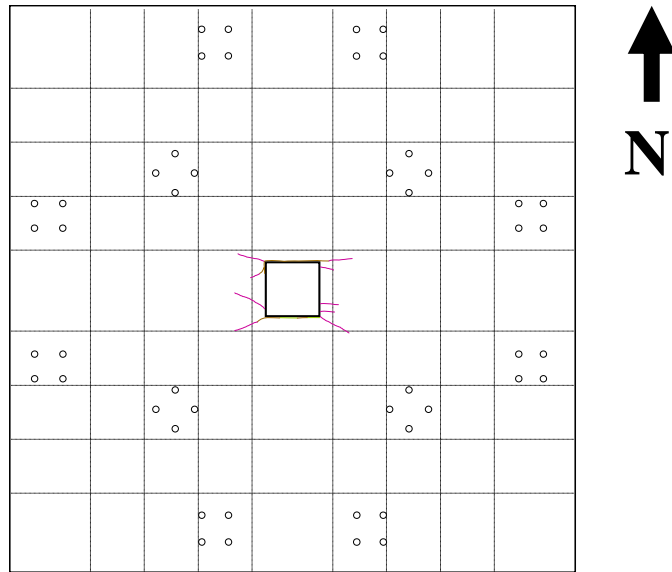


Figure 4.34 *Bottom of the Slab at 1.25% Lateral Drift (Specimen LR_{ST}G0.5)*

4.3.6 Specimen LG1.0

Crack plots for specimen LG1.0 are presented in Figure 4.35 through Figure 4.40. The following color code was used to plot cracks: gravity load (red), 0.25% drift (blue), 0.5% drift (black), 0.75% drift (green), 1% drift (brown), 1.5% drift (purple). The specimen remained uncracked when the gravity load was applied. Similarly to what was observed for specimens L0.5, LG0.5 and LR_{ST}G0.5, torsional cracking on the East and West sides of specimen LG1.0 increased at 0.75% drift, when the top reinforcement of the slab yielded. Hairline cracks started to develop at 0.5% drift on the bottom of the slab. Results for crack lengths and densities are presented in Table 4.4.

Table 4.4 *Length and density of cracks in Specimen LG1.0*

Story Drift (%)	Crack Length (ft)	Crack Density (in/sqf)
0	0	0
0.25	48	3
0.5	108	7
0.75	160	10
1	191	12
1.25	221	14

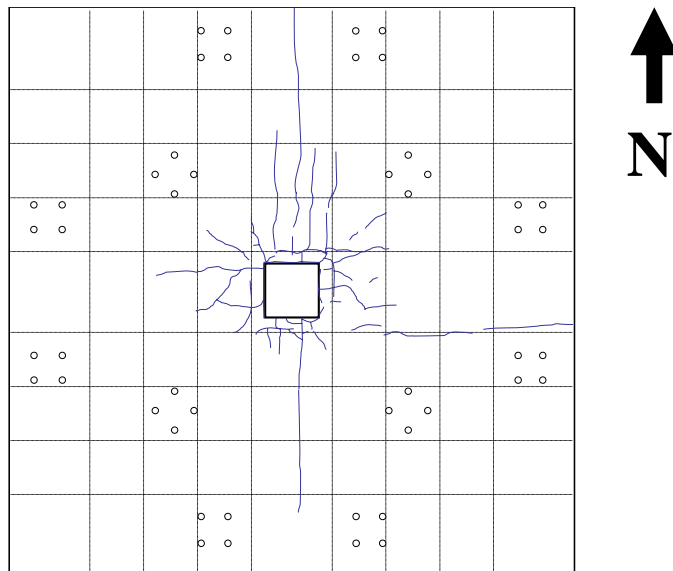


Figure 4.35 *0.25% Lateral Drift (Specimen LG1.0)*

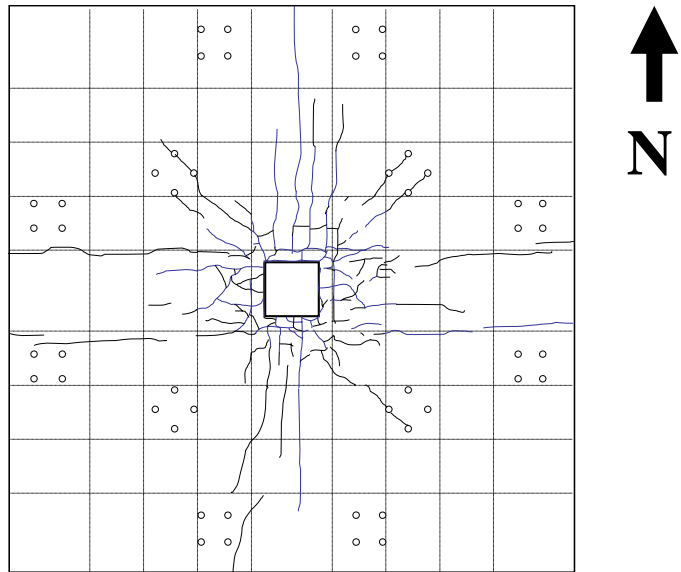


Figure 4.36 0.5% Lateral Drift (Specimen LG1.0)

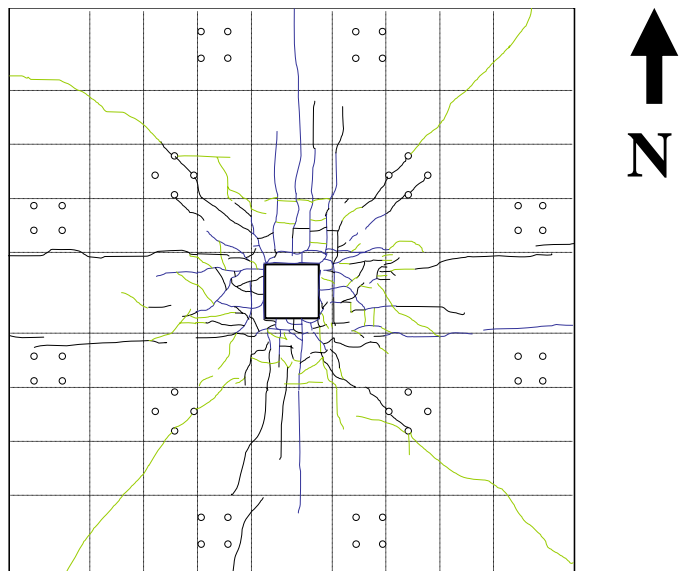


Figure 4.37 0.75% Lateral Drift (Specimen LG1.0)

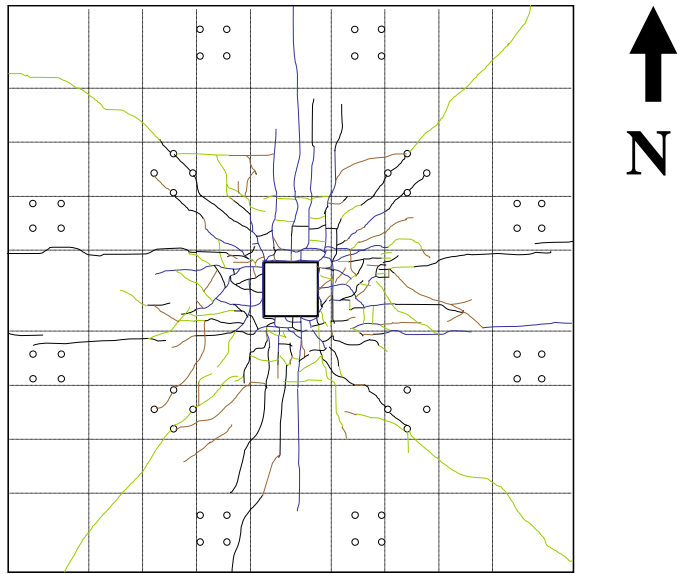


Figure 4.38 1% Lateral Drift (Specimen LG1.0)

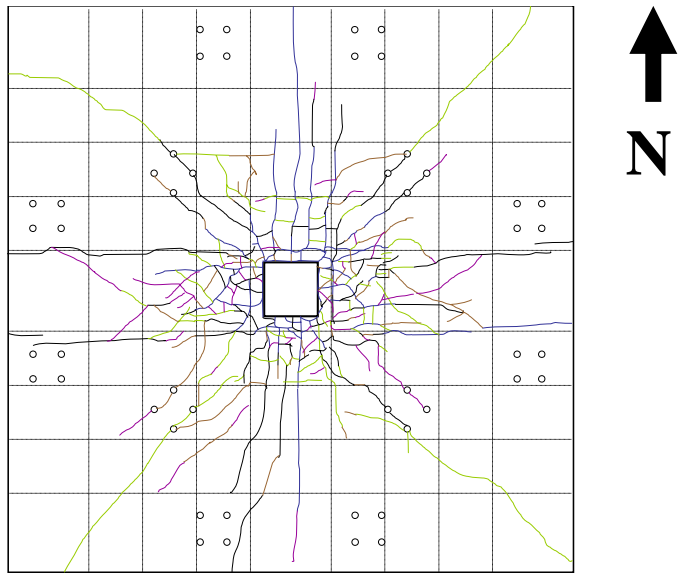


Figure 4.39 1.25% Lateral Drift (Specimen LG1.0)

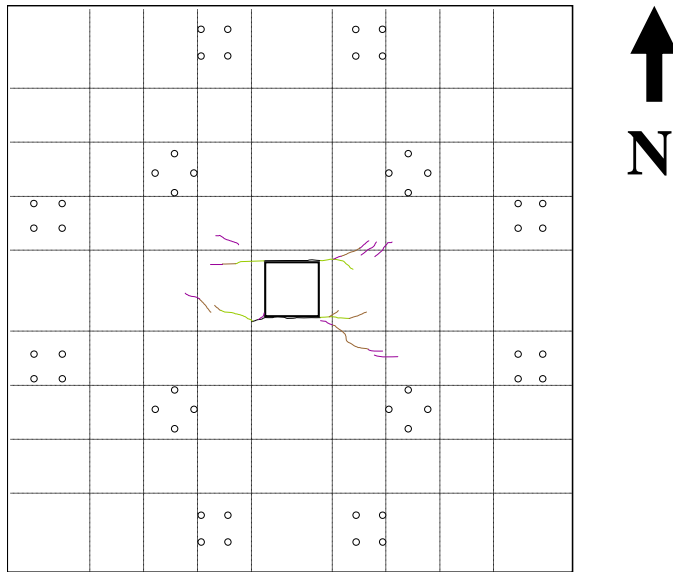


Figure 4.40 Bottom of the Slab at 1.25% Lateral Drift (Specimen LG1.0)

4.3.7 Analysis of combined crack density data for all specimens

Crack densities for all specimens are presented in Figure 4.41. Analysis of the combined data leads to the following observations:

- i. Two factors contributed to significant data scattering and lack of good correlation between crack density and story drift, when story drifts were below 0.5%. The first was the accidental preloading of specimen L0.5, which caused cracking that exceeded the cracking expected during the application of gravity loads. The second was the greater top reinforcement ratio (1%) for specimen LG1.0 that caused this

specimen to remain uncracked when gravity loads were applied, while other specimens with lower top reinforcement ratio (0.5%) cracked.

- ii. For drift levels 0.5% and above, there is a good correlation between crack density and story drift. Regardless of the loading history and top reinforcement ratio, data from all specimens converge to a similar trend when story drifts are equal or greater than 0.5%.

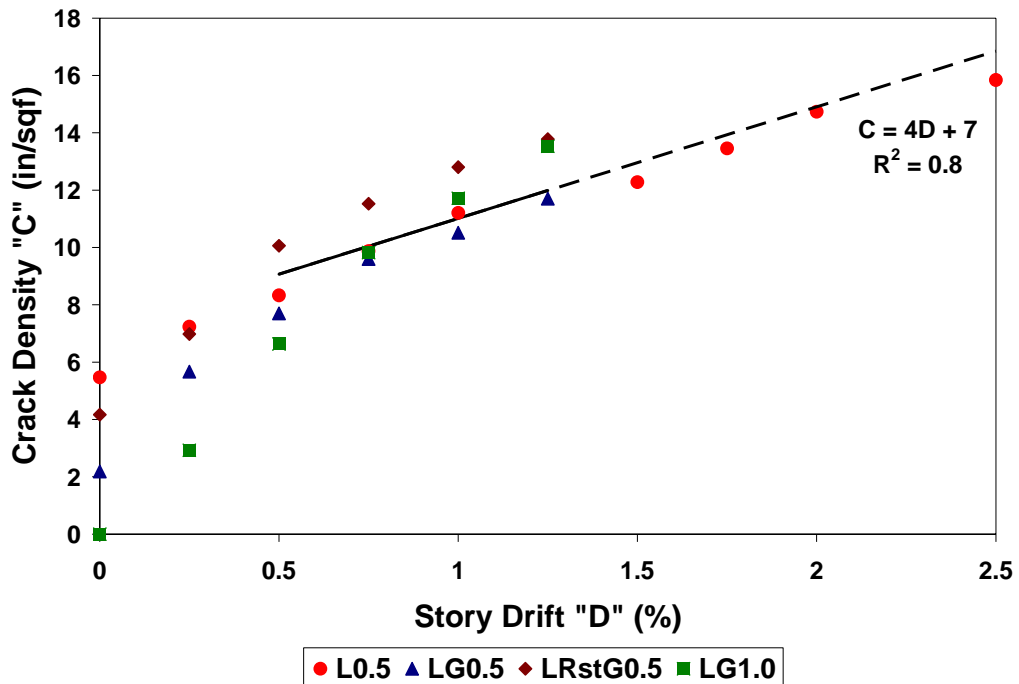


Figure 4.41 Relationship between Crack Density and Story Drift

4.3.8 Relationship between crack density and story drift

Data for story drifts equal to or greater than 0.5% were used to conduct a linear regression analysis, from which the following relationship was obtained:

$$C = 4D + 7 \quad ; D \geq 0.5 \quad \text{Equation 4-1}$$

Where D is Story Drift (%) and C is Crack Density (in./sqf).

Solving for D in Equation 4-1, the following relationship is obtained:

$$D = 0.3C - 2 \quad ; C \geq 9 \quad \text{Equation 4-2}$$

Data below 0.5% were very scattered and therefore were not used to compute the regression line $C = 4D + 7$. Such regression line can be used to estimate story drifts from 0.5% to 1.25%, where data from four specimens were available. The regression line is not recommended to be used above 1.25% drift because data from only one specimen (L0.5) were available.

4.3.9 Conclusions on the use of Crack Densities to predict Story Drifts

Crack densities determined from this study provide an indicator of the drifts using the following criteria:

- i. When the Crack Density was less than 9 in./sqf, the Story Drift was less than 0.5%.

- ii. When the Crack Density was equal to or greater than 9 in./sqf and equal to or smaller than 12 in./sqf, the Story Drift could be estimated by using Equation 4-2.
- iii. When the Crack Density was greater than 12 in./sqf, the Story Drift was equal to or greater than 1.5%.

It should be noted that this criterion was developed based on limited number of data; therefore its applicability is limited to slab-column connections that are similar to those tested in laboratory. Results should be considered applicable to slab column connections with 0.5% to 1% reinforcement ratio within the (c+3h) region. This criterion could be improved if additional tests become available in the future.

It is expected that above 0.5% drift, specimens with more than 1% reinforcement ratio in the (c+3h) region could develop a larger density of cracks than specimens with 0.5% to 1% reinforcement, because heavy reinforced slabs tend to have a larger number of narrow cracks than lightly reinforced slabs.

In tests conducted in the laboratory, the effects of creep were considered negligible, because measurements were conducted soon after lateral loads were applied. In field applications, creep may increase crack density, if measurements are conducted several days after an earthquake.

Shrinkage cracks were not observed in the laboratory because the specimens' slab was not restrained to deformations caused by shrinkage. In a

building, cracking due to restrained shrinkage is expected occur and therefore crack density would be affected in the field by the effects of shrinkage.

Crack density was found not to be a function of crack width. Specimens with 0.5% reinforcement ratio in the (c+3h) region had larger crack widths than the specimen with 1% reinforcement ratio; however their crack density data felt within the same trend for drifts greater than 0.5%.

CHAPTER 5

Non-Destructive Techniques for Damage Assessment

5.1 INTRODUCTION

The feasibility of using non-destructive techniques for damage assessment in a flat-plate building is studied in this chapter.

Damage assessment implies the identification of the degree of lateral load damage that a slab-column connection has experienced after an earthquake and the subsequent estimation of strength (gravity load carrying capacity of the connection) based on the degree of damage. For this purpose, good correlation between measurements from any non-destructive technique and the degree of damage experienced by the connection is needed.

Following a preliminary evaluation of a variety of NDT techniques, five methods were studied in detail and are presented in this chapter: Spectral Analysis of Seismic Waves (SASW), Impulse Response (IR), Ultrasonic Pulse Echo (UPE), Nonlinear Elastic Wave Spectroscopy (NEWS) and Impact Echo (IE). Other methods such as the Ultrasonic Pulse Velocity (UPV), Ground Penetration Radar (GPR) and High Energy Radiography (HER) were not considered to be adequate for assessing damage in flat-plate buildings. The preliminary evaluation was based on a literature review of available NDT techniques and their

applicability to assess damage in concrete structures. The study of Shaw and Xu (1998) on the effectiveness of several NDT techniques to detect damage in concrete and their rating according to reliability and usefulness was a key reference for such a preliminary evaluation.

5.2 SPECTRAL ANALYSIS OF SURFACE WAVES (SASW)

5.2.1 Background

Spectral Analysis of Surface Waves (SASW) is a non-destructive test method based on the propagation of surface waves through a conductive media. SASW was originally developed to determine Young's modulus profiles at pavement sites and shear modulus profiles at soil sites, but it has also been used in structural integrity studies (Kalinski, et al., 1994).

The SASW method uses a source of impulsive or sinusoidal signal, or random noise, and two receivers (geophones or accelerometers) located at variable source-receiver spacing d_1 and receiver spacing D (Figure 5.1). A piezoelectric shaker is used to generate high frequency waves (1 to 50 kHz) and accelerometers are required for thin members. To avoid the effects of body waves produced in the near field, an array $d_1 = D$ (Figure 5.1) has been recommended (Nazarian, et al., 1988). Typically D is varied geometrically (for example 3, 6 and 12 inches).

The time history records from the accelerometers $\ddot{x}(t)$ and $\ddot{y}(t)$, located at a distance d_1 and d_2 from the source (Figure 5.1), are transformed into the frequency domain by a FFT procedure to obtain $X(f)$ and $Y(f)$ real functions. $X^*(f)$ and $Y^*(f)$ are the complex conjugates of $X(f)$ and $Y(f)$ respectively.

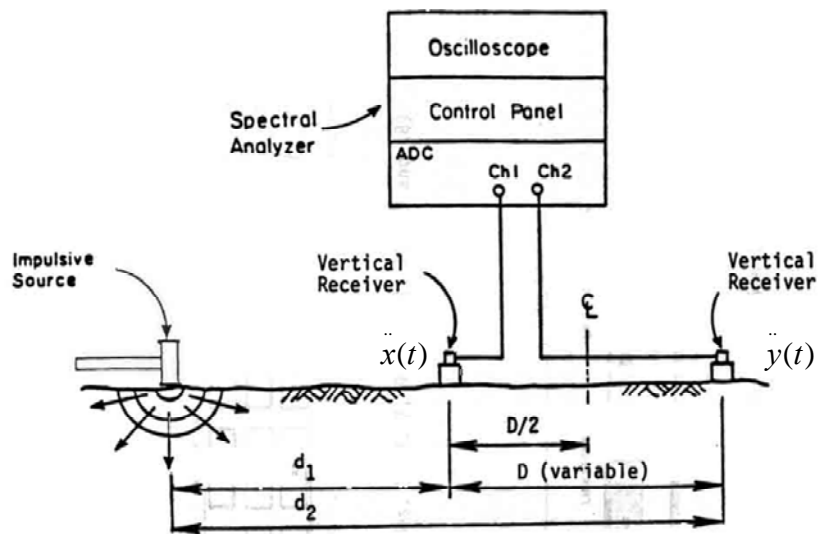


Figure 5.1 General configuration of SASW testing (Nazarian, et al., 1988).

The cross power spectrum is defined as:

$$G_{XY} = X^*(f) \cdot Y(f) \quad \text{Equation 5-3}$$

The coherence function is defined as:

$$\gamma^2 = \frac{G_{XY} \cdot G_{XY}^*}{G_{XX} \cdot G_{YY}} \quad \text{Equation 5-4}$$

A coherence value $\gamma^2 = 1$, means a high signal-to-noise ratio (good quality of acquired data). The effects of wave reflections caused by discontinuities in the material such as cracks, boundaries or material interfaces, typically produce coherence values less than one. In such situations, wave filters should be used carefully to obtain cross power spectra records which are smooth and therefore representative of plane Rayleigh waves. Discontinuities in the material introduce noise in the power spectra records and wave filters are required to eliminate such noise.

Exponential functions $W(t) = e^{-t/\tau}$ have been used successfully as wave filters in studies on discontinuous rock masses, where τ is a time factor that controls the abruptness of the filtering window. An exponential windowing function with τ 1 to 1.5 times D/V_R has been recommended by previous studies (Madianos, et al., 1992), where V_R is the Raleigh wave phase velocity. If the intention is to include effects of reflection in the phase information, then a large τ shall be used, if the intention is to eliminate such effects, then a small τ should be used. Values of τ that are too small will cause loss of coherence and can make the length of the time signal too short for meaningful analysis. If the SWA method is used in cracked slab-column connections, it is known that significant noise due to wave reflections at opened cracks will be produced and wave filters such as

exponential functions would be required either to include the effects wave reflections or to exclude them from the cross power spectra records.

For the frequency domain in which $\gamma^2 = 1$ is achieved, the phase angle of the cross power spectrum $\phi_{XY}(f)$ is obtained as follows:

$$\phi_{XY}(f) = \tan^{-1}\left(\frac{\text{Im}[G_{XY}(f)]}{\text{Re}[G_{XY}(f)]}\right) \quad \text{for } -\pi \leq \phi_{XY} \leq \pi \quad \text{Equation 5-5}$$

The difference in arrival time of a Rayleigh wave of frequency f at the accelerometers can be computed from the phase angle as follows:

$$t(f) = \frac{\phi_{XY}(f)}{2 \cdot \pi \cdot f} \quad \text{Equation 5-6}$$

The wave length is computed as a function of the arrival time difference $t(f)$, the frequency f and the receiver spacing D as follows:

$$L_R(f) = \frac{D}{f \cdot t(f)} = \frac{2 \cdot \pi}{\phi_{XY}(f)} \cdot D \quad \text{Equation 5-7}$$

The Raleigh wave phase velocity is obtained as follows:

$$V_R(f) = \frac{D}{t(f)} = f \cdot L_R(f) = \frac{2 \cdot \pi \cdot f \cdot D}{\phi_{XY}(f)} \quad \text{Equation 5-8}$$

For concrete, the shear wave velocity V_S can be computed using:

$$V_S = 1.1V_R \quad \text{Equation 5-9}$$

The shear modulus G is:

$$G = \rho \cdot V_S^2 \quad \text{Equation 5-10}$$

Where ρ is the material density.

The equivalent modulus of elasticity E is:

$$E = 2 \cdot G \cdot (1 + \nu) \quad \text{Equation 5-11}$$

Where ν is the Poisson's ratio of the material (in example, concrete).

A dispersion curve of Raleigh wave phase velocity (V_R) versus wavelength (L_R) is constructed for all available frequencies. The shape of the dispersion curve is used to locate layer interfaces and discontinuities such as honeycombs, boundaries, etc. For concrete members without discontinuities, the dispersion curve will tend to be a horizontal line, since no significant changes in E and V_R can be measured in a homogeneous and continuous material. An example of a dispersion curve for a two layered material is shown in Figure 5.2. The top layer has an open crack to a depth h and therefore surface wave velocity and equivalent modulus of elasticity are equal to zero to the depth of the crack.

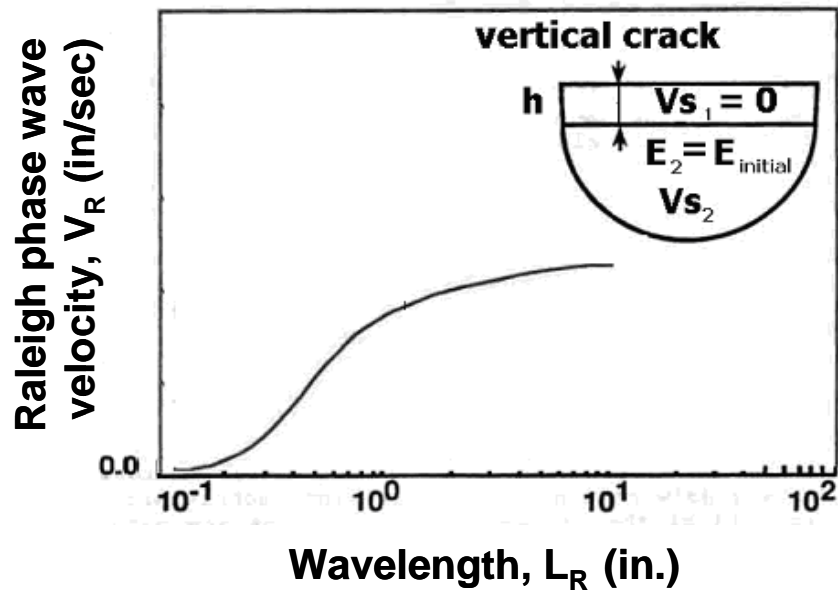


Figure 5.2 Expected dispersion curve for a concrete member with a vertical crack to a depth h (Roesset, J.M., et al, 1990).

Bowen (1992) conducted studies on concrete beams with and without saw-cut cracks opened to a known depth, to investigate changes in dispersion curves between undamaged and damaged states. He concluded that further studies are required to establish whether there is clear relationship between changes in the dispersion curve and the depth of cracks. The information provided by dispersion curves is qualitative; and it could be used to detect the presence of cracks but not to measure crack depths accurately.

5.2.2 Damage assessment applications

In previous SASW tests for structural integrity studies, damaged areas in concrete members were identified by evaluating changes in the equivalent elastic modulus of the material. SASW was used by Kalinski, et al. (1994), to investigate a damaged prestressed concrete beam by measuring changes in the surface wave velocity. The results indicated the qualitative ability of the SASW method to confirm and delineate internal cracking within a damaged concrete structural element.

Bowen and Stokoe (1992) investigated a cracked reinforced concrete column subjected to cyclic loading. Damage was detected from dispersion curves when the crack was open, but was undetectable when a crack closed under compression. A crack closed under compressive stresses behaved as sound material. They concluded that further work was necessary to evaluate attenuation characteristics when cracks are under compressive loads.

Bowen (1992) investigated the detection of crack depths from dispersion curves and found that the Raleigh wave phase velocity decreased when 1", 2" and 3" deep cracks were present. However, as shown in Figure 5.3, Bowen (1992) did not find good correlation between crack depth and wave velocity. The trend of data was not consistent, showing the Raleigh wave phase velocity more affected by a 1" deep crack than by a 2" deep crack.

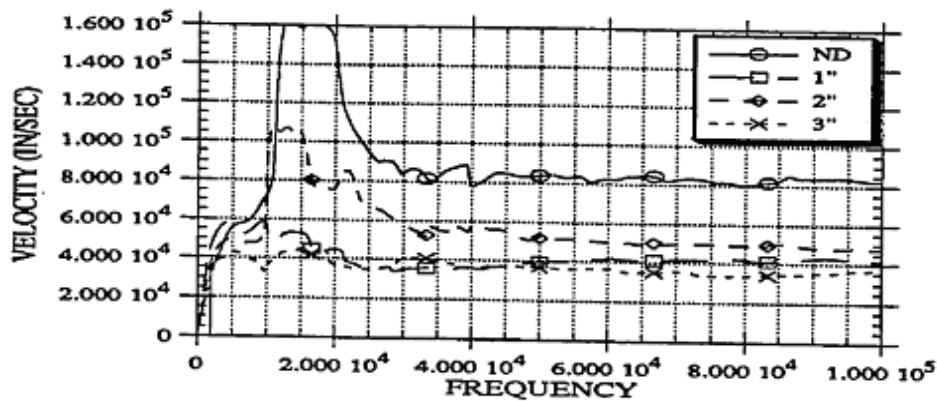


Figure 5.3 Dispersion curve for a 6" deep beam with No Damage, 1", 2" and 3" deep cracks (Bowen, 1992).

5.2.3 Feasibility of using SASW method for damage assessment in flat-plate buildings

Although previous studies indicated that the SASW method could be used to detect and map damaged areas, the use of this method to assess damage in flat-plate buildings was not considered feasible for the following reasons:

- i. The identification of damaged areas in flat-plate buildings could be achieved by visual observations; therefore the ability of the SASW method to detect and map damaged areas is not required.
- ii. Non-destructive testing is required to understand how cracks propagate internally into the material, particularly to measure crack depths. The SASW approach to measure crack depths from dispersion curves is

complex and inaccurate and the use of this method was not convenient for such purposes.

- iii. Without an accurate relationship between Raleigh phase wave velocity and crack depth within the frequency domain, a relationship between SASW measurements and the degree of damage in the connection would be impossible to develop.

5.3 IMPULSE RESPONSE (IR)

5.3.1 Background

The impulse response method is a non-destructive test originally developed for quality control of driven concrete piles and drilled shafts, and currently also used for the evaluation of concrete pavements and slabs on grade. The IR method uses a low-strain impact to send stress waves through the tested element. The impact source is a hammer with a built-in load cell in the hammer head. Response to the input stress is measured using a velocity transducer (geophone), as shown in Figure 5.4.

Time records for the hammer force and the geophone velocity response are processed using a Fast Fourier Transform (FFT) algorithm. The resulting velocity FFT spectrum V is divided by the force FFT spectrum F to obtain a transfer function, referred to as the mobility V/F . The graph of mobility V/F

plotted against frequency f contains information on the condition and the integrity of the concrete in the tested element, Davis, (2003).



Figure 5.4 Slab Impulse Response Test (Olson, 2004)

5.3.2 Parameters involved in the IR test

5.3.2.1 Dynamic stiffness

The slope of the portion of the mobility plot below 50 Hz defines the compliance or flexibility of the area around the test point for a normalized force

input. The inverse of the flexibility is the dynamic stiffness K' of the element at the test point. The dynamic stiffness is a function of concrete quality, element thickness and element support conditions.

The dynamic stiffness is defined by the following equation:

$$K' = \frac{2\pi \cdot f_m}{V/F_m} \quad \text{Equation 5-12}$$

Where, f_m and V/F_m are the frequency and mobility, respectively, at point m . The point m is selected on the initial linear portion of the mobility curve. Figure 5.5 shows an example of a mobility plot for sound concrete, where the dynamic stiffness has been computed.

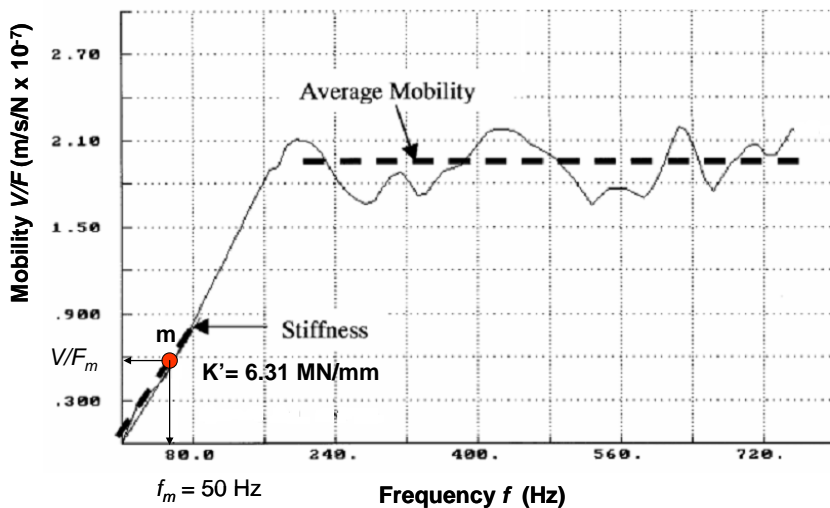


Figure 5.5 Typical mobility plot for sound concrete (Davis, 2003)

5.3.2.2 Mobility and damping

The element's response to the stress waves will be damped by the element's intrinsic body damping. The mean mobility value over the 100 – 800 Hz range is directly related to the density and thickness of the element. For example, a reduction in thickness corresponds to an increase in mean mobility.

5.3.2.3 Peak/mean mobility ratio

The ratio of the peak to mean mobility is an indicator of the presence and degree of either debonding within the element or voiding/loss of support beneath a slab on grade. When debonding or delamination is present within a structural element, or when there is loss of support beneath a concrete slab on grade, the peak mobility below 100 Hz becomes appreciably higher than the mean mobility from 100 to 800 Hz.

5.3.3 Examples of mobility plots for sound and defective slabs

Figure 5.6 and Figure 5.7 show mobility plots for a sound 6.7-in thick box-girder bottom slab on a freight rail bridge and a thin 2.6-in thick box-girder bottom slab on a light rail bridge. The mobility plots are in units of velocity/force (inches per second / pounds force).

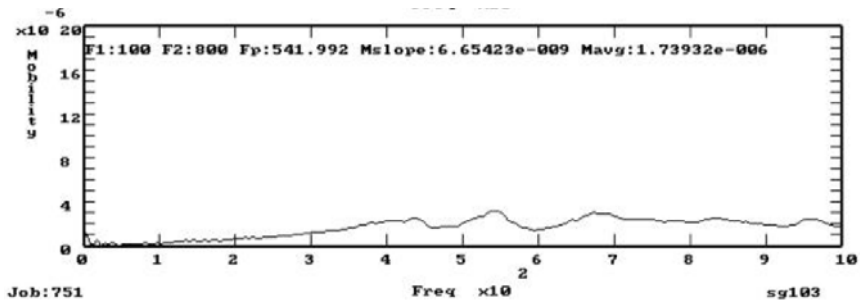


Figure 5.6 Mobility record for a sound 6.7-in thick slab (Olson, 2004)

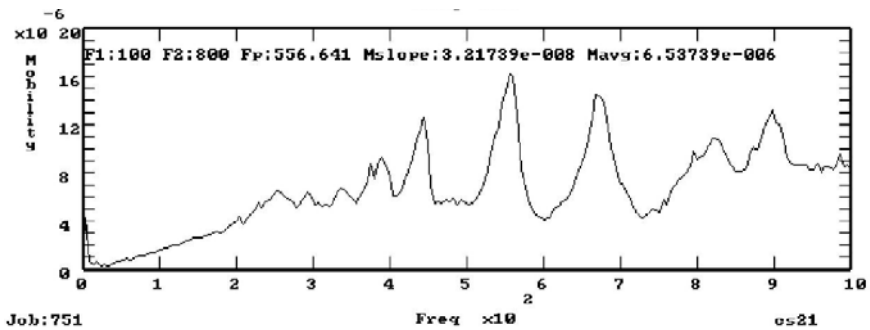


Figure 5.7 Mobility record for a thin 2.6-in thick damaged slab (Olson, 2004)

By comparing Figure 5.6 and Figure 5.7, the differences in stiffness between a sound thick slab and a thin damaged slab can be seen. It is evident that the damaged slab has an irregular mobility plot and high mobility values (high flexibility). The sound slab has a smooth mobility shape (sound) and low mobility values (low flexibility). The average mobility between 100 and 800 Hz for the

sound slab is $1.7 \text{ E-6 in/sec/lbf}$ and the average value for the damaged slab is $6.5 \text{ E-6 in/sec/lbf}$ (Olson, 2004).

The slope of the portion of the mobility plot below 50 Hz for the thin slab is almost 5 times higher than that for the sound slab, which means that the thin slab is 1/5 as stiff as the thick slab.

5.3.4 Damage assessment applications

Typical applications of IR testing include assessing the condition of large concrete members such as driven piles, shafts, slabs on grade, pavements, bridge decks, walls and tanks. The IR test provides a rapid approach in finding defective areas, such as poor concrete consolidation, poor ground slab support, honeycombs and delamination. Presently, there is no information in the literature on the application of this method to floor slabs. IR tests conducted on bridge decks appear to be the most closely related application to floor slabs. However, tests on bridge decks have been limited to the identification of areas of poor concrete consolidation, honeycombs and delamination and have not been used to estimate the degree of damage due to external loading.

5.3.5 Feasibility of using IR method for damage assessment in flat-plate buildings

Tests were conducted on a reinforced concrete slab to investigate the feasibility of using the IR method. Results from tests are presented in Appendix A and the applicability of the IR method to flat plates was assessed. Based on test results, it was concluded that the IR method is unsuitable for assessing damage in flat-plate buildings. From the data in Appendix A, no correlation was found between average mobility and damage experienced by a tested slab.

5.4 ULTRASONIC PULSE ECHO

5.4.1 Background

The Ultrasonic-Pulse-Echo method is a suitable way to inspect structures with access from one side only. The method has been successfully and extensively used on homogeneous materials such as steel. It has not been used extensively on non-homogeneous materials such as concrete. In this method, a tomographic presentation of output data is ideal for imaging internal defects.

Improvements in the Ultrasonic-Pulse-Echo method have been significant during the last few years. This is due to the development of broadband phased array transducers in the desired frequency range having a short pulse response and the application of synthetic aperture measuring and evaluation techniques. The use of the Synthetic Aperture Focusing Technique (SAFT) offers a powerful

approach for creating high resolution images from the inside of the element or specimen under inspection (Krause, et al., 2003).

An ultrasonic phased array is a structure of piezoelectric ceramic rods inserted in a polymer material (Figure 5.8) having a specified geometry. The piezo-composite transducers work as transmitters and receivers, and are installed in a probe used to scan the structure's surface (Figure 5.9).

The scanning process consists of introducing a beam of stress waves through the element being tested by activating different apertures in turn. Each aperture is made up of one or several piezoelectric ceramic rods of the phased array probe. While a certain aperture is transmitting stress waves (green), the remaining rods (gray) in the array are receiving signals (Figure 5.10). Using SAFT, signals from different apertures are processed and a tomographic image of the structure is obtained.

5.4.2 Damage assessment applications

The Ultrasonic–Pulse-Echo method has been used successfully to determine areas of honeycombing and poor consolidation in concrete elements. (Hillger, 2000). However, due to the non-homogeneity of the material, non-destructive testing of concrete is limited to large defects. Ultrasonic measurements are disturbed by scattering at random arrangements of aggregates which are constituent parts of the material. Scattering at aggregates leads to grain noise and to a speckle structure in SAFT-images. Therefore, small cracks are impossible to trace using this method.

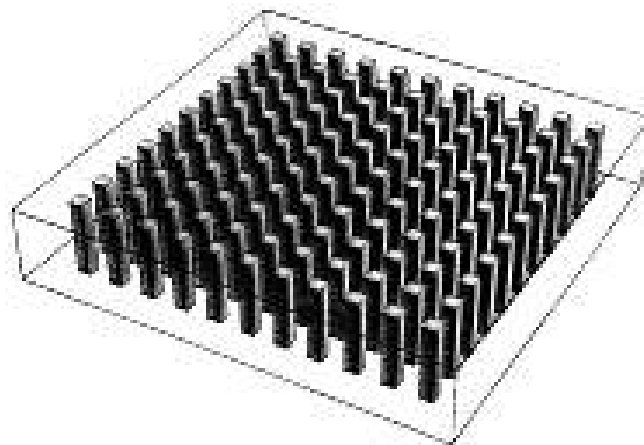


Figure 5.8 Ultrasonic phased array of piezo-composite transducers (Dumas, et al., 2002)



Figure 5.9 Ultrasonic phased array probe (Acoustic Control Systems, 2006)

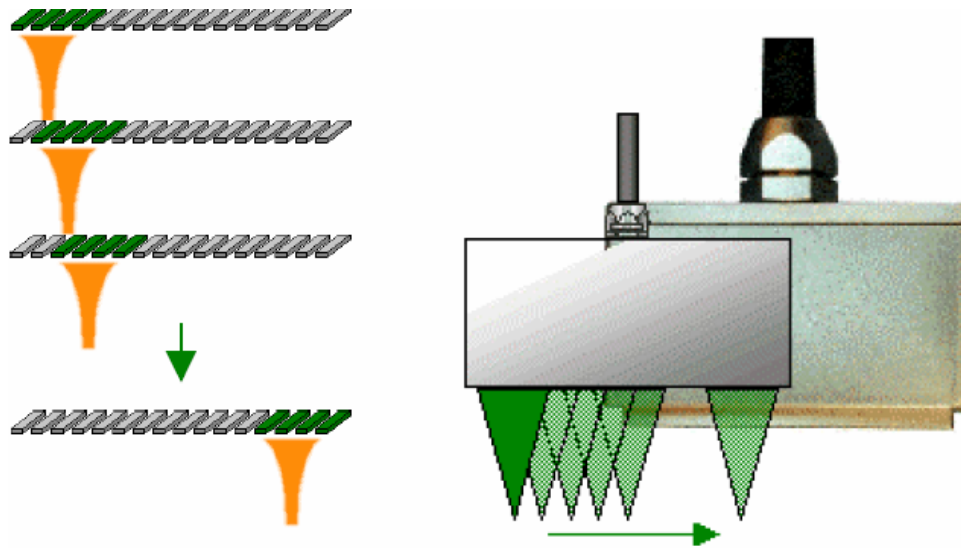


Figure 5.10 View of electronic scanning (Poguet, et al, 2002)

5.4.3 Feasibility of using Ultrasonic-Pulse-Echo method for damage assessment in flat-plate buildings

Although the Ultrasonic Pulse Echo method is widely used to detect and map defects in steel elements, the use of this method to assess damage in flat-plate buildings was not considered feasible for the following reasons:

- i. The ability of the Ultrasonic Pulse Echo method to detect and map internal damage in concrete is excellent for the case of large voids, such as honeycombs. Identification and mapping of internal cracks is difficult due to the combined effects of scattering of ultrasonic waves

at the paste-aggregate interfaces and diffraction of waves at opened cracks. Mathematical models are used to consider such effects, but the practical application of such models would be complex and unreliable due to the large number and density of cracks that are opened in a damaged slab-column connection.

- ii. Even in the case that a reliable tomography (identification and mapping of internal and external cracks) could be obtained, it is possible that a tomographic image alone would not be sufficient to identify the degree of damage in a slab-column connection. Extensive studies of a variety of crack patterns and their relationships to the degree of damage in the connection would be required before tomographic images could be used as a damage assessment tool. The use of this method would be costly and not very effective.

5.5 NONLINEAR ELASTIC WAVE SPECTROSCOPY (NEWS)

5.5.1 Background

NEWS is a non-destructive test method developed by Johnson (1999). It is based on the study of the nonlinear behavior of the materials in response to stress waves. The nonlinear behavior starts after cracking and is clearly distinguished from the linear elastic behavior of an uncracked material.

The linear versus nonlinear wave resonance behavior in a bell is illustrated in Figure 5.11. The bell behaves in an expected manner when intact. When struck with a hammer, the resonance modes of the bell are excited. If the bell has a very small crack present, the modal frequencies depend on how hard the bell is struck. Thus, in the frequency spectrum associated with the damaged bell, the modal frequencies depend on how hard the bell was stricken. This is a nonlinear effect: a change in wave frequency with wave amplitude.

Another characteristic of nonlinear behavior is the generation of harmonics and sideband frequencies, which is illustrated in Figure 5.12. The undamaged bell is subjected to an input of two frequencies by means of a speaker. The frequency spectrum of the uncracked bell shows the same two frequencies as an output. In the cracked bell shown nonlinear mixing is observed (multiplication). The two frequencies multiply with themselves creating harmonics, and with each other creating sum and difference frequencies (sidebands).

The nonlinear behavior due to the presence of cracks is an indicator of the presence of damage. The undamaged portion of the sample produces nearly zero nonlinear effects, while the damaged portion acts as a nonlinear mixer. Using a frequency spectrum analysis, the differences between an undamaged and a damaged object become very evident.

5.5.2 Damage assessment applications

Johnson (1999) performed wave mixing experiments in undamaged and damaged automobile engine bearing caps to discern whether or not damage was present. In these tests, one high frequency wave and several low frequency waves were used simultaneously as input. Figure 5.13 shows the frequency wave spectrum of the undamaged and damaged samples. For the damaged specimen, many harmonics and sideband frequencies in the spectrum were created.

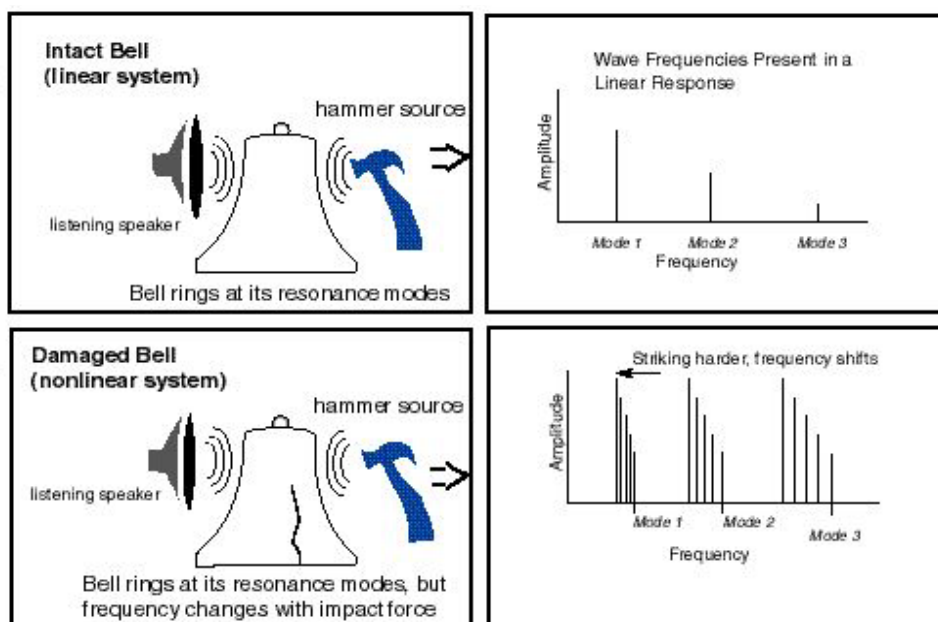


*Figure 5.11 Nonlinear effect of cracks on natural frequencies of a bell
(Johnson, 1999)*

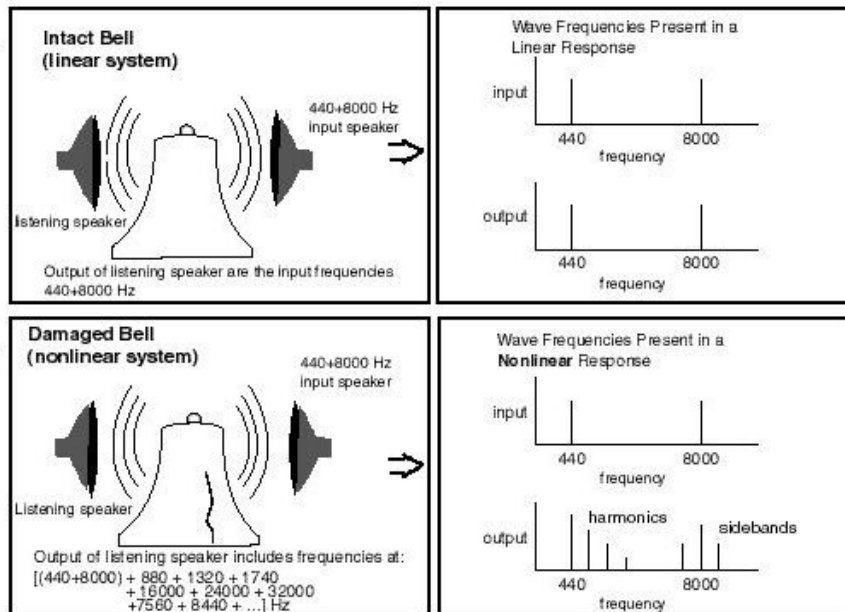


Figure 5.12 Generation of harmonic and sideband frequencies in a nonlinear system (Johnson, 1999)

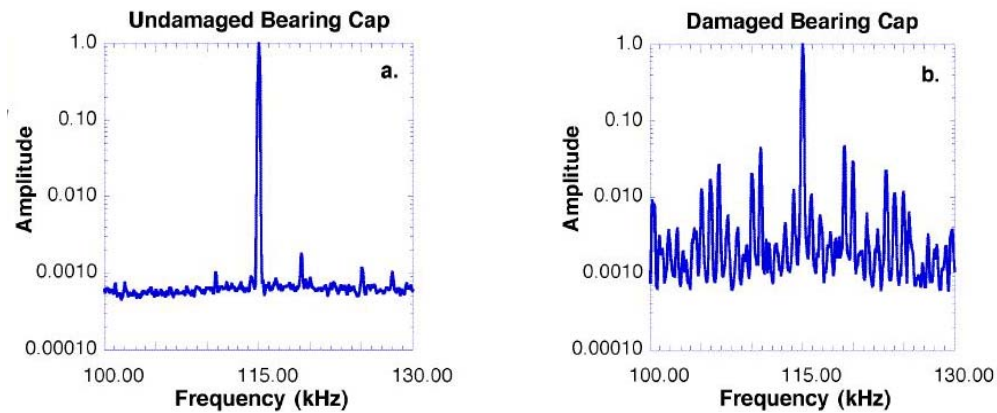


Figure 5.13 Spectroscopy of automobile engine bearing caps (Johnson, 1999)

NEWS method has great potential and further development of this method is expected in the near future.

5.5.3 Feasibility of using NEWS method for damage assessment in flat-plate buildings

Although the NEWS method has a great potential for damage assessment, its use was not considered feasible for the following reasons:

- i. Commercial equipment for wave spectroscopy tests is not available in the market, as the method is new and is not widely used. The hardware for wave spectroscopy tests has to be built using components from different manufacturers. The source of vibration should be able to input steady state or impulse response motions at variable known frequencies. Only a few piezoelectric high frequency shakers are available on the market that could be used for such purpose. They are fairly expensive compared to the cost of the input energy used in other techniques (impact hammers, steel balls, etc.). The hardware consists of a piezoelectric shaker, piezoelectric accelerometers, signal conditioning modules, and a data acquisition system.
- ii. In the future, one of the potential uses of this method could be the identification and mapping of damaged areas through tomographic imaging. However, the mathematical approach to obtain tomographic images from wave spectroscopy tests has not been developed yet.

Similarly to what was discussed in section 5.4.3 for the UPE method, tomographic images that could be obtained using the NEWS will have to be correlated with the degree of damage through an extensive study of different cracking patterns for a slab-column connection. The use of this method would be costly and not very effective.

5.6 IMPACT ECHO

5.6.1 Background

In the early 1970s, impact methods began to be used for integrity testing of deep foundations, such as piles. Hammers were used to generate very low frequency waves (less than 1 kHz) that could be used to determine the length of piles (Sansalone and Carino, 1986; Malhotra and Carino, 1991). In the early 1980s research engineers at the U.S. National Bureau of Standards explored the use of short duration mechanical impacts, produced by small steel spheres, as a source of stress waves for testing concrete structural elements, such as slabs (Sansalone, 1986; Sansalone and Carino, 1986). They found that by carefully choosing the diameter of the sphere, it is possible to generate stress waves with frequencies up to about 80 kHz that propagate through concrete as though it were a homogeneous elastic medium, but are reflected from internal flaws and interfaces. Researchers at National Bureau of Standards coined the term impact-echo to describe this method, and to set it apart from pulse-echo methods in which transducers are used to generate stress waves.

Impact-echo is based on the use of transient stress waves generated by elastic impact. A diagram of the method is shown in Figure 5.14. A short-duration mechanical impact, produced by tapping (or dropping) a small steel sphere against a concrete or masonry surface, is used to generate low-frequency stress waves that propagate into the structure and are reflected by flaws and/or external surfaces.

Surface displacements caused by reflections of these waves are recorded by a transducer, located adjacent to the impact. The resulting displacement-versus-time signals are transformed into the frequency domain, and plots of amplitude versus frequency (spectra) are obtained. Multiple reflections of stress waves between the impact surface, flaws, and/or other external surfaces give rise to transient resonances, which can be identified in the spectrum and used to evaluate the integrity of the structure or to determine the location of flaws.

It is the patterns present in the waveforms and spectra (especially the latter) that provide information about the existence and locations of flaws, or the dimensions of the cross-section of the structure where a test is performed, such as the thickness of a pavement. For each of the common geometrical forms encountered in concrete structures (plates; circular and rectangular columns; rectangular, I-, and T-beams; hollow cylinders; etc.), impact-echo tests on a solid structure produce distinctive waveforms and spectra, in which the dominant patterns—especially the number and distribution of peaks in the spectra—are easily recognized. If flaws are present (cracks, voids, delaminations, etc.) these patterns are disrupted and changed, in ways that provide qualitative and quantitative information about the existence and location of the flaws.

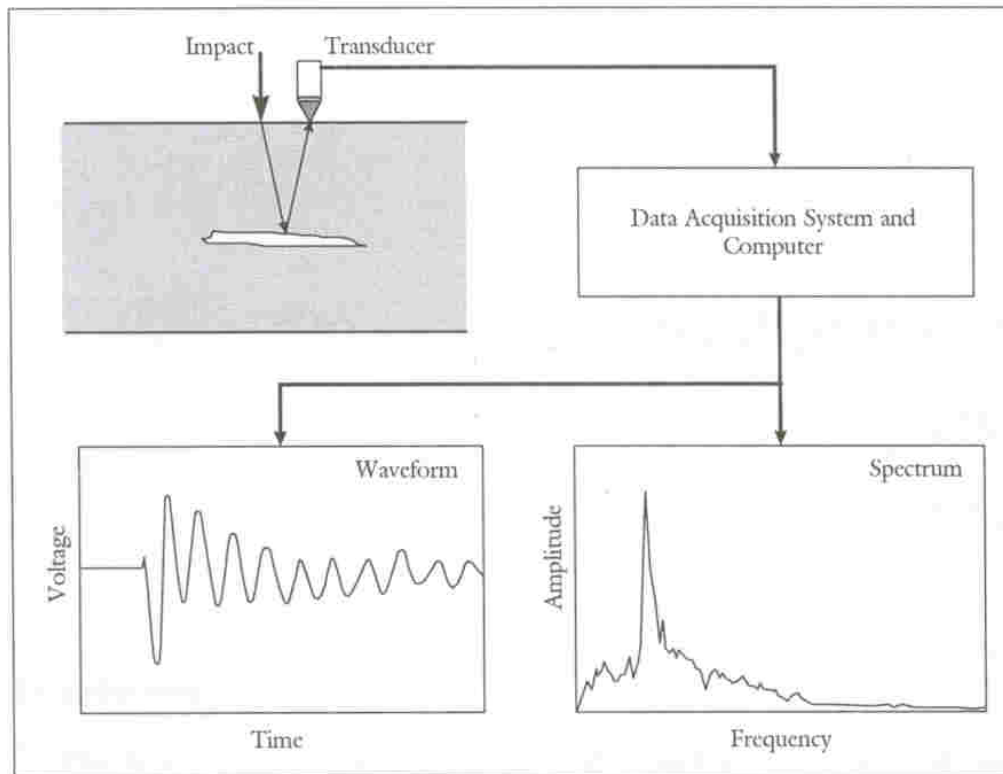


Figure 5.14 Outline of the Impact-Echo Method

(Sansalone and Streett, 1998)

5.6.1.1 Signal Analysis Method

During the initial development of the impact-echo technique, interpretation of the recorded waveforms was performed in the time domain. This required establishing the time of impact initiation and the arrival time of the first

P-wave echo. While this could be done, it was found to be time-consuming. An alternative approach is frequency analysis of the displacement waveforms.

The principle of frequency analysis is illustrated in Figure 5.15, which shows a solid plate of thickness T subjected to an impact-echo test.

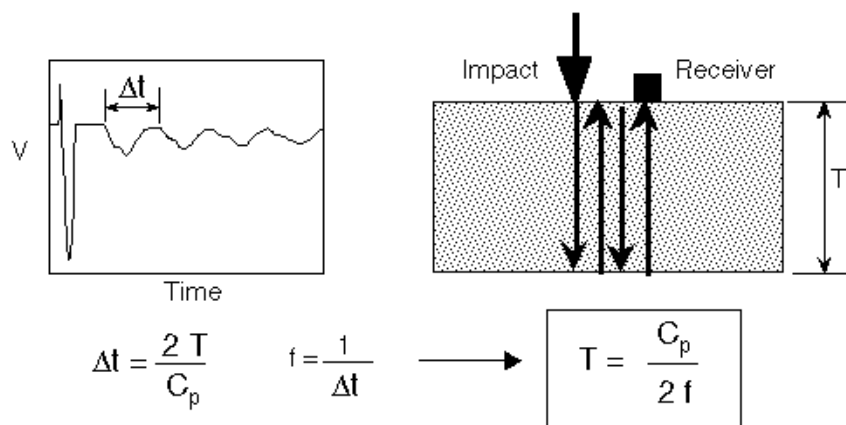


Figure 5.15 *The principle of frequency analysis in the Impact-Echo Method (Sansalone and Streett, 1997)*

The P-wave generated by the impact propagates back and forth between the top and bottom surfaces of the plate. Each time the P-wave arrives at the top surface it produces a characteristic displacement. Thus the waveform is periodic, and the period, t , is equal to the travel path, $2T$, divided by the P-wave speed C_p . Since frequency is the inverse of the period, the frequency, f , of the characteristic displacement pattern is:

$$f = C_p/2T$$

Equation 5-13

Laboratory experiments and finite – element based computer simulations of stress wave propagation in concrete structures, covering a wide variety of geometric shapes, have shown that for each shape the frequency of the fundamental or first mode of vibration excited by impact is also related to a shape factor β determined by the geometry (Sansalone and Streett, 1998). Therefore:

$$f = \beta C_p/2T$$

Equation 5-14

Sansalone (1996) showed that the shape factor β is required because an apparent P-wave speed C_p measured through impact-echo tests is used and not the true P-wave speed measured from a through-transmission pulse velocity test, the value of β is equal to 0.96 for solid plates. The apparent P-wave speed C_p is related to a fundamental mode of vibration excited by multiple reflections of the P wave. In the case of solid plates, the fundamental mode is the thickness mode shown in Figure 5.16. If the frequency of an experimental waveform can be determined, the thickness of the plate (or distance to a reflecting interface) can be calculated as follows:

$$T = 0.96C_p/2f$$

Equation 5-15

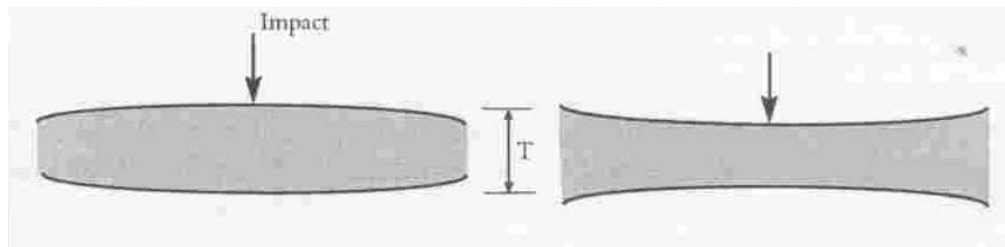


Figure 5.16 *The P-wave thickness mode of vibration of a plate (Sansalone and Streett, 1997)*

5.6.1.2 Illustrative Example

Figure 5.17 illustrates how frequency analysis is used in impact-echo testing. In Figure 5.17(a) an impact-echo test was performed over a solid portion of a 0.5-m thick concrete slab. There is a frequency peak at 3.42 kHz in the amplitude spectrum. This frequency corresponds to multiple reflections between the bottom and top surfaces of the slab. Solving for C_p , the P-wave speed is calculated to be 3410 m/s. Figure 5.17(b) shows the amplitude spectrum obtained from a test over a portion of the slab containing a disk-shaped void. The peak at 7.32 kHz results from multiple reflections between the top of the plate and the void. Solving for T , the calculated depth of the void is $3410/(2 * 7320) = 0.23$ m, which compares favorably with the known distance of 0.25 m.

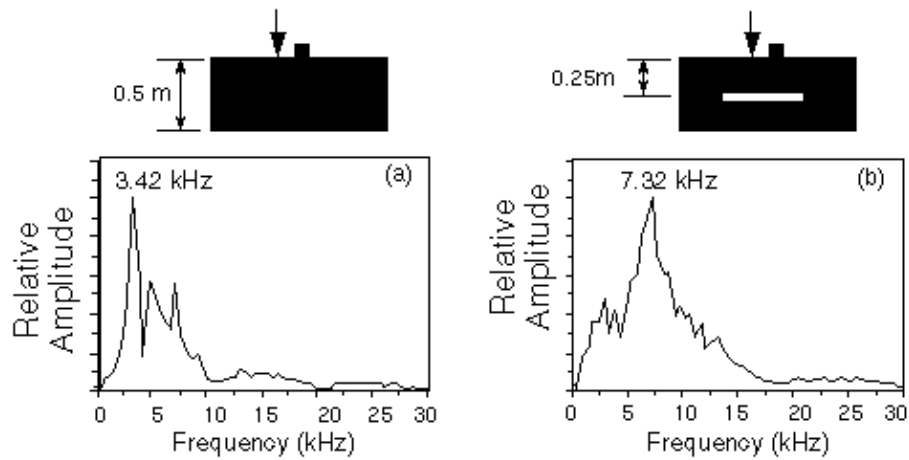


Figure 5.17 Example of the use of the Impact-Echo Method (Sansalone and Streett, 1997)

5.6.2 Damage assessment applications

Impact-echo can be used to determine the location and extent of flaws such as cracks, delaminations, voids, honeycombing, and debonding in plain, reinforced, and post-tensioned concrete structures, including plates (slabs, pavements, walls, decks), layered plates (including concrete with asphalt overlays), columns and beams (round, square, rectangular and many I and T shaped cross-sections), and hollow cylinders (pipes, tunnels, mine shaft liners, tanks). The method can be used to locate voids in the grouted tendon ducts of many types of post-tensioned structures. It can provide thickness measurements of concrete slabs with accuracy better than three percent, and it can locate voids in the subgrade directly beneath slabs and pavements. The method can be used to

determine thickness or to locate cracks, voids, and other defects in masonry structures where the brick or block units are bonded together with mortar.

When properly used the impact-echo method has achieved success in locating flaws and defects in highway pavements, bridges, buildings, tunnels, dams, piers, sea walls, and many other types of structures.

5.6.3 Feasibility of using the Impact Echo method for damage assessment in flat-plate buildings

The Impact Echo method could be used to measure the depth of critical cracks and detect areas of concrete delamination, following the approach proposed by Sansalone and Streett, 1998. Information on the depth of critical cracks and areas of concrete delamination could be used to infer the drift level experienced by a slab-column connection. The use of the Impact Echo method to assess damage in flat-plate buildings is presented in Chapter 6.

5.7 CONCLUSIONS ON THE USE OF NON-DESTRUCTIVE TECHNIQUES FOR DAMAGE ASSESSMENT OF FLAT-PLATE BUILDINGS

The only available NDT technique recommended for damage assessment of flat-plate buildings is the Impact Echo method, through which information on crack depths and delaminated areas can be gathered and used to predict the drift level experienced by a slab-column connection.

As an alternative to the Impact Echo Method, the Seismic Wave Attenuation method (SWA) was developed. The SWA method is presented in Chapter 7.

CHAPTER 6

Damage Assessment using Impact Echo Method

6.1 INTRODUCTION

As explained in Section 5.6, the Impact Echo Method can be used to locate cracks and other defects in concrete. Damage assessment of slab-column connections using the Impact Echo Method was performed by monitoring the depth of a critical crack and detecting areas of delamination on the slab surface. A critical crack is defined as a crack that opens parallel to a column face, at a distance equal or less than 6 in. (the slab depth). From visual observations, it was found that critical cracks are part of the punching shear failure surface and tend to be wider and deeper than other cracks near the column.

6.2 IMPACT ECHO TECHNIQUE TO DETERMINE CRACK DEPTH

Sansalone M. J. and Streett W. B. (1997) developed the time-of-flight technique, a method to obtain a good approximation of the depth of a crack measured perpendicular to the surface, for cracks that are oriented perpendicular to the surface, inclined or curved.

For the case of a crack perpendicular to the surface, the time interval Δt between the beginning of the impact and the arrival of the diffracted P-wave at the transducer is the time required for a P-wave to travel the distance $AB + BC$ in Figure 6.1. This distance is equivalent to the wave speed C_p multiplied by Δt .

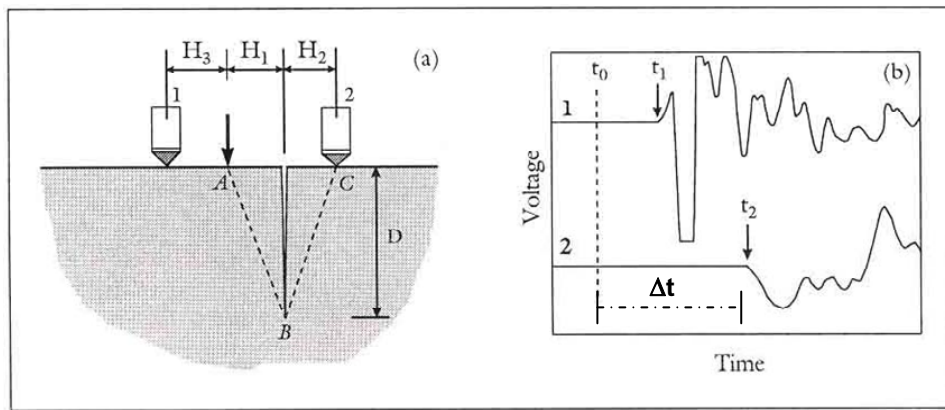


Figure 6.1 Scheme of the Time of Flight technique to determine crack depth
(Sansalone and Streett, 1997)

If H_1 , H_2 , Δt and C_p are known, the depth D of the crack can be calculated from the following three equations:

$$(AB)^2 = H_1^2 + D^2 \quad \text{Equation 6.1}$$

$$(BC)^2 = H_2^2 + D^2 \quad \text{Equation 6.2}$$

$$AB + BC = C_p \cdot \Delta t \quad \text{Equation 6.3}$$

For $H_1 = H_2 = H$, $AB = BC$ and solving for D , the following equation is found:

$$D = \sqrt{\frac{(C_p \cdot \Delta t)^2}{4} - H^2} \quad \text{Equation 6.4}$$

Because the precise time of the beginning of the impact t_0 is difficult to measure directly, Δt is measured through a second transducer placed on the same side of the crack as the impact and monitored by the same timing device as the other transducer, as shown in Figure 6.1, where t_0 is the impact time, t_1 is the time of arrival of the direct P-wave at transducer 1 and t_2 is the time of arrival of the diffracted P-wave at transducer 2.

The time difference $t_1 - t_0$ is the distance H_3 divided by the P-wave speed, as expressed in the following equation:

$$t_1 - t_0 = \frac{H_3}{C_p} \quad \text{Equation 6.5}$$

By choosing $H_3 = H$, the time interval $\Delta t = t_2 - t_0$ can be expressed as a function of the known variables t_1 , t_2 , H and C_p , as follows:

$$\Delta t = (t_2 - t_1) + \frac{H}{C_p} \quad \text{Equation 6.6}$$

Finally, the crack depth D can be expressed as a function of the known variables t_1 , t_2 , H and C_p , as follows:

$$D = \sqrt{\frac{C_p^2 \cdot \left[(t_2 - t_1) + \frac{H}{C_p} \right]^2}{4} - H^2} \quad \text{Equation 6.7}$$

6.3 IMPACT ECHO TECHNIQUE TO DETERMINE AREAS OF CONCRETE DELAMINATION

Sansalone M. J. and Streett W. B. (1997) developed a technique to locate areas of delamination in a concrete slab of thickness T . Figure 6.2a through Figure 6.2c show the response for a slab without delamination. As explained in Section 3.5, the period of the thickness mode response is t_T and the thickness mode frequency is $f_T = 1/t_T$. When a delamination occurs inside the slab, at a distance d from the surface, the P-waves are diffracted at the horizontal crack and then propagate back up through the slab producing a response equivalent to a plate of thickness d , resulting in a time-history response of higher frequency. Figure 6.2d through Figure 6.2f show the response of a slab with a concrete delamination.

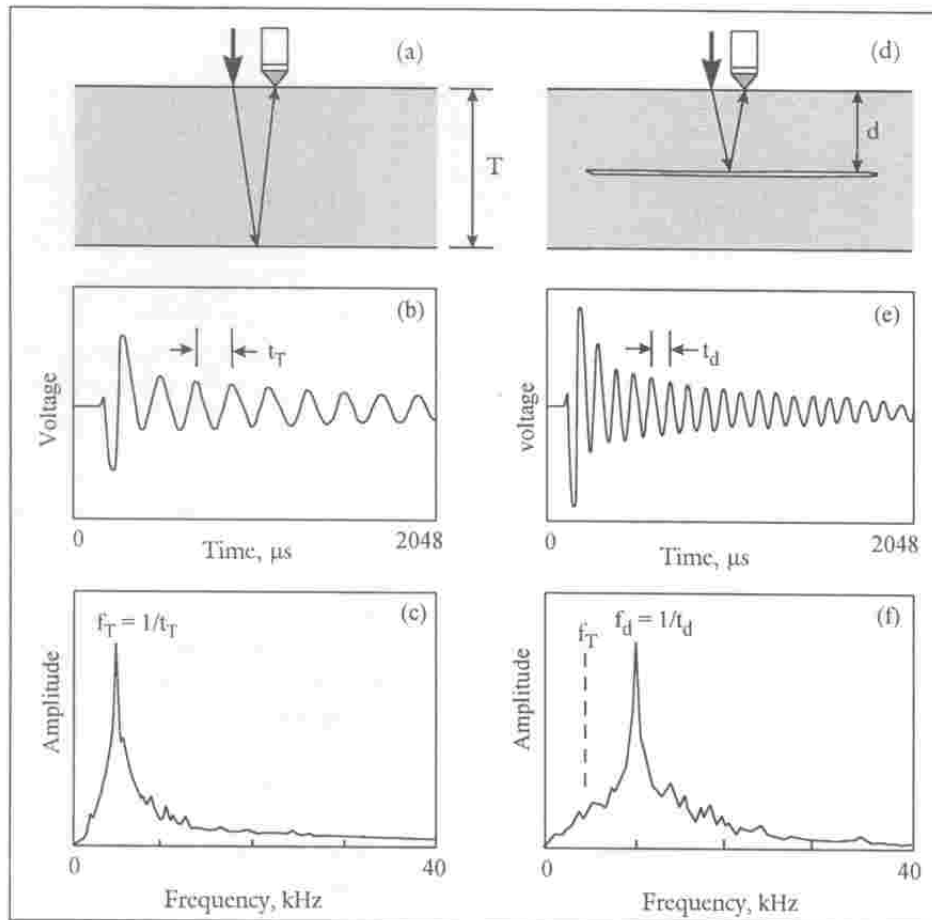


Figure 6.2 *Impact Echo response of a concrete slab with and without delamination (Sansalone and Streett, 1997).*

When the horizontal delamination is long enough (greater than $1.5d$) a shadow zone is created below the crack. In the shadow zone, reflected waves from the opposite surface of the slab are again diffracted around the flaw before they reach to the top surface and the thickness mode frequency f_T is not present in the Fourier Amplitude Spectrum (Figure 6.2f).

Delaminated areas can be easily detected by impacting the slab at several points around the flaws, with a steel ball that has a maximum frequency of usable energy f_{\max} greater than f_T and f_d . The maximum frequency of usable energy is the largest frequency from the excitation that can be detected by sensors after an impact. f_{\max} is a function of the steel ball diameter and potential energy, as explained in Section 7.4.

6.4 TEST CONDUCTED ON SPECIMEN L0.5

6.4.1 Load-deformation envelope for specimen L0.5

Tests were conducted on specimen L0.5 up to failure under lateral loading following the procedure described in Section 3.1

From strain gages installed in the specimen, it was found that the top and bottom reinforcement crossing the critical crack within the $(c+3h)$ region yielded at 0.75% and 1.35% lateral drift respectively. Failure of the specimen was observed at 2% drift; however the specimen was loaded up to 2.5% drift to obtain the residual lateral load carrying capacity of the connection.

The load-deformation envelope curve for specimen L0.5 is presented in Figure 6.3, where points A through F show relevant stages at which data were collected.

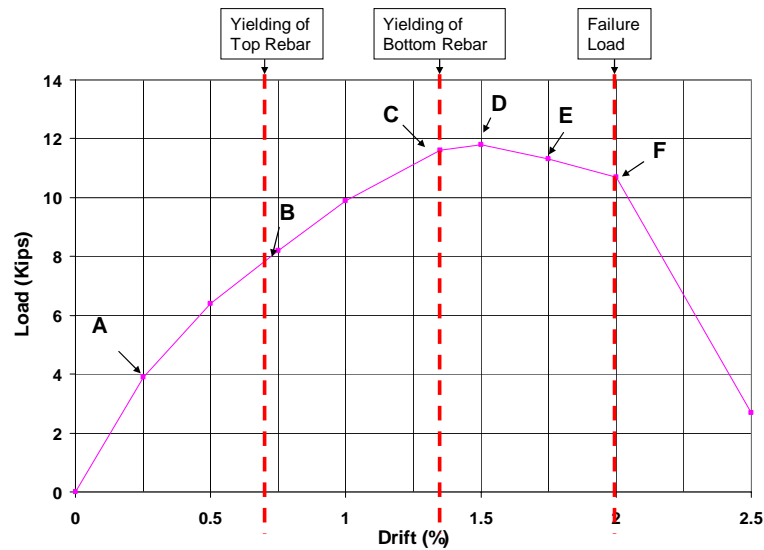


Figure 6.3 Load Deformation Envelope Curve for Specimen L0.5

6.4.2 Crack depth measurements in specimen L0.5

The crack depth was monitored at a critical crack located on the North side of the column, 3 in. from the column face.

6.4.2.1 Unconstrained P-wave velocity measurements

Prior to measure crack depths, the unconstrained P-wave velocity C_p must be determined. As explained in Section 5.6, C_p is a function of the thickness frequency f_T and slab thickness T , as follows:

$$C_p = 2 \cdot T \cdot f_T / 0.96$$

Equation 6.8

The thickness frequency was detected by installing a low sensitivity accelerometer on the slab and dropping a 19/32 in. diameter steel ball, 2 to 3 in. away from the sensor. The low sensitivity accelerometer was chosen to avoid saturation of the sensor due to the proximity of the impact and the 19/32 in. ball was selected because its maximum frequency $f_{\max} = 19.3$ kHz is consistent with the maximum usable frequency of the data acquisition system (20 kHz) and larger than the expected thickness frequency ($f_{\max} = 19.3$ kHz was determined using Equation 7-3). Several measurements were conducted and the time-history that shows the best resonance response was chosen from the various records. The best resonance response was the FFT record that showed the sharpest and best defined resonant peak. The Fourier Spectrum of the selected record was obtained and is shown in Figure 6.4, from which the thickness frequency was found to be $f_T = 11.75$ kHz.

The slab thickness H at the point of measurements was estimated to be 6 ¼ in. H was measured at nearby holes that were used to install the loading struts for the punching shear tests. The specimen was cast with a somewhat higher depth than its nominal thickness (6 in.). Using Equation 6.8, the unconstrained P-wave velocity was calculated as follows:

$$C_p = 2 \cdot 6.125 \cdot 11750 / 0.96 / 12 = 12,500 \text{ ft/sec}$$

The unconstrained P-wave velocity obtained by using the Impact Echo technique is very close to the value obtained in Appendix B ($V_c = 12,431 \text{ ft/sec}$) by conducting Resonance and Direct Arrival Tests on 6 in. x 12 in. concrete cylinders.

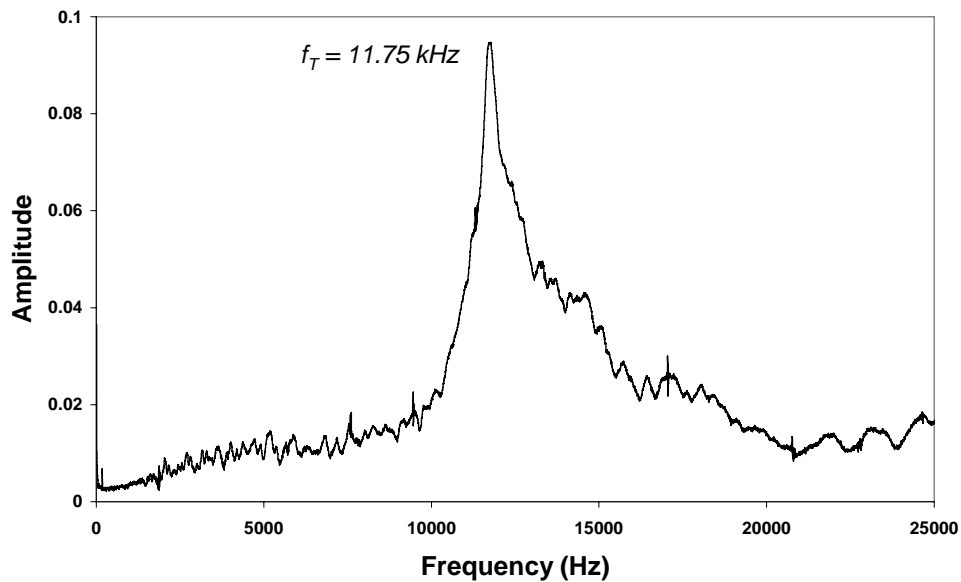


Figure 6.4 *Detection of the Thickness Frequency in Specimen L0.5*

6.4.2.2 *Procedure and results from crack depth measurements*

Following the procedure described in Section 6.2, two low sensitivity accelerometers (Channel 1 and Channel 2) were installed as shown in Figure 6.5. The distances from the impact location to the crack (H_1), from Channel 2 to the

crack (H_2) and from Channel 1 to the impact location (H_3) were set equal to 1.75 in. ($H_1 = H_2 = H_3 = H = 1.75in.$).

A steel pipe was used to drop the ball at the precise location of impact between sensors (Figure 6.6).

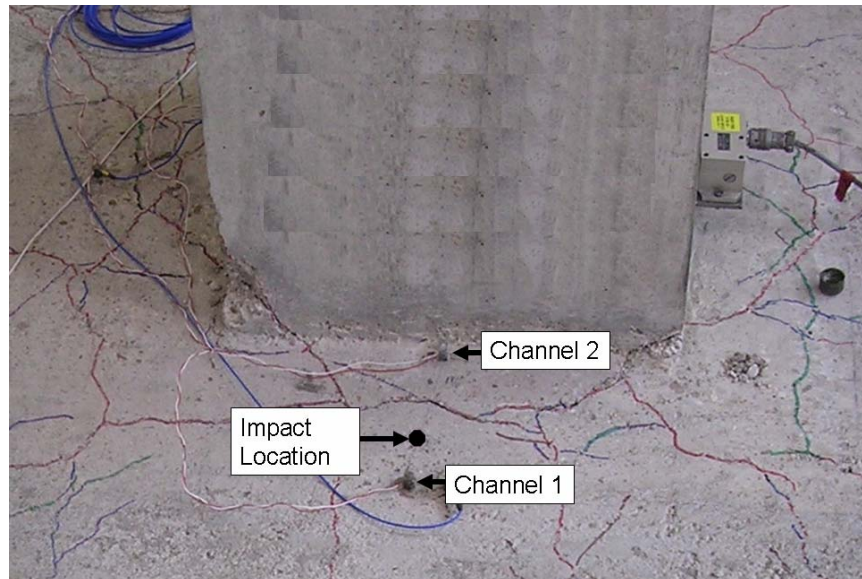


Figure 6.5 *Layout of accelerometers used to measure depth of critical crack in Specimen L0.5 (North Axis)*

Crack depth measurements were conducted at 0.25%, 0.5%, 0.75% and 1% drift, when the top of the slab at the position of the critical crack was in tension (crack fully opened). Results are presented in Table 6.1, where every crack depth reported is the result of a set of ten measurements. Crack depths were

not measured above 1% drift because it became evident from visual observations and strain gage readings that the critical crack opened through the full depth of the slab before 1.5% drift. The bottom reinforcement yielded at 1.35% drift allowing a bottom crack at the slab column interface to significantly increase in width. At 1.5% drift, water was poured in the critical crack and rapidly reached the bottom of the slab where the crack at the slab column interface was located.



Figure 6.6 *Crack depth measurements using a steel pipe to drop the ball at the precise position of impact*

In Table 6.1, results from crack depth measurements on a critical crack using the Impact Echo method are consistent with visual observations of non-critical crack depths performed on the slab edges and in 2-in. holes through the slab used to install vertical struts for the punching shear tests. Crack depths in 2-in. holes and at slab edges were obtained using a measuring tape and measurements were rounded to the nearest 1/2-in. significant digit. Locations where crack depths were measured visually and with the Impact Echo method are indicated in Figure 6.7.

Crack depths measured in drilled holes and slab edges were expected to be smaller than the critical crack depth measured near the column, because moments should be smaller near the edge of the specimen. However, because the edge is not restrained, cracks propagated to the slab edges and appeared to have similar crack depths along their entire length.

Table 6.1 *Crack Depth Measurements in Specimen L0.5*

Story Drift (%)	Crack Depth (in.) Impact Echo Method	Crack Depth (in.) Visual Observations
0.25	3.0	3.0
0.5	3.6	4.0
0.75	3.7	N/A
1	4.6	5.0

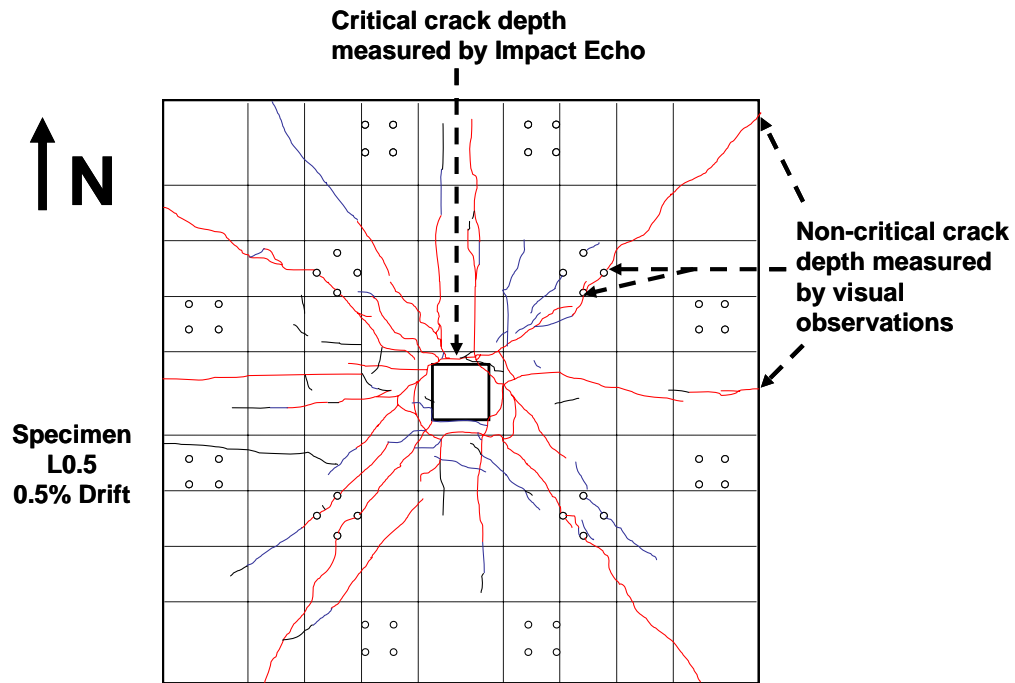


Figure 6.7 *Typical locations where crack depths were measured using the Impact Echo method and visual observations*

An example of the computation for D at 0.25% story drift is given below:

- i. The time-history records for a single measurement are presented in Figure 6.8(a) and Figure 6.8(b). Enlargements of the records containing information on P-wave arrival times are presented in Figure 6.8(c) and Figure 6.8(d), from where $t_1 = 1235\mu s$ and $t_2 = 1274\mu s$. The delay time ($t_2 - t_1$) between sensors was $39\mu s$.

- ii. The sampling interval was $13\mu s$ (77,000 samples per second), therefore several measurements are required to minimize inaccuracies due to a low sampling rate. After processing ten time-history records the average delay time was found to be $(t_2 - t_1) = 35\mu s$. Figure 6.8(c) and Figure 6.8 (d) show that the resolution of the time history records was not sufficient.
- iii. Using Equation 6.7, the crack depth D was calculated for $H = 1.75in.$, $C_p = 12,495 ft/sec$ and $(t_2 - t_1) = 35\mu s$ as follows:

$$D = \sqrt{\frac{(12,495 \cdot 12)^2 \cdot \left[(0.000035) + \frac{1.75}{(12,495 \cdot 12)} \right]^2}{4}} - (1.75)^2 = 3.0in.$$

6.4.3 Areas of concrete delamination in specimen L0.5

Areas of concrete delamination were detected on the north side of specimen L0.5 using the procedure described in Section 6.3. The detection of horizontal cracks was done using the Fourier Spectra of time history records measured at the position of Channel 1.

At 1.5% drift, Fourier Spectra showed two peaks at 11.8 kHz and 14.4 kHz. The first peak corresponded to the thickness frequency f_T and the second peak f_d to a horizontal crack located at a depth $d = 5in.$. A delamination was

found at the interface between the bottom reinforcement layer and concrete above the reinforcement. Dropping the steel ball at a variable distance from Channel 1, it was found that this delamination extended approximately 3 in. perpendicular to the critical crack (Figure 6.12).

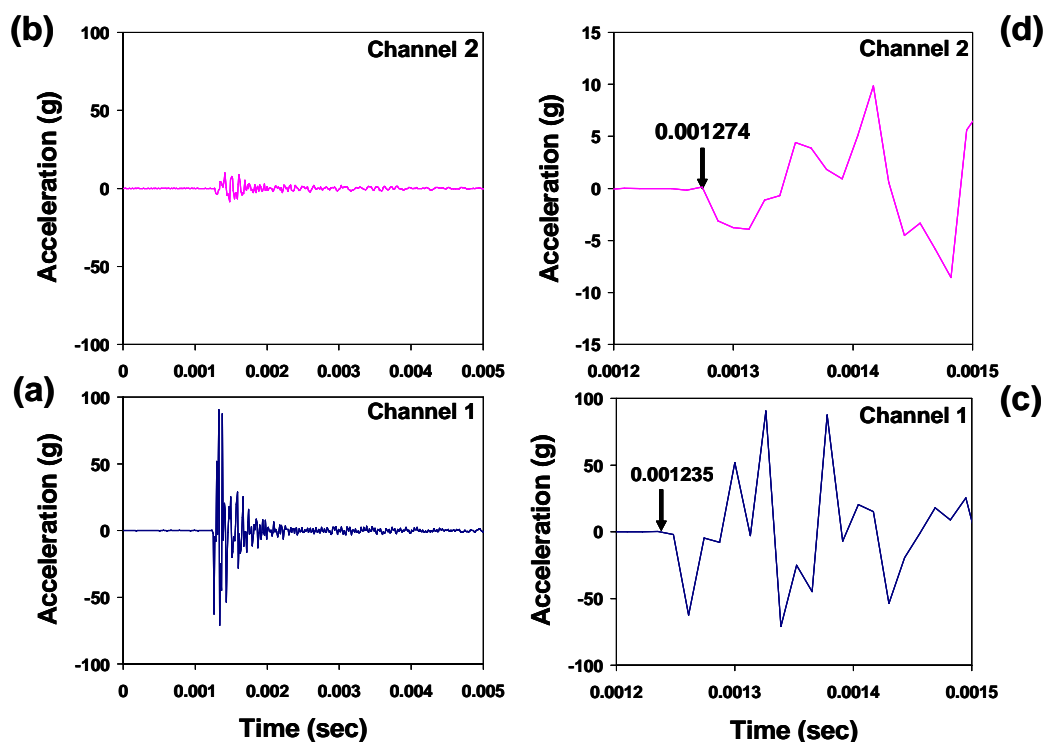


Figure 6.8 Example of the use of time-history records to measure crack depth in specimen L0.5

At 1.75% drift, Fourier Spectra showed high frequency peaks ranging from 35 to 45 kHz that correspond to a horizontal crack 1.5 to 2 in. deep. The

thickness frequency f_T was not present in the spectrums, denoting the existence of a horizontal crack over a large area. The delamination was found at the interface between the top reinforcement layer and concrete below the reinforcement. Dropping the steel ball at a variable distance from Channel 1, it was found that this delamination extended approximately 30 in. north from the critical crack (Figure 6.13).

Areas of concrete delamination were detected based on a frequency domain analysis conducted during testing of Specimen L0.5. Records were not saved and therefore can not be used to support results described in this Section.

6.4.4 Progression of damage and collapse mechanism for specimen L0.5

Combining visual observations with information provided in Sections 6.4.2 and 6.4.3, the progression of damage and collapse mechanism of specimen L0.5 is presented in this Section.

When the gravity load was applied, flexural cracks appeared parallel to the column faces (Figure 4.11) about 3 in. from the column. These cracks were considered critical because cracks at that location were found to be wide and deep and formed the failure surface when the shear capacity was reached. The critical nature of this crack was recognized as soon as it formed. ACI 318 05 defines the critical punching shear perimeter at a distance $d/2$ from the column (2.5 in. for the slab in specimen L0.5).

When lateral loads were applied to produce a 0.25% drift, few new cracks were formed. At that drift level, the critical crack width and depth were measured. Crack depth was measured using the Impact Echo method and visual observations in drilled holes and slab edges. A cross section is shown in Figure 6.9. The critical crack grew in depth and width when the story drift was increased from 0.25% to 1% (Table 6.1). At 0.75% drift the top reinforcement yielded in tension and when the load was reversed to input tension to the bottom fibers, a tiny crack (< 0.01 in. wide) opened on the bottom of the slab at the slab column interface (Figure 6.10). The critical crack grew to the full depth of the slab somewhere between 1% and 1.35% drift. At this latest drift the bottom reinforcement was found to yield in tension (Figure 6.11). When the story drift was 1.5% and 1.75% concrete delamination was found at the interface between the bottom reinforcement layer and concrete below and the top reinforcement layer and concrete above (Figure 6.12 and Figure 6.13).

Finally, the specimen failed in shear at 2% drift and the regions of top and bottom delamination spalled (Figure 6.14). The failure mechanism described was observed on the North and South sides of the column where flexural action predominated because the loading was in this direction (North-South). On the East and West sides, the failure surface formed closer to the column and the cracking indicated torsional actions in the slab on those faces of the column. The failed specimen is shown in Figure 6.15.

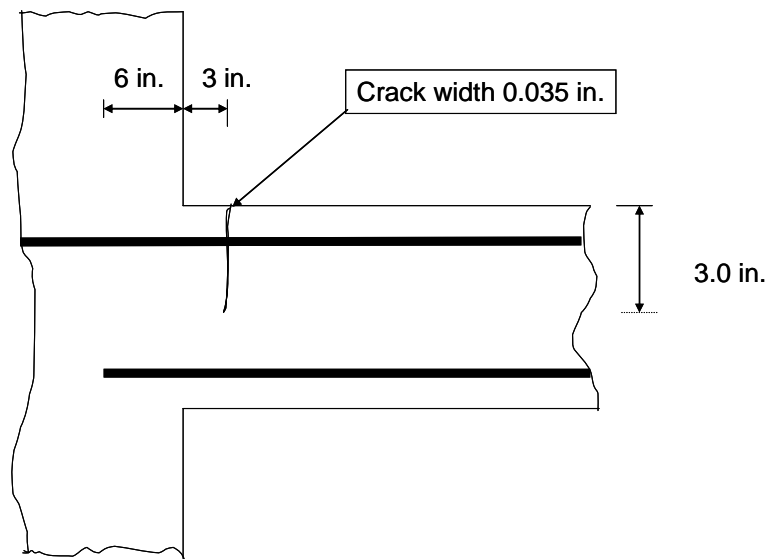


Figure 6.9 Specimen L0.5 at 0.25% Lateral Drift (North Axis)

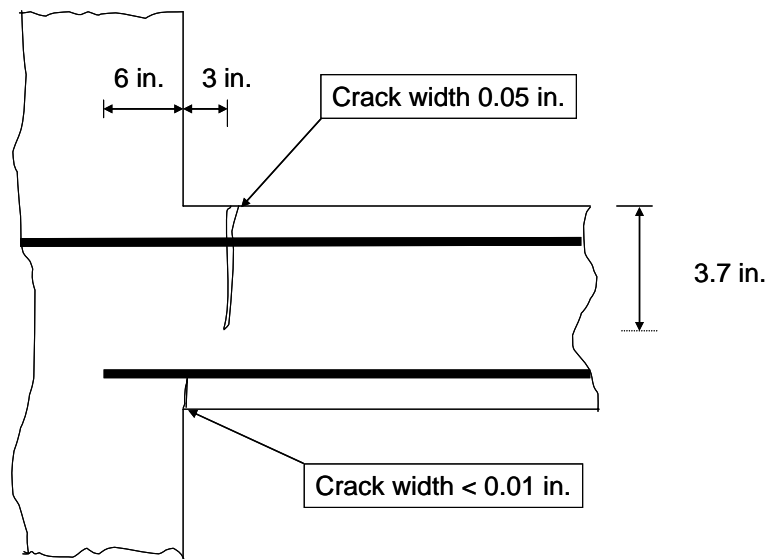


Figure 6.10 Specimen L0.5 at 0.75% Lateral Drift (North Axis)

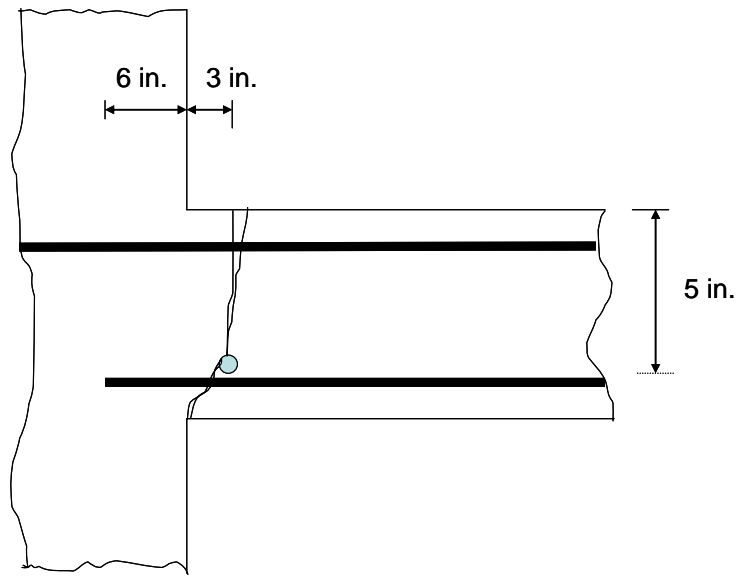


Figure 6.11 Specimen L0.5 at 1.35% Lateral Drift (North Axis)

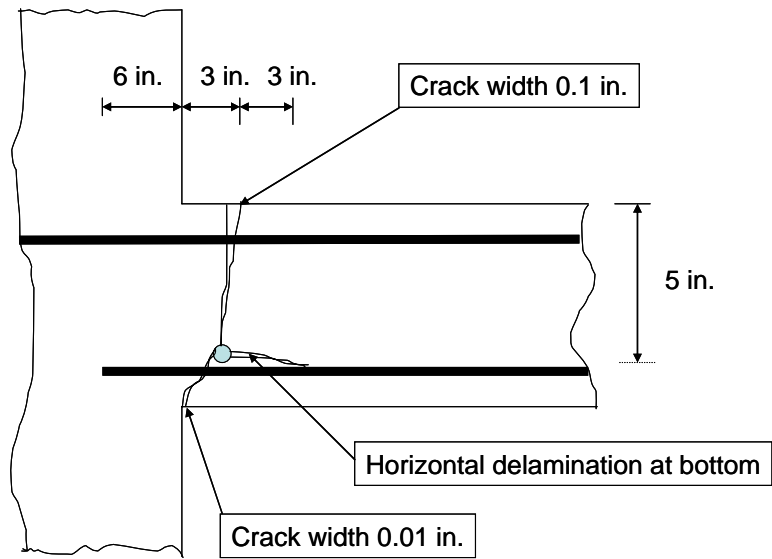


Figure 6.12 Specimen L0.5 at 1.5% Lateral Drift (North Axis)

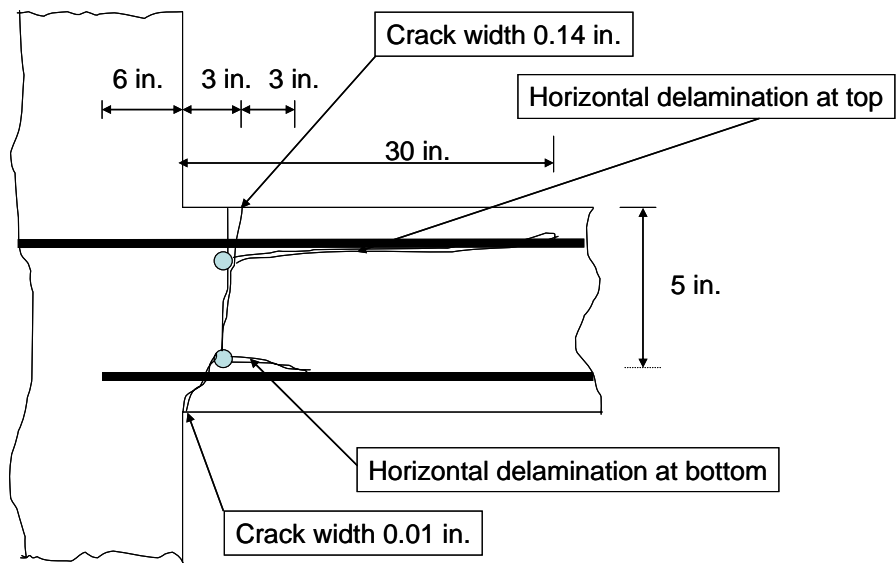


Figure 6.13 Specimen L0.5 at 1.75% Lateral Drift (North Axis)

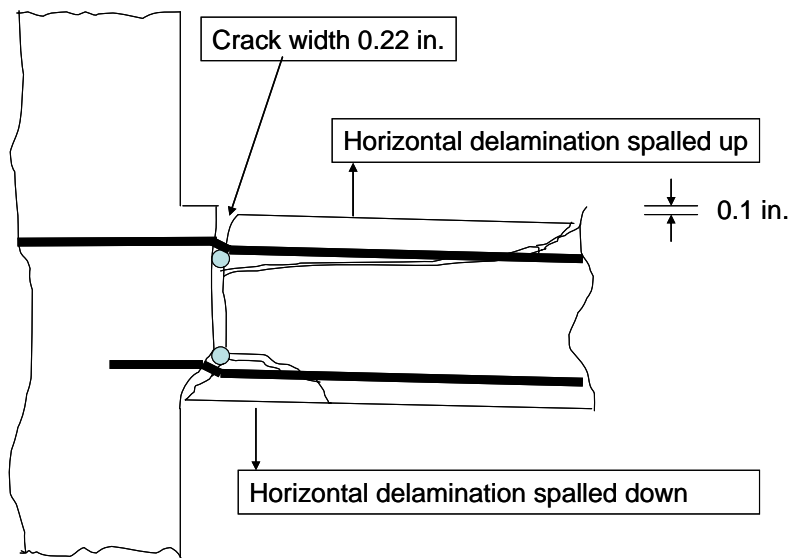


Figure 6.14 Specimen L0.5 at 2% Lateral Drift (North Axis)

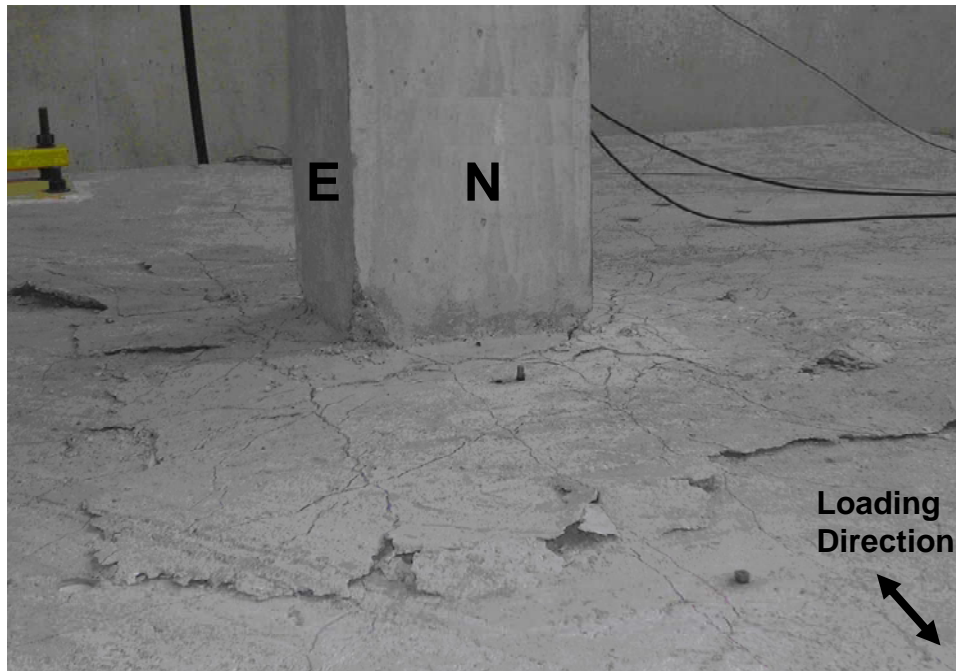


Figure 6.15 Failure of Specimen L0.5

6.5 CRACK DEPTH MEASUREMENTS IN SPECIMEN LR_{ST}G0.5

The crack depth was monitored at a critical crack located on the South side, 2 in. from the column face.

6.5.1 Unconstrained P-wave Velocity

The Unconstrained P-wave Velocity was determined following the procedure described in Section 6.4.2.1. The fourier spectrum of a time-history

record showing a resonant response was obtained and is presented in Figure 6.16, where the thickness frequency was found to be $f_T = 12.77$ kHz.

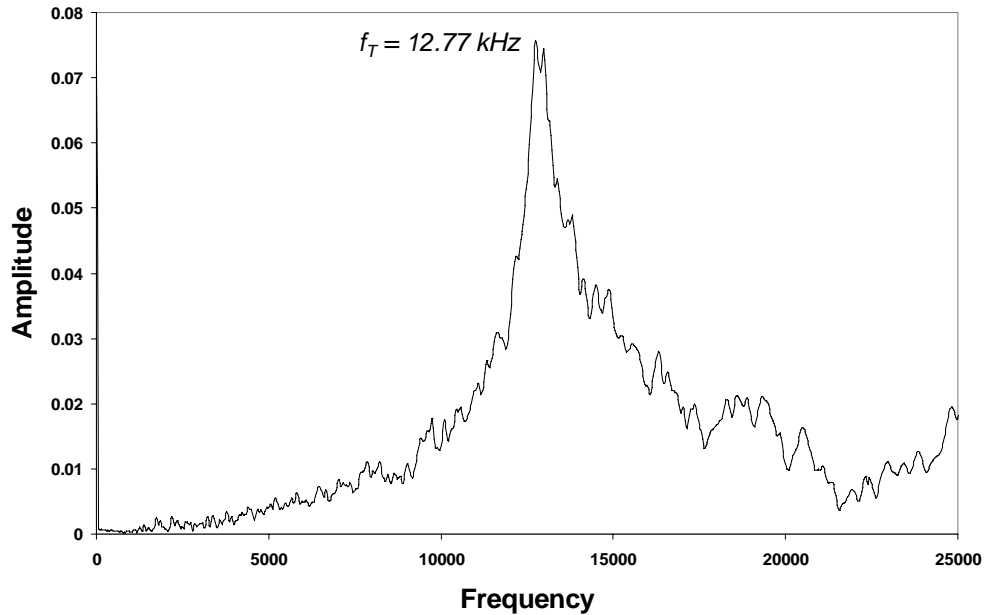


Figure 6.16 *Detection of Thickness Frequency in Specimen LR₅₇G0.5*

The slab thickness H at the point of measurements was estimated to be 6 in. H was measured at 2-in. holes that were built to install struts for punching shear tests. Using Equation 6.8, the Unconstrained P-wave velocity was found as follows:

$$C_p = 2 \cdot 6 \cdot 12766 / 0.96 / 12 = 13,300 \text{ ft/sec}$$

The value of C_p obtained using the Impact Echo technique is close to the value obtained in Appendix B ($V_c = 12,955 \text{ ft/sec}$) by conducting Resonance and Direct Arrival Tests on 6 in. x 12 in. concrete cylinders.

6.5.2 Procedure and Results from Crack Depth measurements

Following the procedure described in Section 6.2, two low sensitivity accelerometers (Channel 1 and Channel 2) were installed as shown in Figure 6.17. The distances from the impact location to the crack (H_1), from Channel 2 to the crack (H_2) and from Channel 1 to the impact location (H_3) were set equal to 1.25 in. ($H_1 = H_2 = H_3 = H = 1.25 \text{ in.}$). Crack depth measurements were conducted at 0.25%, 0.5%, 0.75%, 1% and 1.25% drift, when the slab was at rest with no gravity and lateral loads applied. Results are presented in Table 6.2, where every crack depth reported is the result of a set of ten measurements. Crack depths were not measured after 1.25% drift because the specimen was not laterally loaded beyond that drift level.

Table 6.2 shows that measurements of critical crack depths using the Impact Echo method are not consistent with visual observations of non-critical-cracks depths performed on the slab edges and in holes used to install vertical struts for punching shear tests.

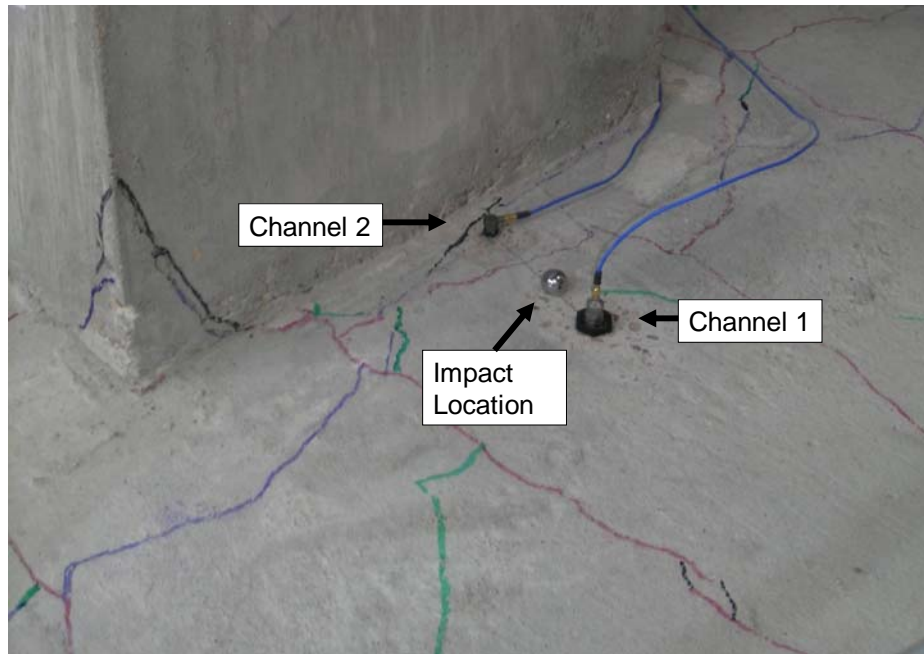


Figure 6.17 Layout of accelerometers used to measure depth of critical crack in Specimen LR_{ST}G0.5 (South Axis)

Table 6.2 Crack Depth Measurements in Specimen LR_{ST}G0.5

Story Drift (%)	Crack Depth (in.) Impact Echo Method	Crack Depth (in.) Visual Observations
0.25	2.7	4.0
0.5	3.2	N/A
0.75	3.7	4.5
1	3.4	N/A
1.25	3.1	5.0

Crack depths reported for specimen LR_{ST}G0.5 using Impact-Echo Method (Table 6.2) have an inconsistent trend and are underestimated with respect to crack depths obtained from visual observations. Crack depths reported for specimen L0.5 (Table 6.1) had a consistent trend; an increase in crack depths with an increase in drift.

6.6 CRACK DEPTH MEASUREMENTS IN SPECIMEN LG1.0

The crack depth was monitored at a critical crack located on the North side, 4 in. from the column face.

6.6.1 Unconstrained P-wave Velocity

The Unconstrained P-wave Velocity was detected following the procedure described in Section 6.4.2.1. The Fourier Spectrum of a time-history record showing a resonant response was obtained and presented in Figure 6.18, where the thickness frequency was found to be $f_T = 12.48$ kHz. The slab thickness H at the point of measurements was estimated to be 6 in. Using Equation 6.8, the unconstrained P-wave velocity was found as follows:

$$C_p = 2 \cdot 6 \cdot 12485 / 0.96 / 12 = 13,000 \text{ ft/sec}$$

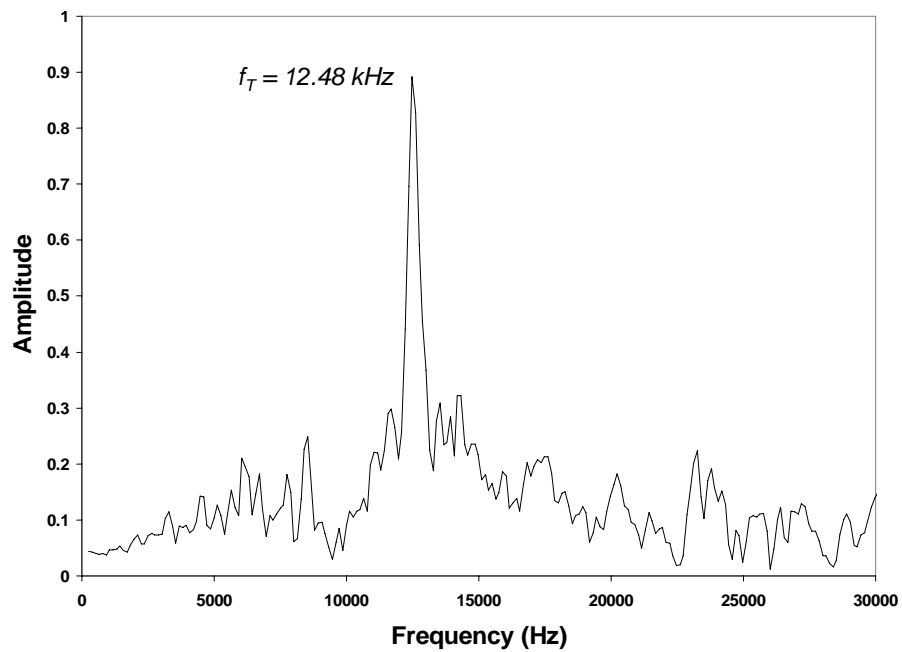


Figure 6.18 *Detection of Thickness Frequency in Specimen LG1.0*

6.6.2 Procedure and Results from Crack Depth measurements

Following the procedure described in Section 6.2, two low sensitivity accelerometers (Channel 1 and Channel 2) were installed as shown in Figure 6.19.

The distances from the impact location to the crack (H_1), from Channel 2 to the crack (H_2) and from Channel 1 to the impact location (H_3) were arbitrary set equal to 1.75 in. ($H_1 = H_2 = H_3 = H = 1.75in.$). Crack depth measurements were conducted at 0.25%, 0.5%, 0.75%, 1% and 1.25% drift, when the slab was at rest with no lateral and gravity loads applied. Results are presented in Table 6.3,

where every crack depth reported is the result of a set of ten measurements. Crack depths were not measured after 1.25% drift because the specimen was not laterally loaded beyond that drift level.

Table 6.3 shows no consistency between measurements of a critical crack depth using the Impact Echo method and visual observations of non-critical crack depths performed on the slab edges and in holes used to install vertical struts for punching shear tests. Crack depths reported for specimen LG1.0 using the Impact-Echo Method are considered underestimated, however they show the correct trend, that is an increase in crack depths with an increase in drifts.

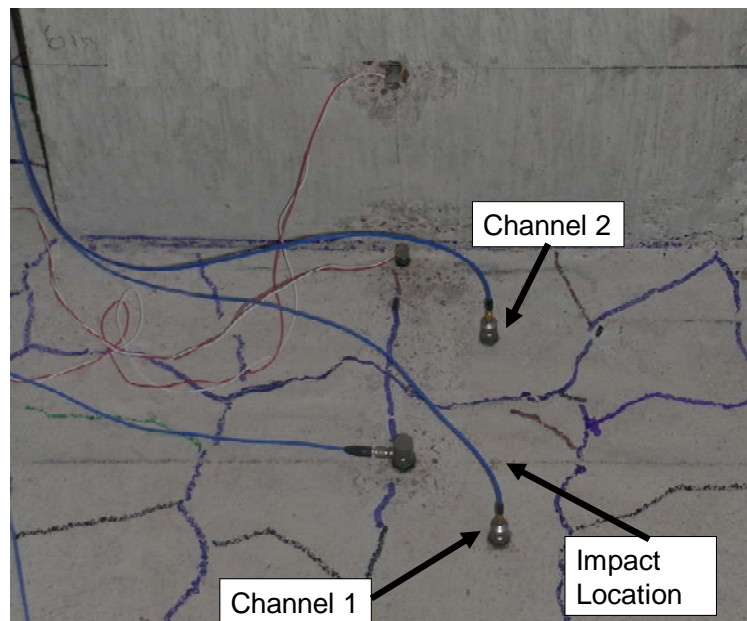


Figure 6.19 *Layout of accelerometers used to measure depth of critical crack in Specimen LG1.0 (North Axis)*

Table 6.3 *Crack Depth Measurements in Specimen LG1.0*

Story Drift (%)	Crack Depth (in.) Impact Echo Method	Crack Depth (in.) Visual Observations
0.25	2.3	3.5
0.5	2.6	N/A
0.75	2.6	4.5
1	2.6	N/A
1.25	2.9	5.0

6.7 EVALUATION OF CRACK DEPTH DATA FOR ALL TESTS

Table 6.4 summarizes results from critical crack depth measurements using the Impact Echo method and visual observations of non-critical crack depths conducted on the side of the slab or in holes drilled for punching shear tests. Visual observations of crack depths reported in Table 6.4 are average values of measurements conducted on specimens L0.5, LR_{ST}G0.5 and LG1.0. Crack depths are presented as a fraction of the slab depth h .

Table 6.4 Summary of Crack Depth Measurements

Story Drift (%)	Crack Depth (Impact Echo Method)			Crack Depth (Visual Observations)
	L0.5	LR _{ST} G0.5	LG1.0	
0.25	0.5h	0.5h	0.4h	0.5h
0.5	0.6h	0.5h	0.4h	0.6h
0.75	0.6h	0.6h	0.4h	0.7h
1	0.8h	0.6h	0.4h	0.8h
1.25	N/A	0.5h	0.5h	0.8h

From Table 6.4, the following observations and conclusions were obtained:

- i. Data obtained using the Impact Echo method when the top of the slab was in tension (specimen L0.5) showed good correlation with visual observations, but data obtained when the slab was at rest (specimens LR_{ST}G0.5 and LG1.0) did not. Measurements conducted when the slab was at rest led to underestimates of crack depths. This discrepancy can be explained by noting that the control crack was fully opened when the slab was in tension and partially opened when the slab was at rest. In a structure damaged by an earthquake, measurement will have to be conducted when the structure is at rest and cracks are partially open. Under such condition, it is likely that Impact Echo measurements will underestimate the value of crack depths.

- ii. Crack depth measurement for specimen L0.5 at 0.75% drift, specimen LR_{ST}G0.5 at 1% and 1.25% drifts and specimen LG 1.0 at 0.75% and 1% drifts seem to be inconsistent with other readings that show the expected trend of an increase in crack depths with an increase in drifts. That could be caused by inaccurate measurement of P-wave arrival times using a data acquisition system with low sampling rate. Improvements to the data acquisition system are explained in Appendix C.
- iii. Data from specimen L0.5 for critical crack depth measurements using Impact Echo method and visual observations of non-critical crack depths for all specimens are consistent and it can be concluded that the critical crack depth is $0.6h$ and $0.8h$ at 0.5% and 1.0% drift, respectively. Impact Echo data from specimens LR_{ST}G0.5 and LG1.0 were not considered in reaching this conclusion because they were not consistent with visual observations for the specimen at rest.
- iv. Using information presented for specimen L0.5 in Sections 6.4.2.2 and 6.4.4 it can be concluded that the critical crack fully opened somewhere in between 1.0% and 1.5% drift.

6.8 USE OF CRACK DEPTH AND DELAMINATION TO PREDICT DRIFT LEVELS

Crack depth measurements and detection of areas of concrete delamination show some promise for predicting story drift levels if the following criteria based on data for specimen L0.5 (Sections 6.4.3 and 6.4.4) and the analysis contained in Section 6.7 are used:

- i. If the critical crack depth was less than 60% of the slab depth, then the story drift experienced by the structure was between 0% and 0.5%.
- ii. If the critical crack depth was between 60% and 80% of the slab depth, then the story drift experienced by the structure was between 0.5% and 1%.
- iii. If the critical crack depth was between 80% and 100% of the slab depth and horizontal cracks or delamination were present between the bottom reinforcement layer and concrete below it, then the story drift experienced by the structure was between 1 and 1.5%.
- iv. If the critical crack depth was equal to the full depth of the slab, horizontal cracks or delaminations were present between the bottom reinforcement layer and concrete below it and between the top reinforcement layer and concrete above it, then the story drift experienced by the structure was likely to have been greater than 1.5%.

Crack depth was not found to be a function of the reinforcement ratio but rather a function of the drift. For the same drift, a section that has more reinforcement also will develop higher moment but the crack depth will be nearly the same as that in a section with less reinforcement and moment because the same deformation are applied to both slab sections.

Due to inconsistencies and inaccuracies in data obtained from crack depth measurements using the Impact Echo method, depth of critical cracks can be detected by extracting concrete cores from the slab. However, this approach may not be feasible in the field because owners may not want to “weaken” the slab at critical sections. Coring may be expensive and determining where to core may be difficult if cracks are not well-defined or inclined relative to the slab surface.

Areas of delamination could be detected by the use of the Impact Echo method or more easily and at less cost by other methods such as chain dragging or hammering.

CHAPTER 7

Seismic Wave Attenuation Method

7.1 INTRODUCTION

The Seismic Wave Attenuation method (SWA) is based on the decrease in amplitude experienced by seismic waves as they travel through a medium. There are many mechanisms that can cause a decrease of amplitude or attenuation. The following mechanisms are the most common and significant sources of attenuation:

i. Attenuation from Dispersion

Seismic waves consist of many frequency components that travel at different speeds and change in form as they propagate through a medium. As waves disperse from the source, they change to longer duration waveforms with lower amplitudes, to conserve energy.

ii. Attenuation from Geometry

Seismic waves lose amplitude as they spread over a larger wavefront. The wavefront is a spherical surface where waves propagate outwards in all directions from the source. To maintain a constant energy, the amplitude of the waves must decrease with increasing distance from the source.

iii. Attenuation from Scattering and Diffraction

Scattering occurs when the waves arrive at geometric boundaries or material interfaces and are reflected. For example, in concrete elements, the coarse aggregate acts as a discontinuity for high frequency waves above 80 kHz, which are scattered and highly attenuated by this phenomenon. Diffraction occurs when a wave arrives at a crack or any sharp edge, and is reflected from such a discontinuity.

7.2 OUTLINE OF THE SWA METHOD

The SWA method measures the attenuation or decrease in amplitude experienced by seismic waves traveling through a medium by using accelerometers installed at various distances from the source of energy. Accelerometers provide signals with low noise and high amplitudes (good signal to noise ratios). The excellent performance of accelerometers becomes more evident when ultrasonic waves (> 20 kHz) and a low magnitude source of energy are used in a highly attenuating material such as concrete. The attenuation of ultrasonic waves is high in concrete due to scattering at the paste-aggregate interfaces.

Figure 7.1 shows the time histories of two accelerometers installed on a concrete slab at 6 in. and 12 in. from a source of energy. The source that produced seismic waves was the impact of a 1.5-in. diameter steel ball. The attenuation of acceleration amplitudes is predominantly due to geometry and dispersion.

Attenuation due to scattering and diffraction is not present, because the steel ball is too large to exert ultrasonic waves (>20 kHz) and the slab is uncracked.

The SWA method characterizes the attenuation between two points through the Peak Acceleration Ratio (PAR) computed from the time history records of such points. From Figure 7.1, $PAR = \left| \frac{-11.4g}{4.8g} \right| = 2.4$. When attenuation due to diffraction is present, the PAR value is expected to increase showing the fact that a cracked material can attenuate more than an uncracked one. Therefore, the SWA method could be used to assess the degree of damage by measuring PAR values on cracked concrete elements. PAR values are also referred to as “attenuation ratios”.

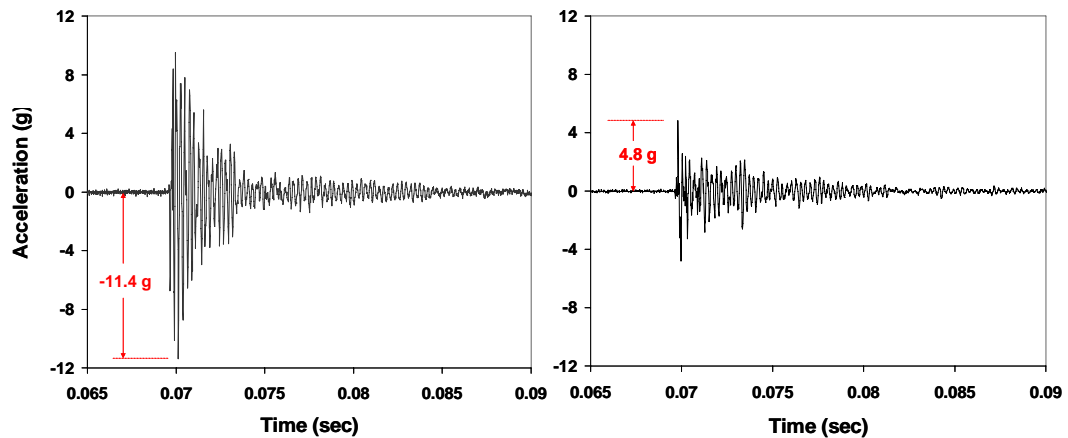


Figure 7.1 Attenuation of acceleration amplitudes in concrete

7.3 DATA ACQUISITION SYSTEM

In order to acquire data for the level of damage in the slab-column connections, a data acquisition system was configured as described below. The data acquisition system had three components (Figure 7.2): a computer with a data acquisition card, a signal conditioning module and accelerometers.

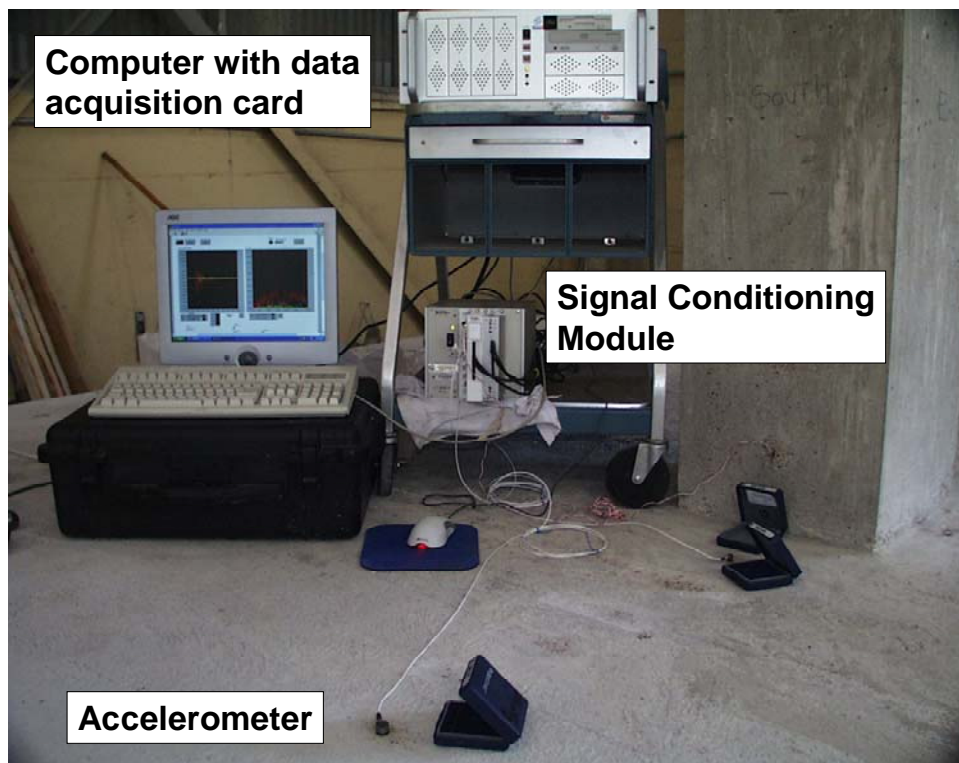


Figure 7.2 Data Acquisition System

7.3.1 Computer and Data Acquisition Card

The computer in the data acquisition system was an Intel Pentium IV with 3 GHz of speed and 2 Giga bytes in Ram. It was equipped with a National Instruments Data Acquisition Card PCI-6052E. The PCI-6052E (Figure 7.3) was a 16-Bit card that can acquire data up to 333.000 samples per second on 16 singled-ended analog inputs.



Figure 7.3 Data Acquisition Card NI PCI-6052E

7.3.2 Signal Conditioning Module

The signal conditioning module in the data acquisition system was a National Instruments SCXI-1531 card designed to power Integrated Electronic Piezoelectric (IEPE) compatible accelerometers. The module had eight input

channels each of which includes a programmable AC instrumentation amplifier, a 4-pole Bessel lowpass filter (2.5, 5, 10, and 20 kHz), and an excitation current source. The NI SCXI-1531 offers simultaneous sampling to preserve interchannel phase relationships. This module also offers programmable gain per channel (1, 10, 100).

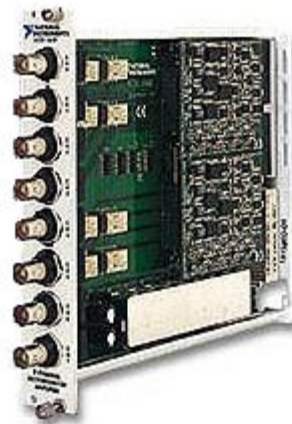


Figure 7.4 *Signal Conditioning Module, NI SCXI-1531*

The NI SCXI-1531 simultaneous-sampling algorithm limits the data acquisition speed to 77,000 samples per second when two channels are used, 62,500 samples per second for three channels and 52,500 samples per second for four channels.

The largest 4-pole Bessel lowpass filter (20 kHz) is recommended for recording the highest frequency waves possible. Using the largest lowpass filter, the usable range of frequencies was from 0 to 20 kHz (subsonic waves).

7.3.3 Accelerometers

Accelerometers used in the Data Acquisition System were fabricated by PCB Piezotronics, Inc. The accelerometers are Ceramic Shear ICP[®] Accelerometers structured with highly sensitive piezoceramic sensing elements; they have an excellent signal-to-noise ratio, high measurement resolution, and are ideal for conducting low-level vibration measurements. Due to their inherent higher sensitivity, a ceramic ICP[®] accelerometer is assembled with a smaller mass than comparable quartz units, resulting in a sensor with lighter weight, higher frequency response, and lower noise. The sensors use shear-mode designs that minimize extraneous signals caused by base bending and other strain effects, such as thermal transient compression, and expansion forces.

Five accelerometer models were used in the data acquisition system:

1. Very High Sensitivity Accelerometer Model 355B04 (Figure 7.5)
Sensitivity ($\pm 10\%$) 1000 mV/g
Frequency Range (± 3 dB) 0.3 to 17,000 Hz
Resonant Frequency ≥ 30 kHz

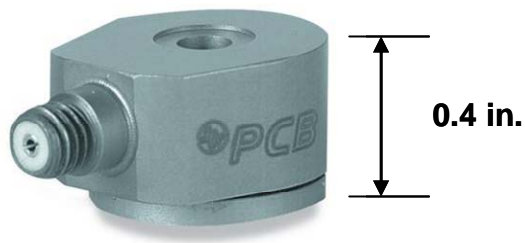


Figure 7.5 Very High Sensitivity Accelerometer Model 355B04

2. High Sensitivity Accelerometer Model 352C65 (Figure 7.6)
Sensitivity ($\pm 10\%$) 100 mV/g
Frequency Range (± 3 dB) 0.2 to 20,000 Hz
Resonant Frequency ≥ 35 kHz

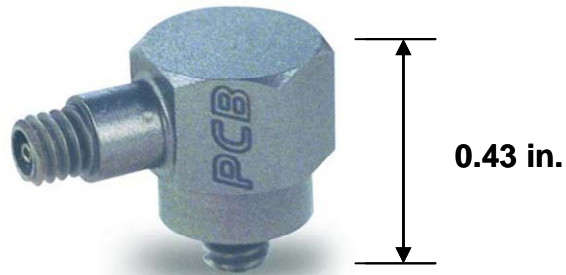


Figure 7.6 *High Sensitivity Accelerometer Model 352C65*

3. High Sensitivity Accelerometer Model 352C33 (Figure 7.7)
Sensitivity ($\pm 10\%$) 100 mV/g
Frequency Range (± 3 dB) 0.3 to 15,000 Hz
Resonant Frequency ≥ 50 kHz

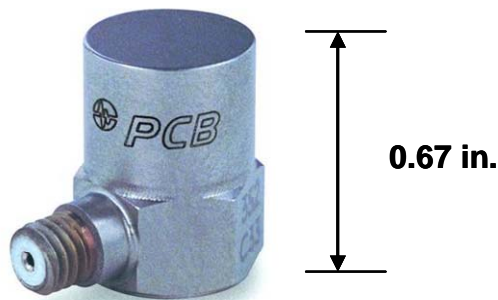


Figure 7.7 *High Sensitivity Accelerometer Model 352C33*

4. Low Sensitivity Accelerometer Model 352C17 (Figure 7.8)
Sensitivity ($\pm 10\%$) 10 mV/g
Frequency Range (± 3 dB) 0.35 to 25,000 Hz
Resonant Frequency ≥ 50 kHz

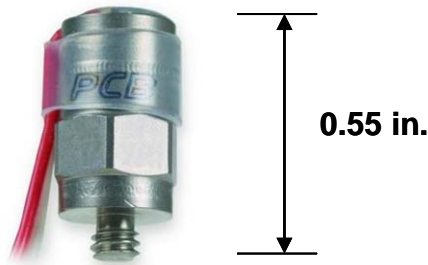


Figure 7.8 *Low Sensitivity Accelerometer Model 352C17*

5. Low Sensitivity Accelerometer Model 352A60 (Figure 7.9)
Sensitivity ($\pm 15\%$) 10 mV/g
Frequency Range (± 3 dB) 5 to 60,000 Hz
Resonant Frequency ≥ 95 kHz

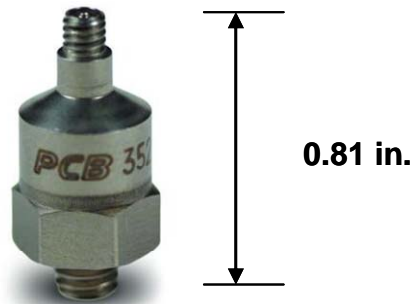


Figure 7.9 *Low Sensitivity Accelerometer Model 352A60*

Most accelerometers produced by PCB have frequency range within 0 to 25 kHz and are a good fit for a signal conditioning unit with a usable range of frequencies between 0 to 20 kHz.

Low sensitivity accelerometers were used near the impact source (6 in. or less), where acceleration values typically ranged from 25g to 150g. A very high sensitivity accelerometer was used far from the impact source (36 in.), where acceleration values typically ranged from 0.5g to 1.5 g. By using accelerometers with variable sensitivity, depending on the impact source distance, sensor saturation was avoided and the signal-to-noise ratio was optimized.

7.4 SEISMIC WAVE SOURCE

Seismic waves can be generated by several mechanisms, such as the collision of solid objects or piezoelectric transducers. The simplest and most economical way to generate seismic waves is by mechanical impact, tapping a steel sphere against the surface of the element being tested. Steel balls are preferred over other objects, because the relationships between the diameter of the sphere D , the duration or contact time of the impact t_c , and the maximum frequency of useful energy f_{max} , are known.

The relationship between D and t_c is explained by the Hertz theory of elastic impact (Goldsmith, 1965). The contact time is a function of the sphere diameter “ D ” and the impact height “ h ”, as follows:

$$t_c = \frac{0.0043 \cdot D}{h^{0.1}} \quad \text{Equation 7-1}$$

Where t_c is in seconds and D and h are in meters. In practice, steel balls are dropped from a distance of approximately 1 m., thus Equation 7-1 is simplified as follows:

$$t_c = 0.0043 \cdot D \quad \text{Equation 7-2}$$

Another important characteristic of seismic waves generated by mechanical impact is the force-time function, which is the variation of the impact force N with time t . This function is represented by a half sine curve, where the maximum force is proportional to the kinetic energy of the sphere at impact and the function ends at $N = 0$ and $t = t_c$. Figure 7.10 shows the force – time function for a 9/16-in. diameter ball. The force-time function is not a function of the properties of the impacted material; it depends on the kinetic energy and diameter of the sphere.

Seismic waves are composed of a wide distribution of frequencies, and this distribution is determined by the force-time function of the impact. The distribution of amplitudes and frequencies in seismic waves produced by the impact of a steel ball on a solid material is shown in Figure 7.11. This distribution is obtained by calculating the Fourier transform of the force-time function of the impact. Because frequency is the inverse of time, the horizontal scale can be expressed in increments of $1/t_c$. The function is zero at $1.5/t_c$, $2.5/t_c$, $3.5/t_c$, etc., which means that the seismic waves have no component with those frequencies. The relative amplitude is very small beyond the first zero. Experience has shown

that the amplitudes of seismic waves can be clearly detected at frequencies below $1.25/t_c$ (Sansalone and Streett, 1997).

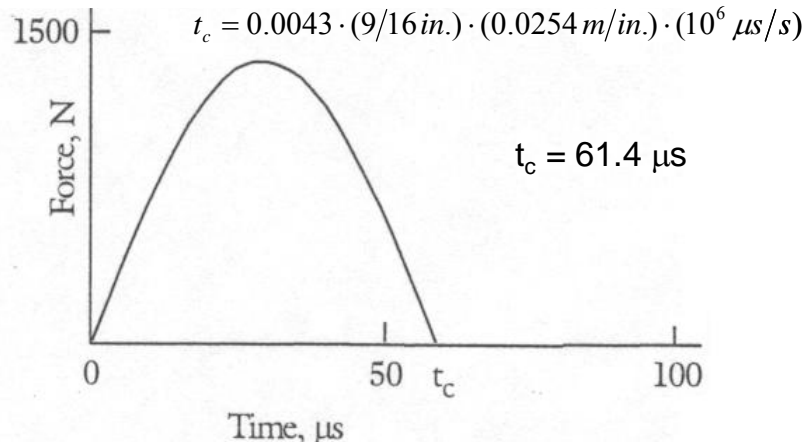


Figure 7.10 Force-time function for the impact of a 9/16 in. ball (Sansalone and Streett, 1997)

Defining $f_{max} = 1.25/t_c$ as the maximum frequency of useful energy, and combining this with Equation 7-2, the result is an approximate relationship between f_{max} and D .

$$f_{max} = \frac{291}{D} \qquad \text{Equation 7-3}$$

Where f_{max} is in Hz and D is in meters.

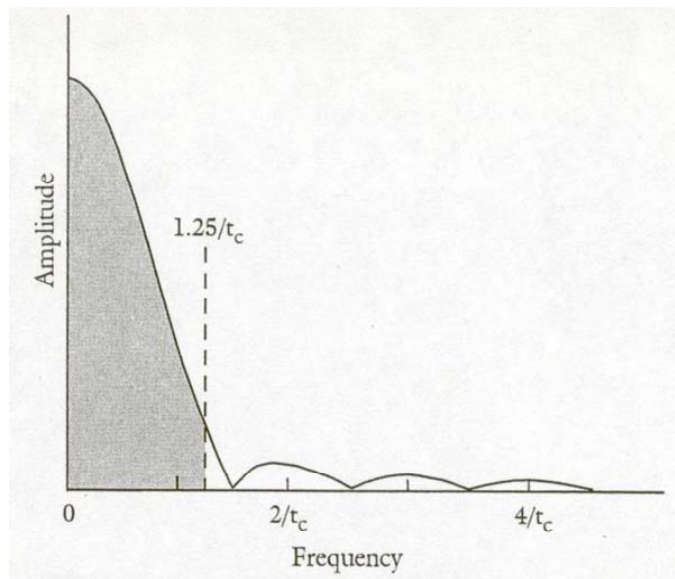


Figure 7.11 Distribution of frequencies corresponding to the force-time function of a steel ball impacting a solid material (Sansalone and Streett, 1997)

For a 9/16-in. diameter steel ball, the maximum frequency of useful energy f_{max} is 20.4 kHz. Such ball is considered a good fit for a data acquisition system with a usable range of frequencies between 0 to 20 kHz.

7.5 USE OF SWA TECHNIQUE ON SLAB-COLUMN CONNECTIONS

The SWA technique was used in four slab-column connections tested in laboratory (specimens L0.5, LG0.5, LRSTG0.5 and LG1.0) to develop a correlation between SWA non-destructive measurements and the lateral drift level experienced by the connections. Such correlation could later be used to assess the degree of damage in flat-plate buildings subjected to earthquakes.

7.5.1 SWA tests on specimen L0.5

7.5.1.1 Energy source and sensor locations

For specimen L0.5 (Figure 7.12), the source of energy was located on the column, 12 in. from the slab, where 9/16-in. and 1 ½-in. steel balls were used to produce seismic waves.

A PVC pipe was used to drop the balls on the column, from a horizontal distance of approximately 1 m from the point of impact (Figure 7.13). To propagate a complete spectra of seismic waves (compressive and shear) along the column axis and the slab, the PVC pipe was inclined 45 degrees from the column axis. To avoid loss of energy due to geometry and dispersion along the column, the position of impact was selected close to the slab-column interface. The position of impact and ball launching device (PVC pipe) were standardized for all tests.

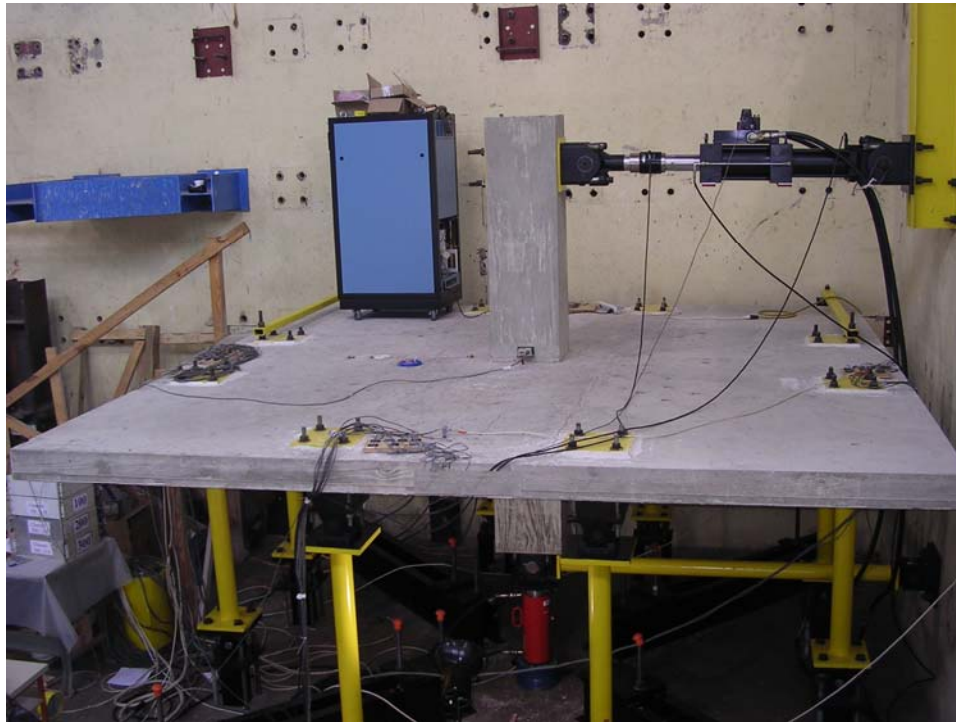


Figure 7.12 Specimen L0.5

The 9/16 in. ball was selected because it has a maximum frequency of useful energy $f_{max} = 20.4$ kHz, which corresponds to the usable range of frequencies (<20 kHz) provided by the signal conditioning module and the frequency range of most accelerometers. The 1½ in. ball has a maximum frequency $f_{max} = 7.6$ kHz. It was chosen because it can provide larger impact energy and thus a better signal to noise ratio than a 9/16 in. ball.

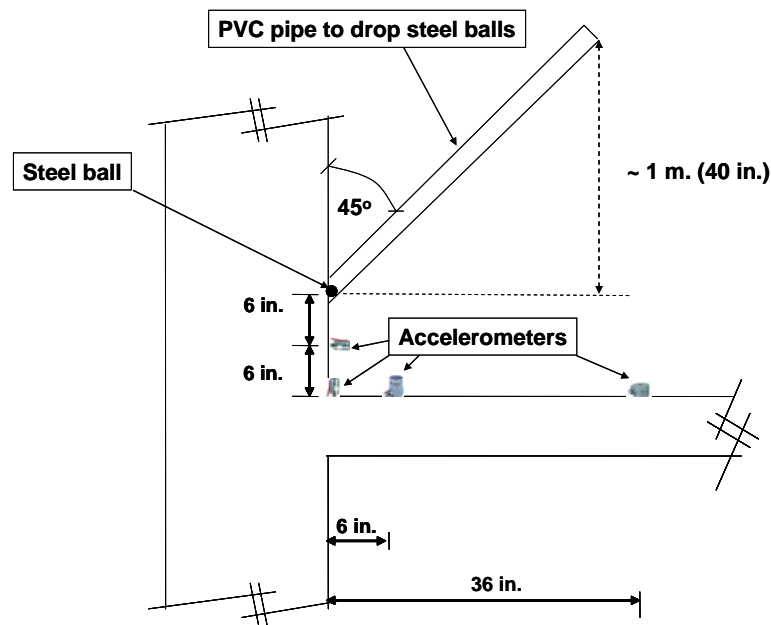


Figure 7.13 *PVC pipe used to drop steel balls on concrete column*

Accelerometers were installed along the North and East axes as shown in Figure 7.14 and Figure 7.15. On the North axis four sensors were installed: a low sensitivity accelerometer (Channel 0) near the impact location at 6 in. from the energy source, another low sensitivity accelerometer (Channel 1) adjacent to the slab-column interface, a high sensitivity accelerometer (Channel 2) on the slab 6 in. away from the column, and a very high sensitivity accelerometer (Channel 3) on the slab at 36 in. from the column. The locations of the accelerometers are shown in Figure 7.16. On the East axis two sensors were installed: a low sensitivity accelerometer on the column at 6 in. from the slab (Channel 0) and a high sensitivity accelerometer on the slab at 6 in from the column (Channel 2). On both, the North and East axes, the sensors were located in a plane that passes through the column centerline perpendicular to the column face.

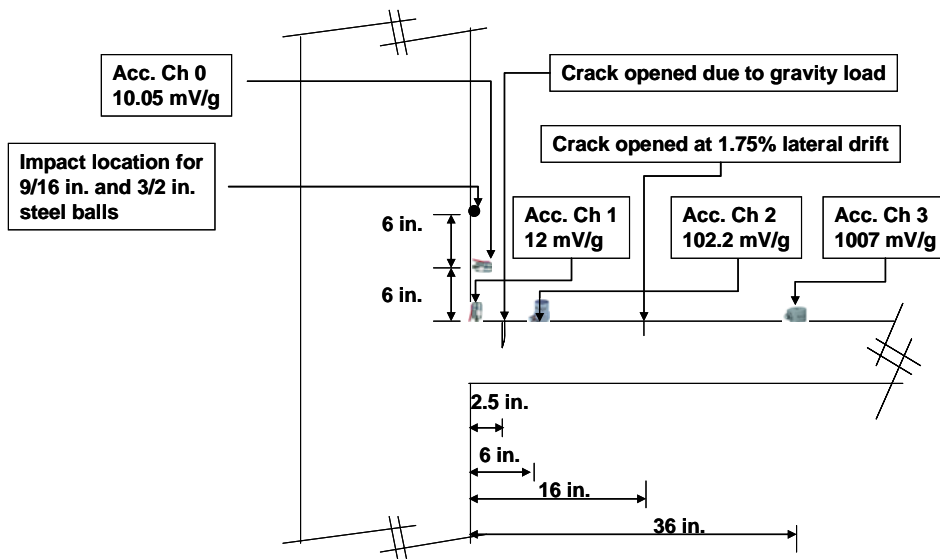


Figure 7.14 SWA tests on Specimen L0.5 along its North Axis

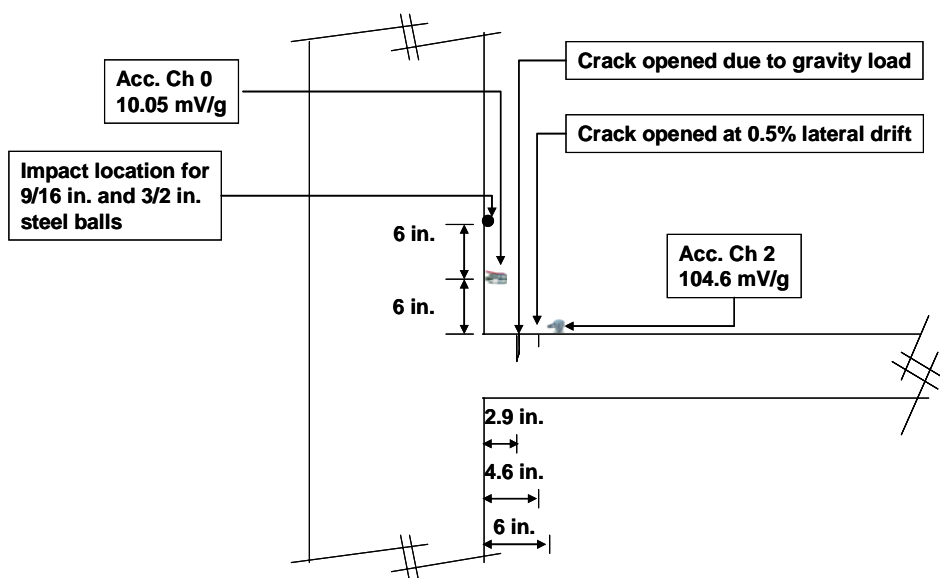


Figure 7.15 SWA tests on Specimen L0.5 along its East Axis

The position of sensors was chosen so that the peak acceleration ratio could be obtained from two time history records of sensors located before and after the cracks. The expected position of cracks determined the position of four sensors on the North axis (that was not the case for the East axis where only two accelerometers were used). The following criteria were used for the North Axis:

- i. A crack could form at the slab column interface. Therefore, one sensor (Channel 0) was installed on the column and a second sensor (Channel 1) was installed on the slab near to the slab-column interface.
- ii. At least one crack is expected to form in the slab between the slab-column interface and a point located 6 in. from the column. It was observed that at a distance equivalent to the slab depth, a primary crack always formed within this distance and was part of the punching shear failure surface. Therefore two accelerometers (Channel 1 and Channel 2) were installed at $\frac{1}{4}$ in. and 6 in. from the column face.
- iii. Additional cracks were expected to form in the slab at a distance greater than 6 in, measured from the column. Therefore, a sensor was installed at 36 in. from the face of the column (Channel 3).

Under lateral loading, specimen L0.5 was extensively cracked, as shown in Figure 7.16. On the North side, a large crack opened during the application of the gravity load at 2.5 in. from the column (between accelerometers Channel 1 and Channel 2). A small crack opened 16 in. from the column face during the

application of a lateral drift equal to 1.75% (between accelerometers Channel 2 and Channel 3), as shown in Figure 7.14.

On the East side, a large crack opened during the application of the gravity load at 2.9 in. from the column and a small crack opened during the application of a lateral drift equal to 0.5% at 4.6 in. from the column (Figure 7.15). No cracks were formed at the column-slab interface on both, the North and East sides.

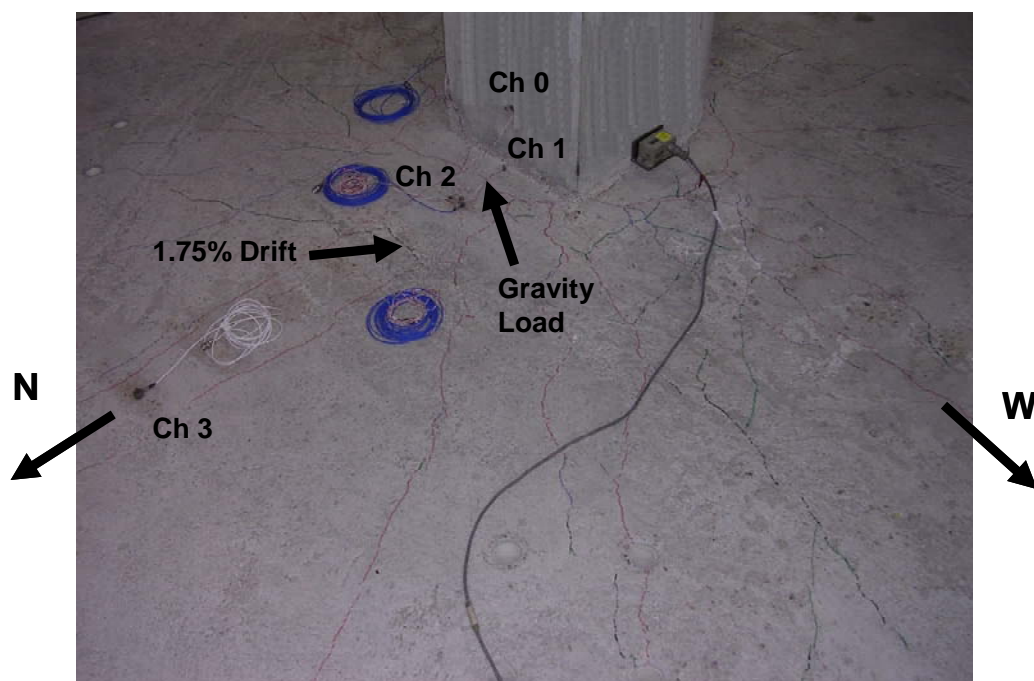


Figure 7.16 Cracking of Specimen L0.5 in the NW quadrant

7.5.1.2 Use of SWA measurements

SWA measurements were conducted by dropping the balls on the column, measuring peak accelerations from time history records and computing peak acceleration ratios (attenuation ratios) following the procedure described in Sections 7.2 and 7.5.1.1. Data points were generated by averaging the peak acceleration ratios for a set of ten SWA measurements conducted at selected drift levels and loading cycles. Samples of time history records used to compute attenuation ratios are presented in Appendix D.

7.5.1.3 North Axis

On the North axis, SWA measurements were conducted at various drift levels and loading cycles, when the top of the slab was in compression (cracks closed), in tension (cracks opened) and at rest (at the end of a loading cycle, when no lateral load was applied). Measurements were conducted prior to the application of gravity loads (uncracked condition), when gravity loads were applied without lateral loads (0% drift) and when lateral loads were applied at drift ratios of 0.25%, 0.5%, 0.75%, 1%, 1.5%, 1.75%, 2% and 2.5% of the story height.

From Figure 7.17 through Figure 7.28 the following observations can be made:

1. Effect of deformed position of connection

In figures Figure 7.17 through Figure 7.28 the attenuation ratios for data obtained when the top of the slab is in compression converge to the value that corresponds to the uncracked slab condition and only increase substantially for 2.5% drift, when the specimen failed. That is attributed to the fact that cracks are closed when the top of the slab is in compression and seismic waves can travel without attenuation caused by diffraction.

Figure 7.17 through Figure 7.28 show that the attenuation ratios for data obtained when the top of the slab is in tension and when the specimen is at rest follow the same trends and have similar order of magnitude. Data from “in tension” condition is somewhat larger than data from “at rest” condition. That is attributed to the fact that cracks are open with similar depth when the top of the slab is in tension and at rest, therefore seismic waves experience similar amount of attenuation due to diffraction.

2. Constant attenuation where there are no cracks

The Ch0/Ch1 attenuation ratio remains approximately constant for any drift level and ball (Figure 7.17 and Figure 7.18). This indicates the absence of cracks in the column or in the slab-column interface, between accelerometers Ch0 and Ch1. There was a nearly constant attenuation due to geometry and dispersion between sensors.

The Ch2/Ch3 attenuation ratio remains approximately constant for any drift level and ball (Figure 7.27 and Figure 7.28). This denotes the absence of cracks between accelerometers Ch2 and Ch3 prior to 1.75% drift. The attenuation between those sensors is nearly constant and is due to geometry and dispersion.

3. Effect of size of ball

Attenuation ratios increases are greater as the drift ratio increases for conditions of slab at rest and top of the slab in tension. The increase is attributed to an increase in depth of a critical crack located between Ch1 and Ch2. The increase in attenuation ratios starts at 0.25% drift for the 9/16 in. ball (Figure 7.19, Figure 7.21, Figure 7.23 and Figure 7.25) and at 2% drift for the 1 ½ in. ball (Figure 7.20, Figure 7.22, Figure 7.24 and Figure 7.26). The 9/16 in. ball produced the largest attenuation ratios, because of its higher frequency content. Frequencies from 7.6 kHz to 20.4 kHz are highly attenuated as the critical crack grows in depth. Frequencies below 7.6 kHz, which correspond to the 1 ½ in. ball, have long wavelengths and can pass through the crack without losing much energy, unless the specimen is severely cracked following shear failure (drift ratio 2.5%).

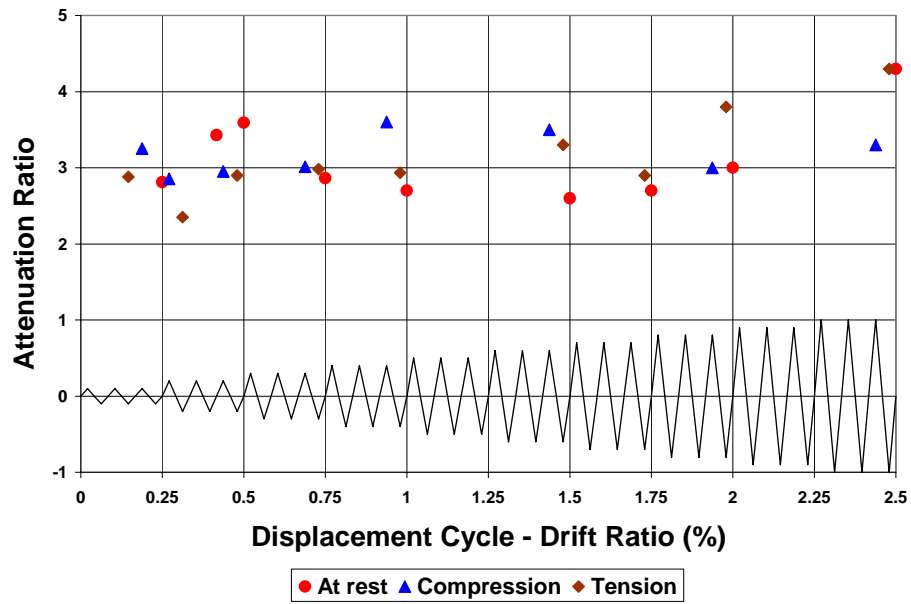


Figure 7.17 Ch0/Ch1 Attenuation Ratios for 9/16 in. ball on North Axis

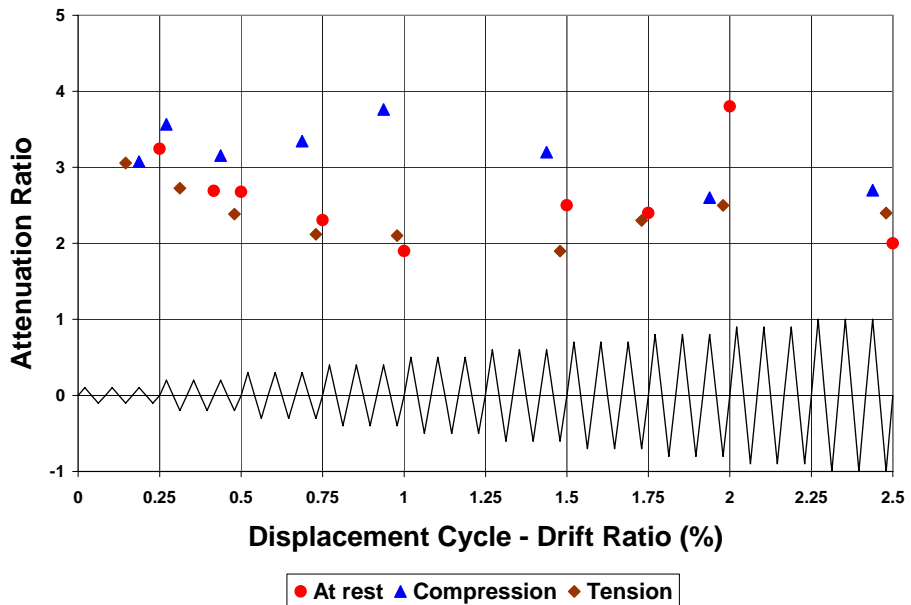


Figure 7.18 Ch0/Ch1 Attenuation Ratios for 1 1/2 in. ball on North Axis

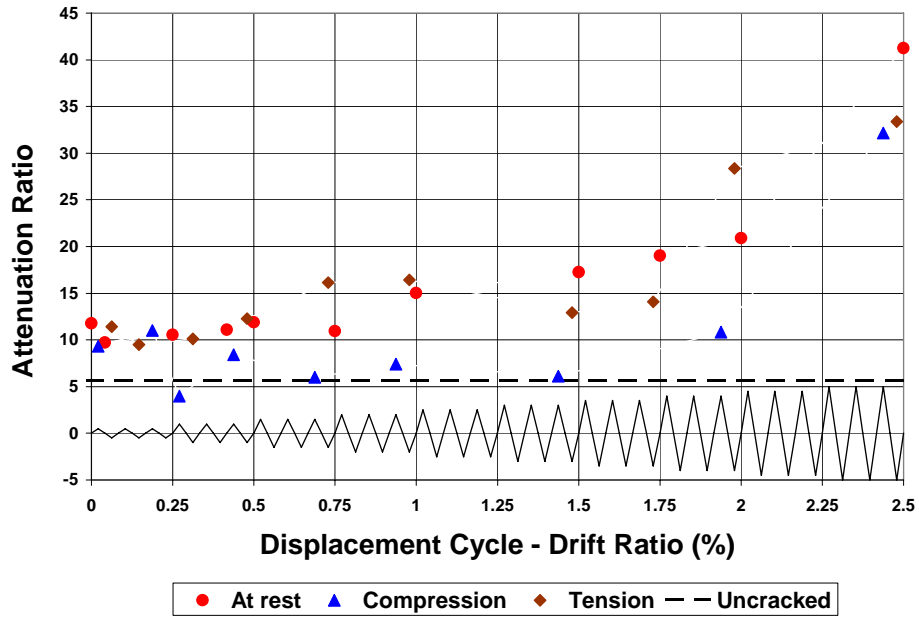


Figure 7.19 Ch0/Ch2 Attenuation Ratios for 9/16 in. ball on North Axis

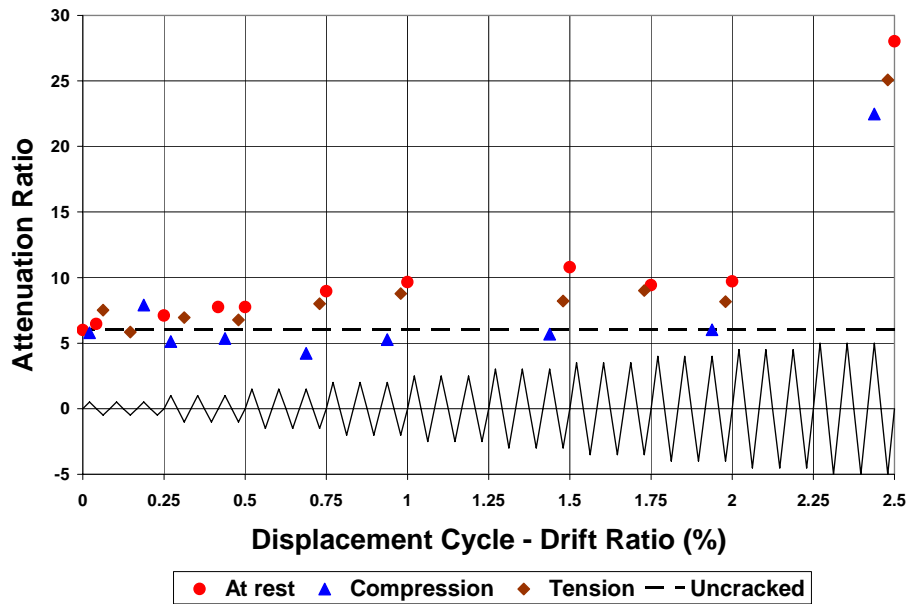


Figure 7.20 Ch0/Ch2 Attenuation Ratios for 1 1/2 in. ball on North Axis

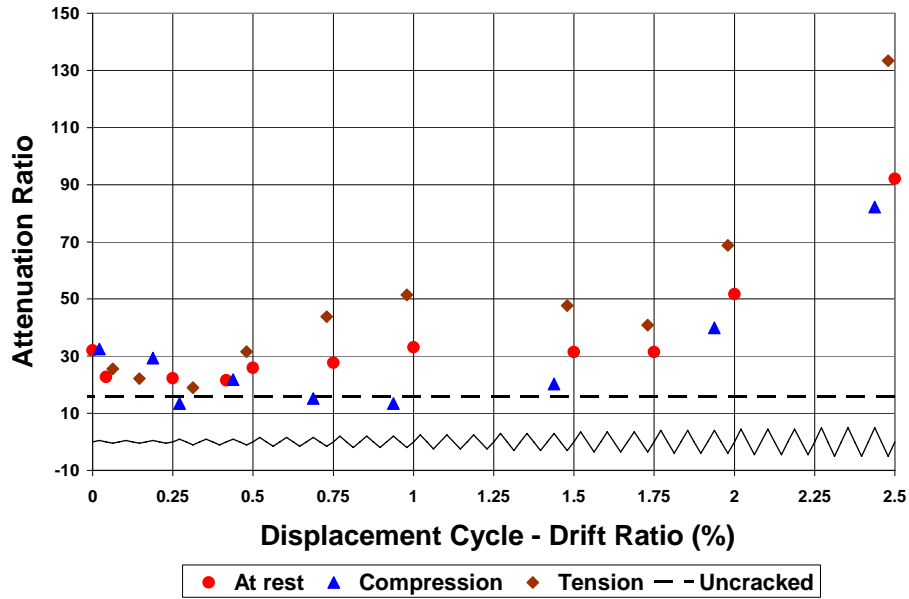


Figure 7.21 Ch0/Ch3 Attenuation Ratios for 9/16 in. ball on North Axis

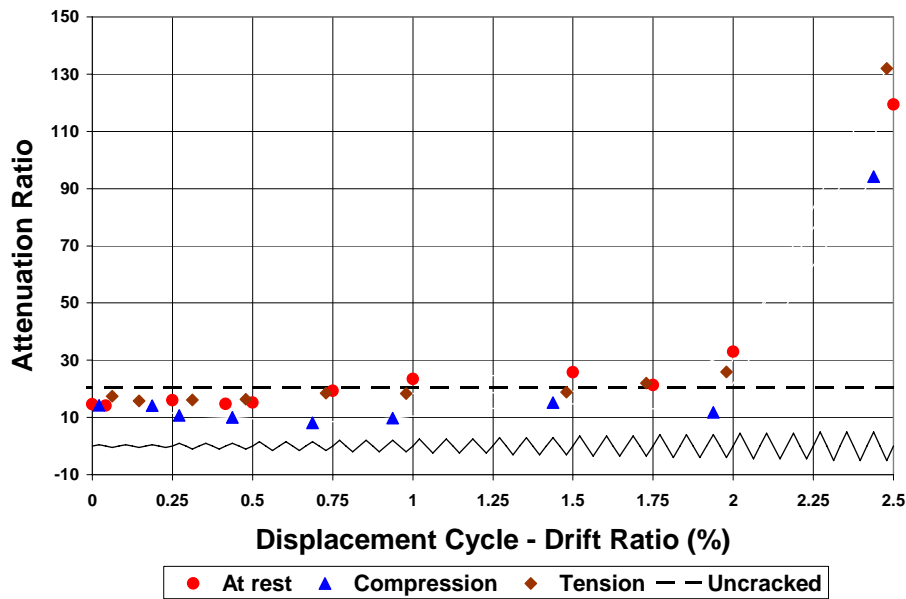


Figure 7.22 Ch0/Ch3 Attenuation Ratios for 1 1/2 in. ball on North Axis

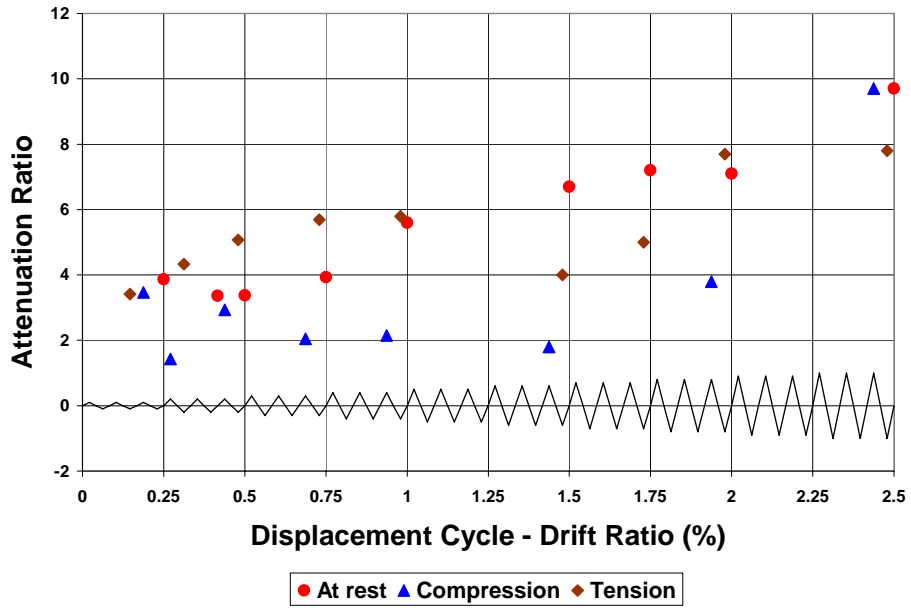


Figure 7.23 Ch1/Ch2 Attenuation Ratios for 9/16 in. ball on North Axis

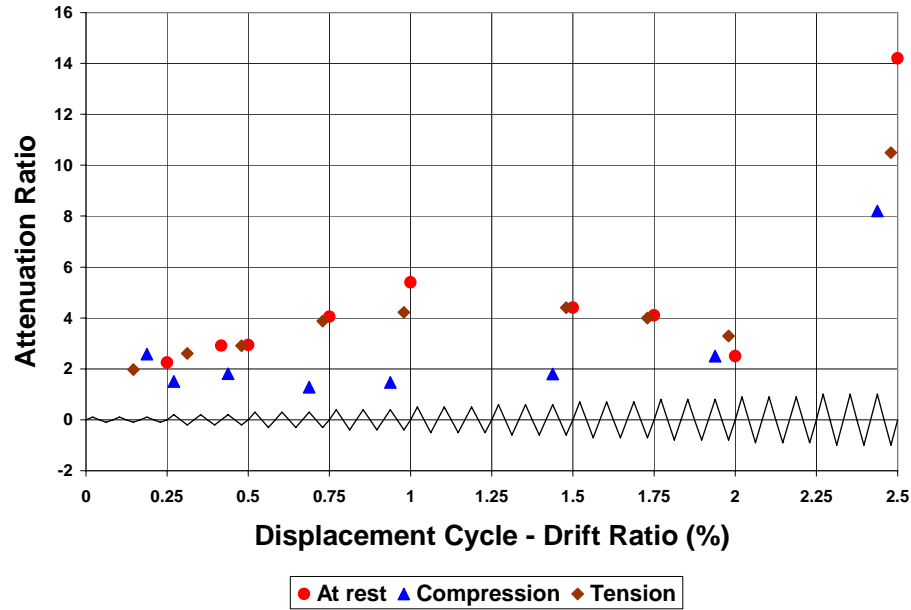


Figure 7.24 Ch1/Ch2 Attenuation Ratios for 1 1/2 in. ball on North Axis

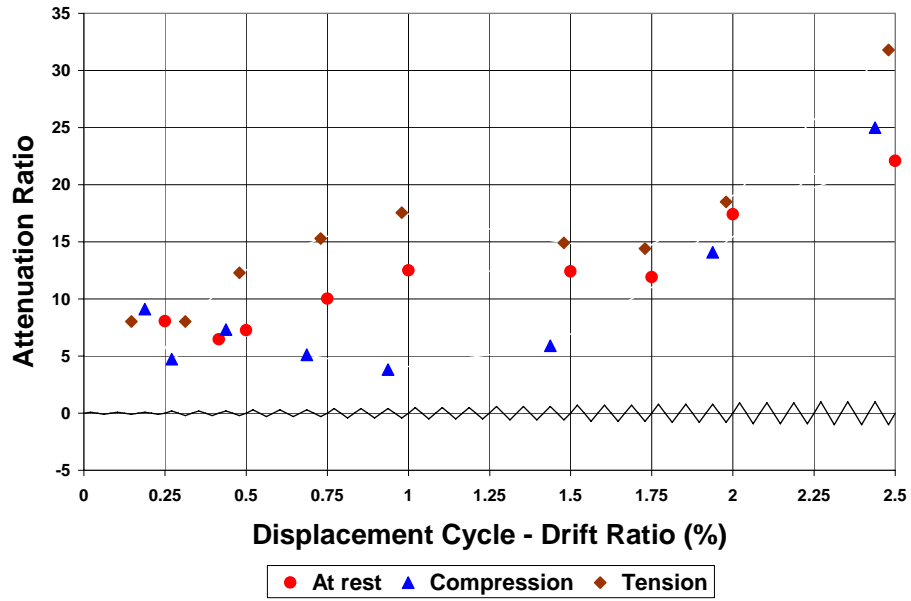


Figure 7.25 Ch1/Ch3 Attenuation Ratios for 9/16 in. ball on North Axis

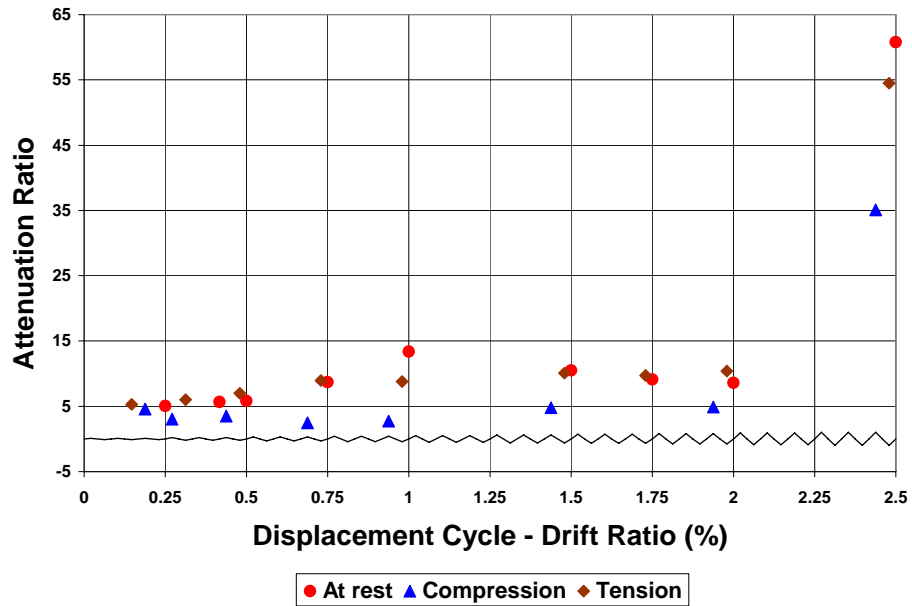


Figure 7.26 Ch1/Ch3 Attenuation Ratios for 1 1/2 in. ball on North Axis

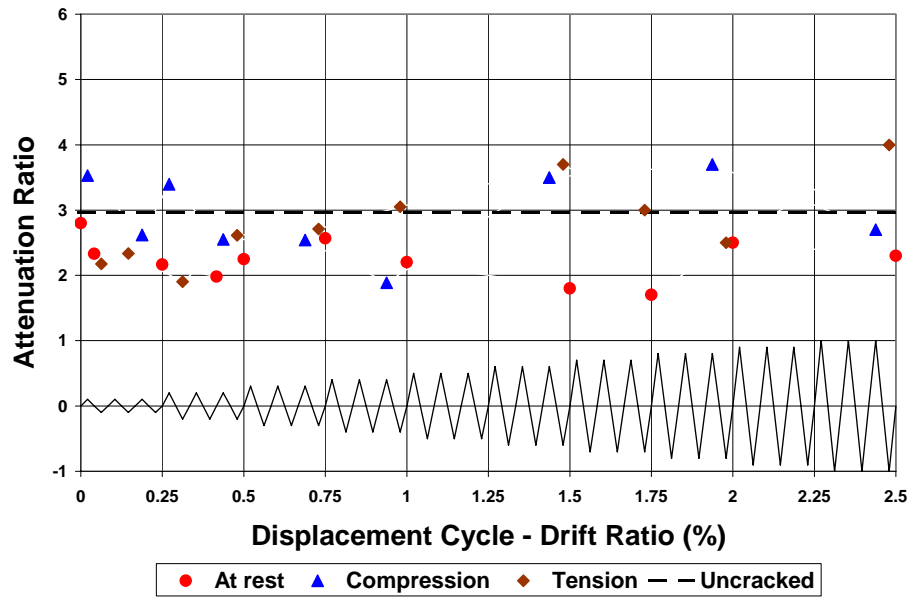


Figure 7.27 Ch2/Ch3 Attenuation Ratios for 9/16 in. ball on North Axis

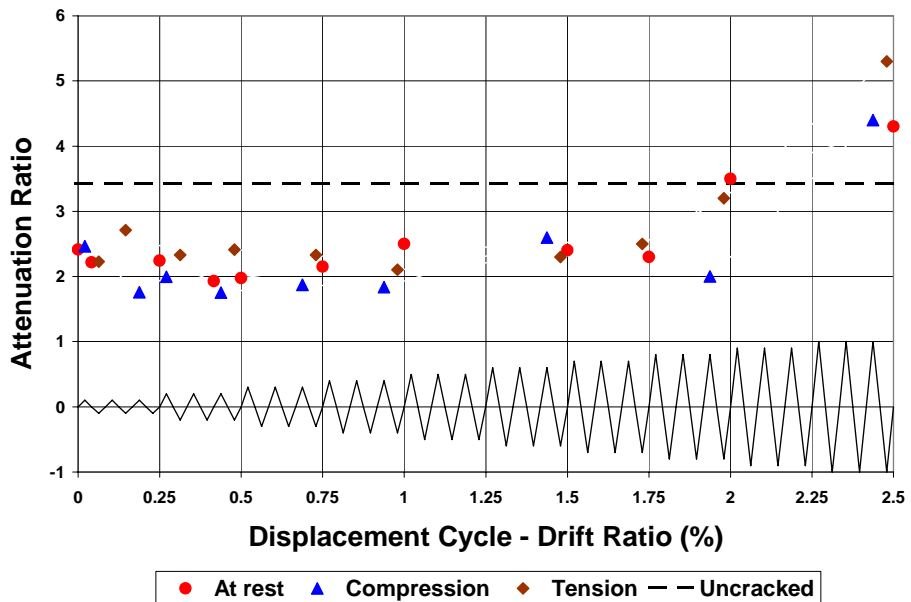


Figure 7.28 Ch2/Ch3 Attenuation Ratios for 1 1/2 in. ball on North Axis

7.5.1.4 East Axis

Results from tests conducted on the East axis with the 9/16 in. and 1 ½ in. balls are presented in Figure 7.29 and Figure 7.30. On the East axis, SWA measurements were conducted when the specimen was at rest, (at the end of a loading cycle when no lateral load was applied) under the following conditions: when gravity loads but no lateral loads were applied (0% drift) and when lateral loads were applied, at drift ratios 0.5%, 0.75%, 1%, 1.5%, 1.75% and 2%.

From Figure 7.29 and Figure 7.30, the following observations are obtained:

1. Correlation between attenuation ratios and damage due to torsion

Damage on the East and West faces of the column was predominantly due to torsion, because direction of lateral loading was along the NS axes. Accelerometers Ch0 and Ch2 were contained in a plane that passes through the column centerline perpendicular to the East column face. In this plane, torsional stresses are zero. That explains why at low to moderate drifts (below 1.5%) cracks between sensors Ch0 and Ch2 showed little activity (grew little in width). Only when substantial stress redistribution occurred above 1.5% drift, cracks between sensors Ch0 and Ch2 grew in width and probably also in depth. Figure 7.31 and Figure 7.32 show the progression of damage on the East face of the column from 0.5% drift to 2% drift.

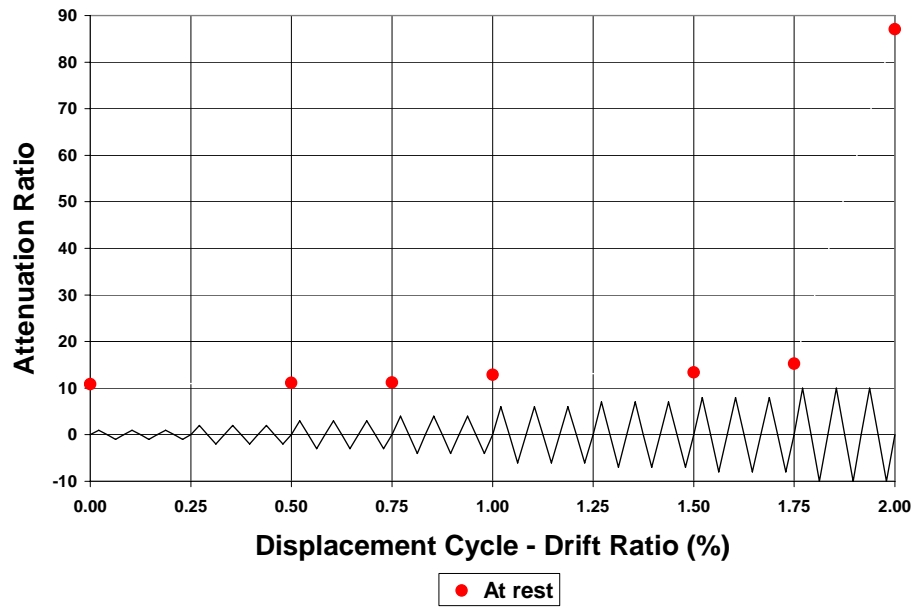


Figure 7.29 Ch0/Ch2 Attenuation Ratios for 9/16 in. ball on East Axis

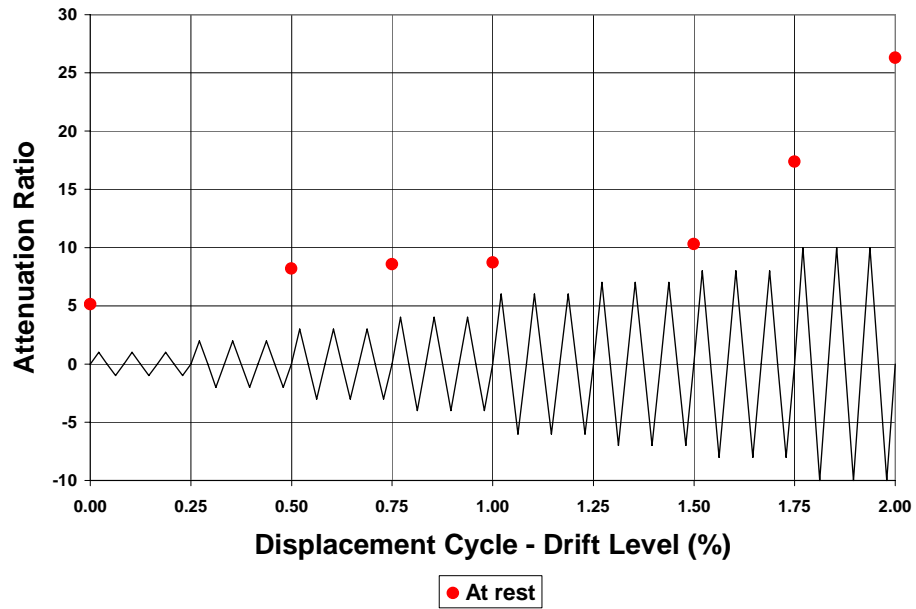


Figure 7.30 Ch0/Ch2 Attenuation Ratios for 1 1/2 in. ball on East Axis

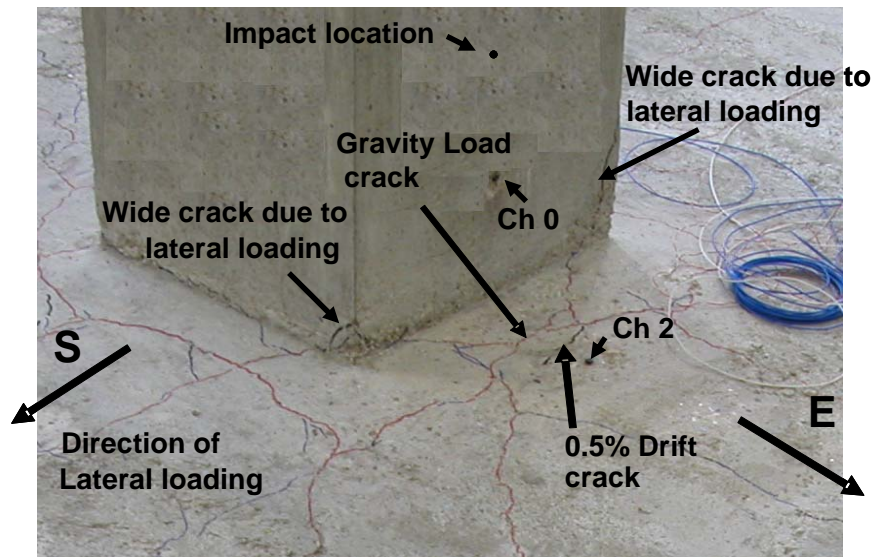


Figure 7.31 Cracking on East Axis of specimen L0.5 at 0.5% drift

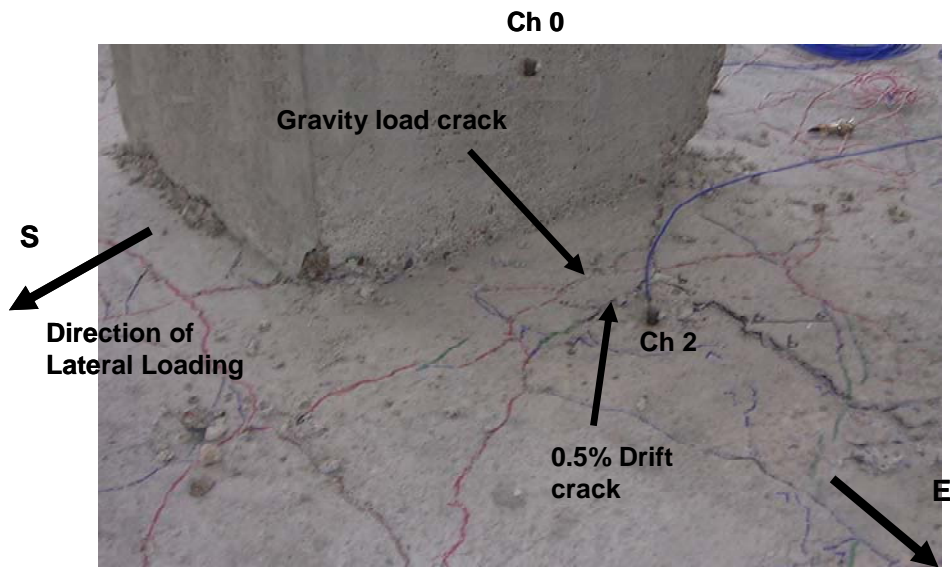


Figure 7.32 Cracking on East Axis of specimen L0.5 at 2% drift

When gravity loads were applied the specimen cracked and the attenuation ratios Ch0/Ch2 were measured as 10.8 (9/16 in. ball) and 5.4 (1 ½ in. ball). For drift ratios from 0% to 1.5%, the Ch0/Ch2 attenuation ratio increased from 10.8 to 13.4 for the 9/16 in. ball and from 5.4 to 10.3 for the 1 ½ in. ball. The increment in attenuation is small, particularly for the 9/16 in. ball, which suggests that the crack depth had experienced little change within the specified drift range.

For drift ratios 1.75% and 2%, the Ch0/Ch2 attenuation ratio increased significantly from 15.3 to 87.0 for the 9/16 in. ball and from 17.4 to 26.3 for the 1 ½ in. ball. This suggests that the crack depth had increased significantly between 1.75% and 2% drift.

After 1.5% drift, extensive damage due to torsion was produced on the East and West sides of the specimen, which is coincident with the increase in Ch0/Ch2 attenuation ratios. This observation is consistent with results from visual observations on crack widths (Section 4.2.1) and crack pattern (Section 4.3.3). Therefore, there is good correlation between attenuation ratios and damage due to torsion.

2. Effect of size of ball

At most drift ratios the Ch0/Ch2 attenuation ratio for the 9/16 ball is larger than that for the 1 ½ in ball. The 9/16 in. ball introduces higher frequencies than 1 ½ in. ball, with frequencies from 7.6 kHz to 20.4 kHz that are not excited by the 1 ½ in. ball. Higher frequency waves

attenuate more than low frequency waves and that is considered to be the reason why attenuation ratios for the 9/16 in. ball are larger than for the 1 ½ in. ball.

Similar observations were obtained for the East and North axes about the effect of size of the ball. It was found convenient to use the 9/16 in. ball and not to use the 1 ½ in. ball, because the first is capable to excite frequencies within the range of 10 – 20 kHz and the second is not. Waves with frequencies between 10 – 20 kHz have wavelengths short enough to experience attenuation due to diffraction at opened cracks. Using the Shear Wave Velocity $V_s = 8,003 \text{ fps}$ (Appendix C) and Equations 5-8 and 5-9, the wavelength L_R was calculated for frequencies $f_1 = 10 \text{ kHz}$ and $f_2 = 20 \text{ kHz}$, as $L_{R1} = 8.7 \text{ in.}$ and $L_{R2} = 4.4 \text{ in.}$

7.5.1.5 Conclusions from tests of specimen L0.5

From tests conducted on specimen L0.5, the following conclusions were obtained:

- i. The 1 ½ in. ball was not suitable for measuring attenuation across cracks. Frequencies of useful energy higher than $f_{max} = 7.6 \text{ kHz}$ are required to measure attenuation at cracks. The 9/16 in. ball with $f_{max} = 20.4 \text{ kHz}$ or smaller balls $f_{max} > 20.4$ will be more appropriate for detecting attenuation due to diffraction at opened cracks. In concrete

with Shear Velocity $V_s = 8,000 \text{ fps}$, ultrasonic waves with frequencies $f > 20\text{kHz}$ and wavelengths $L_R < 4.4\text{in.}$ (approximately two thirds or less the slab depth) seems to be ideal for measuring diffractive attenuation through open cracks.

- ii. The “at rest” condition appears to provide satisfactory attenuation ratios. The data obtained were consistent and repeatable. In addition, the “at rest” condition represents the state at which buildings are assessed after earthquake loads have been applied.
- iii. The configuration of sensors was sufficient for the North axis. In case of the East axis, at least one more sensor was needed. This additional sensor should be located on the slab, $\frac{1}{4}$ in. from the column face.
- iv. Sensors on the East axis could be located in a plane eccentric to the column centerline and perpendicular to the column face (Figure 7.33). By so doing, damage will be monitored in a region where torsional stresses are not zero and it can be expected that cracks between sensors will grow in width and depth at low drifts and attenuation ratios will gradually increase according to the progression of damage.

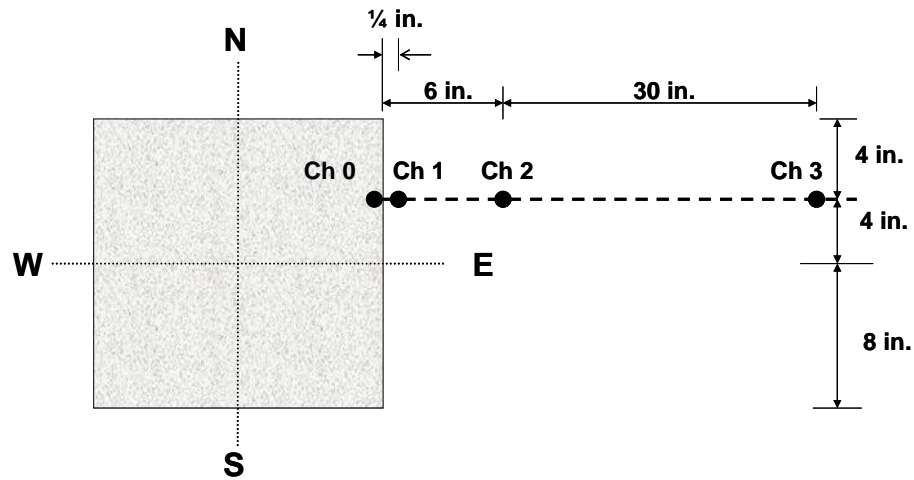


Figure 7.33 Alternative location of sensors for the East axis, in a plane eccentric to column centerline

7.5.2 SWA Tests on Specimen LG0.5

7.5.2.1 Energy source and sensor locations

The source of energy for specimen LG0.5 (Figure 7.34) was applied on the column, 12 in. from the slab, as it was for specimen L0.5. For this test, 5/16 in. and 9/16 in. steel balls were impacted against the column to produce seismic waves, following procedure describe in Section 7.5.1.1. The 9/16 in. ball provided good data for specimen L0.5, the high frequencies exerted (10 to 20 kHz.) were adequately attenuated by diffraction at cracks, and a correlation between attenuation ratios and lateral drifts could be determined. The 5/16 in. ball has a

maximum frequency of useful energy $f_{max} = 36.7$ kHz. It was chosen because it can provide higher frequency content than the 9/16 in. ball and a larger attenuation at cracks could be expected, potentially improving the quality of data at low drift levels.



Figure 7.34 Specimen LG0.5

Accelerometers were installed along the North and East axes as shown in Figure 7.35 and Figure 7.36. On the North axis four sensors were installed: one low sensitivity accelerometer (Channel 0) was installed 6 in. from the impact

location, another low sensitivity accelerometer (Channel 1) was installed on the slab and adjacent to the slab-column interface, a high sensitivity accelerometer (Channel 2) was located on the slab 6 in. away from the column, and a very high sensitivity accelerometer (Channel 3) was placed on the slab at 36 in. from the column. The sensors were installed in a plane that passes through the column centerline perpendicular to the column face.

On the East axis four accelerometers were installed with the same layout as accelerometers on the North axis, except that sensors were located in a plane that is perpendicular to the column face but eccentric from the column centerline, four inches to the North (Figure 7.33).

With the application of lateral loads, specimen LG0.5 cracked extensively. On the North side, a large crack opened 2.5 in. from the column during the application of the gravity load. The crack was between accelerometers Channel 1 and Channel 2. A hairline crack (0.01 in. width) opened at the slab-column interface, between accelerometers Channel 0 and Channel 1 (Figure 7.35), during the application of a lateral drift equal to 0.25%, but remained unchanged at higher drift levels.

On the East side, between Channel 1 and Channel 2, a large crack opened during the application of gravity load 1 in. from the column. A second crack opened at 0.25% lateral drift, 4.5 in. away from the column. Between Channel 2 and Channel 3, three more cracks opened as lateral loads increased; at 0.75% drift, 10.5 in. from the column; at 1% drift, 18 in. from the column; and at 1.25% drift, 25 in. from the column (Figure 7.36). No cracks were formed at the column-slab interface on the East side.

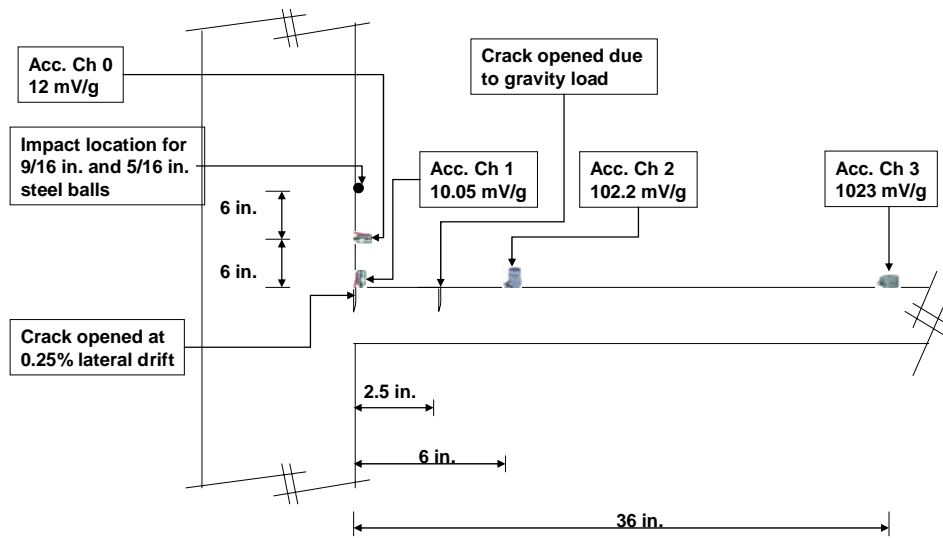


Figure 7.35 SWA tests on specimen LG0.5 along its North axis

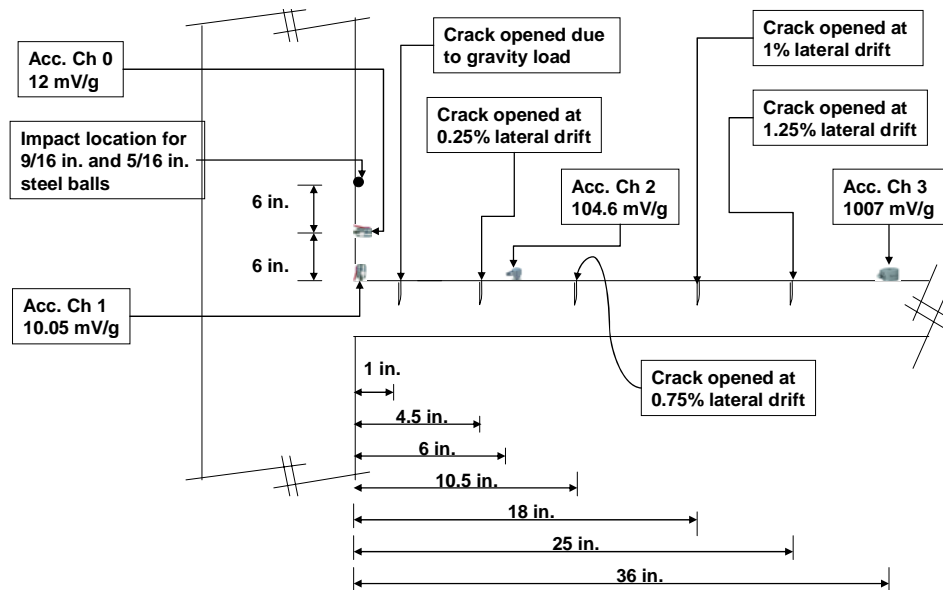


Figure 7.36 SWA tests on specimen LG0.5 along its East axis

7.5.2.2 SWA measurements

SWA measurements were conducted following the same procedure described in Section 7.5.1.2 for L0.5.

7.5.2.3 North Axis

Results from tests conducted on the North axis with the 9/16 in. and 5/16 in. balls are presented in Figure 7.37 through Figure 7.42. SWA measurements were conducted when the specimen was at rest under the following conditions: uncracked with no gravity loads applied, when gravity loads but no lateral loads were applied (0% drift) and when lateral loads were applied (0.25%, 0.5, 0.75%, 1% and 1.25% drift).

From Figure 7.37 through Figure 7.42, the following observations can be made:

1. Constant attenuation where there is no crack

As expected, the Ch1/Ch3 and Ch2/Ch3 attenuation ratios shown in Figure 7.41 and Figure 7.42 remained approximately constant as the drift level increased, because there were no cracks located between Ch2 and Ch3.

2. Constant attenuation where hairline cracks are formed

The Ch0/Ch1 attenuation ratio remained approximately constant for any drift level (Figure 7.37). That is not consistent with the fact that at 0.25% drift, a hairline crack opened in the slab-column interface. However, the crack did not result in any attenuation due to diffraction because it was very shallow and narrow (0.01 in.)

3. There is a correlation between attenuation ratios and damage where cracks are formed

The Ch0/Ch2, Ch1/Ch2 and Ch0/Ch3 attenuation ratios shown in Figure 7.38 through Figure 7.40 increased when the drift level increased. The increase is attributed to an increase in depth of cracks located between Ch1 and Ch2. The correlation between attenuation ratio and drift level is roughly linear, with significant data scattering.

4. Uncracked condition showed higher attenuation ratios than cracked conditions

The attenuation ratio for the uncracked condition was larger than for other conditions where the specimen was cracked. That is not consistent with the theory of wave propagation, which suggests that more attenuation shall be produced when cracks are present. It should be noted that this inconsistency was not found for specimen L0.5. In L0.5, SWA measurements for the uncracked condition were taken

when the specimen was resting on the forms, while for LG0.5 and all other specimens measurements were conducted when the specimen was in test position resting on steel struts, a ram under the column, and the horizontal actuator was attached. This inconsistency is probably related to an external source of attenuation or damping that affects the specimen prior to the application of loads. Such source was unidentified, but seems to be related to the specimen's boundary conditions.

5. No improvements with the 5/16 in. ball

Attenuation ratios measured with the 5/16 in. ball were of similar order of magnitude than those measured with the 9/16 in. ball. Therefore, no improvements were made by dropping a smaller ball (5/16 in.).

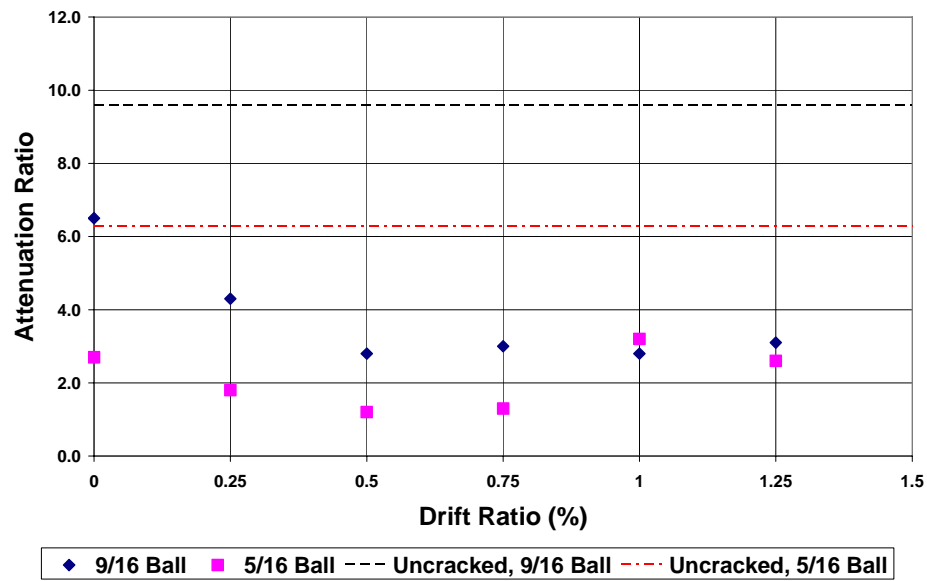


Figure 7.37 Ch0/Ch1 Attenuation Ratios, 9/16 and 5/16 in. balls (North Axis)

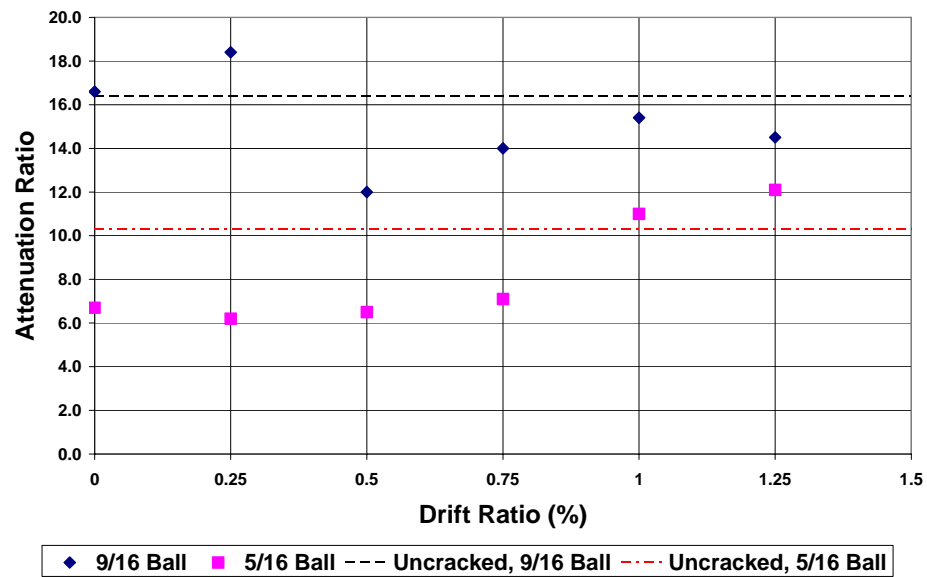


Figure 7.38 Ch0/Ch2 Attenuation Ratios, 9/16 and 5/16 in. balls (North Axis)

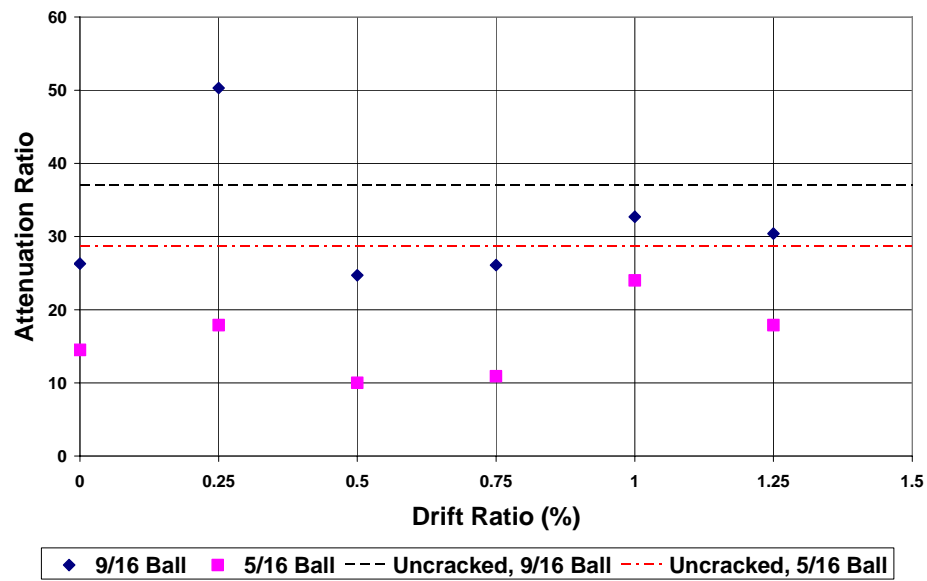


Figure 7.39 Ch0/Ch3 Attenuation Ratios, 9/16 and 5/16 in. balls (North Axis)

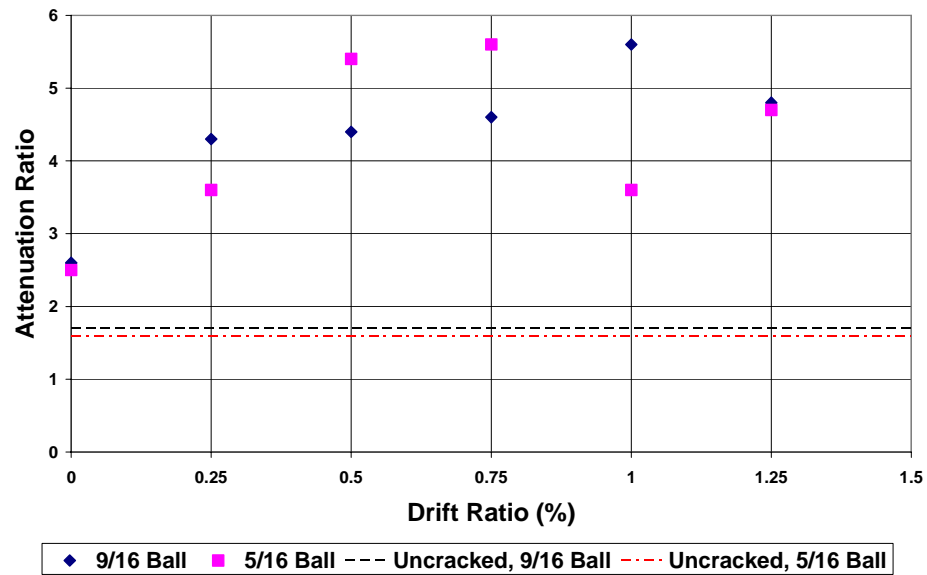


Figure 7.40 Ch1/Ch2 Attenuation Ratios, 9/16 and 5/16 in. balls (North Axis)

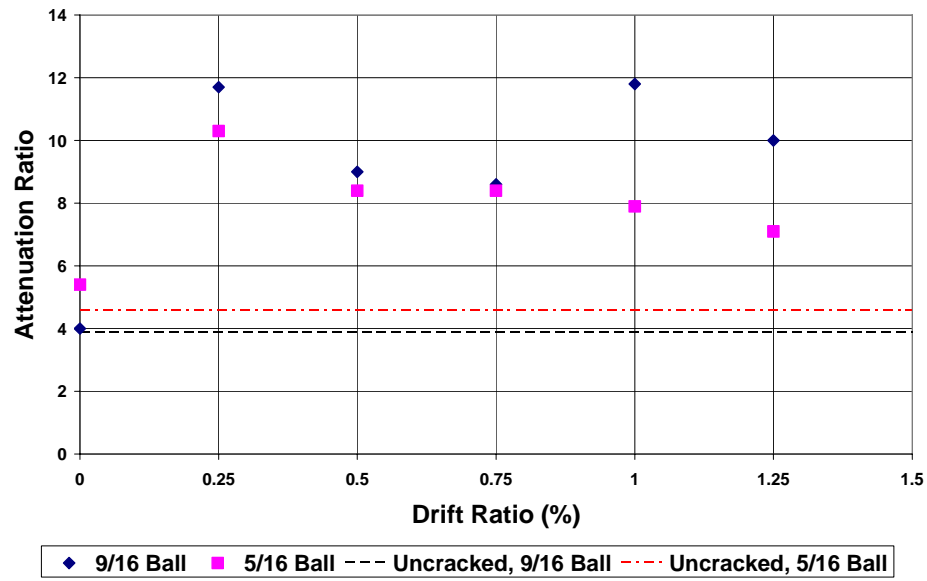


Figure 7.41 Ch1/Ch3 Attenuation Ratios, 9/16 and 5/16 in. balls (North Axis)

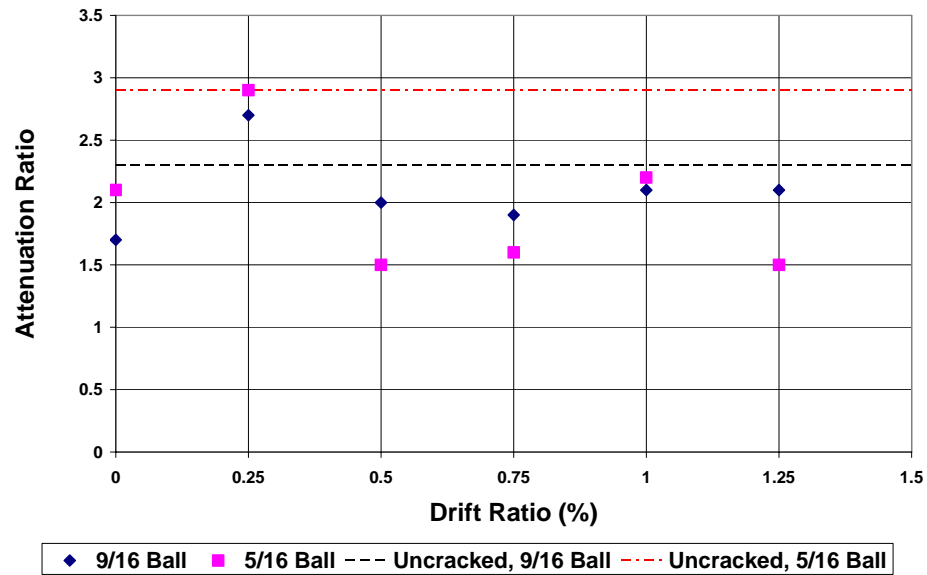


Figure 7.42 Ch2/Ch3 Attenuation Ratios, 9/16 and 5/16 in. balls (North Axis)

7.5.2.4 East Axis

Results from tests conducted on the East axis with the 9/16 in. and 5/16 in. balls are presented in Figure 7.43 through Figure 7.48. On the East axis, SWA measurements were conducted for the same conditions described in Section 7.5.2.3 for the North Axis.

Using Figure 7.43 through Figure 7.48, the following trends were observed:

1. Constant attenuation where there is no crack

The Ch0/Ch1 attenuation ratio remained approximately constant for all drift level (Figure 7.43), which is consistent with the fact that there are no cracks in the column and in the slab-column interface.

2. There is a correlation between attenuation ratios and damage where cracks are formed

The Ch0/Ch2, Ch1/Ch2 and Ch0/Ch3 attenuation ratios shown in Figure 7.44 through Figure 7.46 increased when the drift level increased. That is attributed to an increase in the depth of cracks located between Ch1 and Ch2. The correlation between attenuation ratio and drift level was linear, with significant data scattering.

3. Almost constant attenuation where hairline cracks are formed

The Ch1/Ch3 and Ch2/Ch3 attenuation ratios shown in Figure 7.47 and Figure 7.48 increased slightly when the drift level increased. The correlation between attenuation ratio and drift level is linear. The small increase is due to the fact that cracks located between Ch2 and Ch3 were hairline cracks (width 0.015 in.) that were probably very shallow.

4. Uncracked condition showed higher attenuation ratios than cracked conditions

Similarly to what was observed for the North axis, the attenuation ratio for the uncracked condition was larger than for other conditions where the specimen was cracked.

5. No improvements with the 5/16 in. ball

Similarly to what was found for the North axis, no improvements were made by dropping the 5/16 in. ball.

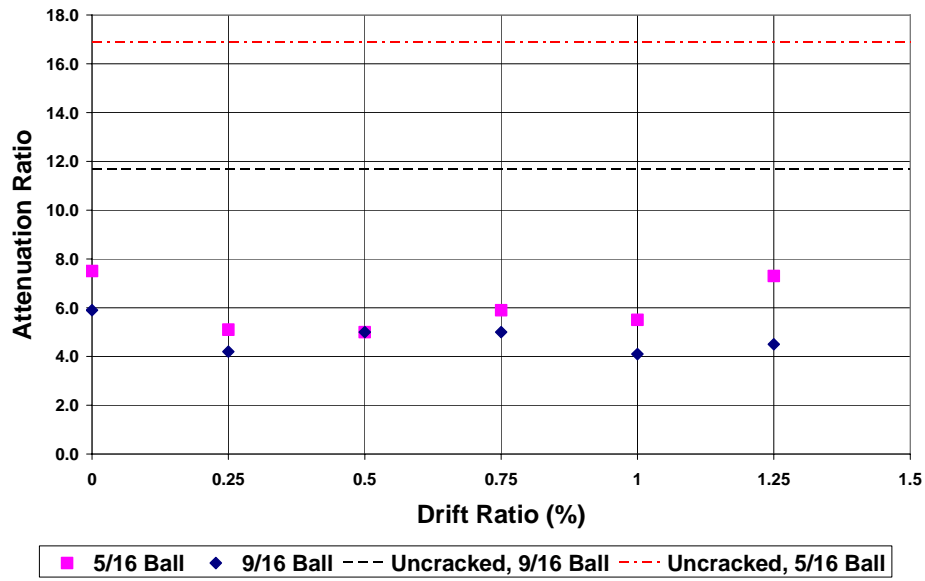


Figure 7.43 Ch0/Ch1 Attenuation Ratios, 9/16 and 5/16 in. balls on East Axis

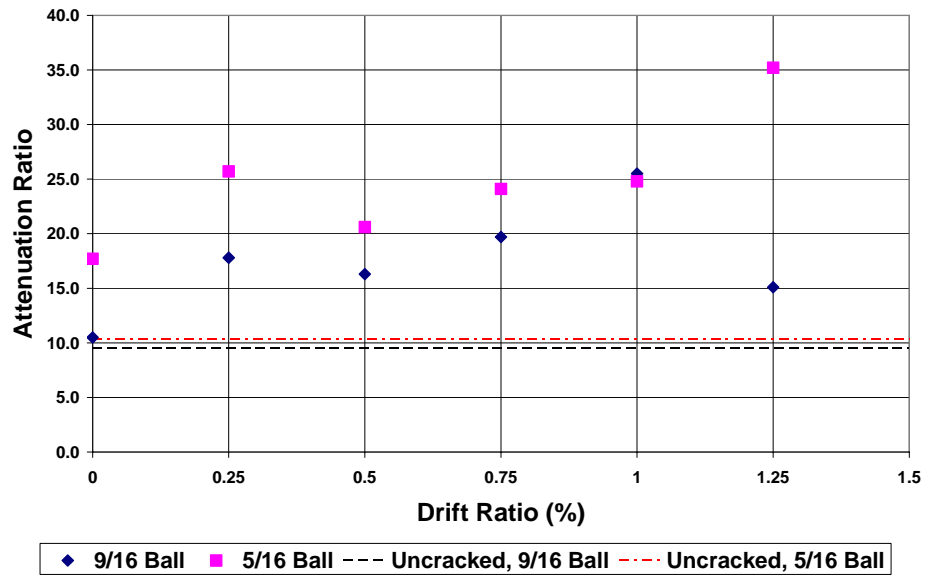


Figure 7.44 Ch0/Ch2 Attenuation Ratios, 9/16 and 5/16 in. balls on East Axis

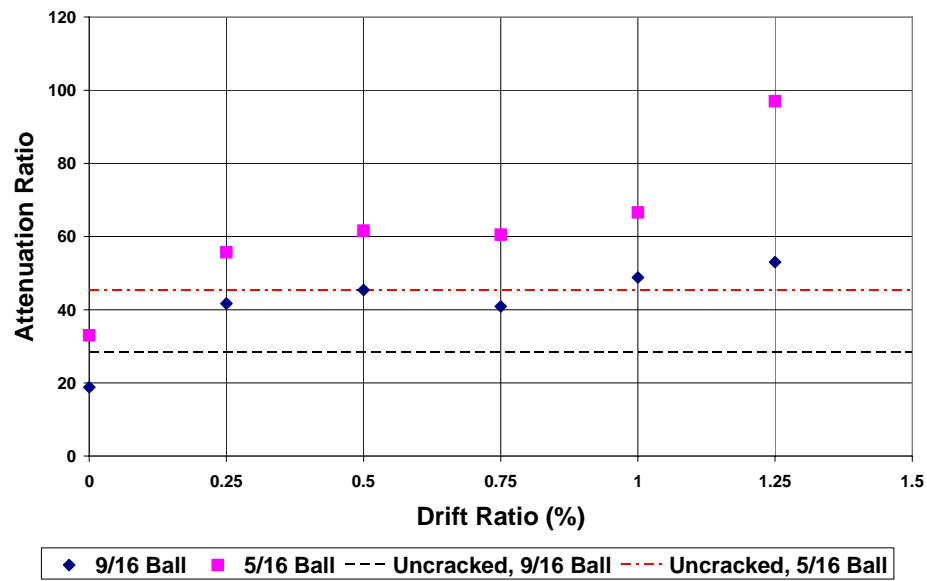


Figure 7.45 Ch0/Ch3 Attenuation Ratios, 9/16 and 5/16 in. balls on East Axis

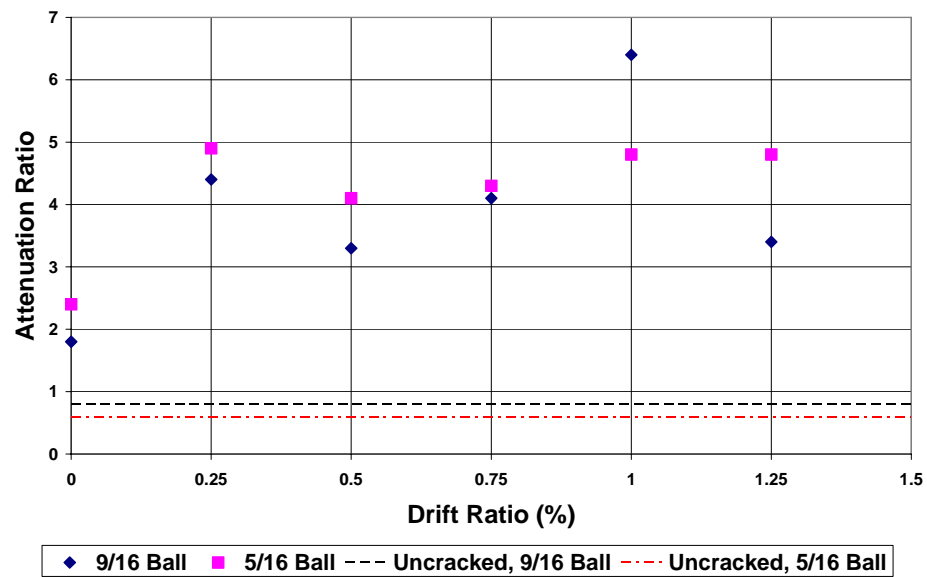


Figure 7.46 Ch1/Ch2 Attenuation Ratios, 9/16 and 5/16 in. balls on East Axis

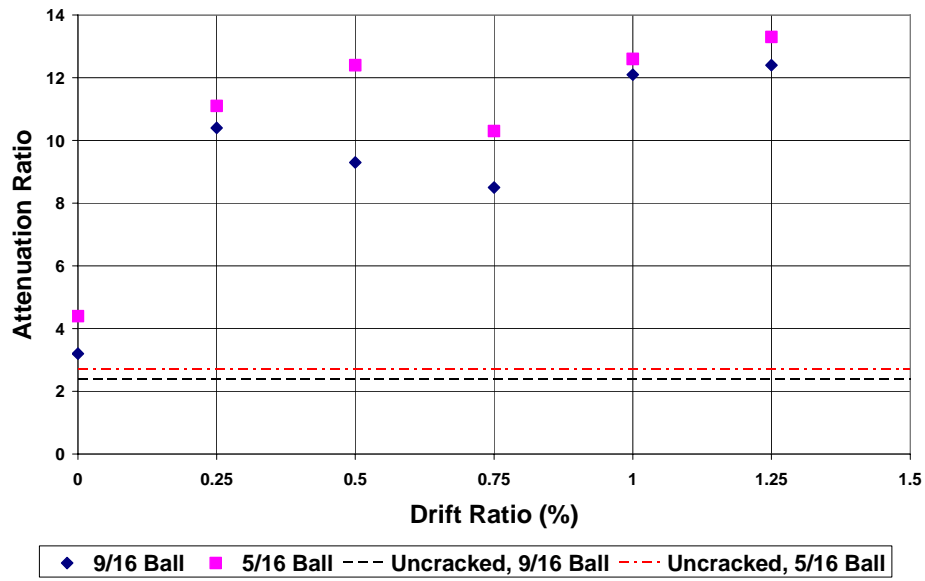


Figure 7.47 Ch1/Ch3 Attenuation Ratios, 9/16 and 5/16 in. balls on East Axis

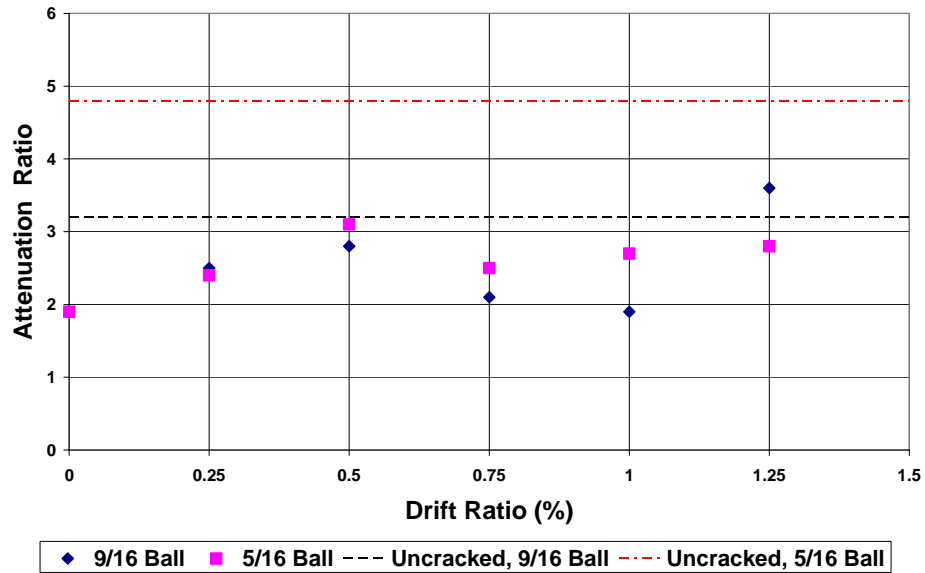


Figure 7.48 Ch2/Ch3 Attenuation Ratios, 9/16 and 5/16 in. balls on East Axis

7.5.2.5 *Conclusions from tests of specimen LG0.5*

The following conclusions were obtained from tests conducted on specimen LG0.5:

- i. The 5/16 in. and 9/16 in. balls were adequate for measuring attenuation at cracks. They produced good results with similar data scattering. The use of frequencies greater than $f_{max} = 20.4$ kHz (ball 5/16 in.) did not improve the quality of data because the data acquisition system had a maximum usable frequency equal to 20 kHz.
- ii. There was no measured attenuation due to diffraction at a hairline crack (0.015 in. width or less), that was observed at the slab-column interface in the North axis. Attenuation was always observed when cracks were 0.015 in. width or more.
- iii. The offset introduced for the accelerometer layout on the East axis produced good results. The offset consisted of placing the sensor in a plane perpendicular to the column face eccentrically located at 4 inches from the column centerline.
- iv. Results obtained from the East and North axis showed similar trends, with attenuation ratios of similar order of magnitude. Therefore, SWA measurements could be performed on either axis. In subsequent tests, measurements were performed on the North axis only, because more data from specimens L0.5 and LG0.5 is available for the North axis than for the East axis.

7.5.3 SWA Tests on Specimen LR_{ST}G0.5

7.5.3.1 Energy source and sensor locations

For specimen LR_{ST}G0.5 (Figure 7.49), the source of energy was applied on the column, 12 in. from the slab, as it was for specimens L0.5 and LG0.5. For this test, the 5/16 in. and 9/16 in. steel balls were impacted against the column to produce seismic waves, following procedure described in Section 7.5.1.1.



Figure 7.49 Specimen LR_{ST}G0.5, after the application of gravity loads

Accelerometers were installed along the North axis only, as shown in Figure 7.50. Four sensors were installed: one low sensitivity accelerometer (Channel 0) was installed 6 in. from the impact location, another low sensitivity accelerometer (Channel 1) was installed on the slab and adjacent to the slab-column interface, a high sensitivity accelerometer (Channel 2) was located on the slab 6 in. away from the column, and a very high sensitivity accelerometer (Channel 3) was placed on the slab at 36 in. from the column. The sensors were installed in a plane that passes through the column centerline perpendicular to the column face.

Following application of lateral loads, specimen LR_{ST}G0.5 was extensively cracked. A large crack opened during the application of the gravity load at the slab-column interface (Figure 7.51), between accelerometers Channel 0 and Channel 1, and two small cracks 3.5 in. and 11 in. from the column opened at 0.5% drift between accelerometers Ch 1 and Ch 2, and Ch 2 and Ch 3, respectively (Figure 7.50). No sensors were placed in the East direction.

7.5.3.2 SWA measurements

SWA measurements were conducted following the same procedure described in Section 7.5.1.2.

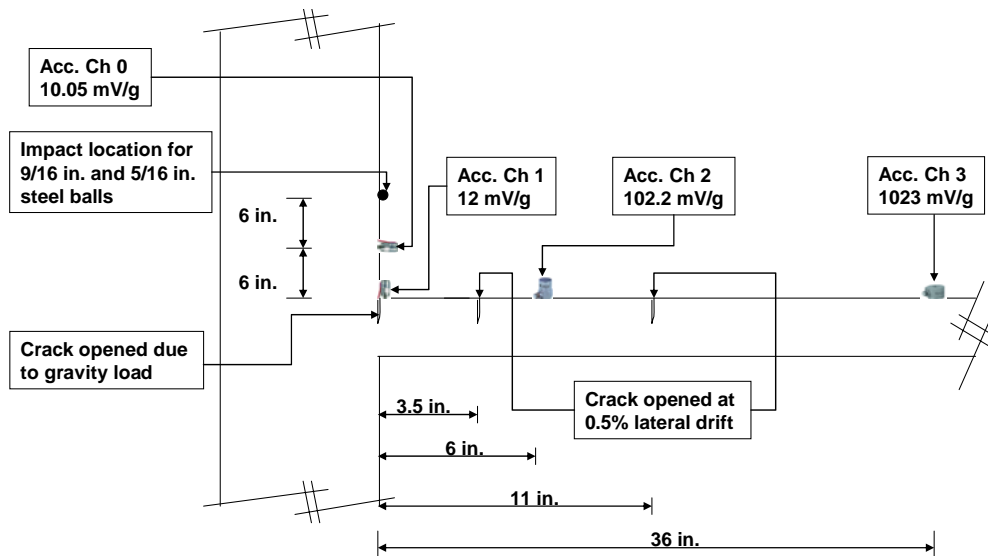


Figure 7.50 SWA tests on specimen $LR_{ST}G0.5$ along its North axis



Figure 7.51 Crack at slab-column interface in specimen $LR_{ST}G0.5$

7.5.3.3 Test Results

Results from tests conducted on the North axis with the 9/16 in. and 5/16 in. balls are presented in Figure 7.52 through Figure 7.57. On the North axis, SWA measurements were conducted when the specimen was at rest under the following conditions: uncracked with no gravity loads applied, when gravity loads but no lateral loads were applied (0% drift) and when lateral loads were applied (0.25%, 0.5, 0.75%, 1% and 1.25% drift).

From Figure 7.52 through Figure 7.57, the following observations are obtained:

1. Correlation between attenuation ratios and damage when a crack is formed at slab-column interface

Attenuation ratios for Ch0/Ch1, Ch0/Ch2 and Ch0/Ch3 shown in Figure 7.52 through Figure 7.54 increased when the drift level increased. The increase is mainly attributed to an increase in the depth of the critical crack located between Ch0 and Ch1. The correlation between attenuation ratio and drift level is linear, with moderate data scattering.

2. Constant attenuation where hairline cracks are formed

Attenuation ratios for Ch1/Ch2 and Ch1/Ch3 in Figure 7.55 and Figure 7.56 show significant data scattering and no increase in attenuation

ratios when lateral drift increases. That was expected because the cracks between sensors Ch1 and Ch2, and Ch2 and Ch3 were less than 0.015 in. width and attenuation due to diffraction at hairline cracks was not possible to detect.

3. Almost constant attenuation where narrow cracks are formed

The Ch2/Ch3 attenuation ratio is shown in Figure 7.57. The correlation between attenuation ratio and drift level is linear. The slope of this correlation is small because the crack located between Ch2 and Ch3 is narrow (0.015 in.) and probably did not grow much in depth.

4. Uncracked condition showed higher attenuation ratios than cracked conditions

For Ch1/Ch2 and Ch1/Ch3, the attenuation ratio for the uncracked condition is larger than for other conditions where the specimen is cracked. This inconsistency was also found for specimen LG0.5 and was discussed in Section 7.5.2.3.

5. No improvements with the 5/16 in. ball

No improvements in attenuation ratios were made by dropping a smaller ball (5/16 in.). The reason was discussed in Section 7.5.2.5.

7.5.3.4 Conclusions from tests of specimen LR_{ST}G0.5

The following conclusions were obtained from tests conducted on specimen LR_{ST}G0.5:

- i. The use of an accelerometer on the column (Ch 0) proved to be necessary because a major crack opened at the slab-column interface and attenuation due to diffraction at such a crack could only be measured by installing an accelerometer on the column.
- ii. The use of the 5/16 in. ball did not improve the quality of the SWA measurements. For optimum results, the ball should have a maximum frequency of useful energy f_{max} equal to the maximum usable frequency of the data acquisition system. That requirement is satisfied by ball 9/16 in.
- iii. Attenuation ratios for specimen LR_{ST}G0.5 exhibited similar data scattering and trends as those for specimens L0.5 and LG0.5. However, critical cracks (0.015 in. or more in width) opened at different positions. Specimen LR_{ST}G0.5 had a critical crack between Ch0 and Ch1, and specimens L0.5 and LG0.5 between Ch1 and Ch2.

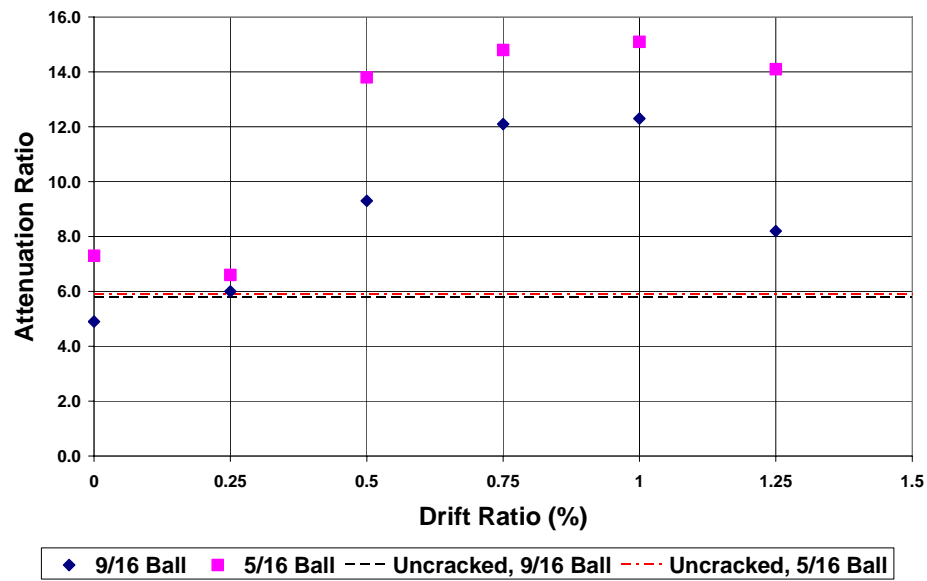


Figure 7.52 Ch0/Ch1 Attenuation Ratios, 9/16 and 5/16 in. balls (North Axis)

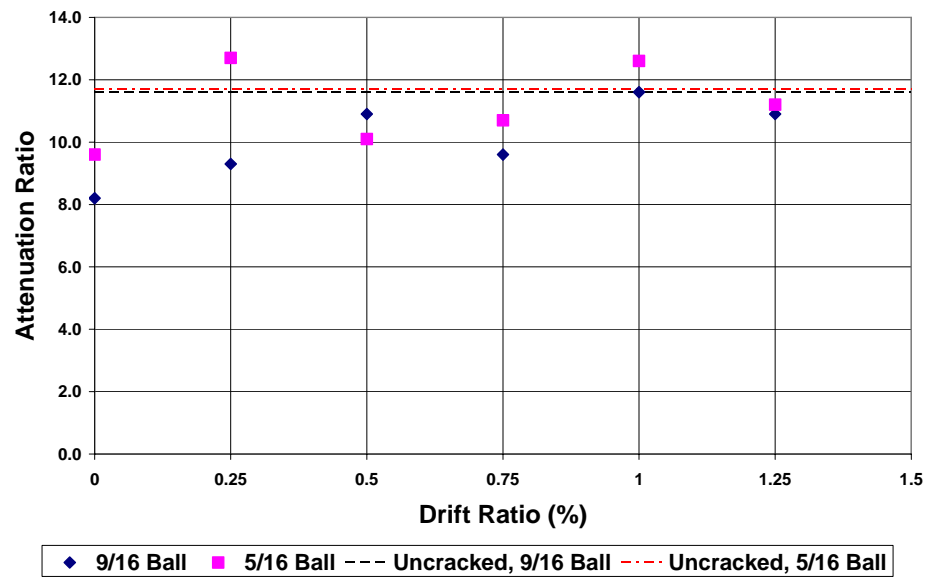


Figure 7.53 Ch0/Ch2 Attenuation Ratios, 9/16 and 5/16 in. balls (North Axis)

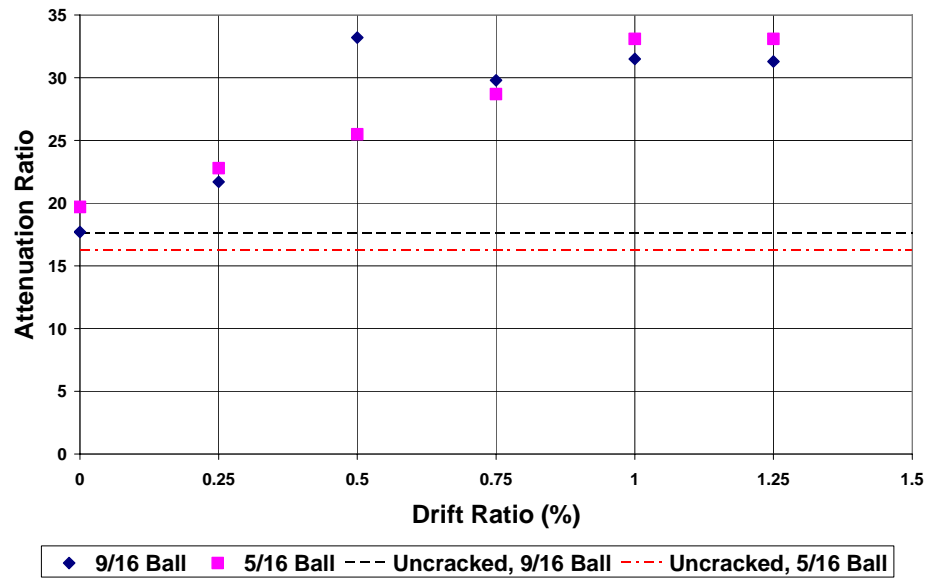


Figure 7.54 Ch0/Ch3 Attenuation Ratios, 9/16 and 5/16 in. balls (North Axis)

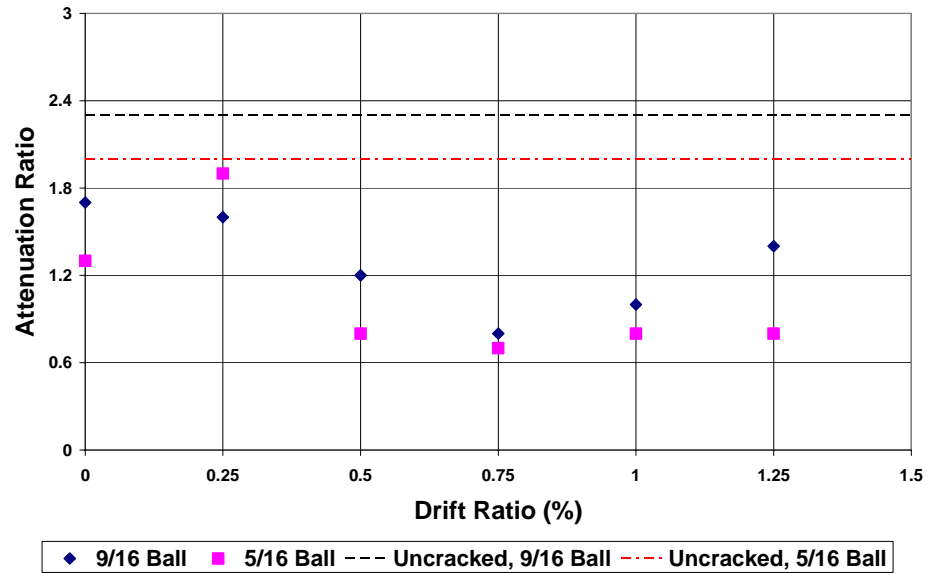


Figure 7.55 Ch1/Ch2 Attenuation Ratios, 9/16 and 5/16 in. balls (North Axis)

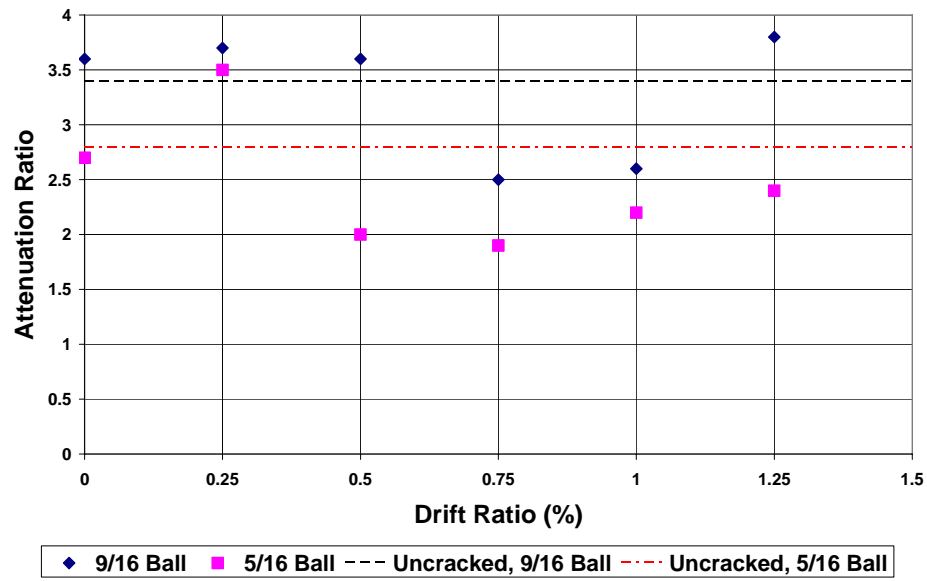


Figure 7.56 Ch1/Ch3 Attenuation Ratios, 9/16 and 5/16 in. balls (North Axis)

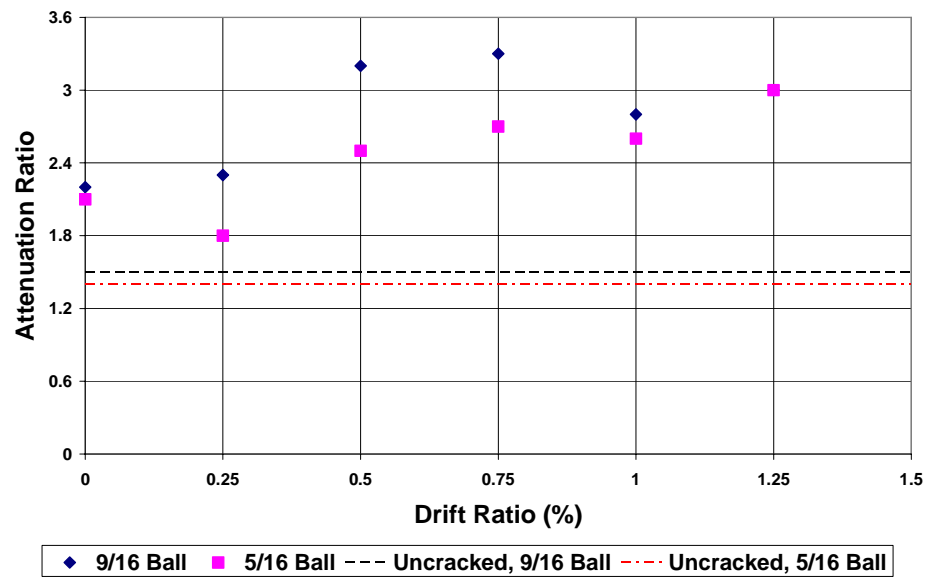


Figure 7.57 Ch2/Ch3 Attenuation Ratios, 9/16 and 5/16 in. balls (North Axis)

7.5.4 SWA Tests on Specimen LG1.0

7.5.4.1 Energy source and sensor locations

For specimen LG1.0 (Figure 7.58), the energy source was applied on the column, 12 in. from the slab, as it was for specimens L0.5, LG0.5 and LR_{ST}G0.5. For this test, a 9/16 in. steel ball was impacted against the column to produce seismic waves, following procedure described in Section 7.5.1.1. The 5/16 in. ball was not used because tests conducted on specimens LG0.5 and LR_{ST}G0.5 showed that no improvements were obtained with that ball.



Figure 7.58 Specimen LG1.0, after application of lateral loads, at 1.25% drift

Accelerometers were installed along the North axis only, as shown in Figure 7.59. A single axis was measured because tests conducted in specimen LG0.5 showed that the East axis provided similar results to that of the North axis. Four sensors were installed: one low sensitivity accelerometer (Channel 0) was installed 6 in. from the impact location, another low sensitivity accelerometer (Channel 1) was installed on the slab and adjacent to the slab-column interface, a high sensitivity accelerometer (Channel 2) was located on the slab 6 in. away from the column, and a very high sensitivity accelerometer (Channel 3) was placed on the slab at 36 in. from the column. The sensors were installed in a plane that passes through the column centerline perpendicular to the column face.

No cracks opened during the application of the gravity load. Following lateral loads, specimen LG1.0 was extensively cracked. At 0.25% drift, a critical crack opened at 4 in from the column (Figure 7.60), between sensors Channel 1 and Channel 2. At 0.75% drift, two cracks opened at 11 in. and 18.5 in. from the column, between Channel 2 and Channel 3.

7.5.4.2 SWA measurements

SWA measurements were conducted following the same procedure described in Section 7.5.1.2.

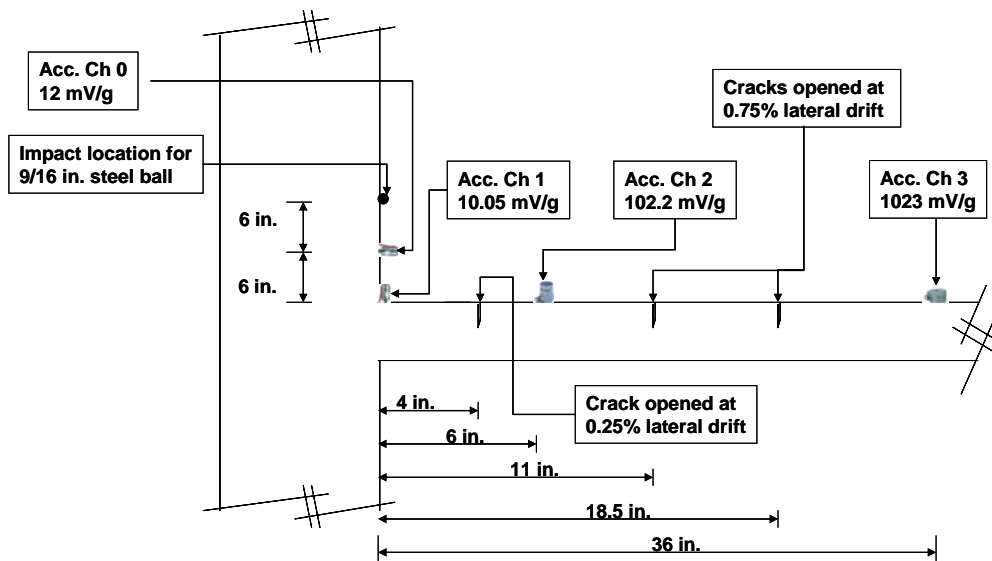


Figure 7.59 SWA tests on specimen LG1.0 along its North axis



Figure 7.60 Critical crack formed in specimen LG1.0 at 4 in. from column

7.5.4.3 Test Results

Results from tests conducted on the North axis with the 9/16 in. ball are presented in Figure 7.61 through Figure 7.66. On the North axis, SWA measurements were conducted when the specimen was at rest under the following conditions: when gravity loads but no lateral loads were applied (0% drift) and when lateral loads were applied (0.25%, 0.5, 0.75%, 1% and 1.25% drift).

From Figure 7.61 through Figure 7.66, the following observations are obtained:

1. No good correlation between attenuation ratios and damage for hairline crack between Ch1 and Ch2

The Ch0/Ch1, Ch0/Ch2 and Ch1/Ch2 attenuation ratios shown in Figure 7.61, Figure 7.62 and Figure 7.64 decreased when the drift level increased. That trend was not consistent with the theory of wave propagation, which suggests that attenuation should increase when cracks are opening due to an increase in lateral drifts. However, it should be noted that the crack between sensors Ch 1 and Ch 2 was narrow (<0.015 in.) and as was found in specimens LG0.5 and LR_{ST}G0.5, the sensors were not capable of measuring any diffraction across such hairline cracks.

2. Good correlation between attenuation ratios and damage for a crack between Ch2 and Ch3

From 0.75% to 1.25% drift, the Ch0/Ch3, Ch1/Ch3 and Ch2/Ch3 attenuation ratios shown in Figure 7.63, Figure 7.65 and Figure 7.66 increased when the drift level increased. The correlation between attenuation ratio and drift level is linear. The opening of cracks between sensors Channel 2 and Channel 3 are considered to be the source of the increase. The crack width at 1.25% drift was about 0.015 in., and opening that appears to be a transition width at which attenuation due to diffraction could or could not be detected.

7.5.4.4 Conclusions from tests of specimen LG1.0

The following conclusions were obtained from tests conducted on specimen LG1.0:

- i. Results are different from those obtained for specimens L0.5, LG0.5 and LR_{ST}G0.5. Attenuation ratios could not be measured at a crack (0.015 in. width at 1.25% drift) opened between Ch 1 and Ch 2. The use of ultrasonic waves with frequency above 20 kHz could improve the sensitivity of the SWA method allowing the detection of diffractive attenuation at cracks smaller than 0.015 in. in width.

- ii. It is not clear why attenuation was measured between Ch2 and Ch3 for cracks 0.015 in. width and not between Ch 1 and Ch2 where a crack of similar width was opened. It was probably because there were two cracks between Ch 2 and Ch3 and only one crack between Ch 1 and Ch2. All tests show that attenuation can be detected when cracks are greater than 0.015 in.

- iii. While specimens L0.5, LG0.5 and LR_{ST}G0.5 were reinforced 0.05% reinforcement ratio in its top reinforcement layer, specimen LG1.0 was reinforced with 1%. That resulted in a well distributed pattern of narrow cracks of less than 0.015 in. width. The data acquisition system was not capable of measuring attenuation ratios at a critical crack located between Ch1 and Ch2, and higher sensitivity is needed.

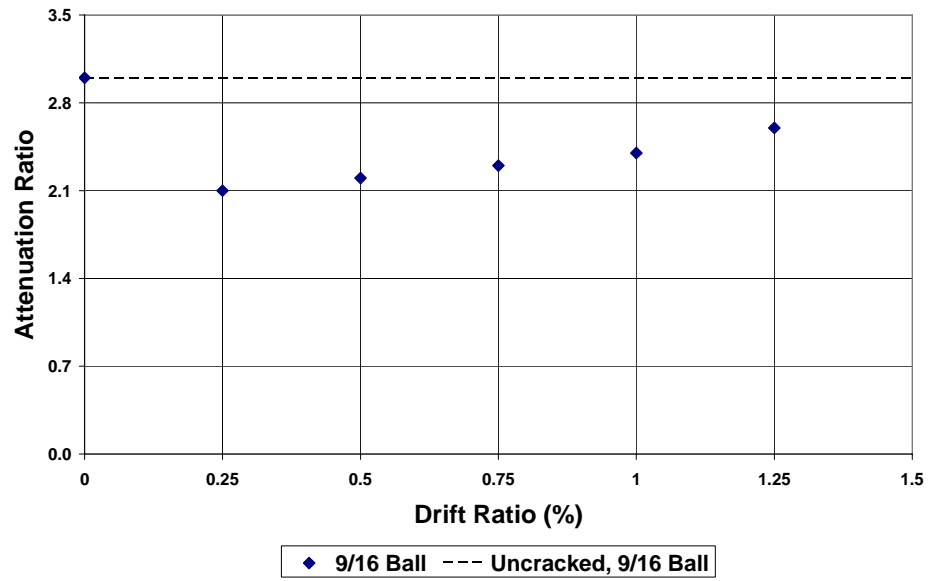


Figure 7.61 Ch0/Ch1 Attenuation Ratios, 9/16 in. ball (North Axis)

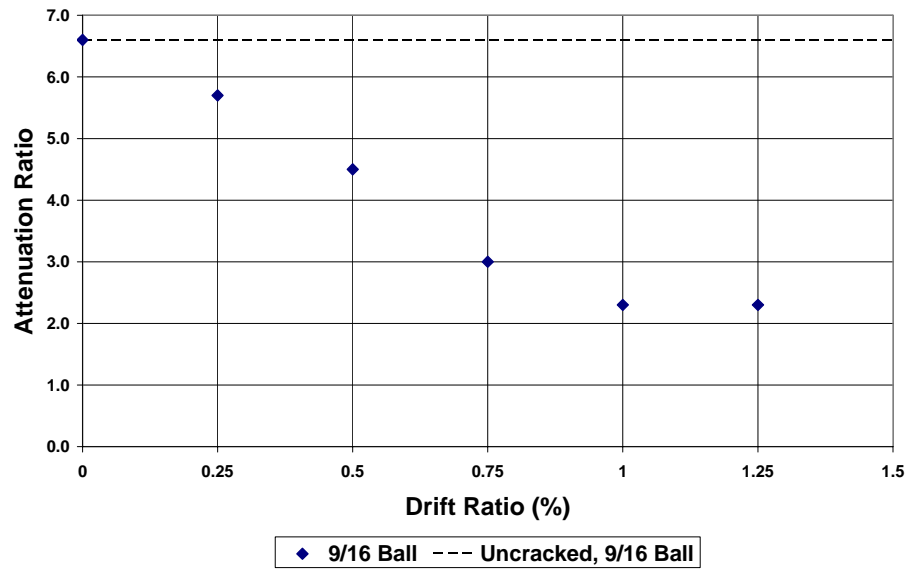


Figure 7.62 Ch0/Ch2 Attenuation Ratios, 9/16 in. ball (North Axis)

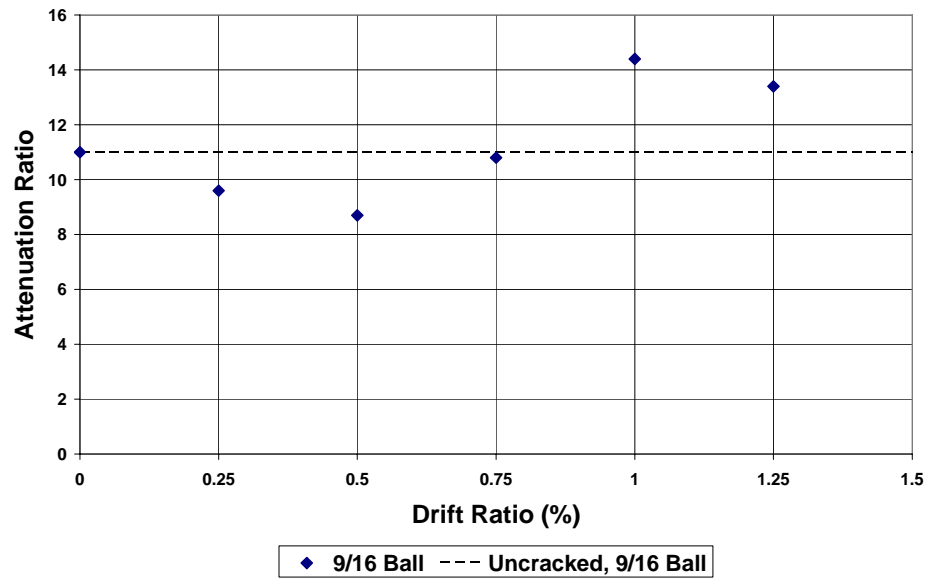


Figure 7.63 Ch0/Ch3 Attenuation Ratios, 9/16 in. ball (North Axis)

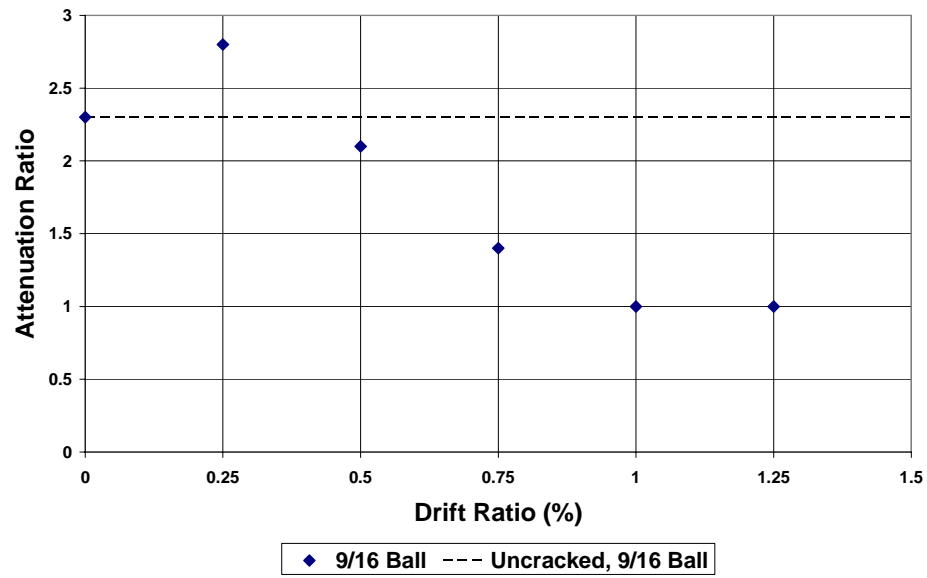


Figure 7.64 Ch1/Ch2 Attenuation Ratios, 9/16 in. ball (North Axis)

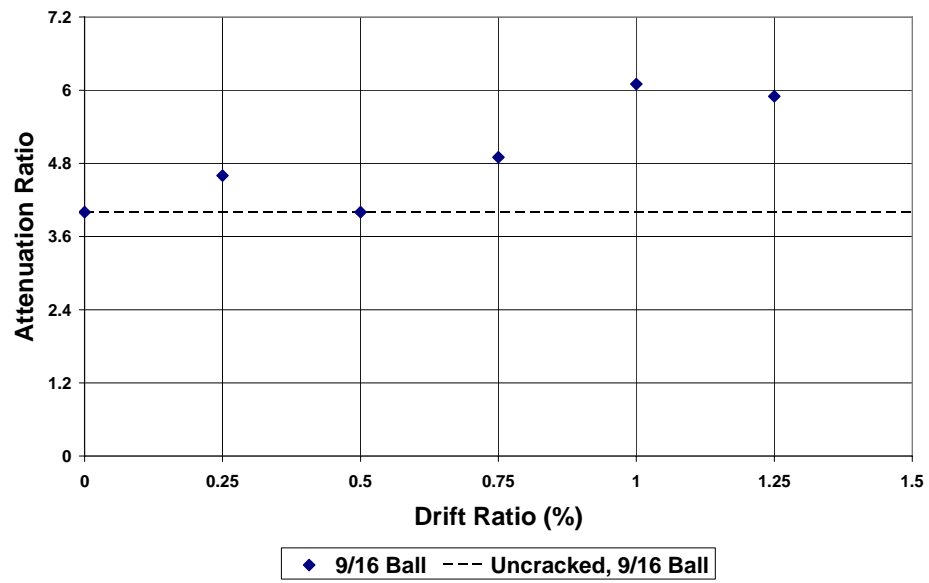


Figure 7.65 Ch1/Ch3 Attenuation Ratios, 9/16 in. ball (North Axis)

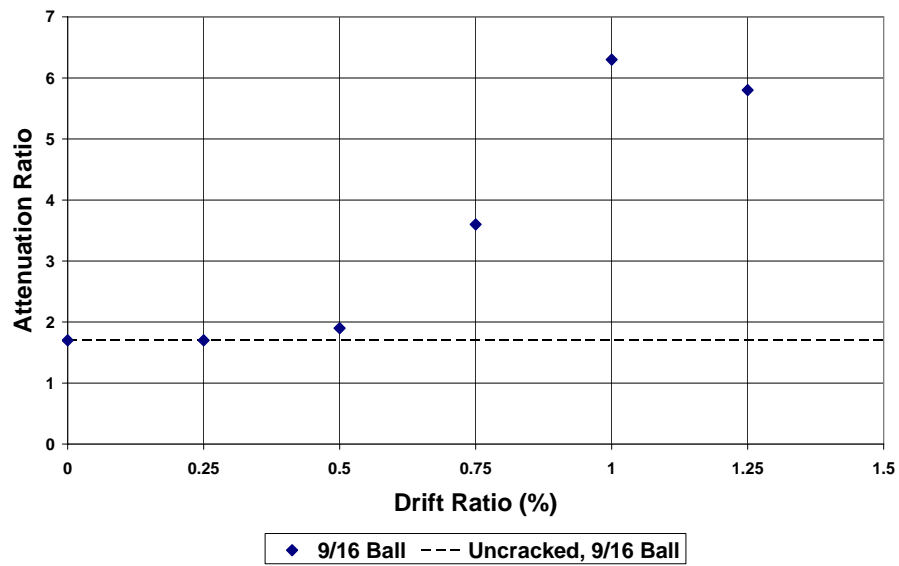


Figure 7.66 Ch2/Ch3 Attenuation Ratios, 9/16 in. ball (North Axis)

7.6 RELATIONSHIP BETWEEN ATTENUATION RATIOS AND DRIFT LEVELS

7.6.1 Analysis of linear correlations obtained for the 9/16-in. ball

Regression lines were developed using data collected on the North and East axes from all specimens, when the source of energy was a 9/16 in. ball. Results are presented in Figure 7.67 through Figure 7.72, from where the following observations are obtained:

- i. Using data from Ch0/Ch1 for specimen LR_{ST}G0.5 (Figure 7.67), the regression line $A = 4.4D + 6.1$ was computed. Specimen LR_{ST}G0.5 had a critical crack opened at the slab-column interface, which was wider than 0.015 in., while other specimens did not have a crack or had a crack less than 0.015 in. width.

When a crack wider than 0.15 in. is opened, the regression line has a positive slope that accounts for the increase in diffractive attenuation when the drift level and damage increases.

When the crack is not open or can not be detected because it is too narrow (< 0.015 in.), the attenuation is approximately constant and it is produced by the effects of geometry and dispersion.

- ii. Data from Ch1/Ch2 (Figure 7.70) and Ch2/Ch3 (Figure 7.72) showed similar features than data from Ch0/Ch1. The regression lines $A = 2.5D + 2.7$ (specimens L0.5 and LG0.5) and $A = 4.1D + 0.9$

(specimen LG1.0) correspond to Ch1/Ch2 and Ch2/Ch3 ratios and were obtained where a critical crack opened between sensors Ch1 and Ch2 (specimen L0.5 and LG0.5), and a non-critical crack opened between sensors Ch2 and Ch3 (specimen L1.0).

- iii. Data from Ch0/Ch2, Ch0/Ch3 and Ch1/Ch3 (Figure 7.68, Figure 7.69 and Figure 7.71) showed similar features as that from Ch0/Ch1, Ch1/Ch2 and Ch2/Ch3. However, the scattering of data for the first group was larger than for the second, because the sensors are located farer apart.

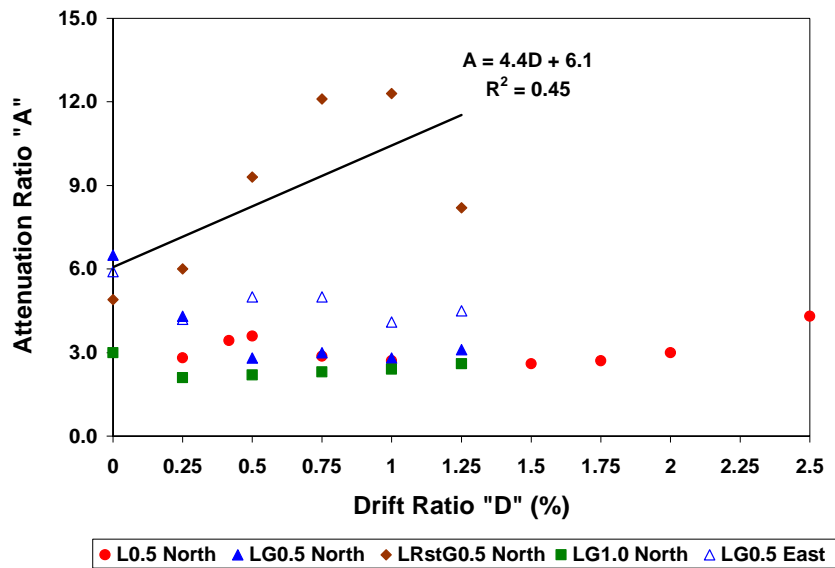


Figure 7.67 Regression lines for Ch0/Ch1 Attenuation Ratios

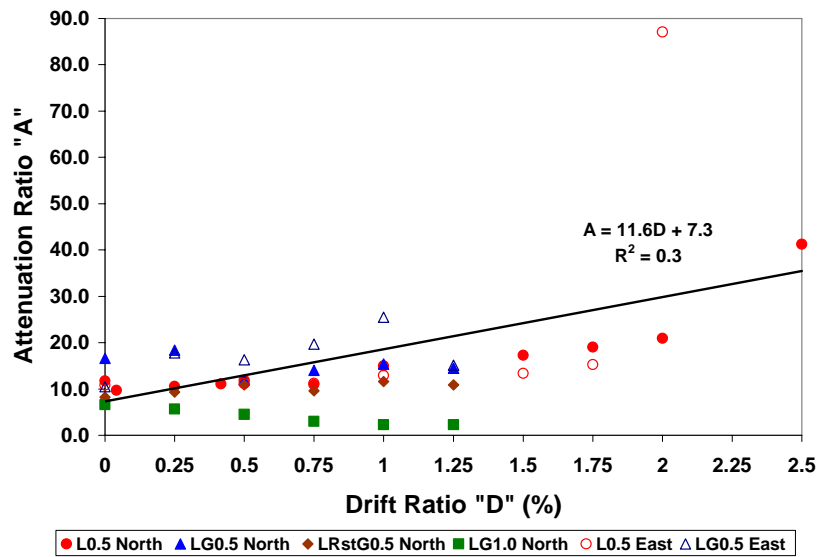


Figure 7.68 Regression lines for Ch0/Ch2 Attenuation Ratios

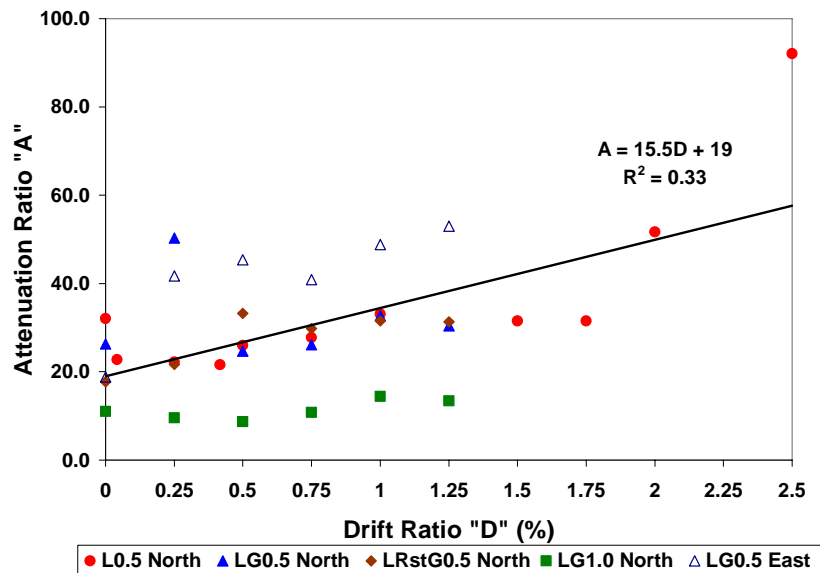


Figure 7.69 Regression lines for Ch0/Ch3 Attenuation Ratios

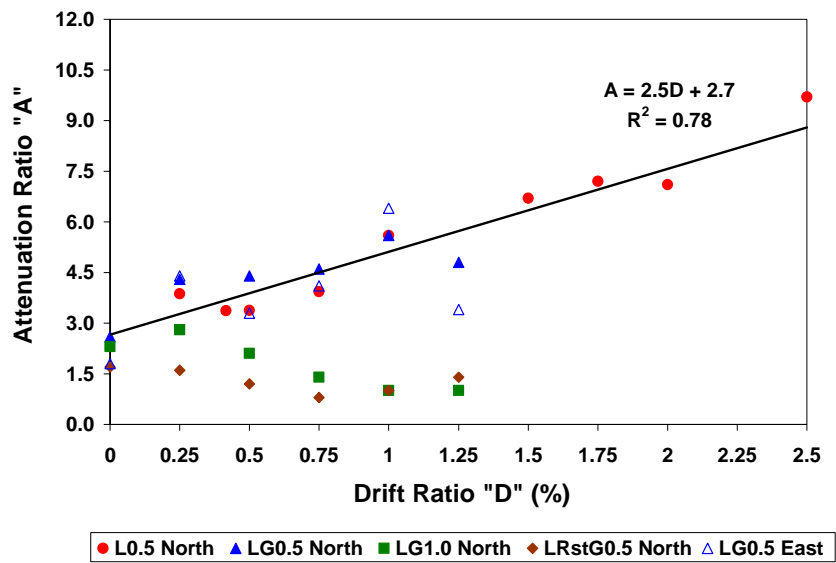


Figure 7.70 Regression lines for Ch1/Ch2 Attenuation Ratios

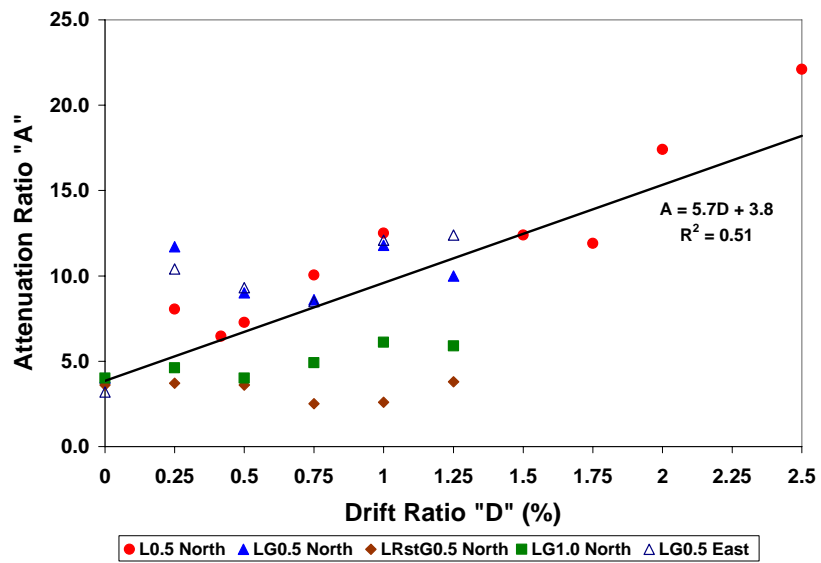


Figure 7.71 Regression lines for Ch1/Ch3 Attenuation Ratios

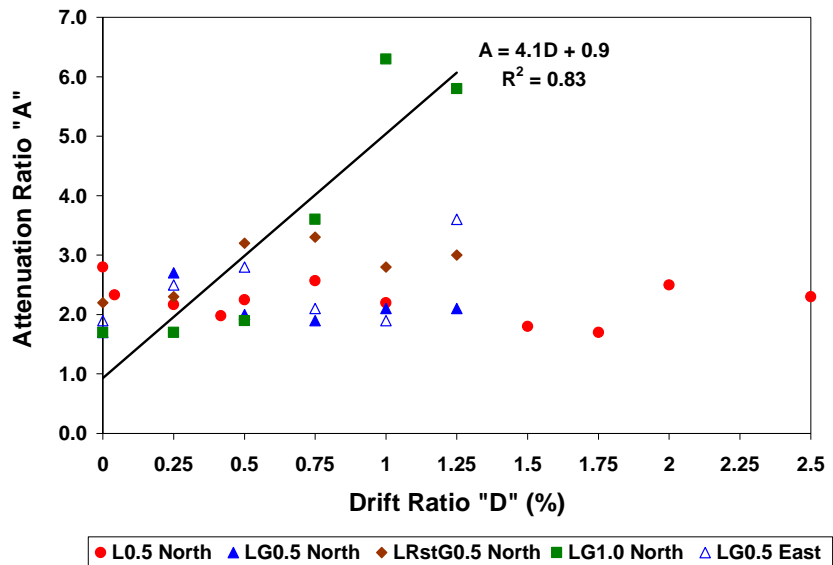


Figure 7.72 Regression lines for Ch2/Ch3 Attenuation Ratios

7.6.2 Data scattering

Data scattering was significant in all specimens. Scattering of data was evaluated considering standard deviations. The standard deviation ranged from 10% to 25% the magnitude of attenuation ratios, for data measured between sensors located 6 in. apart. When sensors were located further apart, the standard deviation of data was greater than 20% the magnitude of the attenuation ratios.

Figure 7.73 presents data from Specimen L0.5 (Ch1/Ch2) plotted with the range defined by attenuation ratios plus and minus one standard deviation. The regression line $A = 2.5D + 2.7$ computed in Section 7.6.1 for all specimens with a critical crack between Ch1 and Ch2 is also shown. In Figure 7.73, it can be noted

that the regression line falls within the range defined by attenuation ratios plus and minus one standard deviation. This situation is characteristic for all regression lines and data measured between sensors located 6 in. apart. Data scattering reduces the accuracy of regression lines, however they can be used to estimate story drift provided that the user understands that attenuation ratios might be affected by an error characterized by plus or minus one standard deviation.

The main sources of data scattering are considered to be:

- i. The use of a data acquisition system with a low sampling rate, which introduces inaccuracies in the detection of the true peak acceleration. When four sensors are used, the data acquisition system acquires 52,500 samples per second and waves with frequencies between 10 to 20 kHz are resolved with 2.5 to 5 data points. That sampling rate is enough for methods that are based on frequency-domain analysis, but it is insufficient for the SWA method that is based on a time-domain analysis. For adequate accuracy, at least 10 points per wave are recommended. That will demand a data acquisition system capable of acquiring data at a rate greater than 200,000 samples per second. If ultrasonic waves are used (>20 kHz) the sampling rate should be increased ever further (i.e. up to 600,000 samples per second to work with frequencies up to 60 kHz). Improvements to the current data acquisition system are explained in Appendix C.
- ii. The use of steel balls. Attenuation is a frequency dependent phenomenon and therefore the source of energy need to be frequency controlled for attenuation due to dispersion and geometry to be

constant between two points. Steel balls are a rudimentary source of frequency controlled energy. They produce energy of known frequency range, but the energy concentrated at different frequencies is variable because no two impacts are alike. Therefore, scattering in the values of “constant” attenuation due to geometry and dispersion is introduced when steel balls are used. As an alternative, a piezoelectric shaker could be used as a source of energy. A piezoelectric shaker can produce vibration energy of known amplitude and frequency.

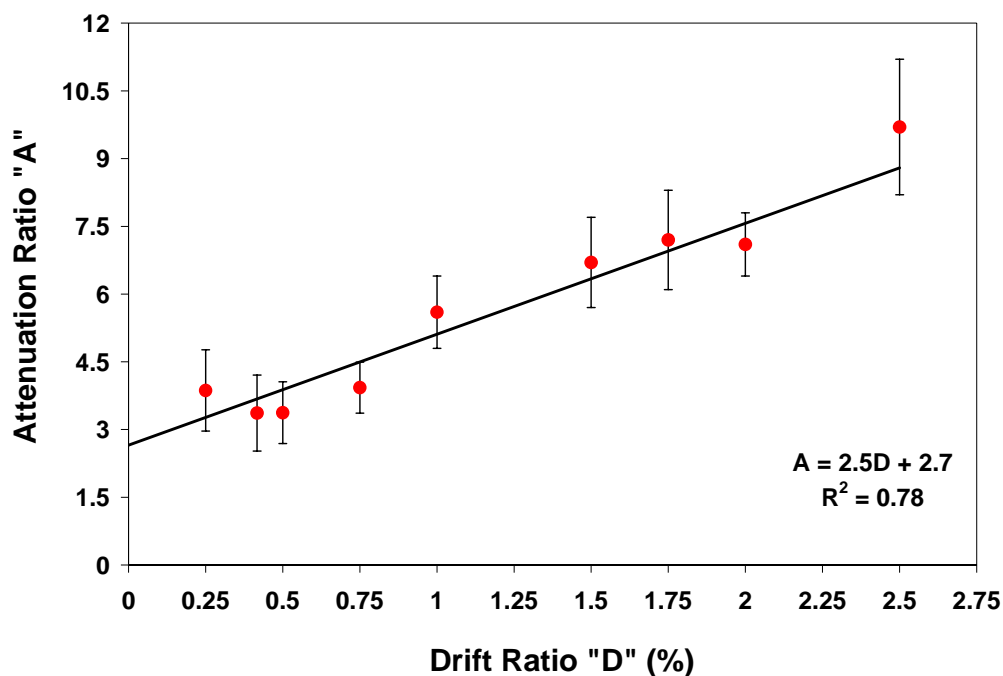


Figure 7.73 Standard Deviation of data for Ch1/Ch2 attenuation ratios in specimen L0.5

7.6.3 Relationships between Drift Levels and SWA measurements

Based on the analysis presented in Section 7.6.1, the equations contained in Table 7.1 were developed for Drift Levels (D) as a function of Attenuation Ratios (A):

Table 7.1 *SWA Equations for Drift Levels as a function of Attenuation Ratios*

Location of crack	Attenuation Ratio “A”	Drift Level “D” (%)	Equation
Ch0/Ch1	$A = 4.4D + 6.1$	$D = 0.2A - 1.4$	<i>Equation 7-4</i>
Ch1/Ch2	$A = 2.5D + 2.7$	$D = 0.4A - 1.1$	<i>Equation 7-5</i>
Ch2/Ch3	$A = 4.1D + 0.9$	$D = 0.2A - 0.2$	<i>Equation 7-6</i>

7.6.4 Use of Drift-SWA relationships

Equations 7-4, 7-5 and 7-6 (Drift-SWA relationships) were proposed in Section 7.6.2 to relate drift levels to attenuation ratios for the specimens tested. Such equations could be used for field assessment of damage in flat-plate buildings damaged by earthquakes; however their use would need to be based on the following conditions:

1. Source of Energy

A 9/16-in. steel ball was used in this study. Wave attenuation is a frequency dependent phenomenon, which means that the frequency content of the energy source matters.

2. Position of Impact

For the tests reported here, the position of impact was located on the axis of symmetry of the column at 12 in. above the slab. Four accelerometers with the layout described in Section 7.5.1.1 for the North axis were used. Attenuation due to geometry and dispersion increases with distance from the energy source therefore the impact location and position of sensors matter. The SWA equations were developed for a fixed impact position and sensor locations where attenuation due to geometry and dispersion was theoretically kept constant. Such conditions need to be reproduced in the field.

3. Location of sensors

Sensors should be placed at the locations described in Section 7.5.4.1 with the same distances between sensors used through out this study. Constant attenuation due to geometry and dispersion was found because the position of impact and sensors was kept the same. Attenuation due to geometry and dispersion will not be constant if sensors are installed at distances different than those used in this study.

4. Drift-SWA equations

In this study, equations were developed for cracks that opened at three different locations between sensors (channels). The position of a crack will determine the Drift-SWA equation that should be used.

CHAPTER 8

Guidelines for damage assessment of reinforced concrete flat-plate buildings

8.1 METHODOLOGY

Guidelines for damage assessment of reinforced concrete flat-plate buildings are provided in this chapter. Guidelines were developed using the following methodology:

- i. The lateral drift level experienced by the structure during an earthquake can be inferred from visual observations of crack density, assessment of crack depth measurement, identification of areas of concrete delamination, normalized slab vertical deflection measurements, and non-destructive measurements using the SWA method.
- ii. After the lateral drift level is estimated, the degree of lateral load damage experienced by the structure can be estimated using results of tests conducted in the laboratory on slab-column connections. Five specimens were subjected to lateral loading tests and four of them were studied in detail through visual observations and non-destructive techniques for damage assessment.

- iii. Finally, the gravity load carrying capacity of the structure can be evaluated based on the degree of lateral load damage experienced by the structure. The relationship between gravity load carrying capacity and degree of lateral load damage was studied in the laboratory, where four slab column connections were subjected to punching shear loading.

8.2 INFERENCE OF THE LATERAL DRIFT LEVEL EXPERIENCED BY THE STRUCTURE

8.2.1 Introduction

Four approaches are recommended to infer the Lateral Drift Level experienced by the structure:

- i. Visual observations of crack density using the procedure recommended in Chapter 4
- ii. Measurement of a critical crack depth and identification of areas of concrete delamination. This is a damage assessment technique explained in Chapter 6
- iii. The normalized vertical deflection of the slab, an approach developed based on results from lateral load tests presented in Chapter 3

- iv. Non-destructive testing using the SWA method, a damage assessment technique presented in Chapter 7

More than one approach or technique should be used to infer the level of lateral drift. Each technique has its own limitations and therefore, redundancy is recommended to achieve a reliable estimation of the lateral drift level experienced by the structure.

If the level of lateral drift estimated by different techniques is not the same, then engineering judgment must be used to decide which technique is providing the most reliable results.

Damage assessment through critical crack depth measurement and identification of areas of concrete delamination are considered to be more reliable than other techniques, because such technique can provide results with less data scattering than other techniques.

Equations 4-1, 7-4, 7-5 and 7-6 are based on experimental data that are scattered and limited in number. Therefore, the direct use of such equations to estimate lateral drift in a mathematical fashion is not recommended. Instead, those equations are tabulated and used in this chapter to estimate drift levels (0 - 0.5%, 0.5 - 1.0%, 1.0 - 1.5% and > 1.5%). Drift levels were selected to reflect changes in the degree of damage experienced by the structure.

8.2.2 Use of the Crack Density Parameter to estimate Drift Level

The detection of cracks in the field may be difficult. Floor finishes, dust, debris or any other material can make cracks undetectable. Therefore, the slab surface needs to be cleaned and be free of dust, debris, architectural finishes or any material that can hide cracks from visual inspection. Incomplete identification of cracks would result in an underestimation of the level of lateral drift.

The relationship between lateral drift and crack density was based on the assumption that crack patterns are not influenced by scales. For example, if the aggregate size used in the prototype changes with respect to that used in the test specimens, crack density could be affected by scaling from the models to the prototype.

The relationship between lateral drift and crack density was based on limited number of data from four specimens with 0.5% to 1.0% reinforcement ratio within the $(c+3h)$ region and was discussed in Sec 4.3.8. The relationships might not be applicable to specimens with more than 1% reinforcement ratio, because heavy reinforced slabs will tend to develop a larger number of cracks than lightly reinforced slabs. Table 8.1 was generated using the data from Section 4.3.8 and converting the information to a step function between drift and crack density.

Table 8.1 *Inference of the Lateral Drift Level based on the Crack Density parameter*

Lateral Drift (%)	Crack density (in/sqf)
0 – 0.5	< 9
0.5 – 1.0	9 – 11
1.0 – 1.5	11 – 13
> 1.5	> 13

8.2.3 Use of Areas of Concrete Delamination and Crack Depth and to estimate Drift Level

A relationship between lateral drift and the depth of a critical crack and areas of concrete delamination was developed in Section 6.8. A critical crack is defined as a crack that opens parallel to a column face, at a distance equal or less than 6 in. (slab depth). Using such relationship, Table 8.2 was created and can be used to estimate the lateral drift level experienced by a structure. In Table 8.2, crack depth is specified as a function of the slab depth h .

Table 8.2 Inference of Lateral Drift Level based on the Depth of a Critical Crack and the Identification of Areas of Concrete Delamination

Lateral Drift (%)	Crack Depth*	Delamination of Concrete Cover	
		Bottom	Top
0 – 0.5	$< 0.6h$	No	No
0.5 – 1.0	$0.6h - 0.8h$	No	No
1.0 – 1.5	$0.8h - h$	Yes	No
> 1.5	h	Yes	Yes

* h is the slab depth

8.2.3.1 Detecting areas of concrete delamination

Areas of concrete delamination should be identified, using the following criteria:

- i. First, areas prone to delamination should be identified. On the bottom of the slab, concrete delamination can occur inside the rectangle formed by the interception of lines parallel to the column faces drawn at a distance h from the column faces, where h is the slab thickness. On the top of the slab, delamination can occur within a fairly large area formed by the interception of lines parallel to the column faces

drawn at a distance of approximately 25% the span length from the column faces.

- ii. Second, delamination of concrete cover should be detected inside the perimeter of areas prone to delamination. Detection can be done by tapping with a hammer the surface of the slab. On the top surface of the slab, chain dragging could be used instead of hammering. The delaminated area is identified when a hollow sound is heard. A hollow sound denotes the existence of a horizontal crack that is reflecting sound waves back to the surface of the slab. Alternatively, concrete delamination can be detected by using the Impact Echo method, following the procedure described in Section 6.3.

8.2.3.2 *Obtaining crack depths in the field*

The depth of a critical crack can be determined by extracting concrete cores from the slab using the following procedure. As indicated below, coring should only be considered in cases where it will not affect the strength of the connection.

- i. The first step is to locate a critical crack located within a distance h from the column, where h is the slab depth. Ideally, this crack should have been opened predominantly under flexural-shear action; it should run parallel to the column face and be part of the potential punching shear failure surface of the slab-column connection

- ii. Extract a 2-in. concrete core at the position where an axis perpendicular to the column face intercepts the critical crack. The reinforcement layout should have been previously identified by using the as-built drawings or a magnetic resonance re-bar locator, to avoid contact with reinforcement bars when drilling.

- iii. It is likely that the critical crack is not vertical or does not project normal to the slab surface. Generally, such critical cracks form along an inclined plane that runs toward the column at an angle of approximately 60-degrees measured from the slab surface. If the crack is very deep, a second and even a third core might be required to completely obtain the trace of the crack.

Areas of concrete delamination shall be detected prior to extraction of concrete cores. Coring shall not be performed when delamination of the top concrete cover is detected, because it would be unsafe to extract cores from the critical punching shear perimeter at a condition in which the slab is severely damaged. When delamination of the top concrete cover is detected, it shall be assumed that the critical crack depth is equal to the full depth of the slab.

8.2.4 Use of the normalized vertical deflection of the slab to estimate Drift Level

Using the relationship between horizontal drift and vertical deflection of the slab presented in Figure 3.3, Table 8.3 was prepared. Two relationships are presented, for slabs with 1% and 0.5% top reinforcement ratio “ ρ ” in the $(c+3h)$ region within the column strip, where c is the column dimension and h is the slab depth. Linear interpolation could be used to infer the lateral drift level for slabs with reinforcement ratio between 0.5% and 1%.

Table 8.3 could be used to estimate the lateral drift level based on the normalized vertical deflection of the slab measured in the field, assuming that the normalized deflection measured in specimens tested in laboratory “ Δ_m ” (Figure 3.4) multiplied by a correction factor “ k ”, is equivalent to the normalized deflection “ Δ_p ” measured in the prototype building (Figure 8.1), as follows:

$$\Delta_p = k \cdot \Delta_m \qquad \text{Equation 8.1}$$

The correction factor k accounts for differences in the boundary conditions between the model and the prototype (single curvature versus double curvature deformed shapes) and the effects of long term deflections that can affect Δ_p . Field investigations are required to estimate k .

Table 8.3 *Inference of the Lateral Drift Level based on the Normalized Vertical Deflection of the slab*

Lateral Drift (%)	Normalized Vertical Deflection of the Slab (%)	
	$\rho = 1\%$	$\rho = 0.5\%$
0 – 0.5	< 1/500	< 1/ 300
0.5 – 1.0	1/500 – 1/300	1/300 – 1/250
1.0 – 1.5	1/300 – 1/250	1/250 – 1/200
> 1.5	> 1/250	> 1/200

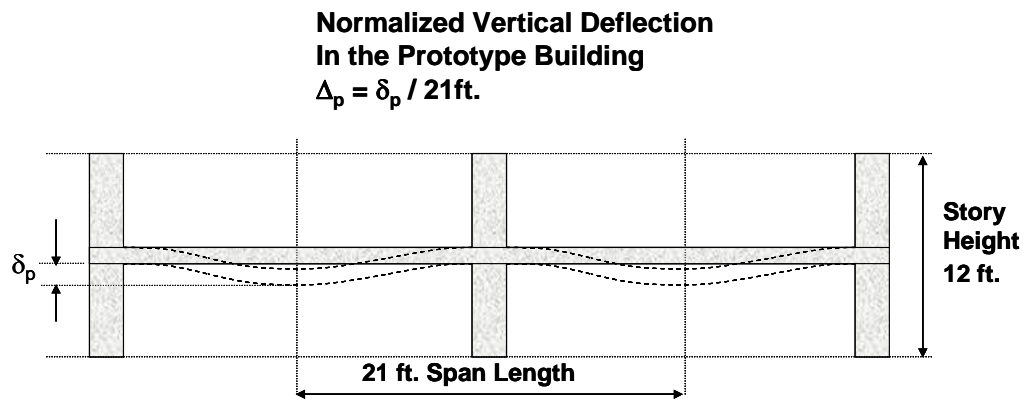


Figure 8.1 *Determination of the Normalized Vertical Deflection of the slab in the prototype building*

8.2.5 Use of the SWA technique to estimate Drift Level

The relationships between lateral drift and SWA measurements were developed in Section 7.9. Using such relationships, Table 8.4 was created and can be used to estimate the lateral drift level experienced by the structure.

8.2.5.1 Relationships and limitations

Care shall be taken when conducting SWA measurements, for the following reasons:

- i. The SWA method uses a different relationship depending on the position of the crack. If the crack is located at the slab-column interface, then the second column of Table 8.4 shall be used. If the crack is located on the slab at a distance of less than 6 in. from the column face, then the third column of Table 8.4 shall be used. Finally, if the crack is located on the slab at a distance from 6 in. to 36 in. from the face of the column, then the fourth column of Table 8.4 shall be used.
- ii. Cracks must be open and clean for SWA measurements to be meaningful. Cracks filled by dirt, water or debris will cause the crack to appear as closed, the SWA method will be unable to detect

attenuation due to diffraction and the lateral drift level would be underestimated.

- iii. SWA measurement were conducted on specimens built at 2/3 scale from the prototype building. Flat-plate buildings will have cracks somewhat larger than those of specimens tested in laboratory. Because of the scaling factor, SWA measurements could overestimate the drift level by detecting in the field higher attenuation ratios than those obtained in the laboratory. The difference between laboratory and field measurements is not expected to be significant, because large scale models were used. However, field investigations are required to calibrate the SWA equations obtained in the laboratory. Field calibration could be done by comparing drift level estimates using the SWA technique with estimates obtained using other methods (normalized vertical deflection of the slab, crack density and critical crack depth measurements and identification of areas of concrete delamination).

8.2.5.2 Procedure for use of the SWA method

- i. Install accelerometers and choose the source of energy according to the specifications described in Section 7.9.3
- ii. Identify and clean cracks. Cracks shall be more than 0.015 in. wide for SWA method to produce good results. Generally, only one crack 0.015

- in. wide or more is expected to be identified between sensors. However, if more than one is identified, then the lateral drift level can be estimated independently for each crack.
- iii. Conduct SWA measurements and compute attenuation ratios according to the procedure described in Section 7.2.
 - iv. Account for data scattering by calculating the range of attenuation ratios defined by the computed attenuation value plus and minus one standard deviation (the standard deviation can be assumed to be from 10% to 25% the magnitude of the computed attenuation ratio).
 - v. For a given crack position, find the suitable relationship from Table 8.4 to obtain the lateral drift level based on the range of attenuation ratios.
 - vi. If more than one crack is identified and the lateral drift levels obtained for different relationships are not the same, then engineering judgment shall be used to decide which crack is providing the most reliable results.

Table 8.4 *Inference of Lateral Drift Level from SWA measurements at a crack formed at three different locations*

Lateral Drift (%)	Attenuation Ratio		
	Slab-column interface	< 6 in. from the column	6 in. to 36 in. from the column
0 – 0.5	< 8	< 4	< 3
0.5 – 1.0	8 – 11	4 – 5	3 – 5
1.0 – 1.5	11 – 13	5 – 7	5 – 7
> 1.5	> 13	> 7	> 7

8.3 RELATIONSHIP BETWEEN DRIFT LEVEL AND DEGREE OF DAMAGE EXPERIENCED BY THE CONNECTION

Using results from lateral load tests conducted on slab-column connections (Chapter 3) and information obtained from strain gages, the relationship between drift level and the degree of damage experienced by the connection was found and is presented in Table 8.5.

Drift levels (0 - 0.5%, 0.5 - 1%, 1 - 1.5% and > 1.5%) were selected based on the identification of critical changes in strength and stiffness experienced by the specimens. The degrees of damage (slight, low, moderate and severe) were selected from the evaluation of the structural condition of the specimens based on visual observations and NDT methods.

8.4 RELATIONSHIP BETWEEN GRAVITY LOAD CARRYING CAPACITY AND DEGREE OF LATERAL LOAD DAMAGE

As explained in Section 3.3, two specimens were subjected to lateral load damage up to 1.25% drift, prior to conduct punching shear tests, and two were not subjected to lateral load damage and tested only in punching shear. Test results showed that there is no reduction in the gravity load carrying capacity of the slab-column connection when the specimens are subjected to a moderate degree of lateral load damage. Therefore, it can be concluded that the gravity load carrying capacity of a slab-column connection that had slight to moderate damage was not reduced from its original punching shear capacity.

Section 3.1 describes the failure of Specimen L0.5 under lateral loads, at 2% drift. The vertical load at failure was equal to dead plus 25% of live load. Based on this information, it is concluded that the gravity load carrying capacity of a slab-column connection that was severely damaged is less than the design capacity. This is an educated guess that is based on the assumption that the gravity load carrying capacity of the connection should decrease from the original design capacity found at 1.25% drift, to a smaller capacity equivalent to a loading condition of dead plus 25% of live load at 2% drift.

The relationship between gravity load carrying capacity and degree of lateral load damage is summarized in Table 8.6. It should be noted that the relationship was developed for specimens with 0.5% to 1% reinforcement ratio in the (c+3h) region. The relationship between gravity load carrying capacity and degree of lateral load damage might vary for specimens with a reinforcement ratio of more than 1% within the (c+3h) region.

Table 8.5 Relationship between Drift Level and Degree of Damage

Lateral Drift (%)	Damage Description	Degree of Damage
0 – 0.5	Almost linear elastic behavior Reinforcement had not yielded	Slight
0.5 – 1.0	Top reinforcement layer had yielded within $(c+3h)$ region in column strip	Low
1.0 – 1.5	Top and bottom reinforcement layers had yielded within $(c+3h)$ region in column strip. Specimen near to or at its maximum lateral load capacity	Moderate
> 1.5	Top and bottom reinforcement layers had yielded within $(c+3h)$ region in column strip. Specimen at a capacity smaller than its maximum with negative stiffness in its load-deformation relationship	Severe

Table 8.6 *Relationship between Gravity Load Carrying Capacity and Degree of Lateral Load Damage*

Degree of Lateral Load Damage	Gravity Load Carrying Capacity
Slight	Equal to the Design Capacity
Low	
Moderate	
Severe	Less than the Design Capacity

CHAPTER 9

Summary, Conclusions and Recommendations

9.1 SUMMARY

The aim of this dissertation was twofold: (1) to develop techniques to evaluate the degree of damage due to lateral load at a slab-column connection using visual observations and non-destructive methods; and (2) to study the relationship between the gravity load carrying capacity and the degree of lateral load damage in a slab-column connection

The overall objective of this dissertation was to develop a procedure to quantify the gravity load carrying capacity of the slab-column connection as a function of earthquake damage. Guidelines for field assessment of earthquake damaged structures were developed to achieve this objective.

The development of guidelines for field assessment of the structural condition of flat-plate buildings damaged by earthquakes was the main goal of this study. A procedure to estimate the lateral drift was developed. The relationships between story drift and degree of lateral load damage and between the degree of lateral load damage and the gravity load carrying capacity of slab-column connections were established using the results of tests on slab column connections. Four independent techniques to infer the level of lateral drift were included in the guidelines. Techniques are based on results from lateral loading

tests, visual observations and NDT tests conducted on slab-column connections in laboratory.

9.2 CONCLUSIONS

9.2.1 Behavior of slab-column connections

- 1. The degree of earthquake damage could be categorized into four levels and as a function of lateral drift experienced by the structure*

The degree of earthquake damage was a function of the lateral drift experienced by the test structures. The degree of damage could be divided into four categories depending on the lateral drift level: slight (0 – 0.5% drift), low (0.5 – 1.0% drift), moderate (1.0 – 1.5% drift) and severe (> 1.5% drift).

- 2. The gravity load carrying capacity of a slab-column connection is preserved when the test specimens were subjected to slight to moderate earthquake damage*

When damage was moderate, no reduction in the gravity load carrying capacity of the structure was observed. Lateral load damage is expected to reduce the gravity load carrying capacity of the connection.

3. *ACI 318-05 overestimates the gravity load carrying capacity of lightly reinforced slab-column connections*

Punching shear tests showed that the gravity load carrying capacity of lightly reinforced slab-column connections and that ACI 318-05 overestimates the gravity load carrying capacity of connections designed with 0.5% and 1% top reinforcement ratio in the $(c+3h)$ region within the column strip, by about 60% and 20% respectively.

9.2.2 Identification of Lateral Load Damage through Visual Observations

1. *Crack density provides a measure of story drift*

Results from experiments showed that crack density was a suitable parameter to assess damage and the story drift level. A relationship between crack density and the drift level experienced by the structure was developed. Such relationship is based on the assumption that crack pattern scales from specimens tested in laboratory to the prototype building. The relationship between crack density and story drift might not be applicable to slabs with more than 1% top reinforcement ratio within the $(c+3h)$ region.

2. *Crack width measurements were not directly related to story drift*

Results from experiments showed that crack widths could not be used to estimate story drifts. They were a function of the reinforcement ratio, loading history and stress redistribution within the specimen, factors that greatly influenced magnitude and rate of change of cracking.

3. *Delamination can be detected by tapping or chain dragging*

As an alternative to the use of the Impact-Echo method, areas of concrete delamination can be detected by tapping or chain dragging.

4. *The normalized vertical deflection of a slab damaged by lateral loading could be used to estimate the drift level*

The normalized vertical deflection of the slab is a function of the top reinforcement ratio in the $(c+3h)$ region and the lateral drift experienced by the structure. The normalized vertical deflection of the slab could be used to estimate story drifts in a slab-column connection, provided that field investigations become available to estimate a correction factor k , which relates the normalized deflections measured in the laboratory to normalized deflections measured in buildings damaged by earthquakes.

9.2.3 Lateral Load Damage Assessment through NDT methods

- 1. The Impact Echo Method is recommended for detecting areas of concrete delamination but did not give consistent measurements of crack depth*

The Impact Echo Method was successfully used to identify areas of concrete delamination, but satisfactory results were not obtained when the method was used to determine crack depths when the structure was at rest. A technique to estimate drift levels based on a critical crack depth and areas of concrete delamination was developed. Using such technique, crack depths could be determined using concrete cores extracted from the slab, but this approach may not be acceptable to building owners.

- 2. The Seismic Wave Attenuation method (SWA) is recommended to infer drift level provided that standardization is developed for field use*

Prior to this dissertation, there was no NDT method available to estimate the level of drift based on direct NDT measurements. The SWA method was developed for such purpose. This method showed promising results, however the following issues need to be addressed for field application:

- i. Cracks in the field could be partially or totally filled with dirt and debris. Measurements could underestimate the level of damage. Care must be taken when using the SWA method. Cracks must be

open and free of dirt and debris. Cracks need to be more than 0.015 in. width for diffractive attenuation to be measured

- ii. Conditions observed in the field are difficult to replicate in the laboratory. A 2/3-scale model was tested in laboratory. It is possible that SWA measurements conducted across a full-scale field crack can overestimate the level of damage. Results from the SWA method used in the field, need to be compared and calibrated with results obtained from other techniques
- iii. Data scattering is significant. Extensive sampling is required to evaluate trends in the data. To account for data scattering it is recommended to estimate drift level based on the measured attenuation ratio plus and minus one standard deviation, which typically varies from 10% to 25% the amplitude of the attenuation ratio.

9.2.4 Guidelines for Field Assessment

- 1. Guidelines for field assessment provide several approaches for estimating drift levels experienced by the structure*

The conventional approach to estimate story drift is based on visual observations of cracks in masonry infill walls and damage experienced by non-structural components and correlates such observations with

previously established drift levels at which such non-structural components could crack or fail. The approaches presented in this dissertation were based on the behavior of slab column connections tested in the laboratory and are based on four independent techniques to estimate story drift levels: crack density, crack depth measurement and identification of areas of concrete delamination, normalized vertical deflection of the slab and non-destructive measurements using the SWA method.

2. *The guidelines lead to a determination of the condition so that an assessment can be made as to whether occupancy can be permitted after an earthquake or if repair and retrofitting will be needed*

A critical decision that must be made following an earthquake is whether occupancy can be permitted or if the building must be vacated. Such decisions will have major financial implications for the owner and the occupants. The guidelines developed in this study provide an approach for making such decisions.

9.3 RECOMMENDATIONS FOR FUTURE RESEARCH

Based on results obtained from this dissertation, the following recommendations for future research are proposed:

- a. To conduct punching shear tests of specimens previously laterally loaded up to 1.5% and 1.75% drift, to investigate an expected reduction in gravity load carrying capacity of the slab-column connection
- b. To perform lateral load tests up to failure on specimens with 1% and 1.5% top reinforcement ratio in the $(c+3h)$ region within the column strip, to observe if specimens with larger reinforcement ratios can develop ductility and fail after 2% drift and to verify that the categorization of the degree of damage recommended in this dissertation is independent of the amount of reinforcement ratio in the $(c+3h)$ region
- c. To conduct field SWA measurements to calibrate the method and compare drift levels with assessments obtained from other methods such as the normalized vertical deflection of the slab, crack depth and areas of delamination and crack density techniques
- d. Improvements in the data acquisition systems for SWA measurements will lead to improved relationships between SWA measurements and story drifts using seismic waves with frequencies over 20 kHz and wavelengths smaller than $2/3$ the slab depth.

APPENDIX A

Impulse Response Test on a Slab

A.1 INTRODUCTION

A.1.1 Objective of the Test

A concrete slab was built and tested using the Impulse Response technique. The objective of the test was to evaluate the applicability of the Impulse Response technique for damage assessment at slab column connections.

As discussed to in Section 5.3.2.2, a mean mobility value over the 100 – 800 Hz range is directly related to the density of the material. A reduction in density corresponds to an increase in mean mobility. Less density corresponds to more flexibility, and therefore it could be hypothesized that an increase in mean mobility would correspond to an increase in flexibility.

Structural damage is characterized by the extent of cracking or by the loss of stiffness and strength. When a concrete element is loaded, its flexibility increases due to cracking. The more the element cracks, the more flexible it becomes, and structural damage can be characterized by the increase in flexibility.

The goal of the Slab Impulse Response (SIR) test was to find a relationship between mean mobility and structural damage due to changes in the flexibility of the element.

A.1.2 Specimen

An 8 x 48 x 108 in. slab shown in Figure A.1 was built to investigate the correlation between structural damage and SIR measurements.



Figure A.1 Reinforced concrete slab for SIR test

The slab was reinforced in the longitudinal direction with the top and bottom reinforcement ratios of $\rho = 0.0068$ and $\rho = 0.0048$ respectively. Temperature reinforcement was provided in the transverse direction. Details are shown in Figure A.2.

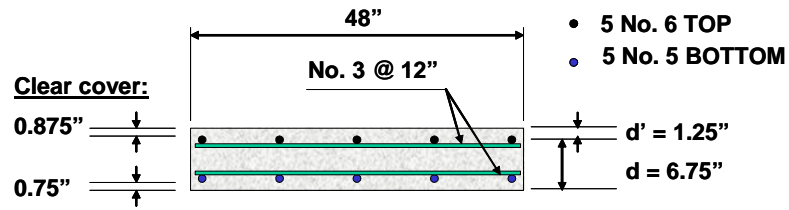


Figure A.2 Reinforcement details for the slab

A.1.3 Slab-Impulse-Response System

A.1.3.1 Data Collection

The top of the slab was impacted with an impulse hammer that has a built-in load cell and the response of the slab was monitored by a geophone placed next to the impact point. The hammer input and the receiver output were recorded by a data acquisition system (Figure A.3).

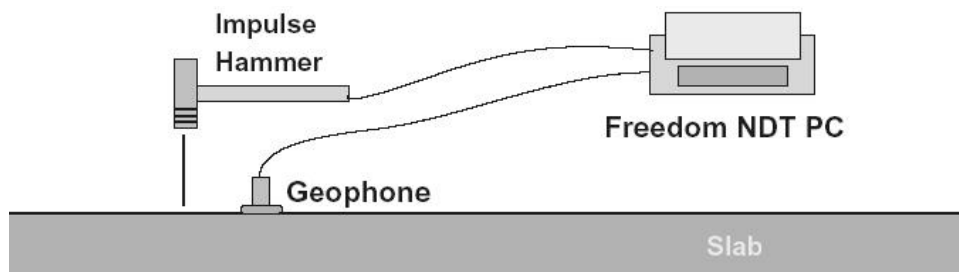


Figure A.3 Slab-Impulse-Response Data Collection (Olson, 2004)

A.1.3.2 Equipment and Technical Assistance

Testing equipment and technical assistance were provided by Olson Instruments. The data acquisition system is shown in Figure A.4. It is a Freedom Data PC equipped with the Slab Impulse Response System (SIR-1).



Figure A.4 Olson Instruments Freedom Data PC

A.2 TEST SET-UP

A.2.1 Loading and Support conditions

A.2.1.1 Simply supported beam with mid point load

First the slab was loaded as a simply supported beam subjected to a mid-point loading. The load was applied by a hydraulic jack located at mid span.

The end supports, which consist of two steel beams over steel plates, were anchored to the reaction floor by tie rods (Figure A.5). For this loading and support conditions, cracks developed on the top of the slab.

Impulse response measurements were conducted at loading steps equal to 15%, 50% and 100% of the yield load P_y .

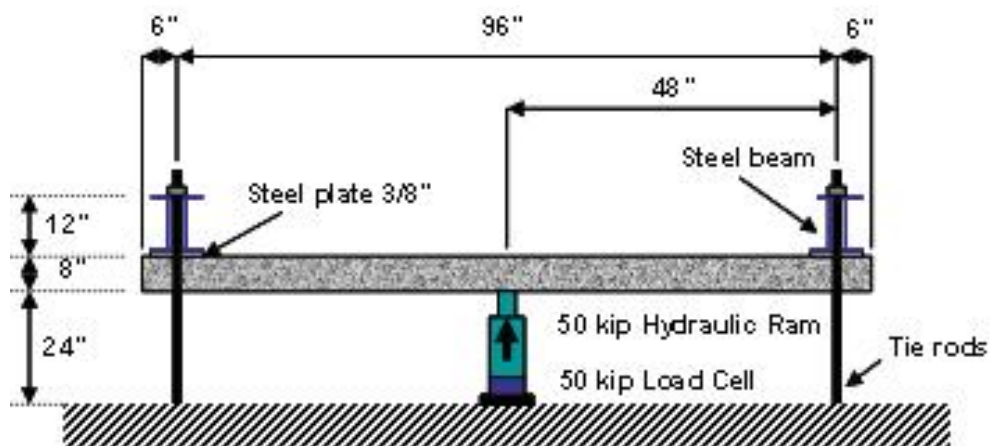


Figure A.5 Simply supported beam loading condition

A.2.1.2 Load applied at end

After the slab was loaded as a simply supported beam and was extensively cracked on its top surface, the loading and support conditions were changed to produce cracking on the bottom surface. The load was applied by a hydraulic jack located at one end of the slab and at the other end a concrete block was placed to

support the slab. At the mid span, one steel beam was anchored to the reaction floor by tie rods (Figure A.6).

Impulse response measurements were conducted at loading steps equal to 10%, 50% and 100% of the yield load P_y .

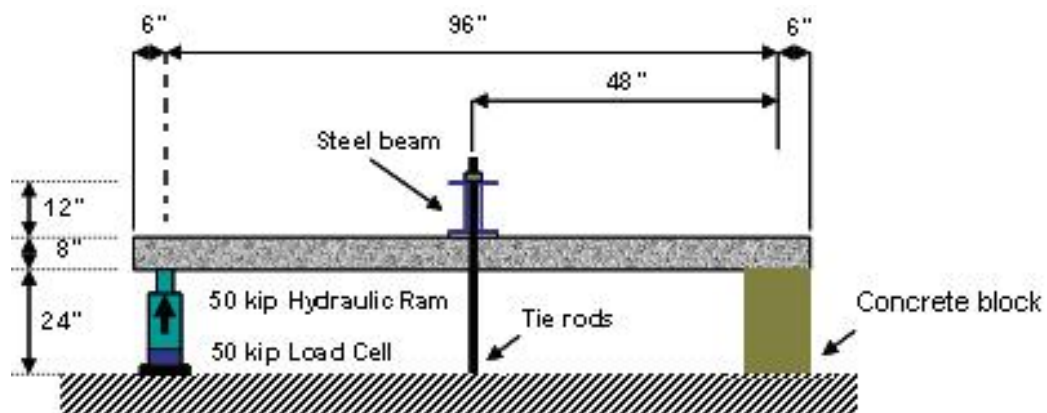


Figure A.6 End loading condition

A.2.1.3 Simply supported beam at rest (without load applied)

Impulse response measurements were conducted when the slab was sound (uncracked), fully cracked on its top surface and fully cracked on its top and bottom surface. Such measurements were conducted at rest (without load applied) with the slab supported by concrete blocks located at both ends, as shown in Figure A.7.

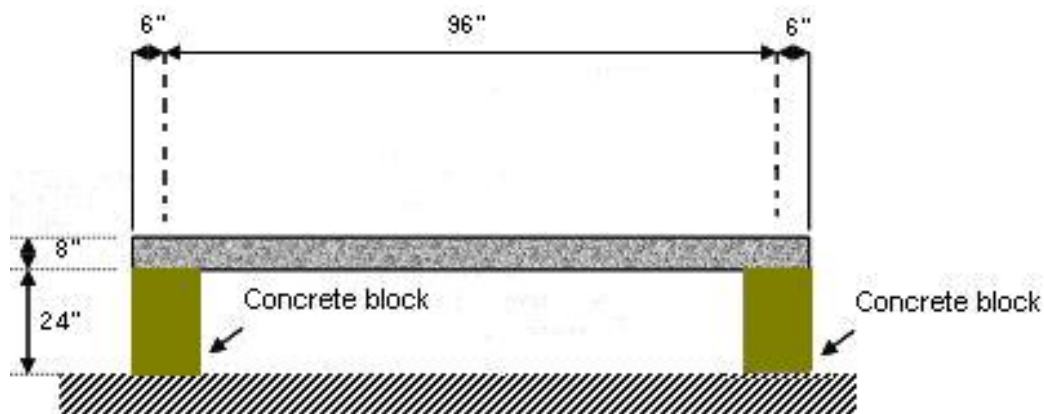


Figure A.7 Support condition for Impulse Response tests conducted at rest

A.2.2 Data points

A grid was drawn on the surface of the slab defining 63 data points where impulse response measurements were carried out. The grid is shown in Figure A.8.

A.3 TEST RESULTS

A.3.1 Average Mobility

An example of a Mobility plot for point E5 is presented in Figure A.9. The plot was obtained for the support condition described in Section A.2.1.1 and a midpoint load equal to P_y . The Average Mobility was calculated for the interval of frequencies from 100 Hz to 500 Hz. The resulting Average Mobility (1.8) was plotted in Figure A.13.

A.3.2 Tests sequence and results

The impulse response test was conducted in nine stages defined by different loading and support conditions. The stages were conducted in the sequence described below. For each stage the Average Mobility was computed and plotted at every point on the grid. A large average mobility value denotes a large flexibility of the slab at that point.

A.3.2.1 Stage 1: Sound slab at rest

Prior to the application of any load, the uncracked slab was evaluated. The slab was simply supported and resting on concrete blocks as described in Section A.2.1.3. Results are shown in Figure A.10.

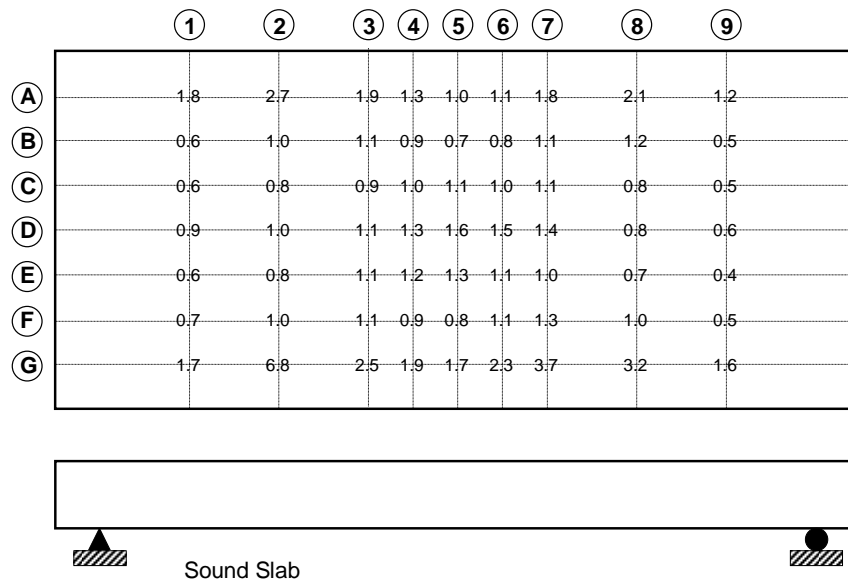


Figure A.10 Average Mobility results for a sound slab at rest, Stage 1

A.3.2.2 Stage 2: First crack on top of the slab (load $0.15P_y$)

A load equal to 15% of the yielding load ($0.15P_y$) was applied to the slab and impulse response measurements were conducted. At $0.15P_y$, the first crack appeared on top of the slab. The slab was simply supported, as described in Section A.2.1.1. Results are presented in Figure A.11.

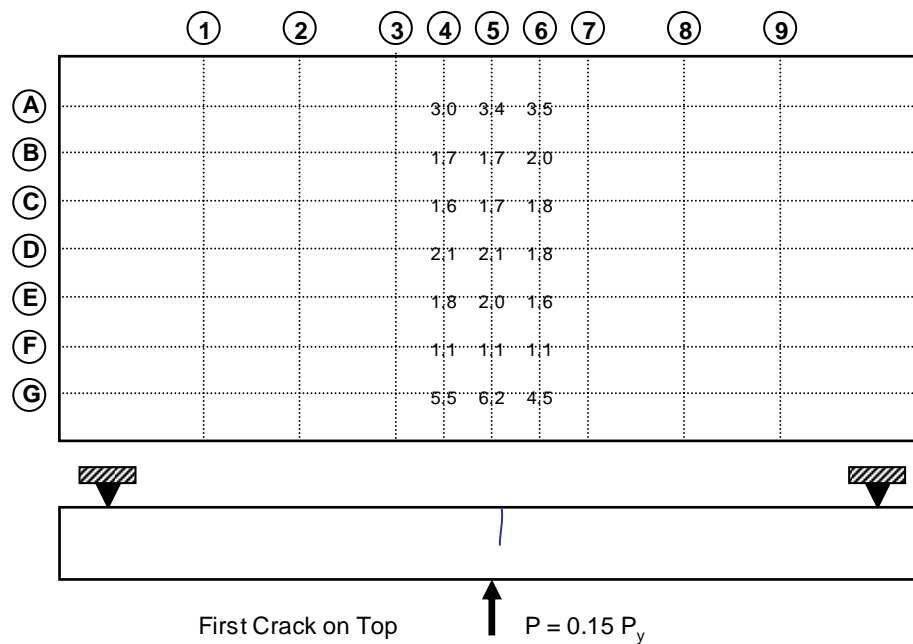


Figure A.11 Average Mobility results for a slab with first crack on top (load $0.15P_y$), Stage 2

A.3.2.3 Stage 3: Slab cracked on top (load $0.5P_y$)

The midpoint load was increased to $0.5P_y$ at which condition additional cracks appeared on top of the slab and impulse response measurements were carried out. The slab was simply supported as described in Section A.2.1.1. Results are presented in Figure A.12.

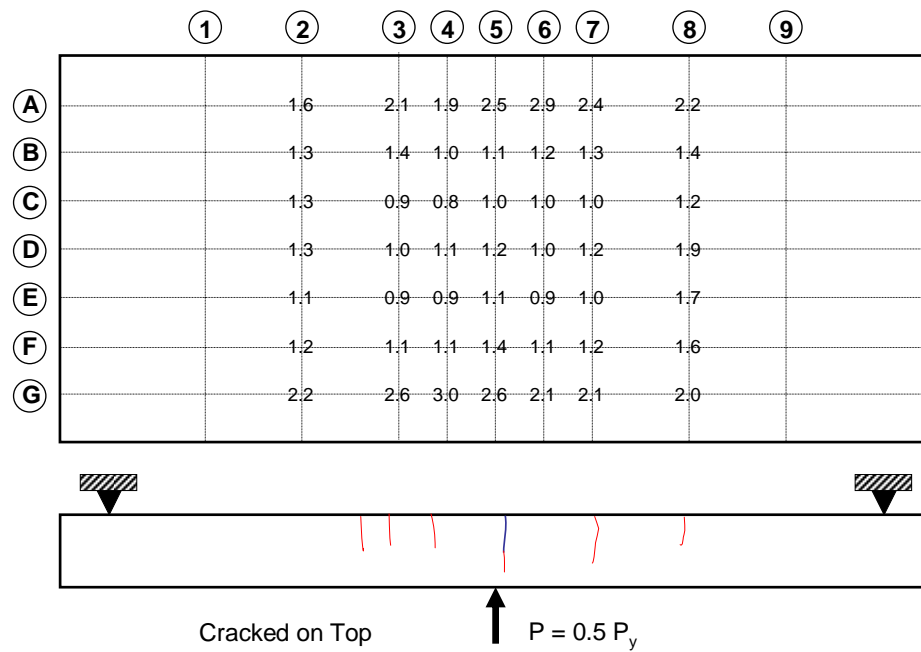


Figure A.12 Average Mobility results for a slab cracked on top (load $0.5P_y$), Stage 3

A.3.2.4 Stage 4: Slab fully cracked on top (load P_y)

The midpoint load was increased to P_y at which condition the top of the slab became fully cracked and impulse response measurements were conducted. The slab was simply supported as described in Section A.2.1.1. Results are presented in Figure A.13.

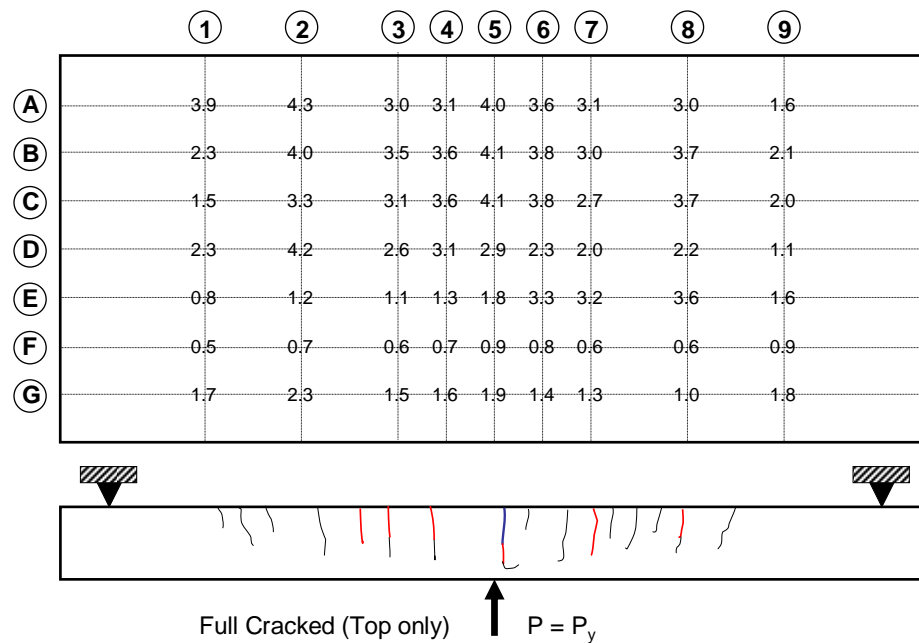


Figure A.13 Average Mobility results for a slab fully cracked on top (load P_y),
Stage 4

A.3.2.5 Stage 5: Slab fully cracked on top and at rest

The slab was unloaded and left simply supported resting on concrete blocks as described in Section A.2.1.3. As a result of previous tests, the slab was fully cracked on top. Impulse response measurements were carried out and the results are shown in Figure A.14.

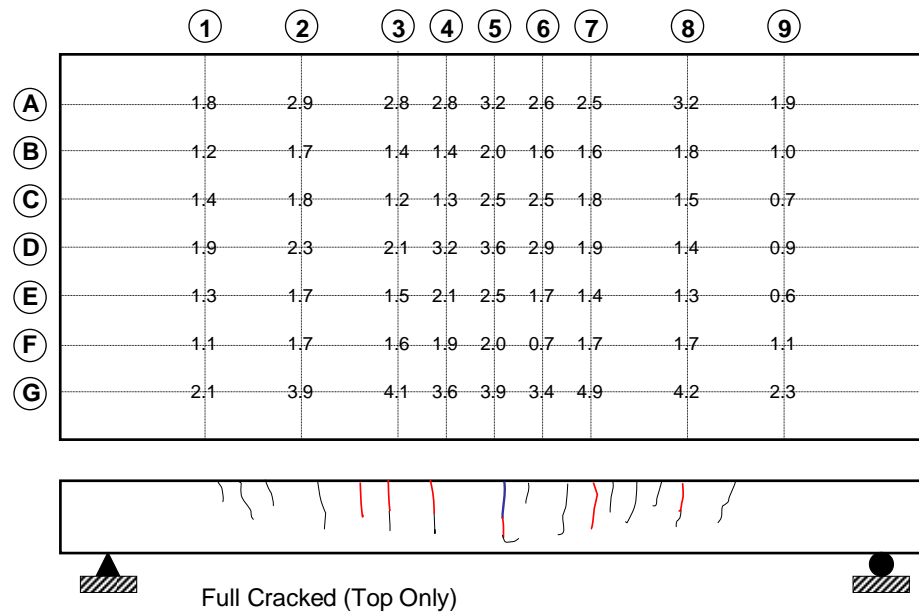


Figure A.14 Average Mobility results for a slab at rest fully cracked on top, Stage 5

A.3.2.6 Stage 6: Slab uncracked on bottom and fully cracked on top (load $0.1P_y$)

The support conditions were changed and the slab was cantilevered as described in Section A.2.1.2. Then, a load equal to 10% of the yielding load ($0.1P_y$) was applied to the slab. At $0.1P_y$, the bottom of the slab remained uncracked, while the top of the slab was fully cracked due to previous loading steps. Impulse response measurements were performed and the results are presented in Figure A.15.

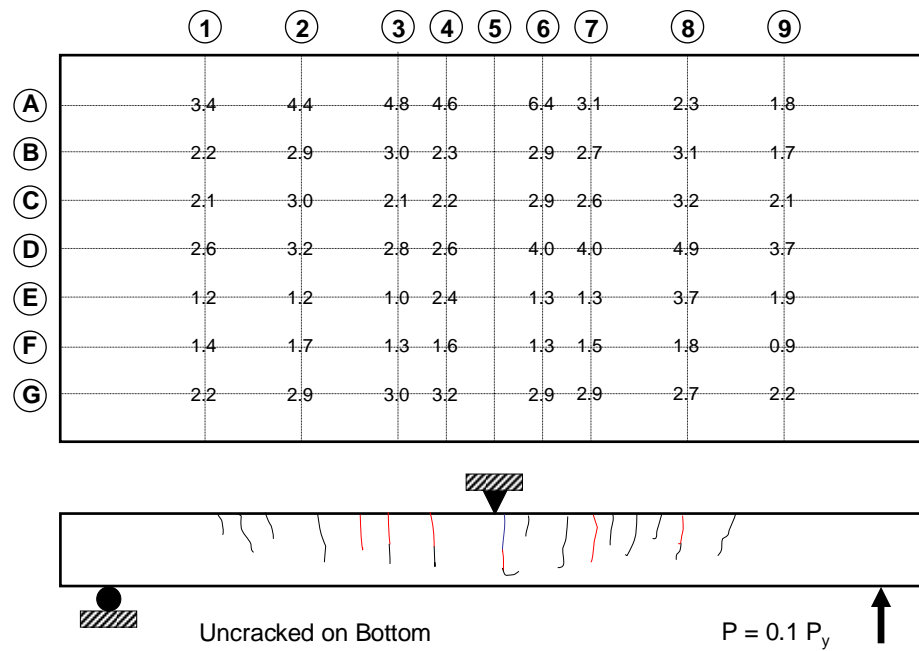


Figure A.15 Average Mobility results for a slab uncracked on bottom and fully cracked on top (load $0.1P_y$), Stage 6

A.3.2.7 Stage 7: Slab cracked on bottom and fully cracked on top (load $0.5P_y$)

The load on the cantilever was increased to $0.5P_y$ at which condition additional cracks appeared on the bottom of the slab and impulse response measurements were carried out. The slab was supported as described in Section A.2.1.1. Results are presented in Figure A.16.

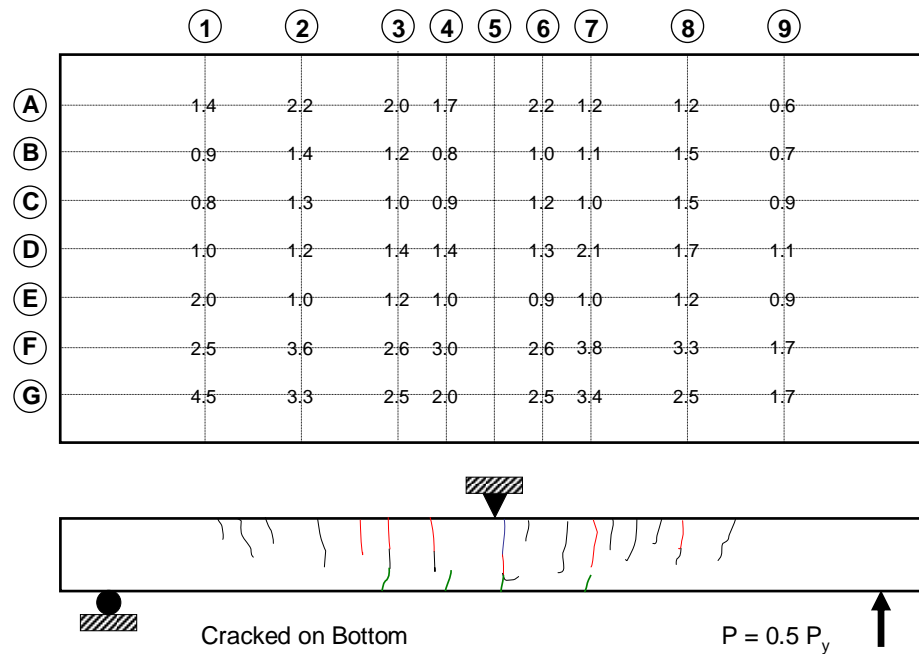


Figure A.16 Average Mobility results for a slab cracked on bottom and fully cracked on top (load $0.5P_y$), Stage 7

A.3.2.8 Stage 8: Slab fully cracked on bottom and top (load P_y)

The load at the cantilever was increased to P_y at which condition the bottom of the slab became fully cracked and impulse response tests were conducted. The slab was supported as described in Section A.2.1.1. Results are presented in Figure A.17.

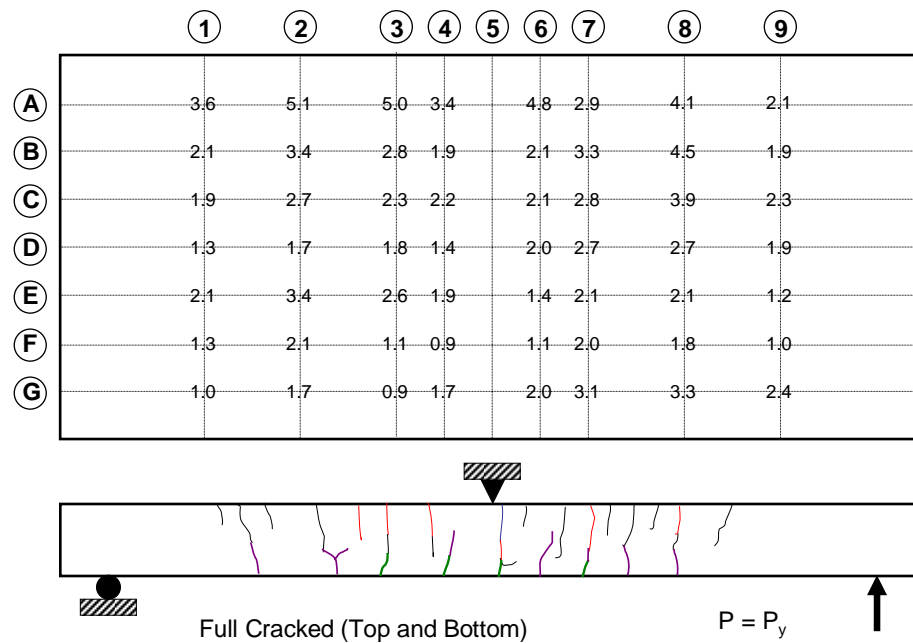


Figure A.17 Average Mobility results for a slab fully cracked on bottom and top (load P_y), Stage 8

A.3.2.9 Stage 9: Slab fully cracked on top and bottom and at rest

The slab was unloaded and left simply supported resting on concrete blocks as described in Section A.2.1.3. As a result of previous tests, the slab is fully cracked on top and bottom. Impulse response measurements were carried out and the results are shown in Figure A.18.

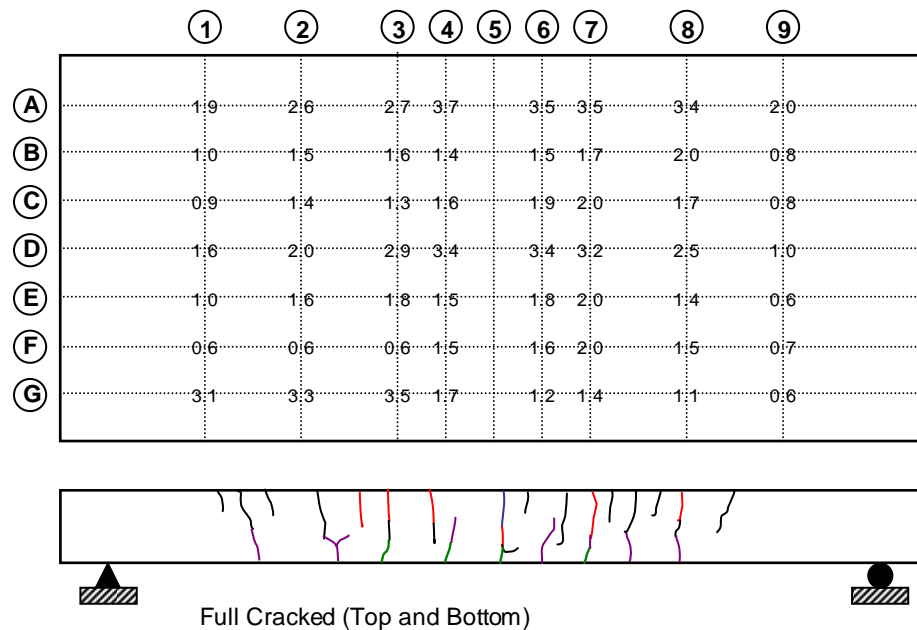


Figure A.18 Average Mobility results for a slab at rest fully cracked on bottom and top, Stage 9

A.4 INTERPRETATION OF RESULTS

A.4.1 Observations

After inspecting the data shown in Figure A.10 through Figure A.18, no clear trend or relationship between the average mobility and the cracking pattern or the intensity of damage was seen.

To investigate if there is a global correlation between average mobility and structural damage, the Mean Average Mobility was computed for each step. Results are presented in Table A.1 through Table A.3. It was found that the Mean Average Mobility does not correlate to the intensity of structural damage.

Table A.1 Mean Average Mobility for a simply supported slab at rest

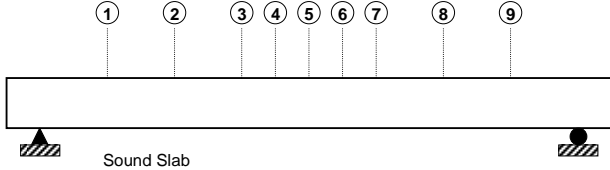
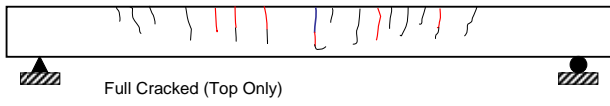
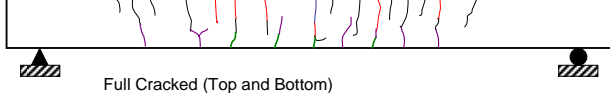
Stage	Damage Condition	Mean Average Mobility
1	 <p>Sound Slab</p>	1.3
5	 <p>Full Cracked (Top Only)</p>	2.1
9	 <p>Full Cracked (Top and Bottom)</p>	1.8

Table A.2 Mean Average Mobility for a simply supported slab under a midpoint load

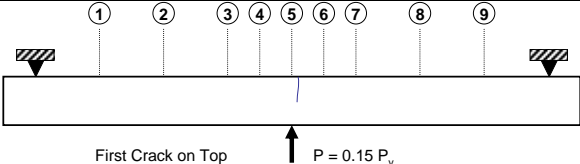
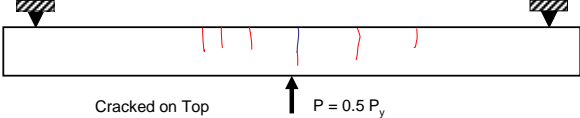
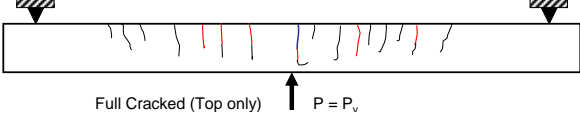
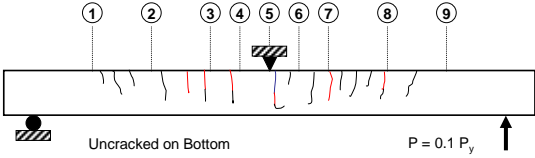
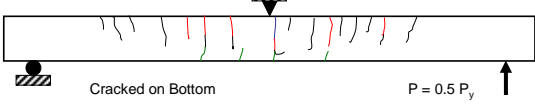
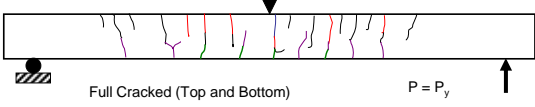
Stage	Damage Condition	Mean Average Mobility
2	 <p>First Crack on Top $P = 0.15 P_y$</p>	2.4
3	 <p>Cracked on Top $P = 0.5 P_y$</p>	1.5
4	 <p>Full Cracked (Top only) $P = P_y$</p>	2.4

Table A.3 Mean Average Mobility for a cantilevered slab under a load applied at the end of the cantilever

Stage	Damage Condition	Mean Average Mobility
6	 <p>Uncracked on Bottom $P = 0.1 P_y$</p>	2.6
7	 <p>Cracked on Bottom $P = 0.5 P_y$</p>	1.7
8	 <p>Full Cracked (Top and Bottom) $P = P_y$</p>	2.4

A.4.2 Conclusions

The hypothesis that an increase in average mobility would correspond to an increase in flexibility was not evident in this specimen. For a given material, less density corresponds to more flexibility because the Modulus of Elasticity decreases as density decreases. However, for the slab tested, an increase in flexibility is produced by cracking and not by a reduction in the Elastic Modulus, therefore the average mobility could not be correlated with the intensity of damage.

In future experiments, a different approach could be used to investigate the applicability of the Impulse Response test. Changes in the dynamic response of the element should be evaluated when structural damage has occurred, which implies the use of a much larger source of energy (bigger hammer) to excite the element in its natural frequencies.

Changes in the dynamic response are expected to occur at low frequencies (0-50 Hz) when damage is experienced. To investigate such changes at low frequencies, the Flexibility should be used. As defined in Section 5.3.2.1, the Flexibility is the slope of the portion of the mobility plot below 50 Hz.

The main disadvantage expected when using low frequencies to excite fundamental modes of the structure is that the response and results are likely to be dependent on boundary and support conditions. Because structural elements and not full scale structures are generally tested in the laboratory, such results would not be applicable to buildings with dynamic characteristics different from those of specimens tested in the laboratory.

APPENDIX B

Resonance and Direct-Arrival Tests

B.1 INTRODUCTION

Six 6 in. by 12 in. cylinders (three from specimen L0.5 and three from specimens LG0.5 and LR_{ST}G0.5) were tested in the Soil Dynamics Laboratory of the Department of Civil, Architectural and Environmental Engineering to measure the un-constrained P-wave velocity V_c or C_p , as defined in Chapters 5 and 6, the constrained P-wave velocity V_p and shear wave velocity V_s .

B.2 TESTS PROCEDURE AND RESULTS

B.2.1 Direct Arrival Tests

Direct arrival tests were conducted to obtain the P-wave velocity by impacting the concrete cylinder on one face and measuring the direct arrival time of the P-wave through a sensor installed on the other face of the cylinder, as shown in Figure B.1.



Figure B.1 Direct Arrival Tests

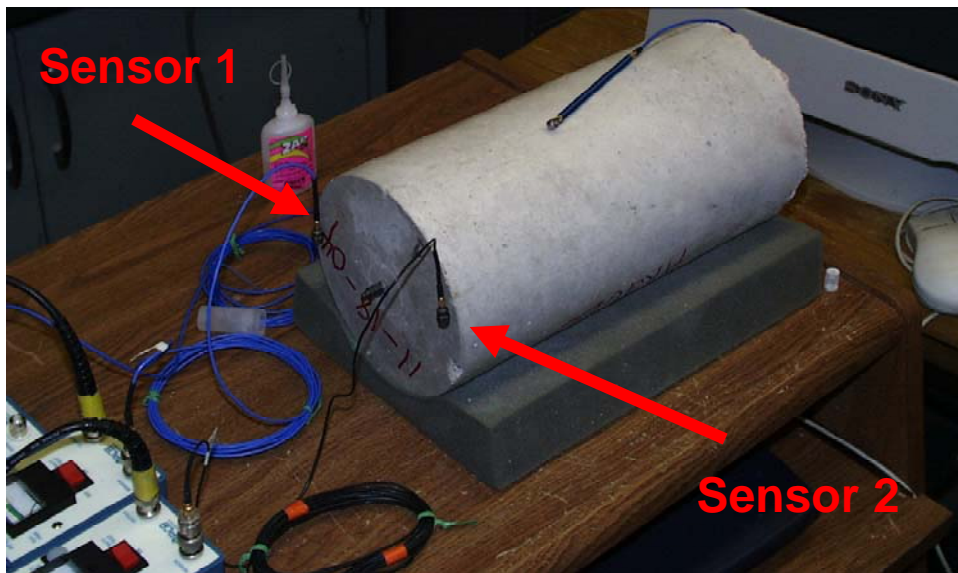


Figure B.2 Resonance Tests – Location of Sensors

B.2.2 Resonance Tests

Resonance tests were conducted to obtain the shear wave velocity by installing two sensors on the perimeter of one face of the cylinder (Figure B.2). The source of energy is the impact produced by a rotational device shown in Figure B.3.



Figure B.3 Resonance Tests – Location of Impact Energy

B.2.3 Results

Results are presented in Table B.1.

Table B.1 Results from Direct Arrival and Resonance Tests

Sample No.	Specimen	Vc (fps)	Vs (fps)	Vp (fps)	Average Vc (fps)	Average Vs (fps)	Average Vp (fps)
1	LG0.5 and LRstG0.5	12860	8185	13833	12955	8268	13819
2	LG0.5 and LRstG0.5	13050	8349	13764			
3	LG0.5 and LRstG0.5	12955	8269	13859			
4	L0.5	12415	7989	13184	12431	8003	13226
5	L0.5	12463	8019	13277			
6	L0.5	12414	8002	13216			

APPENDIX C

Upgraded Data Acquisition System for SWA and Impact Echo measurements

C.1 INTRODUCTION

Upgrading of the data acquisition system was recommended in Chapters 6 and 7 to increase the sampling rate to at least 600,000 samples per second and to acquire data from ultrasonic seismic waves with frequencies above 20 kHz.

C.2 CONFIGURATION OF THE UPGRADED DATA ACQUISITION

C.2.1 Accelerometers

Accelerometers with frequency range above 20 kHz are needed. PCB Piezotronics, Inc. manufactures a low sensitivity accelerometer Model 352A60 (Figure 7.9) that satisfies such requirement. It has a frequency range from 5 to 60 kHz at ± 3 dB and a resonant frequency ≥ 95 kHz. Other sensors described in Chapter 7 (Figure 7.5 through Figure 7.8) have a frequency range below 25 kHz and should not be used with an upgraded data acquisition system.

C.2.2 Data Acquisition Card

The Data Acquisition Card NI 6120 (Figure C.1) fabricated by National Instruments is recommended for upgrading the data acquisition system. The NI 6120 card is recommended because it is a 16 bits card and therefore it has a greater resolution than other high sampling 12-bit cards. It can sample at 800,000 samples per second, a speed considered sufficient to acquire data from ultrasonic seismic waves within the range of 20 to 80 kHz.

S Series Multifunction DAQ 12 or 16-Bit, 800 kS/s to 10 MS/s, 4 Analog Inputs

S Series

- 2 or 4 analog inputs; dedicated A/D converter per channel
- Analog and digital triggering
- AC or DC coupling
- 8 input ranges from ± 200 mV to ± 42 V
- 2 analog outputs at 4 MS/s single channel or 2.5 MS/s dual
- 8 digital I/O lines (5 V TTL/CMOS)
- Two 24-bit counter/timers

NI 6115, NI 6120

- Per-channel on/off antialias filters
- 32 or 64 Msample onboard memory
- Hardware timed and digital I/O
- Phase locking for multiboard synchronization (PXI only)

Families

- NI 6120 *New!*
- NI 6115
- NI 6111
- NI 6110

Operating Systems

- Windows 2000/NT/XP
- Real-Time Performance with LabVIEW (page 134)
- Others such as Linux and Mac OS X (page 187)

Recommended Software

- LabVIEW
- LabWindows/CVI
- Measurement Studio
- VI Logger

Other Compatible Software

- Visual Basic, C/C++ and C#


Driver Software (included)

- NI-DAQ 7

Calibration Certificate Included

See page 21.

NEW



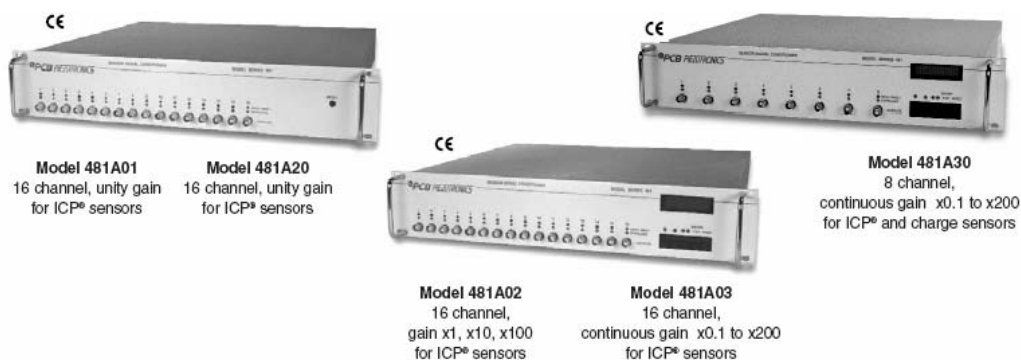
Family	Bus	Analog Inputs	Input Resolution	Sampling Rate	Input Range	Analog Outputs	Max Output Rate	Output Range	Digital I/O	Counter/ Timers	Triggers
NI 6120	PCI, PXI	4	16 bits	800 kS/s	± 0.2 to ± 42 V	2	4 MS/s ¹	± 10 V	8 ²	2, 24-bit	Analog, digital
NI 6115	PCI, PXI	4	12 bits	10 MS/s	± 0.2 to ± 42 V	2	4 MS/s ¹	± 10 V	8 ²	2, 24-bit	Analog, digital
NI 6111	PCI	2	12 bits	5 MS/s	± 0.2 to ± 42 V	2	4 MS/s ¹	± 10 V	8	2, 24-bit	Analog, digital
NI 6110	PCI	4	12 bits	5 MS/s	± 0.2 to ± 42 V	2	4 MS/s ¹	± 10 V	8	2, 24-bit	Analog, digital

¹4 MS/s single channel, 2.5 MS/s on two channels ²Hardware timed and FIFOs

Figure C.1 Upgraded Data Acquisition Card

C.2.3 Signal Conditioning Module

The Signal Conditioning Module 481A02 is recommended (Figure C.2). This module is fabricated by PCB Piezotronics, Inc. Among others, the 481A02 is recommended because it has selectable gain and a Frequency Response from 0.5 to 100 kHz.



Multi-Channel Signal Conditioners					
Model Number	481A01	481A02	481A03	481A20	481A30
Style	unity gain	selectable gain with keypad & display	continuous gain adjust with keypad & display	unity gain	dual mode, continuous gain adjust with keypad & display
Channels	16 channels	16 channels	16 channels	16 channels	8 channels
Sensor excitation (1)	24 volt, 3 to 20 mA	24 volt, 3 to 20 mA	24 volt, 3 to 20 mA	24 volt, 3 to 20 mA	24 volt, 3 to 20 mA
Gain (each channel)	unity	autoranging x1, x10, x100	continuous x0.1 to x200	unity	continuous x0.1 to x200
Frequency response ($\pm 5\%$)	0.5 to 100k Hz	0.5 to 100k Hz	0.5 to 90k Hz (2)	0.05 to 1M Hz	0.5 to 90k Hz (2)
Broadband noise (at unity gain)	11 μ V rms	11 μ V rms	4 mV	11 μ V rms	100 μ V
Power required	100 to 240 VAC 47 to 63 Hz	100 to 240 VAC 47 to 63 Hz	100 to 240 VAC 47 to 63 Hz	100 to 240 VAC 47 to 63 Hz	100 to 240 VAC 47 to 63 Hz
Keypad control	no	yes	yes	no	yes
Computer control	no	RS-232 and RS-485 (3)	RS-232 and RS-485 (3)	no	RS-232 and RS-485 (3)
Input connectors	DB50 and BNC	DB50 and BNC	DB50 and BNC	BNC	10-32 and BNC
Output connectors	DB37 and BNC	DB37 and BNC	DB37 and BNC	BNC	BNC
Size (height x width x depth)	3.5 x 19.0 x 16.25 in (9 x 48 x 41 cm)	3.5 x 19.0 x 16.25 in (9 x 48 x 41 cm)	3.5 x 19.0 x 16.25 in (9 x 48 x 41 cm)	3.5 x 19.0 x 16.25 in (9 x 48 x 41 cm)	3.5 x 19.0 x 16.25 in (9 x 48 x 41 cm)
Weight	15 lb (6.8 kg)	15 lb (6.8 kg)	15 lb (6.8 kg)	15 lb (6.8 kg)	15 lb (6.8 kg)

NOTE: 1. Current is factory set at 4 mA but is user adjustable between 3 and 20 mA.
2. Attains 90k Hz with filter disabled.
3. Supplied with Windows[®] based control software program.

Figure C.2 Upgraded Signal Conditioning Module

APPENDIX D

Typical Time History Records and Fast Fourier Transform (FFT) Plots from SWA and Crack Depth Measurements

D.1 TYPICAL TIME HISTORY RECORDS AND FFT PLOTS FROM SWA MEASUREMENTS

Typical time history records and FFT plots from SWA measurements are presented in Figure D.1 through Figure D.35. Records were selected from measurements conducted on Specimen L0.5 (North Axis) when the specimen was at rest. The first of ten available records was always selected for every drift level.

D.2 TYPICAL TIME HISTORY RECORDS AND FFT PLOTS FROM CRACK-DEPTH MEASUREMENTS

Typical time history records and FFT plots from Crack-Depth measurements are presented in Figure D.36 through Figure D.45. Records were selected from measurements conducted on Specimen LG1.0 (North Axis) when the specimen was at rest. The first of ten available records was always selected for every drift level.

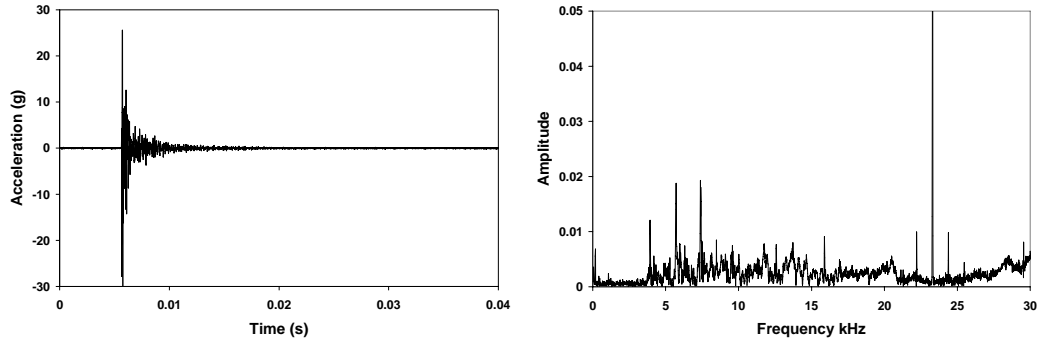


Figure D.1 *Time History and FFT for SWA Record 001, Ch 0, Specimen L0.5, North Axis, Condition at Rest, 0% Drift*

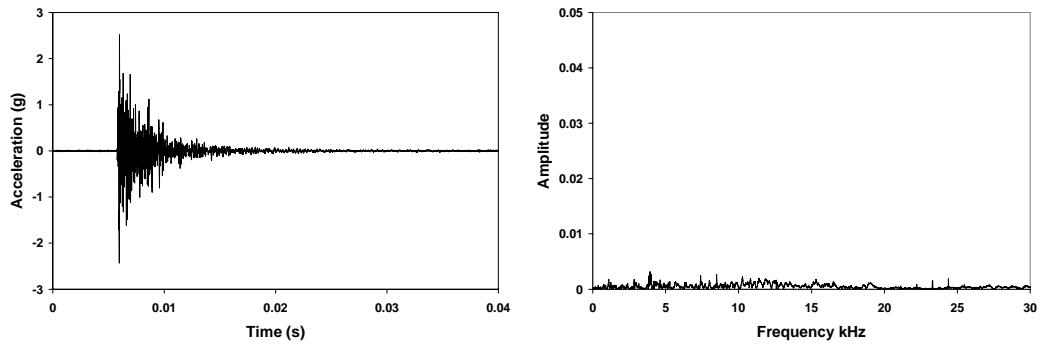


Figure D.2 *Time History and FFT for SWA Record 001, Ch 2, Specimen L0.5, North Axis, Condition at Rest, 0% Drift*

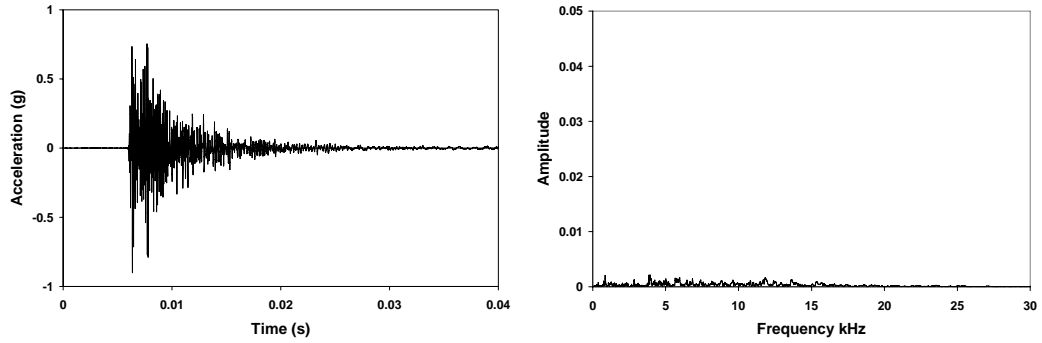


Figure D.3 *Time History and FFT for SWA Record 001, Ch 3, Specimen L0.5, North Axis, Condition at Rest, 0% Drift*

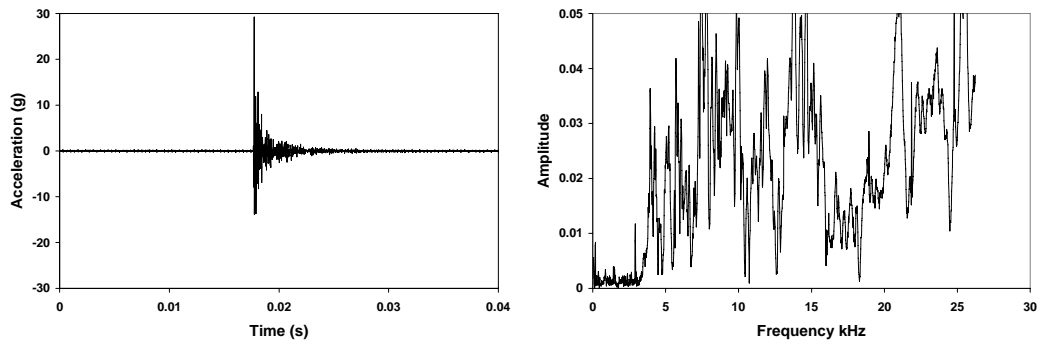


Figure D.4 *Time History and FFT for SWA Record 001, Ch 0, Specimen L0.5, North Axis, Condition at Rest, 0.25% Drift*

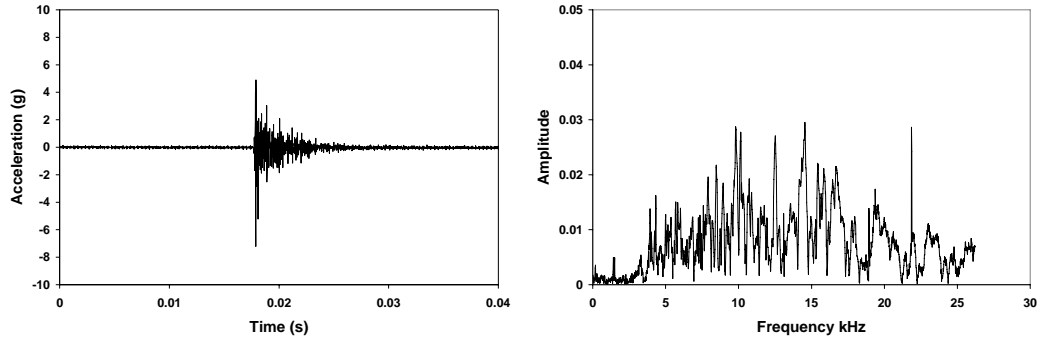


Figure D.5 Time History and FFT for SWA Record 001, Ch 1, Specimen L0.5, North Axis, Condition at Rest, 0.25% Drift

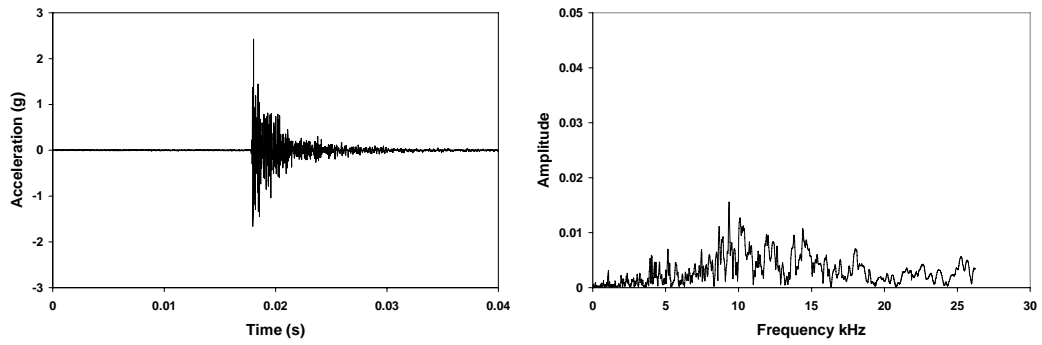


Figure D.6 Time History and FFT for SWA Record 001, Ch 2, Specimen L0.5, North Axis, Condition at Rest, 0.25% Drift

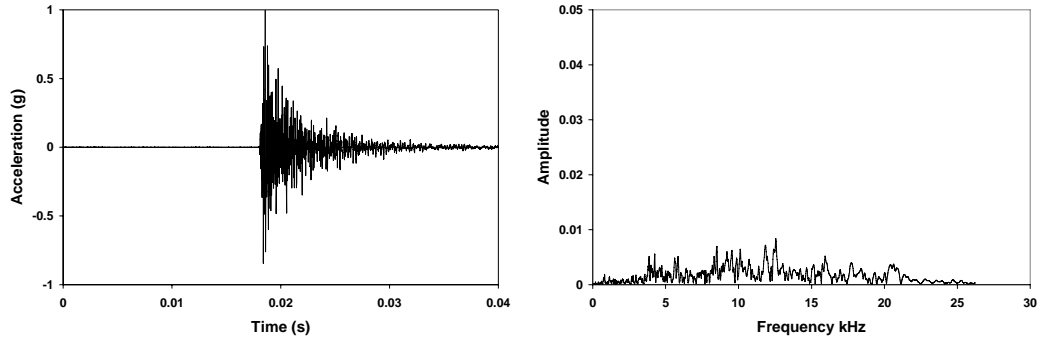


Figure D.7 *Time History and FFT for SWA Record 001, Ch 3, Specimen L0.5, North Axis, Condition at Rest, 0.25% Drift*

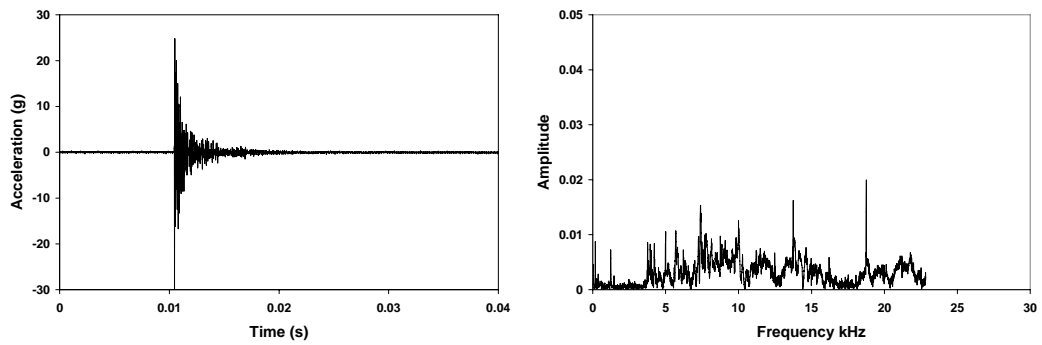


Figure D.8 *Time History and FFT for SWA Record 001, Ch 0, Specimen L0.5, North Axis, Condition at Rest, 0.5% Drift*

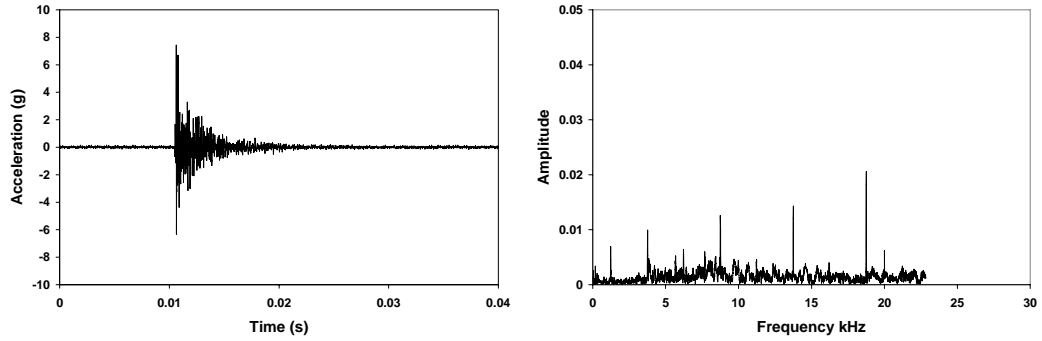


Figure D.9 *Time History and FFT for SWA Record 001, Ch 1, Specimen L0.5, North Axis, Condition at Rest, 0.5% Drift*

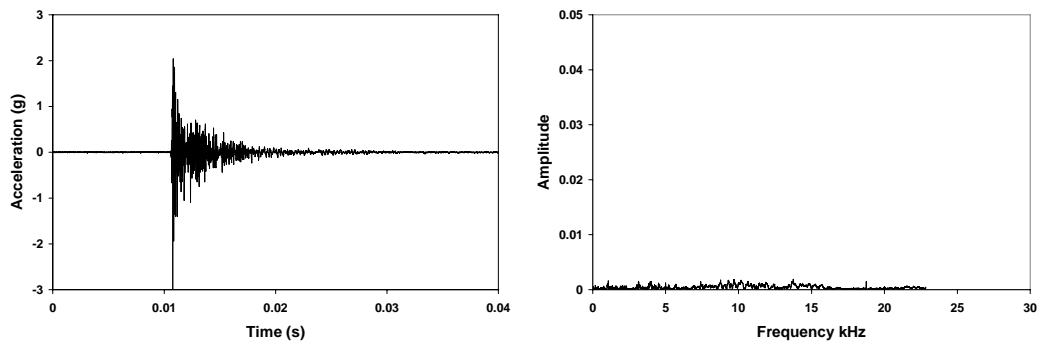


Figure D.10 *Time History and FFT for SWA Record 001, Ch 2, Specimen L0.5, North Axis, Condition at Rest, 0.5% Drift*

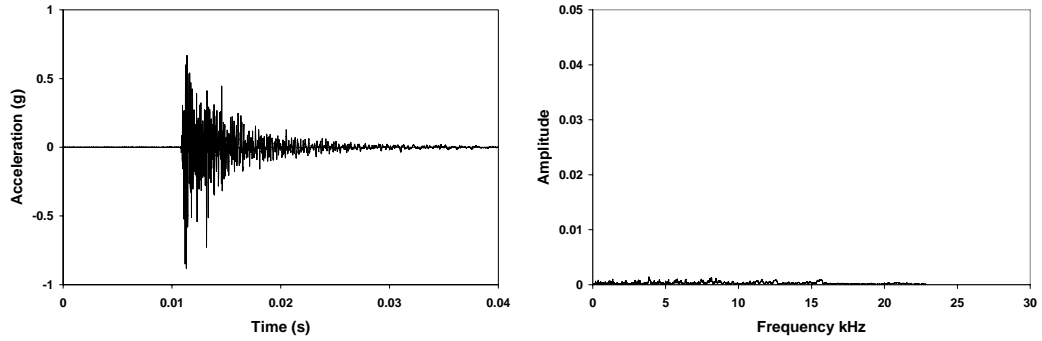


Figure D.11 *Time History and FFT for SWA Record 001, Ch 3, Specimen L0.5, North Axis, Condition at Rest, 0.5% Drift*

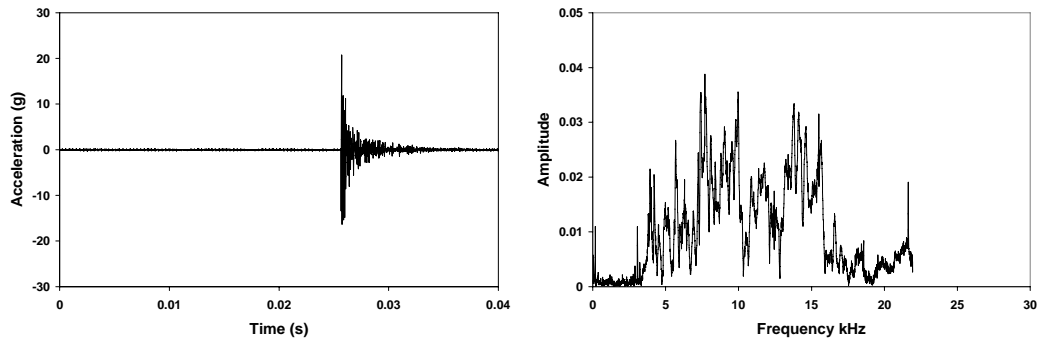


Figure D.12 *Time History and FFT for SWA Record 001, Ch 0, Specimen L0.5, North Axis, Condition at Rest, 0.75% Drift*

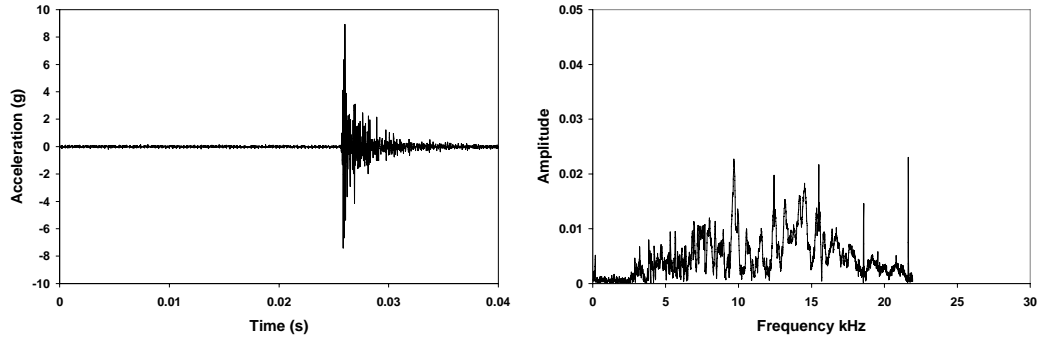


Figure D.13 *Time History and FFT for SWA Record 001, Ch 1, Specimen L0.5, North Axis, Condition at Rest, 0.75% Drift*

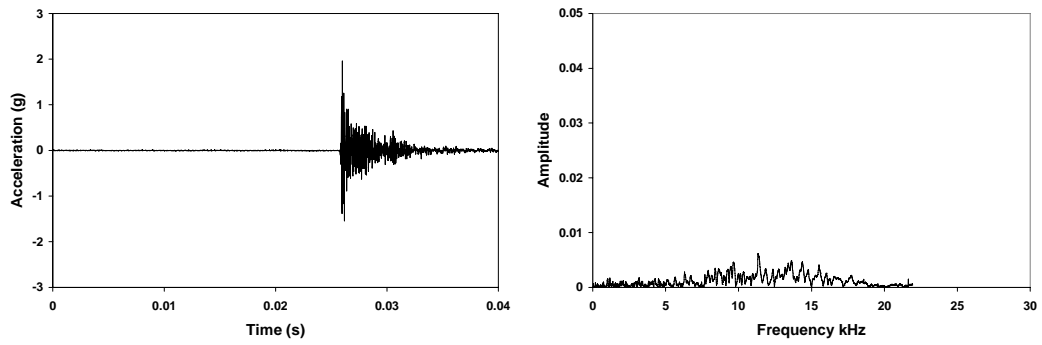


Figure D.14 *Time History and FFT for SWA Record 001, Ch 2, Specimen L0.5, North Axis, Condition at Rest, 0.75% Drift*

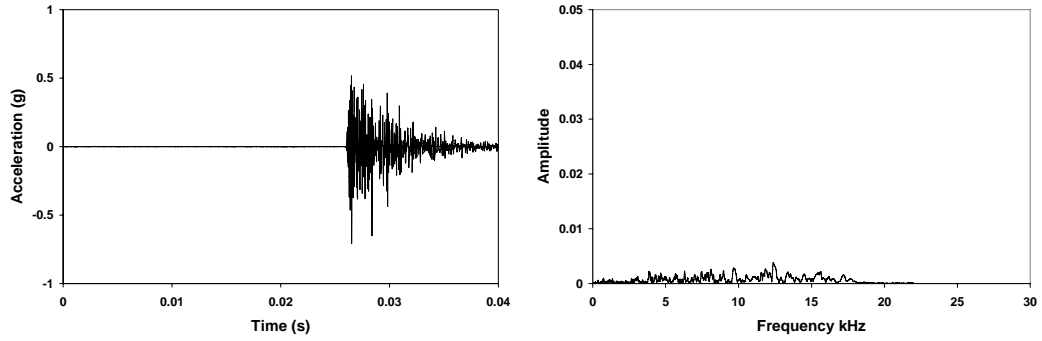


Figure D.15 *Time History and FFT for SWA Record 001, Ch 3, Specimen L0.5, North Axis, Condition at Rest, 0.75% Drift*

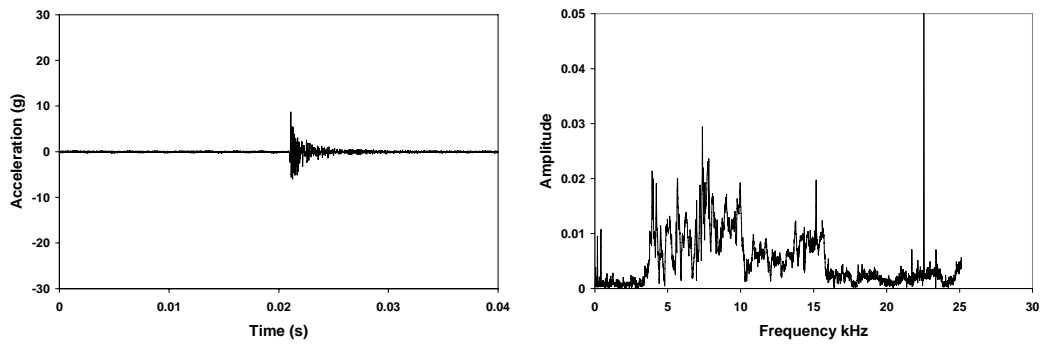


Figure D.16 *Time History and FFT for SWA Record 001, Ch 0, Specimen L0.5, North Axis, Condition at Rest, 1% Drift*

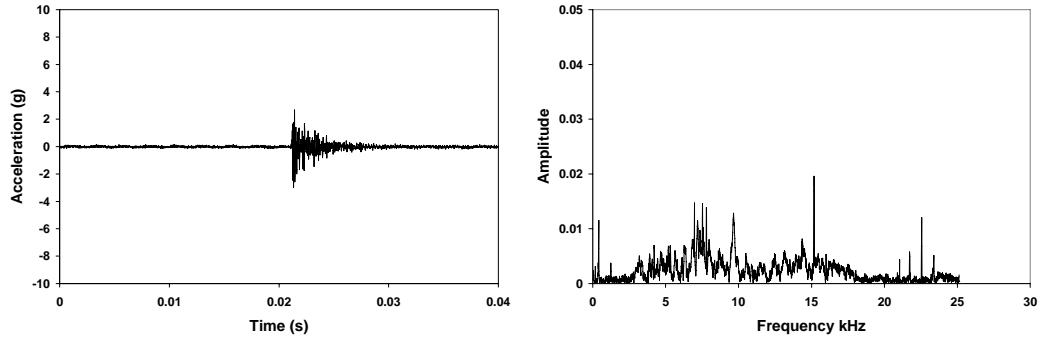


Figure D.17 *Time History and FFT for SWA Record 001, Ch 1, Specimen L0.5, North Axis, Condition at Rest, 1% Drift*

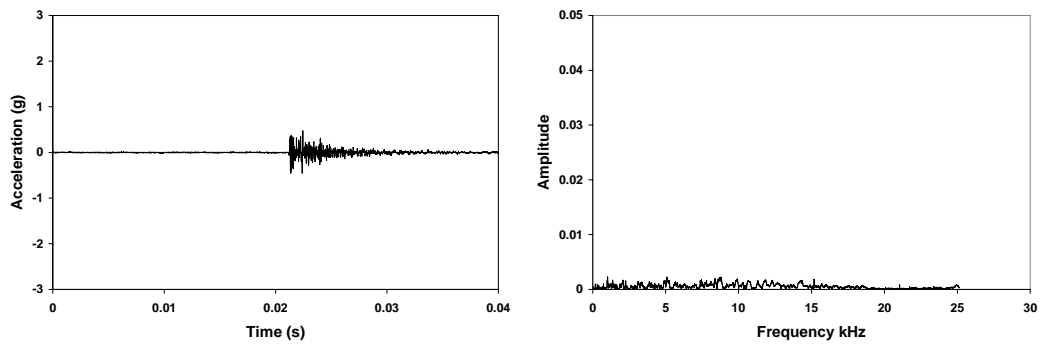


Figure D.18 *Time History and FFT for SWA Record 001, Ch 2, Specimen L0.5, North Axis, Condition at Rest, 1% Drift*

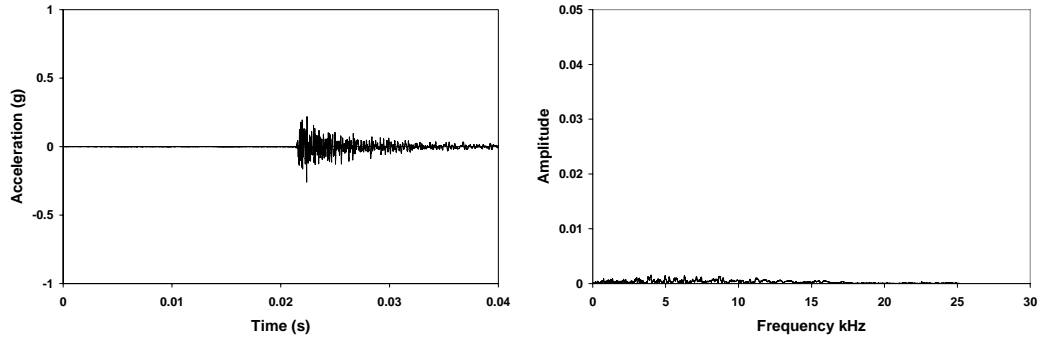


Figure D.19 *Time History and FFT for SWA Record 001, Ch 3, Specimen L0.5, North Axis, Condition at Rest, 1% Drift*

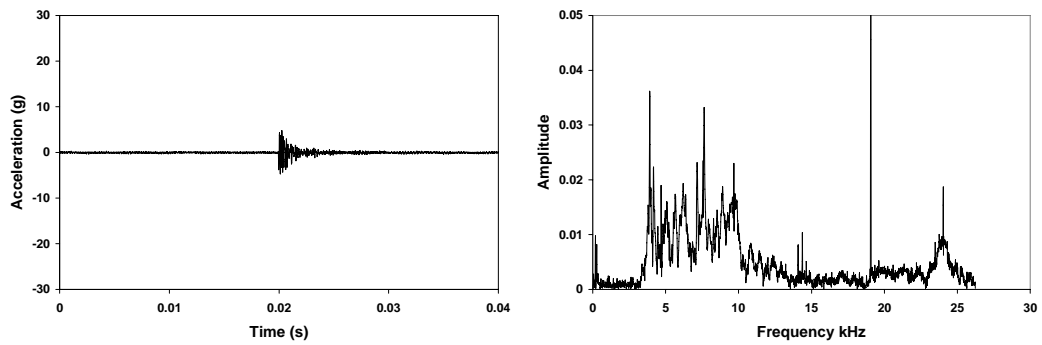


Figure D.20 *Time History and FFT for SWA Record 001, Ch 0, Specimen L0.5, North Axis, Condition at Rest, 1.5% Drift*

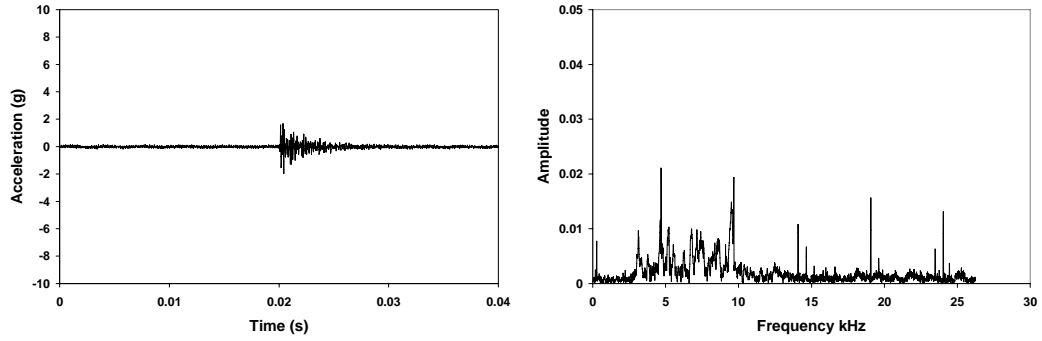


Figure D.21 *Time History and FFT for SWA Record 001, Ch 1, Specimen L0.5, North Axis, Condition at Rest, 1.5% Drift*

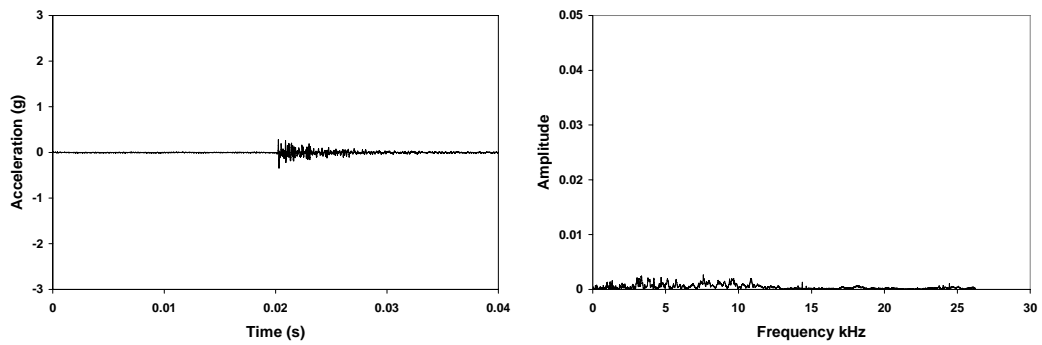


Figure D.22 *Time History and FFT for SWA Record 001, Ch 2, Specimen L0.5, North Axis, Condition at Rest, 1.5% Drift*

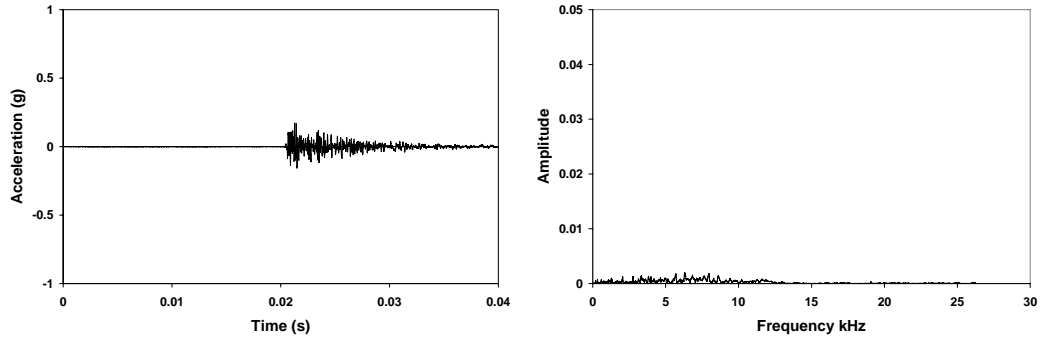


Figure D.23 *Time History and FFT for SWA Record 001, Ch 3, Specimen L0.5, North Axis, Condition at Rest, 1.5% Drift*

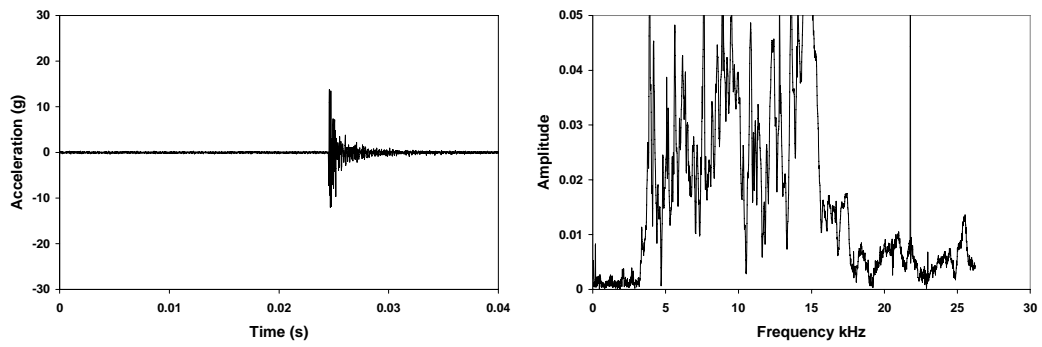


Figure D.24 *Time History and FFT for SWA Record 001, Ch 0, Specimen L0.5, North Axis, Condition at Rest, 1.75% Drift*

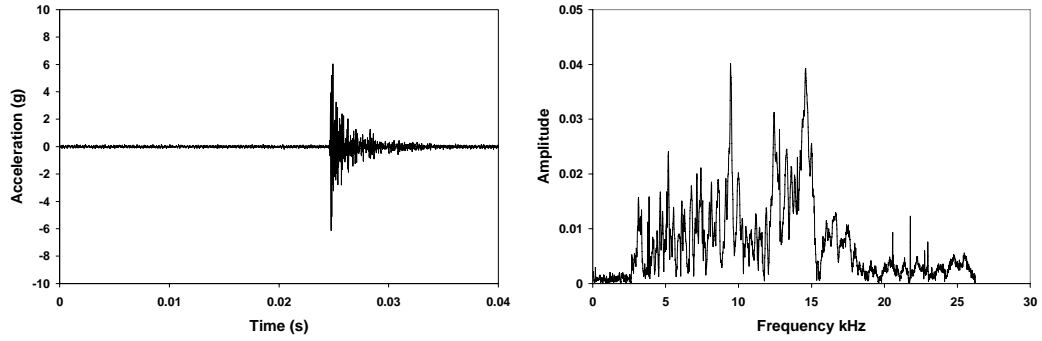


Figure D.25 *Time History and FFT for SWA Record 001, Ch 1, Specimen L0.5, North Axis, Condition at Rest, 1.75% Drift*

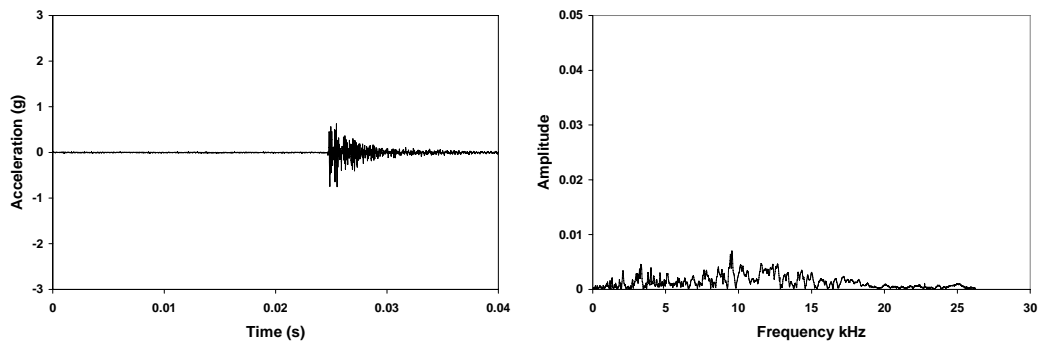


Figure D.26 *Time History and FFT for SWA Record 001, Ch 2, Specimen L0.5, North Axis, Condition at Rest, 1.75% Drift*

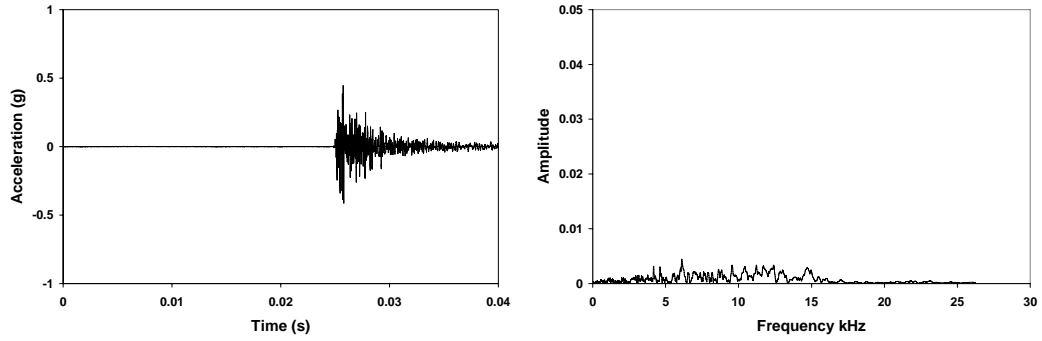


Figure D.27 *Time History and FFT for SWA Record 001, Ch 3, Specimen L0.5, North Axis, Condition at Rest, 1.75% Drift*

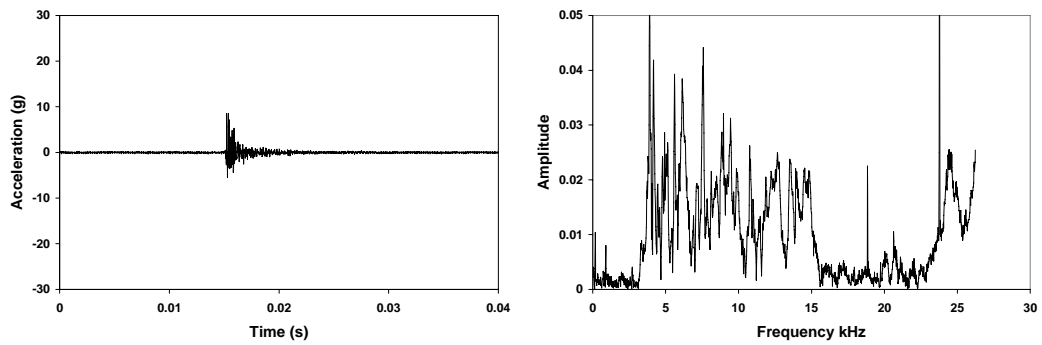


Figure D.28 *Time History and FFT for SWA Record 001, Ch 0, Specimen L0.5, North Axis, Condition at Rest, 2% Drift*

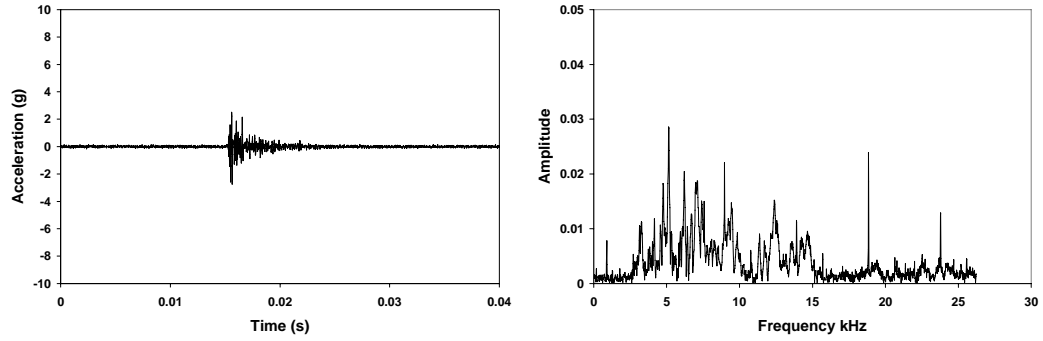


Figure D.29 *Time History and FFT for SWA Record 001, Ch 1, Specimen L0.5, North Axis, Condition at Rest, 2% Drift*

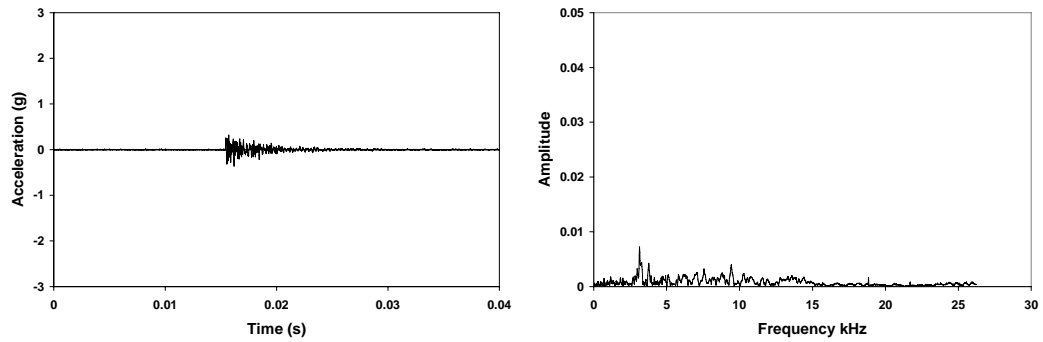


Figure D.30 *Time History and FFT for SWA Record 001, Ch 2, Specimen L0.5, North Axis, Condition at Rest, 2% Drift*

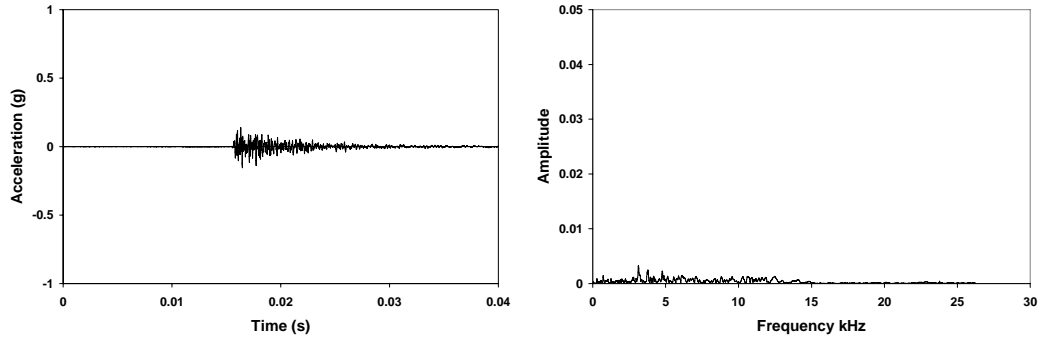


Figure D.31 *Time History and FFT for SWA Record 001, Ch 3, Specimen L0.5, North Axis, Condition at Rest, 2% Drift*

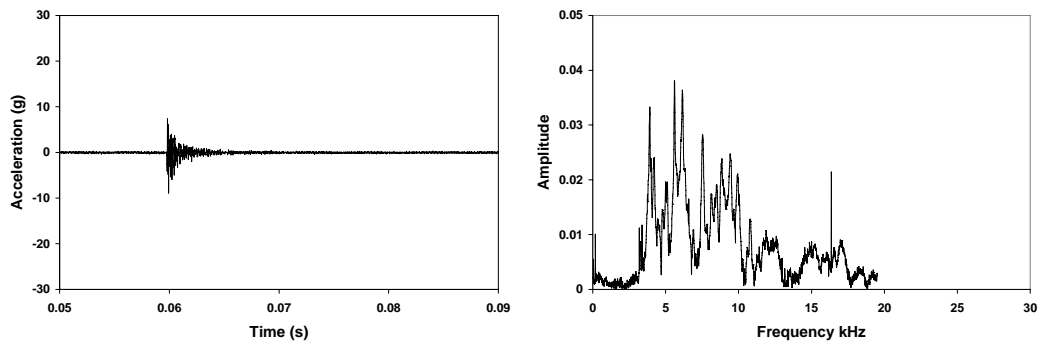


Figure D.32 *Time History and FFT for SWA Record 001, Ch 0, Specimen L0.5, North Axis, Condition at Rest, 2.5% Drift*

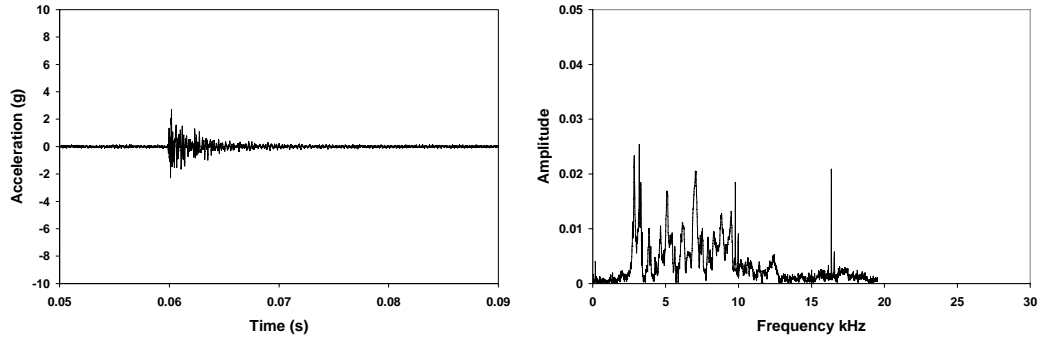


Figure D.33 *Time History and FFT for SWA Record 001, Ch 1, Specimen L0.5, North Axis, Condition at Rest, 2.5% Drift*

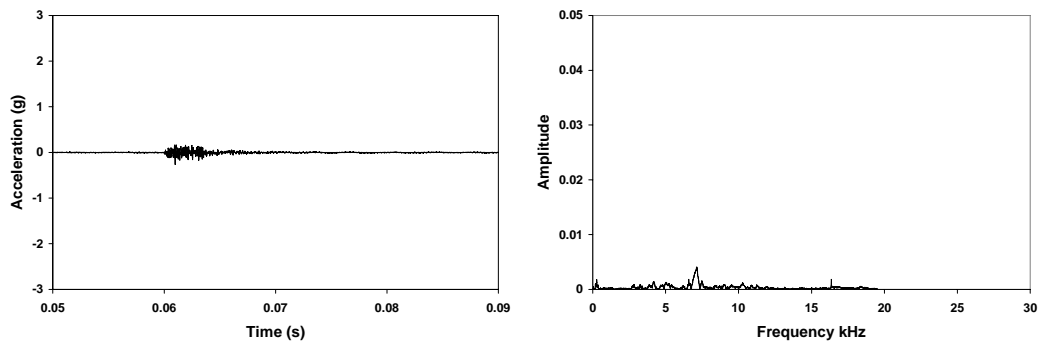


Figure D.34 *Time History and FFT for SWA Record 001, Ch 2, Specimen L0.5, North Axis, Condition at Rest, 2.5% Drift*

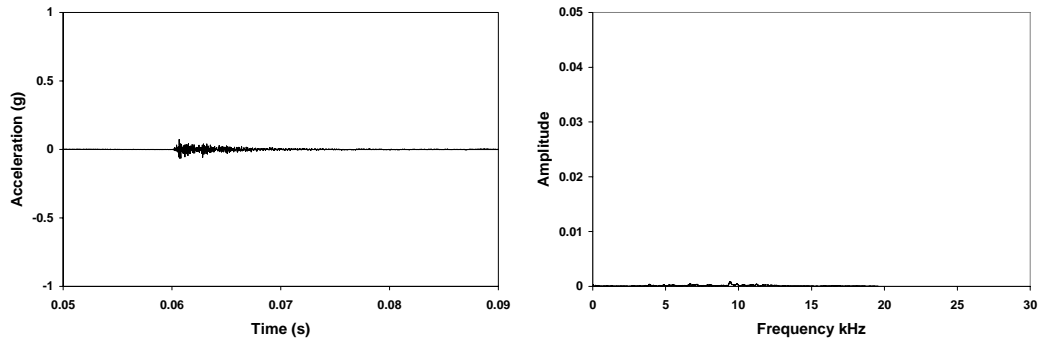


Figure D.35 *Time History and FFT for SWA Record 001, Ch 3, Specimen L0.5, North Axis, Condition at Rest, 2.5% Drift*

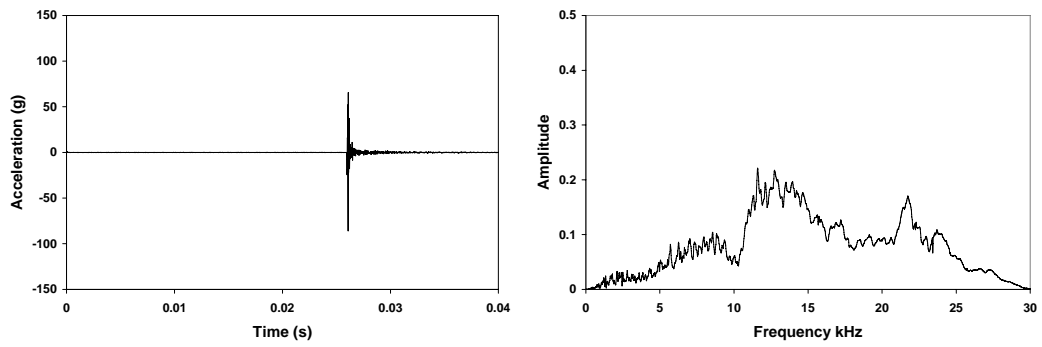


Figure D.36 *Time History and FFT for Crack-Depth Record 001, Ch 1, Specimen LG1.0, North Axis, Condition at Rest, 0.25% Drift*

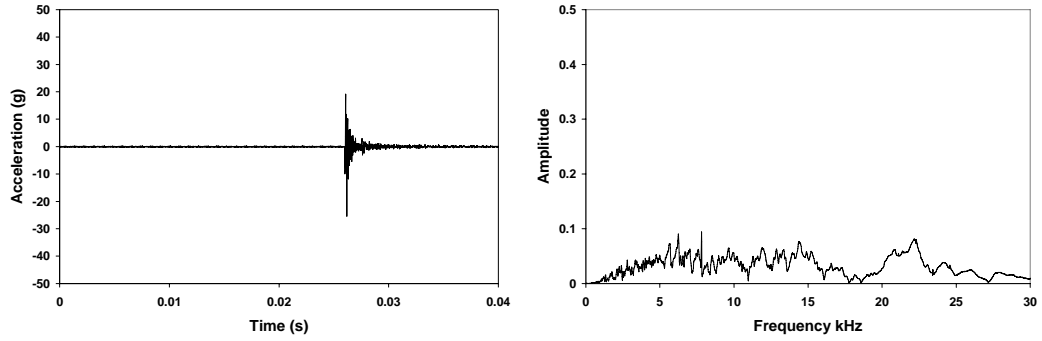


Figure D.37 Time History and FFT for Crack-Depth Record 001, Ch 2,
Specimen LG1.0, North Axis, Condition at Rest, 0.25% Drift

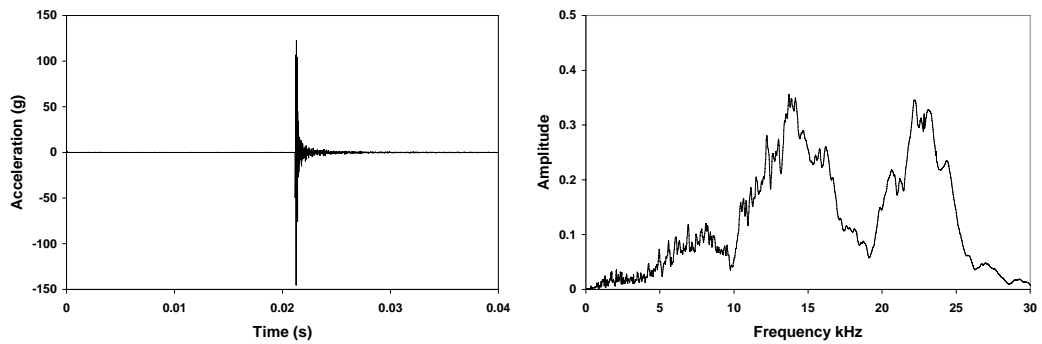


Figure D.38 Time History and FFT for Crack-Depth Record 001, Ch 1,
Specimen LG1.0, North Axis, Condition at Rest, 0.5% Drift

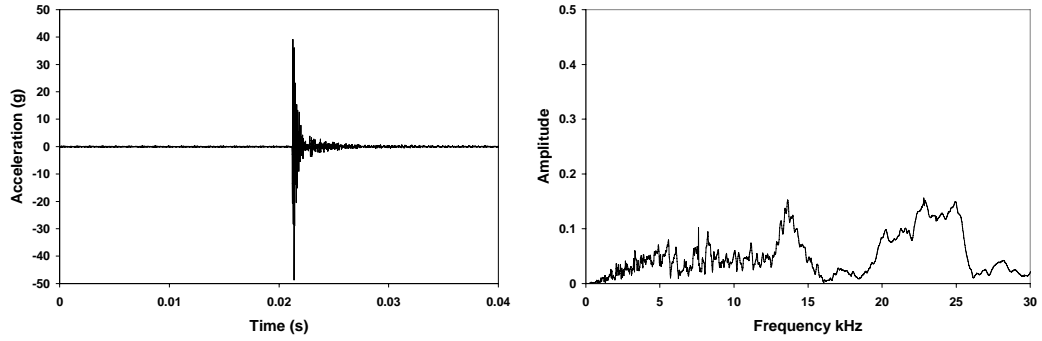


Figure D.39 Time History and FFT for Crack-Depth Record 001, Ch 2,
Specimen LG1.0, North Axis, Condition at Rest, 0.5% Drift

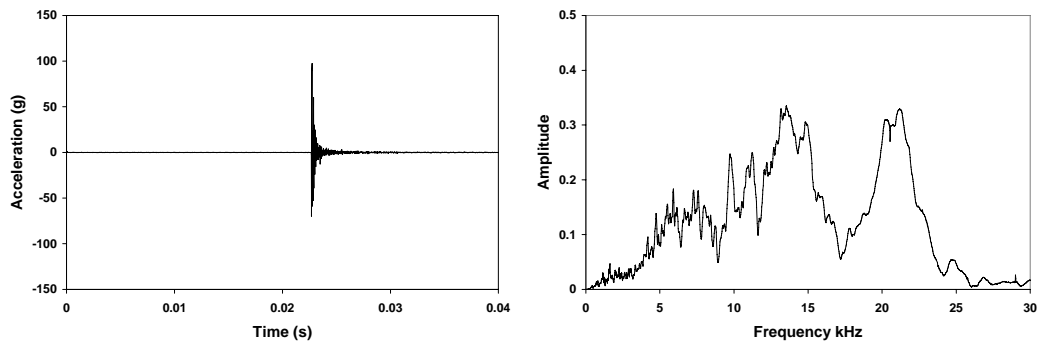


Figure D.40 Time History and FFT for Crack-Depth Record 001, Ch 1,
Specimen LG1.0, North Axis, Condition at Rest, 0.75% Drift

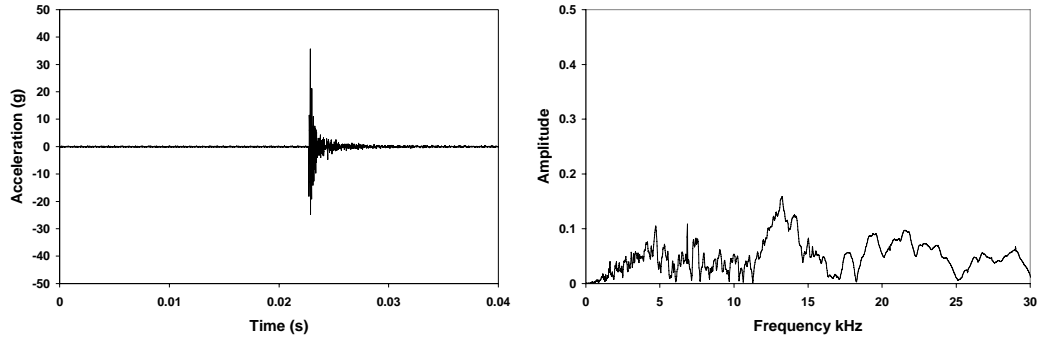


Figure D.41 Time History and FFT for Crack-Depth Record 001, Ch 2,
Specimen LG1.0, North Axis, Condition at Rest, 0.75% Drift

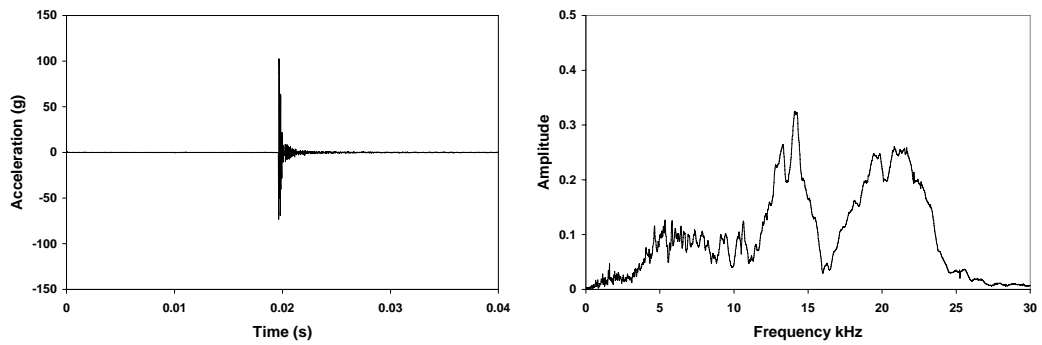


Figure D.42 Time History and FFT for Crack-Depth Record 001, Ch 1,
Specimen LG1.0, North Axis, Condition at Rest, 1% Drift

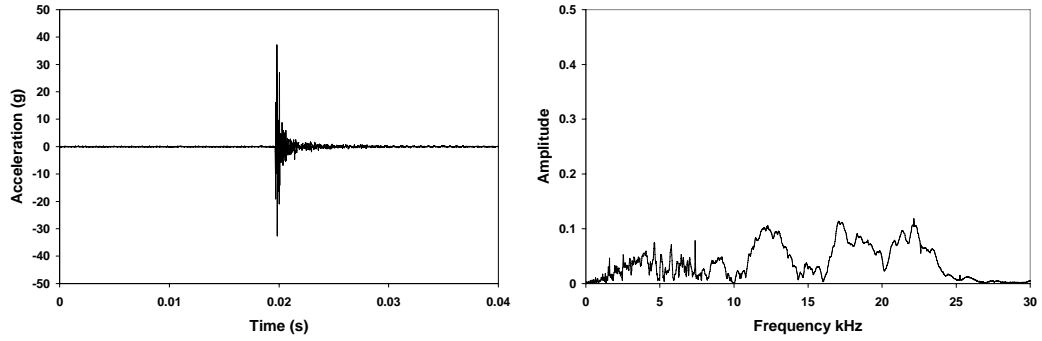


Figure D.43 *Time History and FFT for Crack-Depth Record 001, Ch 2, Specimen LG1.0, North Axis, Condition at Rest, 1% Drift*

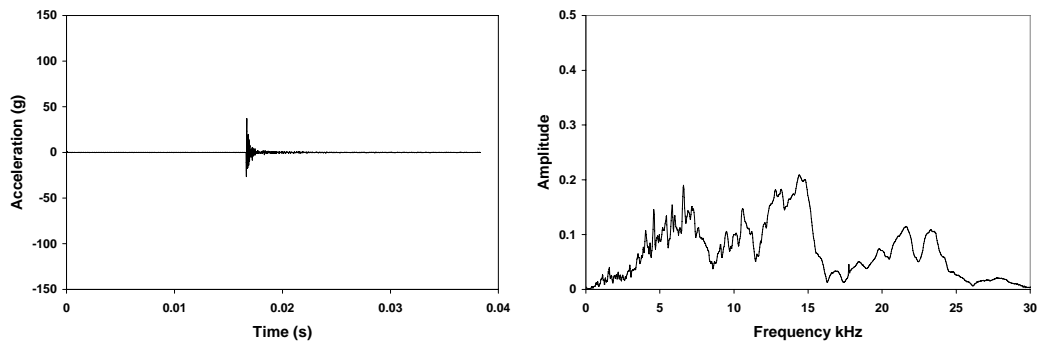
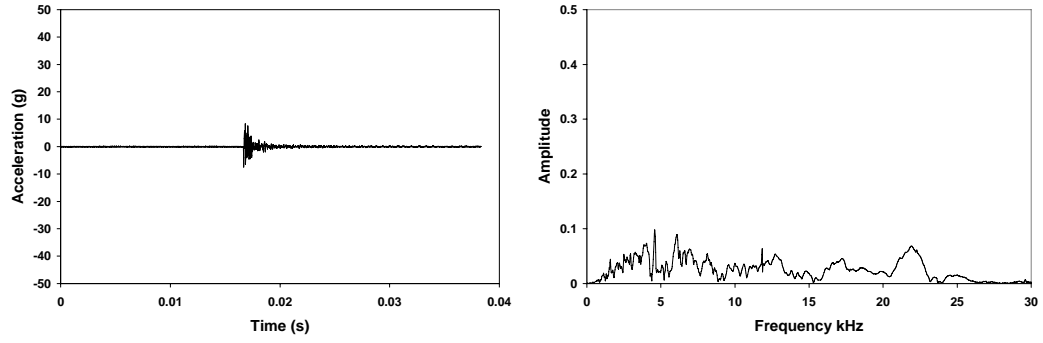


Figure D.44 *Time History and FFT for Crack-Depth Record 001, Ch 1, Specimen LG1.0, North Axis, Condition at Rest, 1.25% Drift*



***Figure D.45 Time History and FFT for Crack-Depth Record 001, Ch 2,
Specimen LG1.0, North Axis, Condition at Rest, 1.25% Drift***

References

- Acoustic Control Systems (ACS) website, "*Ultrasonic Tomograph A1230*," April, 2006, <http://acsys.ru/eng2/prod/a1230/ea1230.htm>
- Bay, J.A. and Stokoe, K.H., II, "*Field and Laboratory Determination of Elastic Properties of PCC Using Seismic Techniques*," Transportation Research Record 1355, pp. 67-74, 1992.
- Bay, J.A. and Stokoe, K.H., II, "*Field Determination of Stiffness and Integrity of PCC Members Using the SASW Method*," Proceedings, Conference on Nondestructive Evaluation of Civil Structures and Materials. University of Colorado at Boulder, October 1990, pp. 71-85.
- Bowen, B., "*Damage Detection in Concrete Elements with Surface Wave Measurements*", Ph.D. Dissertation, The University of Texas at Austin, 1992.
- Bowen, B. R., and Stokoe, K., H., II, "*Evaluation of cracked and repaired beams and columns using surface stress waves*," Proceedings of the Tenth World Conference on Earthquake Engineering, Madrid, Spain, 1992.
- Davis, A. G., "*The nondestructive impulse response test in North America: 1985 – 2001*," NDT&E International 36, 2003, pp. 185-193.
- Dumas, P., Poguét, J., and Fleury, G., "*Piezocomposite technology, an innovative approach to the improvement of N.D.T. performance using ultrasounds*," 8th European Congress on Non Destructive Testing, June 2002, Barcelona, Spain.
- Goldsmith, W., "*Impact: The Theory and Physical Behavior of Colliding Solids*," Edward Arnold Press, Ltd., pp. 24-50, 1965.
- Hillger, W., "*Ultrasonic imaging of defects in concrete components by pulse-echo-technique*," <http://www.dr-hillger.de/concr.pdf>, 2000.
- Johnson, P. A., "*Nondestructive Testing of Materials by Nonlinear Elastic Wave Spectroscopy (NEWS)*," Materials World, The Journal of the Institute of Materials, September 1999.

Kalinski, M.E., Stokoe, K.H., II, Jirsa, J.O. and Roesset, J.M., ***“Nondestructive Identification of Internally Damaged Areas of Concrete Beam Using the SASW Method,”*** Transportation Research Record, No. 1458, pp. 14-19, 1994.

Krause, M., Mielentz, F., Millmann, B., Streicher, D., and Muller. W., ***“Ultrasonic Imaging of concrete elements: State of the art using 2D synthetic aperture,”*** BAM International Symposium (NDT-CE 2003), <http://www.ndt.net/article/ndtce03/papers/v051/v051.htm>

Madianos, M., Nelson, P.P. and Stokoe, K.H., II, ***“Evaluation of Discrete Discontinuities and Repeated Monitoring of Rock Mass Characteristics with SASW Testing,”*** Proceedings, 8th Annual Workshop, Generic Mineral Technology Center, U.S. Bureau of Mines, Reno, Nevada, 1990, pp. 15-23.

Madianos, M.N., Nelson, P.P. and Stokoe, K.H., II, ***“Characterization of Discontinuous Rock Masses in the Field with Surface Waves,”*** Proceedings, International Society of Rock Mechanics Regional Conference on Fractured and Jointed Rock Masses, Lake Tahoe, CA, June 3-5, 1992.

Malholtra, M. and Carino, N.J., editors, ***“Handbook on Nondestructive Testing of Concrete,”*** CRC Press, Inc., 1991.

Nazarian, S., Briggs, R.C., Stokoe, K.H., II, and Rogers, R.B., ***“Determination of Pavement Layer Thickness by SASW Method,”*** Transportation Research Record 1196, 1989, pp. 133 – 150.

Nelson, P.P. and Stokoe, K.H., II, ***“Nondestructive Testing Using Borehole and Surface Seismic Techniques to Evaluate Rock Mass Damage Zones,”*** Proceedings, 2nd International High Level Radioactive Waste Management Conference and Exposition, Las Vegas, Nevada, 1991, pp. 802-809.

Olson, L.D., Sack, D.A., Stokoe, K.H., II, and Buchinski, K.W., ***“Stress-Wave Nondestructive Testing of Tunnels and Shafts,”*** Transportation Research Record, No. 1415, 1993, pp. 88-94.

Olson, L.D., ***“Stress Wave NDE Methods for Condition Assessment of the Superstructure and Substructure of Concrete Bridges,”*** The IEE Library & Archives, 2004.
<http://www.iee.org/oncomms/sector/manufacturing/Articles/Heading/297>

Poguet, J., Marguet, J., Pichonnat, F., Garcia, A., and Vasquez, J., ***“Phased Array technology : Concepts, probes and applications,”*** 8th European Congress on Non Destructive Testing, June 2002, Barcelona, Spain

Rix, G.J., Bay, J.A. and Stokoe, K.H., II, "***Assessing In Situ Stiffness of Curing Portland Cement Concrete with Seismic Tests,***" Transportation Research Record 1284, 1990, pp. 8-15.

Roesset, J.M., Chang, D.-W., Stokoe, K.H., II and Aouad, M., "***Modulus and Thickness of the Pavement Surface Layer from SASW Tests,***" Transportation Research Record 1260, 1990, pp. 53-63.

Rosenblad, B.L., Chiang, C.C., Stokoe, K.H., II and Roesset, J.M., "***Suitability of Stress Waves to Detect Flaws in Rigid Pavements While Moving,***" 74th Annual Transportation Research Board Meeting, Washington, D.C., January 22-28, 1995.

Sansalone, M., "***Flaw Detection in Concrete Using Transient Stress Waves,***" Ph. D. Dissertation, Cornell University, 1986, 220 pp.

Sansalone, M. J. and Carino, N. J., "***Impact-Echo: A Method for Flaw Detection in Concrete Using Transient Stress Waves,***" NBSIR 86-3452, National Bureau of Standards, Gaithersburg, Maryland, Sept. 1986, 222 pp.

Sansalone, M. J., and Streett, W.B., "***The Impact-Echo Method,***" NDTnet 1998 February, Vol 3 No.2, <http://www.ndt.net/article/0298/streett/streett.htm#ref>

Sansalone, M. J., and Streett, W.B., "***Impact-Echo: Nondestructive Evaluation of Concrete and Masonry,***" Bullbrier Press, 1997.

Shaw, P., and Xu, A., "***Assessment of The Deterioration of Concrete in NPP - Causes, Effects and Investigative Methods,***" NDTnet, Vol.3 No.2, February 1998, Helsingborg, Sweden, <http://www.ndt.net/article/0298/shaw/shaw.htm>

Tian, Y., "***Behavior and Modeling of Low-Reinforced Flat Plate-Column Connections under Different Loading Histories,***" Ph.D. Dissertation, The University of Texas at Austin, 2006.

Watson, B.B., Bay, J.A., Stokoe, K.H., II and Fowler, D.W., "***Is There a Difference Between "Static" and "Dynamic" Moduli of Concrete?"***" Proceedings, Society of Exploration Geophysicists Sixty-First Annual International Meeting and Exposition, Houston, TX, November 10-14, 1991, pp. 526-529.

Widianto, Tian Y., Argudo J., Bayrak O. and Jirsa J., ***"Rehabilitation of Earthquake-damaged Reinforced Concrete Flat-plate Slab-column Connections for Two-way Shear."*** Submitted for publication to the 8th National Conference on Earthquake Engineering (8NCEE), San Francisco - California, April 2006.

VITA

Jaime Fernando Argudo was born in Guayaquil, Ecuador on October 3, 1963, the son of Carlos Vicente Argudo, MD and Alba Esperanza Rodríguez. He received his Bachelor of Science in Civil Engineering from Universidad Católica de Santiago de Guayaquil, in 1986. He has been professor in the School of Engineering of Universidad Católica de Guayaquil since 1987 and, from 1998 to 2001 he served as Director for its Research and Development Institute (IIFIUC). From September 1989 to July 1990, he attended the Earthquake Engineering Course in the International Institute of Seismology and Earthquake Engineering (IISEE), in Tsukuba, Japan. He also attended courses in Peru (1992), Italy (1993), Mexico (1998), and Sweden (2001), in the area of Disaster Mitigation and Management. From 1992 to 2001, he worked as consultant to various organizations such as United Nations, Organization of The American States, World Health Organization and the Municipal Government of Guayaquil, in the fields of Structural Vulnerability Assessment and Seismic Risk Mitigation. From 1996 to 2001, he worked as a researcher and project manager to Universidad Católica and the National Foundation for Science and Technology in the fields of Earthquake Engineering and Low-cost Housing. In July 2001, he became a member of the International Existing Building Code Committee (IEBC) of the International Code Council (ICC). In January 2002, he entered the Graduate Program in Structural Engineering at The University of Texas at Austin, where he received the degree of Master of Science of Engineering, in August 2003 and started his Ph.D. studies in September 2003.

Permanent Address: Urdesa Norte, Ave. 4ta #418 y Calle Quinta (Planta Baja)
Guayaquil, Ecuador

The author typed this Dissertation